Testing the Field Content of Cosmic Inflation

LAURA IACCONI

SUPERVISORS:
Prof. David Wands
Dr. Matteo Fasiello
Dr. Hooshyar Assadullahi

Institute of Cosmology and Gravitation
UNIVERSITY OF PORTSMOUTH

The thesis is submitted in partial fulfilment of the requirements for the award of the degree of DOCTOR OF PHILOSOPHY of the University of Portsmouth.

JUNE 2022

Abstract

In this thesis we study cosmological inflation, a period of accelerated expansion in the very early universe. According to the simplest models, inflation is driven by a single scalar field that slowly rolls down its own potential. Despite the great success of single-field inflation, usually high-energy theories beyond the standard model accommodate a richer particle content. For this reason, in this thesis we explore different ways of testing extra fields present during inflation, especially considering their effects in the gravitational wave sector.

In the first part of this thesis, we examine light spin-2 fields, described within an effective field theory approach. We show that when the helicity-2 sound speed decreases during inflation, the spin-2 fields can induce primordial gravitational waves growing towards small scales. We explore the region of parameter space which can be probed by the upcoming LISA mission at interferometer scales. These light spin-2 fields would also mediate the tensor 3-point correlation function, and we therefore study the properties of the bispectrum signal, its amplitude in the equilateral and squeezed configurations and shape. We also discuss a possible way of indirectly testing the bispectrum on small scales, and identify the parameter space generating percent level anisotropies at scales to be probed by SKA and LISA.

In the second part of this thesis, we consider the presence of an additional scalar field, working in the framework of cosmological α–attractors, originally formulated in terms of a radial and angular field living in a hyperbolic field space. We focus on potentials endowed with an inflection point, and compare single- and two-field models leading to enhanced scalar fluctuations on small scales. While in the single-field case ultra-slow-roll dynamics at the inflection point is responsible for the growth of the power spectrum, in the multi-field set-up we study the effect of geometrical destabilisation and non-geodesic motion in field space. We show that compatibility with CMB measurements on large scales constrains the small-scale phenomenology, with primordial black holes that can only be produced with very light masses, $M \lesssim 10^8\,\mathrm{g}$, and GWs induced at second-order peaked at ultra-high frequencies, $f \gtrsim 10\,\mathrm{kHz}$.

Acknowledgements and Dedication

I cannot possibly thank enough my amazing supervisors, Prof. David Wands, Dr. Matteo Fasiello and Dr. Hooshyar Assadullahi, for guiding me in this journey and teaching me basically everything I know (and for bearing with me thorough our *very* long meetings). I am extremely grateful for the time you devoted to me. In particular, I would like to thank David for his support, endless patience and for the friendly environment he created, encouraging me to discuss ideas and ask questions, and for being someone I can talk to about what (good or bad) is going on.

I would like to thank my examiners, Prof. David Seery and Dr. Johannes Noller, for carefully reading my thesis, and for the fruitful discussion we had about this work.

A special mention to my friends in the UK, especially my fellow ICG Colleagues, as well as my dear old friends from Italy, for all the happiness they have given me, for being there for me always, particularly when long phone calls were everything we had.

I would like to thank my English family, Jean, David, Elizabeth, Colin and Catherine, for their kind generosity and for making me feel part of their beautiful family.

I want to express all my love and gratitude to Chiara, Mum and Dad, thank you for always trying to find a way to be part of my life, especially when we couldn't see each other for months. I will always treasure the time we devoted to each other, mostly the long walks we shared between Dorset and Formigine.

Finally, and most importantly, I want to thank Michael, for being on my side every day, even (and especially) when it is not easy. Let's continue to climb mountains together.

I would like to dedicate this thesis to Michael, Chiara, Mum and Dad.

AUTHOR'S DECLARATION

Whilst registered as a candidate for the above degree, I have not been registered for any other research award. The results and conclusions embodied in this thesis are the work of the named candidate and have not been submitted for any other academic award.

Chapters 1, 2 and 3 are introductory chapters, written by myself and drawn from many references, as cited where appropriate. Chapter 4 is based on [1], while chapter 5 is based on [2]. Chapter 6 is based on [3] and chapter 7 contains discussions about work in progress following from the research accomplished in this thesis.

I am the first author of each publication that this thesis is based on, and in each of these I performed all of the analytic and numerical calculations, either originally or as checks for my co-authors.

Table of Contents

List of Tables

List of Figures

Figure **Page**

CHAPTER 1

INTRODUCTION

Cosmology is a branch of physics studying the evolution of the universe, aiming at understanding its origin and all cosmological observations in terms of a complete physical model.

At the foundations of all modern studies of cosmology there are two assumptions. First that the laws of gravity are described by general relativity (GR), the theory of gravity put forward by Albert Einstein in 1915 [5]. A first observational test of GR was performed during the 1919 expedition to Prìncipe and Sobral lead by the astronomers Eddington and Dyson, who detected a deflection of starlight due to the presence of the Sun in accordance with the value predicted by GR [6]. The final confirmation of GR arrived in 2016 with the first direct detection of gravitational waves emitted by a black hole binary merger [7], whose existence was predicted by Einstein a century before. This discovery marked a landmark in modern physics, from theoretical cosmology to observational astrophysics.

Extensive tests of GR have been performed since then, from experiments looking at effects of gravity on very large scales to laboratory-size probes, and up to now no deviations from GR have been detected [8]. We therefore work under the assumption that the theory describing gravity in the universe is GR.

The second pillar of cosmology is the cosmological principle. The first detection of large angular scale anisotropies of cosmological origins in the Cosmic Microwave Background by the COBE mission in 1992 [9], together with observations of the distribution of galaxies [10], shows that the universe is homogeneous and isotropic on scales larger than

100 Mpc. Clearly on smaller scales the universe is filled with inhomogeneous structures, such as galaxies and clusters of galaxies, but at early times the universe looks the same at each point and in every direction. The cosmological principle entails that the laws of physics governing the universe are the same for all observers, crucially making it knowable to us.

Based on the cosmological principle and GR, the Hot Big Bang model of cosmology stands as our current best understanding of the history of the universe, from an initial very hot and dense state to the universe we observe today, filled with clusters of galaxies separated by voids.

Approximately 13.8 billion years ago, there was no concept of spacetime and the entire universe was in a state where the distance between points in it vanished, usually called the *Big Bang singularity* [11, 12]. The physical laws we use to understand the world around us break down at such high energies, and cannot be used to describe such a state, where even space and time lose their meaning [12]. The universe then started to expand from an initial explosion, the *Big Bang*, that originated spacetime itself and took place in each point of the universe. We note here that, regarding GR as the low-energy effective field theory (EFT) of some unknown theory of quantum gravity, one expects perturbative calculations in GR to remain valid only up to some cut-off scale of the order of the Planck mass, M_P. In light of this, predicting an initial singularity state relies on extrapolating the EFT treatment beyond its regime of validity, and needs therefore to be regarded as our *current* (and possibly inadequate) picture of the universe initial state, which will necessarily be updated once we understand the super-Planckian physics that actually regulates processes at those high-energies.

At the very beginning, the universe was very dense and hot and not much is known about it; the laws governing gravity and fields at these high energies are beyond our current understanding of physics. For example, today we see the four forces of nature, i.e. the gravitational, electromagnetic, strong, and weak force, acting separately, but they would probably be unified in a single force at very high energies, very soon after the Big Bang. The progressive separation of the four forces is caused by phase transitions, e.g. as the temperature of the universe decreases, it crosses specific values that trigger changes in the way particles interact. Some speculative theories have been put forward to unify the strong nuclear force with the electroweak interaction at energies as high as 10^{17} GeV (see e.g. the textbook [13]), while the mechanism to unify these with gravity is still unknown, possibly constituting the holy grail of theoretical physics. In the following we assume that, as the universe expands and cools down, two phase transitions signal

the separation of the gravitational and strong forces, while the electromagnetic and weak forces are still unified at this point. The exact temperature triggering these phase transitions is not known, due to the incomplete theoretical knowledge we have about the high energy theory.

When the energy drops below 10^{18} GeV, also known as the Planck scale, gravity can be described by general relativity and the fields making up the universe's content by quantum field theory.

At this stage, the universe possibly underwent a period of accelerated expansion, that increased its size at least by a factor of e^{60} in a tiny fraction of a second, between approximately 10^{-34} s and 10^{-33} s after the Big Bang. This phase is known as cosmological inflation (see e.g. [14] for a review), which we review in great detail in section 2 and will be the main focus of this thesis. In the simplest models of inflation, a scalar field slowly rolling down its own potential is responsible for the (quasi-)exponential expansion of the universe. At the end of inflation the scalar field decays into standard model particles during a process called reheating [15], which provides the initial conditions for the subsequent evolution of the universe.

At this point the temperature of the universe is too high to allow quarks and gluons to form baryons and mesons, 3-quark and quark-antiquark systems respectively, and the quark-gluon plasma is thermalised.

When the temperature drops below 100 GeV the electroweak phase transition takes place: the Higgs field acquires a vacuum expectation value and the W and Z bosons acquire their masses through the Higgs mechanism [16, 17]. The weak force is separated from the electromagnetic interaction, that is now mediated by massless photons.

At 150 MeV the Quantum Chromodynamics phase transition [18] takes place, with quarks and gluons, previously forming a plasma, bonding to form baryons and mesons, and their antiparticles.

At 1 MeV the neutrinos decouple from the primordial plasma and start streaming freely as the Cosmic Neutrino Background (CνB) [19], analogous to the Cosmic Microwave (CMB) background, a free stream of photons released later on. The neutrinos making up the CνB have very low energies, which makes the CνB practically impossible to detect, even if indirect evidence of its existence is given by observations of the CMB photons [19].

As the temperature continues dropping, the hadron/antihadron pairs created are no longer thermalised and annihilate each other, producing high-energy photons. An initial asymmetry between particles and antiparticles explains why a residue of baryonic

matter is left behind in this process, while the corresponding antimatter is completely wiped out [20]. The process accounting for the initial asymmetry between matter and antimatter is called baryogenesis [21], and whereas a lot of theories have been proposed to explain it, there is no compelling model supported by observational evidence at the moment. When the temperature drops to 500 keV also leptons and antileptons annihilate each other, leaving the universe filled with photons, neutrinos, some leptons and hadrons in the form of protons and neutrons.

Around 3 minutes after the Big Bang, or when the temperature dropped to 100 keV, the light elements nuclei, i.e. deuterium, helium, lithium and beryllium, were formed in a process known as Big Bang nucleosynthesis [22, 23]. The light elements abundance in old galaxies and in the intergalactic medium provides one of the strongest proofs of evidence for Big Bang cosmology.

When the temperature dropped below 0.75 eV, the universe became dominated by non-relativistic matter. From this point small perturbations in the primordial plasma, seeded by quantum fluctuations produced during inflation, are no longer erased by the high energy photons and can start evolving to form denser regions.

As the temperature continues dropping, the photons are not energetic enough to break proton-electron bound states, and stable neutral hydrogen forms. This process is called *recombination*. After recombination the number of free electrons drops, and Thompson scattering between photons and electrons becomes inefficient. As a consequence, the photons decouple from the primordial plasma and start freely streaming. While we cannot observe electromagnetic light emitted before the photon decoupling, now for the first time the universe is transparent to electromagnetic radiation and we can observe the freely streaming photons as the Cosmic Microwave Background. Discovered by accident in 1965 by the radio astronomers Penzias and Wilson [24], the CMB constitutes our best source of information about the early universe.

After photon decoupling, the only photons streaming through the universe were the CMB ones and those released by a rare electron transition in neutral hydrogen atoms, emitted with wavelength of 21 cm [25, 26]. Stars and galaxies have not formed yet, there are no sources emitting light in the universe and this period is therefore known as the *dark ages*. Hundreds of millions years after the Big Bang, the first generation of stars and the earliest galaxies started forming [27], ending the dark ages. These old stars, galaxies and quasars emit intense radiation that reionises universe, i.e. the high-energy photons emitted break neutral hydrogen atoms into a plasma of protons and electrons. This process is known as *reionisation* [28]. In the meantime, perturbations in the matter

distribution continue to grow to form younger stars, galaxies and clusters of galaxies.

About 9 billions of years after the Big Bang, the energy density of matter became comparable to that of dark energy, an unknown form of energy that behaves like a cosmological constant and accounts for 70% of the universe energy density today [29]. Due to the effect of dark energy the universe expansion accelerates, as first discovered in 1998 by observations of type Ia supernovae [30, 31] and later confirmed by the analysis of CMB anisotropies [32]. We live in this epoch of the universe's history, known as the dark-energy-dominated era.

In the following we provide more mathematical details on some specific aspects of the Big Bang model outlined above. In section 1.1 we introduce the description of spacetime in general relativity, specialising the discussion on the only metric compatible with the cosmological principle in section 1.2.1. In sections 1.2.2 and 1.2.3 respectively, we describe the dynamics of the universe as dictated by general relativity and introduce the *Lambda Cold Dark Matter* cosmological model, or ΛCDM, which constitutes the current, leading cosmological model to explain the universe content and dynamics. We close the chapter with a review of the three main puzzles within the Big Bang cosmological model in section 1.2.4.

The entire chapter is based on the classic textbooks [13, 33], as well on Baumann's lectures on Cosmology [34].

1.1 The dynamics of spacetime in General Relativity

The dynamics of spacetime is first specified by its metric, which connects the *observer-dependent* spacetime coordinates, $x^\mu = (t, \mathbf{x})$, with an *invariant* quantity describing the spacetime distance between two events, the line-element ds^2. In general relativity the spacetime metric is $g_{\mu\nu}(t, \mathbf{x})$, where the explicit dependence on space and time encodes the effects of gravity, which deforms the spacetime, hence changing the invariant distance between events. The invariant line-element ds^2 is then

$$ds^2 = g_{\mu\nu}(t, \mathbf{x}) dx^\mu dx^\nu \,, \tag{1.1}$$

where the greek indices μ and ν run from 0 to 3. Throughout this thesis we use a mostly plus convention for the metric signature, $(-,+,+,+)$, as well as natural units, $c = \hbar = k_b = 1$.

The time coordinate separation between two events, Δt, is not the same as measured by all observers, therefore it is convenient to introduce the invariant proper-time interval,

$\Delta\tau$. Assuming that two events A and B are separated by a time-like interval, $ds^2 < 0$, we can parametrise the curve connecting them, γ, with the parameter λ, such that e.g. $\gamma(0) = A$ and $\gamma(1) = B$. The proper-time interval $\Delta\tau$ between A and B is

$$\Delta\tau \equiv \int_\gamma \sqrt{-ds^2} = \int_0^1 d\lambda \sqrt{-g_{\mu\nu}\frac{dx^\mu}{d\lambda}\frac{dx^\nu}{d\lambda}} \,. \tag{1.2}$$

Massive, freely-falling particles moving in a curved spacetime are described by the action

$$S = m\int d\tau \,, \tag{1.3}$$

where m is the rest-frame particle's mass. Their motion follows a geodesic trajectory, $X^\mu(\tau)$, defined as the time-like trajectory which extremises the proper-time interval $\Delta\tau$, eq.(1.2), between the initial and final points of motion. The geodesic trajectory is obtained by solving the Euler-Lagrange equation for the action (1.3) and it satisfies

$$\frac{d^2X^\mu}{d\tau^2} = -\Gamma^\mu_{\rho\sigma}\frac{dX^\rho}{d\tau}\frac{dX^\sigma}{d\tau} \,, \tag{1.4}$$

where $\Gamma^\mu_{\rho\sigma}$ is the Christoffel symbol associated with the metric $g_{\mu\nu}$,

$$\Gamma^\mu_{\rho\sigma} = \frac{1}{2}g^{\mu\nu}\left(\partial_\rho g_{\nu\sigma} + \partial_\sigma g_{\nu\rho} - \partial_\nu g_{\rho\sigma}\right) . \tag{1.5}$$

For massless particles, the line element separating two space-like points is $ds^2 = 0$, therefore the definitions given in (1.2) and (1.4) do not hold. By defining the 4-velocity of a particle as $U^\mu \equiv dX^\mu/d\tau$ and its 4-momentum as $P^\mu = mU^\mu$, where $P^\mu = (E, \mathbf{p})$ and $E^2 = m^2 + p^2$, it is possible to recast eq.(1.4) into the compact form

$$P^\mu\nabla_\mu P^\nu = 0 \,, \tag{1.6}$$

which holds also for massless particles. In eq.(1.6), ∇^μ is the covariant derivative associated with the metric $g_{\mu\nu}$,

$$\nabla_\mu P^\nu = \partial_\mu P^\nu + \Gamma^\nu_{\mu\sigma}P^\sigma \,. \tag{1.7}$$

After looking into the kinematics of particles in general relativity spacetime, we describe now the dynamics of spacetime and matter. Let us consider the action of generic matter in a spacetime with metric $g_{\mu\nu}(t, \mathbf{x})$ and cosmological constant Λ [35, 36],

$$S = \frac{M_p^2}{2}\int d^4x\sqrt{-g}\,(R - 2\Lambda) + \int d^4x\sqrt{-g}\,\mathscr{L}_{\text{matter}} \,, \tag{1.8}$$

where M_p is the reduced Planck mass, defined in terms of Newton's gravitational constant G as $M_p = 1/\sqrt{8\pi G}$, g is the determinant of the metric $g_{\mu\nu}$ and $\mathscr{L}_{\text{matter}}$ is the lagrangian density describing matter. The first term in eq.(1.8) is known as the Einstein-Hilbert action, where R is the Ricci scalar, a geometrical quantity built from the metric $g_{\mu\nu}$. In particular, the Riemann tensor is defined in terms of the Christoffel symbol of the metric, eq.(1.5), as

$$R^{\sigma}_{\rho\mu\nu} = \partial_\mu \Gamma^{\sigma}_{\rho\nu} - \partial_\nu \Gamma^{\sigma}_{\rho\mu} + \Gamma^{\sigma}_{\lambda\mu}\Gamma^{\lambda}_{\rho\nu} - \Gamma^{\sigma}_{\lambda\nu}\Gamma^{\lambda}_{\rho\mu} \,. \tag{1.9}$$

By contracting two indices in $R^{\sigma}_{\rho\mu\nu}$, one obtains the Ricci tensor,

$$R_{\mu\nu} = R^{\sigma}_{\mu\sigma\nu} \tag{1.10}$$

and the contraction of $R_{\mu\nu}$ with the inverse metric $g^{\mu\nu}$ yields the Ricci scalar, or scalar curvature,

$$R = g^{\mu\nu} R_{\mu\nu} \,. \tag{1.11}$$

Applying the principle of least action to eq.(1.8), we can derive the equations of motion for this system. We introduce a small variation in the metric, $g_{\mu\nu} \to g_{\mu\nu} + \delta g_{\mu\nu}$, vary the action with respect to the small perturbation $\delta g_{\mu\nu}$ and impose this variation to vanish. This yields the Einstein equations

$$G_{\mu\nu} = \frac{1}{M_p^2} T_{\mu\nu} - \Lambda g_{\mu\nu} \,, \tag{1.12}$$

where the Einstein tensor $G_{\mu\nu}$ is defined as

$$G_{\mu\nu} \equiv R_{\mu\nu} - \frac{1}{2} R g_{\mu\nu} \tag{1.13}$$

and the energy momentum tensor for the matter fields $T_{\mu\nu}$ is defined as

$$T_{\mu\nu} \equiv \frac{-2}{\sqrt{-g}} \frac{\delta\left(\sqrt{-g}\,\mathscr{L}_{\text{matter}}\right)}{\delta g^{\mu\nu}} \,. \tag{1.14}$$

In the Einstein equations (1.12), the left-hand side, related to the spacetime geometry, is directly connected with the matter content of the spacetime, in the form of matter or a cosmological constant. Matter and geometry are two sides of the same coin, with the geometry of spacetime dictating to matter how to move and the matter setting the curvature of the spacetime itself.

Conservation of the Einstein tensor, known as the Bianchi identity, $\nabla^\mu G_{\mu\nu} = 0$, yields the local conservation of the energy-momentum tensor,

$$\nabla^\mu T_{\mu\nu} = 0\,, \tag{1.15}$$

where the $\nu = 0$ component corresponds to the conservation of energy, while the three remaining space-like components correspond to momentum conservation.

We note that the conservation of the energy-momentum tensor is compatible with the presence of a cosmological constant in eq.(1.8), as the metric $g_{\mu\nu}$ is covariant, $\nabla^\mu g_{\mu\nu} = 0$. As we show later, cosmological observations clearly point to the presence in the universe of energy in the form of a cosmological constant, which justifies why we have introduced it in eq.(1.8) in the first place[1].

1.2 The Friedmann–Lemaître–Robertson–Walker universe

1.2.1 FLRW metric

While in the previous section we have worked in a generic spacetime with metric $g_{\mu\nu}(t, \mathbf{x})$, we specialise here to the Friedmann–Lemaître–Robertson–Walker (FLRW) metric, which is the only form of metric compatible with the cosmological principle [34]. In FLRW the invariant line element reads

$$ds^2 = -dt^2 + a(t)^2 \left[\frac{dr^2}{1 - Kr^2} + r^2 \left(d\theta^2 + \sin^2(\theta) d\phi^2 \right) \right] , \tag{1.16}$$

where $a(t)$ is the scale factor, describing the time-evolution of the universe, usually dimensionless and normalised at unity today, $a(t_0) = 1$. In eq.(1.16), r is the radial comoving coordinate and θ and ϕ are the comoving angular coordinates, and the factor in $[\cdots]$ is the line element of a maximally-symmetric 3D space with constant curvature, K. Here K will take only three, discrete, values: $K = 0$ or flat space, corresponding to a 3D Euclidean space, $K = 1$ or positively-curved space, corresponding to a 3-sphere embedded into a 4D Euclidean space, and $K = -1$ or negatively-curved space, corresponding to an hyperboloid embedded into a 4D Lorentzian space. We note that for the metric in eq.(1.16), only a function of time, $a(t)$, and a constant, K, are sufficient to describe all the degrees of freedom of the universe spacetime.

[1] In other words, a term proportional to $g_{\mu\nu}$ is the single relevant infrared operator allowed by the symmetries, so it would be surprising if we did not include it.

In the FLRW metric time and space coordinates are treated on a different footing, e.g. the scale factor $a(t)$ multiplies only the spatial line element. Especially for the study of light propagation, it is useful to introduce the concept of conformal time η, defined as

$$d\eta \equiv \frac{dt}{a(t)}\,, \tag{1.17}$$

where t is the coordinate time. Using conformal time, the FRLW metric (1.16) reads

$$ds^2 = a(\eta)^2 \left[-d\eta^2 + \frac{dr^2}{1-Kr^2} + r^2 \left(d\theta^2 + \sin^2(\theta) d\phi^2 \right) \right]\,, \tag{1.18}$$

where $a(\eta)$ is the conformal scale factor.

An important quantity in modern cosmology is the *Hubble parameter*, defined as

$$H \equiv \frac{\dot{a}}{a}\,, \tag{1.19}$$

which gives the expansion rate of the universe. In general H is not a constant, while its value measured today, H_0, is usually called the *Hubble constant*.

When describing distances between points using the metric (1.16), e.g. the distance of an object from the origin $r = 0$, it is important to distinguish between the *comoving* distance r, which remains the same as the universe expand, and the *physical* distance $r_{\rm phys} = a(t)r$, which increases as the universe expands. It follows that the physical velocity of a point is

$$v_{\rm phys} \equiv \frac{dr_{\rm phys}}{dt} = a\dot{r} + Hr_{\rm phys}\,, \tag{1.20}$$

where eq.(1.19) has been used. The first contribution to $v_{\rm phys}$ is the peculiar velocity, i.e. the velocity of the object with respect to the coordinate grid, and the second term takes into account the physical velocity of the point due to the expansion of the coordinate grid itself.

For galaxies moving in the Hubble flow, i.e. distant enough that their peculiar velocities are smaller than the velocity due to the expansion, eq.(1.20) becomes

$$v_{\rm phys} = Hr_{\rm phys}\,, \tag{1.21}$$

known as the *Hubble law*. In other words, galaxies are moving away from the Earth at speeds proportional to their physical distance, with their motion only due to the expansion of the universe. The proportionality constant gives an indication of the present rate of expansion, H_0. The first observation of the Hubble law in 1929 by Edwin Hubble

[37], yielding $H_0 = 500\,\mathrm{km\,s^{-1}\,Mpc^{-1}}$, was the first confirmation of the expansion of the universe and constitutes a strong evidence supporting the Big Bang model.

Efforts to measure the Hubble constant continued over the decades after the 1929 measurement. In more recent years, H_0 is usually inferred from Cosmic Microwave Background measurements assuming a specific cosmological model, or directly measured from the luminosity of type Ia supernovae in the local universe in a model-independent way. Assuming the ΛCDM model, analysis of the *Planck* data yields $H_0 = 67.44 \pm 0.58\,\mathrm{km\,s^{-1}\,Mpc^{-1}}$ [29], while late-time measurements produce $H_0 = 73.04 \pm 1.04\,\mathrm{km\,s^{-1}\,Mpc^{-1}}$ [38]. The two results are in tension at more than 5σ, possibly hinting at unknown systematic errors in the supernovae data analysis or at physics beyond the ΛCDM model that could shift to higher values the H_0 inferred from CMB measurements. The H_0 tension is a pressing issue in modern cosmology, see [39] for a review.

As for the H_0 measurements described above, most of the ways we observe the universe involve detecting light coming from astrophysical and cosmological sources[2]. The momentum of every particle travelling across an expanding universe as seen by comoving observers decays with the expansion, $p \propto 1/a$, which has a fundamental consequence for the light we observe. Consider light being emitted with wavelength λ. Given that the wavelength of light is inversely proportional to its momentum, it scales as $\lambda \propto a$. Therefore for a photon emitted at time t and detected on Earth at time t_0, the wavelength at detection is

$$\lambda(t_0) = \frac{a(t_0)}{a(t)}\lambda(t)\,. \tag{1.22}$$

For an expanding universe the scale factor increases with time, $a(t_0) > a(t)$, therefore the wavelength at detection is larger than the wavelength at emission, $\lambda(t_0) > \lambda(t)$. By defining the *redshift parameter* as the fractional shift in wavelength for a photon emitted at time t and detected today on Earth,

$$z \equiv \frac{\lambda(t_0) - \lambda(t)}{\lambda(t)}\,, \tag{1.23}$$

and using eq.(1.22), one finds $1 + z = a(t_0)/a(t)$. The usual normalisation for the scale factor, $a(t_0) = 1$, yields

$$1 + z = \frac{1}{a(t)}\,. \tag{1.24}$$

As it is connected with the time-dependent scale factor, z is often used to give an indication of the time when specific events happened during the universe history.

[2] In addition to this, a new and exciting chapter in observational cosmology has been opened after the first direct detection of gravitational waves in 2016 [7].

1.2.2 Dynamics of the FLRW universe

The dynamics of the FLRW universe is described by the Einstein equations, eq.(1.12), where now the metric $g_{\mu\nu}$ is the FLRW metric (1.16). We need to specify the matter content of the universe, described by the energy-momentum tensor $T_{\mu\nu}$ on the right-hand side of eq.(1.12). The only type of matter which is compatible with the cosmological principle is in the form of a perfect fluid. The energy-momentum tensor of a perfect fluid is

$$T_{\mu\nu} = (\rho + P)u_\mu u_\nu + P g_{\mu\nu} \,, \tag{1.25}$$

where the pressure, P, and the density of the fluid, ρ, are functions only of time, which ensures homogeneity and isotropy, and are measured in the rest-frame of the fluid. The 4-vector u_μ is the (normalised) 4-velocity of the fluid with respect to an observer and it takes the simple form $u_\mu = (-1, \mathbf{0})$ for a comoving observer. In this case, the energy-momentum tensor is

$$T^\mu{}_\nu = \mathrm{diag}(-\rho, P, P, P) \,. \tag{1.26}$$

The perfect fluids relevant for cosmology are typically characterised by a constant equation of state parameter w, defined as

$$w \equiv P/\rho \,. \tag{1.27}$$

Ordinary matter obeys the strong energy condition [13]

$$w \geq -1/3 \,. \tag{1.28}$$

The $\nu = 0$ component of the energy-momentum conservation equation, eq.(1.15), yields the continuity equation

$$\dot{\rho} + 3H\rho(1 + w) = 0 \,, \tag{1.29}$$

where eq.(1.27) has been used. Solving the equation above for ρ as a function of the scale factor yields

$$\rho(t) = \rho(t_0)\, a(t)^{-3(1+w)} \,, \tag{1.30}$$

where $\rho(t_0)$ is todays energy density and the scale factor is normalised, $a(t_0) = 1$. This equation shows how the energy density evolves in an expanding universe, with the scaling with respect to $a(t)$ fixed by w.

Let us consider four different types of perfect fluid relevant for cosmology and use eq.(1.30) to derive the energy density scaling with the scale factor in each case:

- pressureless matter: in this case $w = 0$, or equivalently $P = 0$, and the energy density scales as $\rho \propto a^{-3}$, due to the expansion of the universe increasing the volume. Ordinary baryonic matter after recombination, i.e. atoms and molecules, and cold dark matter, a type of matter that interacts only gravitationally (or very weakly), behave like pressureless matter;

- radiation: a fluid made of relativistic particles, described by $w = 1/3$, has energy density scaling as $\rho \propto a^{-4}$, where the additional dilution is due to the redshift of the energy of each particle, $E \propto 1/a$;

- cosmological constant: Λ violates the strong energy condition for ordinary matter, with $w = -1$. This implies that $\rho \propto$ const; energy is created as the universe expands, a behaviour radically different to all the other types of matter considered so far.

The actual energy content of the universe is given by a combination of the fluids mentioned above, e.g. the total energy density is given in terms of the single components ρ_n as

$$\rho = \sum_n \rho_n \,, \tag{1.31}$$

where the sum runs over all the components. For each component, the equation of state parameter is $w_n = P_n/\rho_n$.

Substituting in the Einstein equations, eq.(1.12), the FLRW metric, eq.(1.16), and the energy-momentum tensor of a collection of different perfect fluids, where for the single fluid $T_{\mu\nu}$ is given in eq.(1.26), yields the *Friedmann equations*

$$H^2 = \frac{\sum_n \rho_n}{3M_p^2} - \frac{K}{a^2} + \frac{\Lambda}{3} \,, \tag{1.32}$$

$$\frac{\ddot{a}}{a} = -\frac{\sum_n \rho_n (1+3w_n)}{6M_p^2} + \frac{\Lambda}{3} \,, \tag{1.33}$$

where we have separated the contributions of pressureless matter and radiation from those of the curvature K and the cosmological constant Λ.

Eq.(1.32) shows that the total energy density, together with Λ and K, determines the expansion rate H. In absence of a cosmological constant ($\Lambda = 0$) and for flat space ($K = 0$), eq.(1.32) implies that the simple presence of matter would cause the scale factor to grow, $H > 0$. Also, eq.(1.33) shows that for $\Lambda = 0$ ordinary matter obeying eq.(1.28) causes the expansion to be decelerated, $\ddot{a} < 0$.

Considering a universe filled with radiation, matter, curvature and cosmological constant, eq.(1.32) can be rewritten as

$$H^2 = \frac{1}{3M_p^2}\left(\rho_r + \rho_m + \rho_K + \rho_\Lambda\right) , \tag{1.34}$$

where ρ_r is the energy density of radiation, ρ_m is the energy density of non-relativitic matter, and $\rho_K \equiv -3M_p^2 K/a^2$ and $\rho_\Lambda \equiv M_p^2\Lambda$ are the effective energy densities associated with the curvature and the cosmological constant respectively.

We can define the *critical energy density* of the universe as the energy density of a flat universe with Hubble parameter H,

$$\rho_{\rm crit}(t) \equiv 3M_p^2 H(t)^2 . \tag{1.35}$$

This allows us to introduce dimensionless parameters to describe the energy density of each component,

$$\Omega_n(t) \equiv \frac{\rho_n(t)}{\rho_{\rm crit}(t)} . \tag{1.36}$$

Considering $\Omega_n(t)$ at the present day, $\Omega_{n,0} \equiv \rho_{n,0}/\rho_{\rm crit,0}$, where $\rho_{\rm crit,0} \equiv 3M_p^2 {H_0}^2$, we can define the set $\{\Omega_{r,0}, \Omega_{m,0}, \Omega_{K,0}, \Omega_{\Lambda,0}\}$ which corresponds to today's values of the energy density of each universe component. In the following we will drop the subscript 0 when refering to the present-day energy-density parameters, unless the context requires us to emphasise the time-dependence of Ω_n.

Together with eq.(1.30), the introduction of eq.(1.36) allows us to rewrite eq.(1.34) as

$$H^2(a) = {H_0}^2\left(\Omega_r a^{-4} + \Omega_m a^{-3} + \Omega_K a^{-2} + \Omega_\Lambda\right) , \tag{1.37}$$

or, equivalently, in terms of redshift, see eq.(1.24), as

$$H^2(z) = {H_0}^2\left[\Omega_r (1+z)^4 + \Omega_m (1+z)^3 + \Omega_K (1+z)^{-2} + \Omega_\Lambda\right] . \tag{1.38}$$

The equations above imply that today

$$1 - \Omega_K = \Omega_r + \Omega_m + \Omega_\Lambda , \tag{1.39}$$

where having Ω_K on the left-hand side shows that the density parameters Ω_r, Ω_m and Ω_Λ add to one if $|\Omega_K| \ll 1$.

1.2.3 The ΛCDM model

The measured values and uncertainties of the cosmological parameters depend on several assumptions, e.g. the data sets considered, the assumed priors for each parameter and the way the analysis is performed. We quote here the present-day energy-density parameters for radiation, matter, curvature and cosmological constant obtained by fitting the *Planck* temperature, polarization and lensing data with a six-parameter ΛCDM model [29]

(1.40)

$$\Omega_r = (9.02 \pm 0.21) \times 10^{-5}\,, \quad \Omega_m = 0.3153 \pm 0.0073\,, \quad |\Omega_K| < 0.005\,, \quad \Omega_\Lambda = 0.6847 \pm 0.0073\,,$$

where measurements are accompanied by the 68% confidence region and upper bounds are given at 95%. We refer the interested reader to [29] for a detailed description of how these measurements are made.

Looking at (1.40), we see that approximately 70% of the universe is an unknown form of energy, for this reason usually called *dark energy*. Measurements of the equation of state parameter for dark energy yield $w = -1.03 \pm 0.03$ (68% C.L.) [29], obtained by combining *Planck* data with Pantheon Supernovae and BAO data. This measurements implies that dark energy behaves like a cosmological constant, Λ, which is why in the following we use the terms *dark energy* and *cosmological constant* interchangeably. Such a large value for Ω_Λ is required to explain the accelerated expansion that the universe is undergoing today. The first detection of a cosmological constant dates back to 1998, when observations of type Ia supernovae showed their luminosity was less than that expected in an universe dominated by matter [30, 31]. This discovery was later confirmed by CMB measurements from the WMAP mission [32]. While explaining the accelerated expansion that the universe is undergoing today, the discovery of the cosmological constant raised fundamental questions in modern cosmology. We do not know what dark energy is, not even if it is an effect induced by, e.g., physics beyond the standard model, or a manifestation of deviations from general relativity explained in the context of modified theories of gravity, see e.g. [40, 41]. A natural candidate for dark energy is the energy density of the vacuum, which can be predicted from quantum field theory to be many orders of magnitude larger that the observed dark-energy energy density. This issue, known as the *cosmological constant problem*, is one of the main challenges of modern physics [42].

Matter makes up around 30% of the universe energy budget, however only 5% of it is constituted by ordinary, baryonic matter, $\Omega_b = 0.049$. It turns out the majority of the matter in the universe is in the form of *cold dark matter*, or CDM, with $\Omega_c = 0.262$.

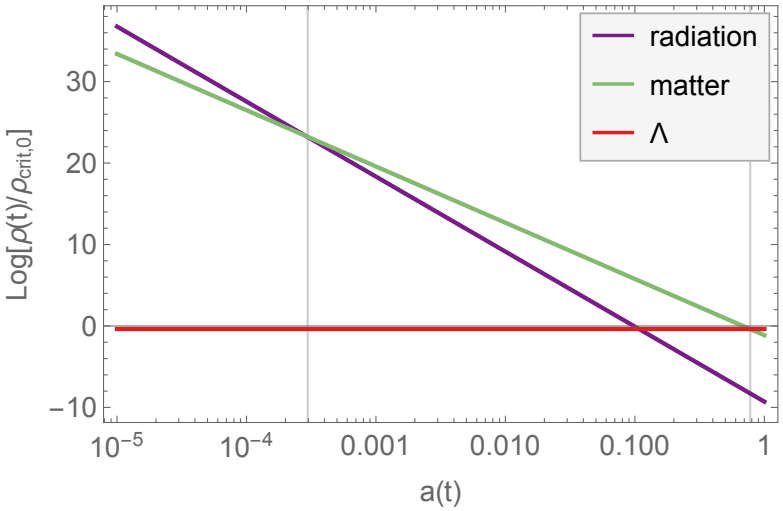

Figure 1.1: Evolution of a dimensionless representation of the energy density, $\rho(t)/\rho_{\text{crit},0}$, as a function of the scale factor for radiation, matter and the cosmological constant in the ΛCDM model.

This is a form of non-relativistic[3], i.e. *cold*, matter that only interacts gravitationally and only very weakly, if at all, through the electromagnetic interaction, which explains the adjective *dark*. CDM plays a fundamental role in structure formation and evidence supporting its existence is provided by rotational curves of galaxies, gravitational lensing and the evolution of galaxy clusters [46]. Nevertheless, we do not know what is the nature of CDM particles, and a lot of effort in modern cosmology is directed to understanding what CDM is.

Radiation only accounts for a very small portion of the universe energy budget today, and is mostly in the form of the CMB photons. Pending a detection, observations suggest that the spatial curvature is very small, pointing to a spatially-flat universe. The smallness of Ω_r and Ω_K imply that Ω_Λ and Ω_m approximately add up to 1 in the ΛCDM model, see eq.(1.39).

Using eq.(1.30) and the ΛCDM parameters in (1.40), we display in figure 1.1 the

[3]The cold dark matter model accounts for the temperature anisotropies in the cosmic microwave background at early times [29], as well as being successful at reproducing the large-scale clustering of galaxies at present day (see e.g. [43]). Using CDM simulations, a number of 'small-scale challenges' have been claimed to afflict the CDM paradigm (see e.g. the review [44]). These motivated dark-matter candidates beyond CDM, e.g. *warm* dark matter, in which the dark matter particles have a non-negligible velocity dispersion in the early universe, or *interacting* dark matter models, where the dark matter particles are coupled with a relativistic species in the early universe. On the other hand, thanks to sophisticated hydrodynamical simulations (see e.g. [45]), it has been shown that the small-scale issues aforementioned can be resolved withing the CDM paradigm by correctly modelling the interaction between CDM and baryons through processes associated with galaxy formation. For this reason, the simplicity of the CDM model and its success in explaining observations made it the leading paradigm for dark matter.

progression of different eras in the universe evolution. The log of the energy density parameter of radiation, matter and cosmological constant is displayed against the scale factor a. Starting from a universe dominated by radiation, ρ_r would decrease rapidly, up to a point when $\rho_r = \rho_m$, also known as matter-radiation equality. After that, the dominant form of energy is matter, until the matter energy density drops below that of the cosmological constant, signalling the transition to the dark-energy-dominated era. This way of looking at the progression of the universe evolution constitutes an account of the thermal history of the universe complementary, and compatible, to that outlined at the beginning of the chapter.

The ΛCDM model, only based on six cosmological parameters, has survived every test posed by observations in the last 20 years[4]. Nevertheless, a lot of work still needs to be done, as the nature of approximately 95% of the universe content, in the form of dark energy and cold dark matter, is still unknown.

1.2.4 Puzzles within the Big Bang cosmology

As outlined in the previous sections, the Big Bang cosmology, together with the universe composition as prescribed by the ΛCDM model, can account for a very broad range of observations, from the existence of a cosmic microwave background to the abundance of light elements, the growth of structure under the gravitational effect of dark matter, the observation of the Hubble law and the current accelerated expansion driven by dark energy.

Nevertheless, from the 1960s it was noted that within the Big Bang model there are some issues; three *problems* emerged, namely the horizon, flatness and monopole problems, signalling fine-tuning was required in the theory to explain some observations. The main issue we will focus on is the horizon problem, as a solution to it would typically solve also the flatness and monopole problems.

The horizon problem is related to the fact that the stunning homogeneity and isotropy of the early universe cannot be a result of causal processes within the standard Big Bang cosmology, and therefore require fine-tuned initial conditions. Cosmological inflation, a phase of accelerated expansion in the very early universe, was put forward in 1980 as a possible solution to the horizon problem [47], naturally driving the universe to homogeneity and isotropy, regardless of the characteristics of its initial state. Before diving into the theory of cosmological inflation in chapter 2, we review the three main

[4]Some might say that the H_0 tension could be the first sign of failure of the ΛCDM model.

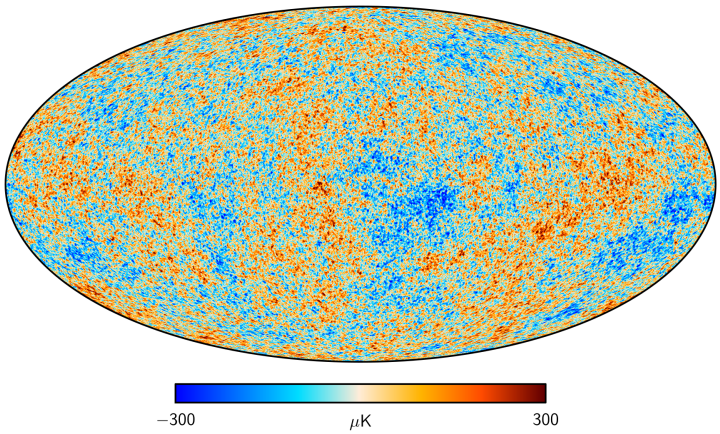

Figure 1.2: *Planck* 2018 map of the temperature anisotropies in the CMB [48]. The red and blue dots represent hotter and cooler spots respectively, with an amplitude $\Delta T/T \simeq 10^{-5}$.

problems of the Big Bang cosmology, discussing in length the horizon problem in section 1.2.4.1, and briefly reviewing the monopole and flatness problems in section 1.2.4.2.

1.2.4.1 The horizon problem

The horizon problem araises from observations of the homogeneity and isotropy of the CMB. The CMB radiation has a thermal black body spectrum, with temperature $T = 2.725\,\mathrm{K}$. The CMB photons temperature is homogeneous and isotropic to a very good level, showing fluctuations in the temperature at the level of 1 in 100,000, $\Delta T/T \simeq 10^{-5}$. Over-dense regions would subsequently evolve to form stars and galaxies filling the universe. In figure 1.2 the CMB anisotropies map as obtained by the *Planck* mission in 2018 is displayed, with red and blue spots corresponding to slightly hotter and colder patches respectively, i.e. regions less or more dense with respect to the background. This is due to the fact that photons corresponding to hotter (colder) spots have to spend less (more) energy to travel out of the potential well created by the slightly larger (smaller) overdensities they come from.

In the following we show that the astonishing homogeneity and isotropy of the CMB cannot be accounted for by causal processes within the standard Big Bang cosmological model.

Let us assume flat space, $K = 0$, and use conformal time η, defined in eq.(1.17) and with the invariant line-element given in eq.(1.18). For particles travelling in the radial direction, $d\theta = d\phi = 0$, eq.(1.18) reduces to

$$ds^2 = a(\eta)^2 \left[-d\eta^2 + dr^2\right] . \tag{1.41}$$

Light travels on null geodesics, $ds^2 = 0$, therefore eq.(1.41) implies that the distance that a photon travels between an initial time η_i and a later time η_f is

$$\Delta\eta \equiv \eta_f - \eta_i = \int_{\eta_i}^{\eta_f} d\eta = \int_{t_i}^{t_f} \frac{dt'}{a(t')}\,, \tag{1.42}$$

where in the last step we use eq.(1.17). Introducing the Hubble radius, defined as $(aH)^{-1}$, the equation above can be rewritten as

$$\Delta\eta = \int_{a_i}^{a_f} (aH)^{-1}\, d\log(a)\,. \tag{1.43}$$

The maximum distance that a CMB photon could have travelled is between the initial singularity at $(a = 0, t = 0)$, and the moment when the CMB was released at recombination,

$$\Delta\eta_{\rm rec} \equiv \eta_{\rm rec} - \eta_i = \int_0^{a_{\rm rec}} (aH)^{-1}\, d\log(a)\,. \tag{1.44}$$

The quantity $\Delta\eta \equiv \eta - \eta_i$ is also known as the *comoving particle horizon*, i.e. the maximum distance from which a particle at time η, e.g. a CMB photon at recombination in eq.(1.44), could have received causal influences in the past.

Using the Friedmann equation (1.32) for flat space, $K = 0$, and without a cosmological constant[5], $\Lambda = 0$, together with eq.(1.30), allows to write the Hubble radius for a universe filled with a fluid with equation of state parameter w as

$$(aH)^{-1} = \left(H_{\rm rec}\, {a_{\rm rec}}^{\frac{3}{2}(1+w)}\right)^{-1} a^{\frac{1}{2}(1+3w)}\,. \tag{1.45}$$

Using (1.45), we can perform the integral in eq.(1.44) and obtain

$$\Delta\eta_{\rm rec} \equiv \eta_{\rm rec} - \eta_i = \frac{2}{1+3w} \left(H_{\rm rec}\, {a_{\rm rec}}^{\frac{3}{2}(1+w)}\right)^{-1} a^{\frac{1}{2}(1+3w)} \Big]_0^{a_{\rm rec}}\,. \tag{1.46}$$

For fluids satisfying $w > -1/3$, see the strong energy condition (1.28), the contribution from early times, i.e. at $a = 0$, vanishes, leading to

$$\Delta\eta_{\rm rec} = \frac{2}{1+3w} \left(H_{\rm rec}\, a_{\rm rec}\right)^{-1}\,, \tag{1.47}$$

which is finite. Eq.(1.47) has profound implications for the standard Big Bang theory: before the CMB photons were emitted at recombination, the universe was filled with

[5]While our purpose here is to illustrate the horizon problem, when quantifying explicitly the angular size of the comoving particle horizon at recombination, see eq.(1.50), we take into account the (small) impact of dark energy at late times.

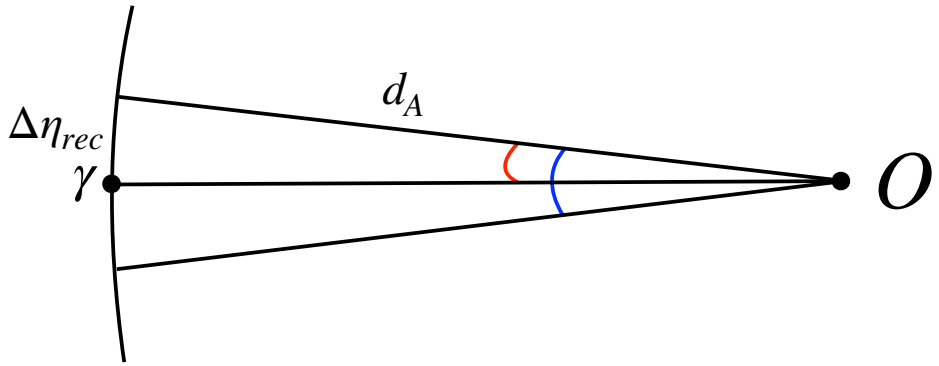

Figure 1.3: Comoving particle horizon of a CMB photon, $\Delta\eta_{\rm rec}$, and comoving distance between an observer O today and a CMB photon γ, d_A. The angles highlighted in red and blue are the angular size of the comoving particle horizon at recombination, $\theta_{\rm hor}$, and the maximum angular separation between two CMB photons that were in causal contact in the past, $\theta_{\rm causal} \equiv 2\theta_{\rm hor}$, respectively.

radiation and non-relativistic matter, obeying the strong energy condition, therefore the CMB photons could only travel a finite distance before recombination.

As a consequence, CMB photons travelling towards us from different patches of the sky could have not been in causal contact in the past. In particular, we can calculate the maximum angular separation in the CMB sky between two photons which were in causal contact in the past. This is defined as twice the angular size of the comoving particle horizon at recombination,

$$\theta_{\rm causal} \equiv 2\theta_{\rm hor} = 2\frac{\Delta\eta_{\rm rec}}{d_A}\,, \tag{1.48}$$

where d_A is the comoving distance between an observer of the CMB today and a CMB photon emitted at recombination, see figure 1.3. Using eq.(1.42) yields

$$\theta_{\rm causal} = 2\frac{\eta_{\rm rec}-\eta_i}{\eta_0-\eta_{\rm rec}} = \frac{\int_{t_i}^{t_{\rm rec}}\frac{dt'}{a(t')}}{\int_{t_{\rm rec}}^{t_0}\frac{dt'}{a(t')}}\,. \tag{1.49}$$

To perform the integrals above, it is useful to use eq.(1.24) to swap the time variable $a(t)$ with redshift, z. This leads to

$$\theta_{\rm causal} = 2\frac{\int_{z_{\rm rec}}^{\infty}\frac{dz'}{H(z')}}{\int_{0}^{z_{\rm rec}}\frac{dz'}{H(z')}} \simeq 2.3\,{\rm deg}\,, \tag{1.50}$$

where the integrals have been performed numerically using eq.(1.38), the ΛCDM parameters in (1.40) and $z_{\rm rec} = 1080$. The result above implies that CMB patches separated

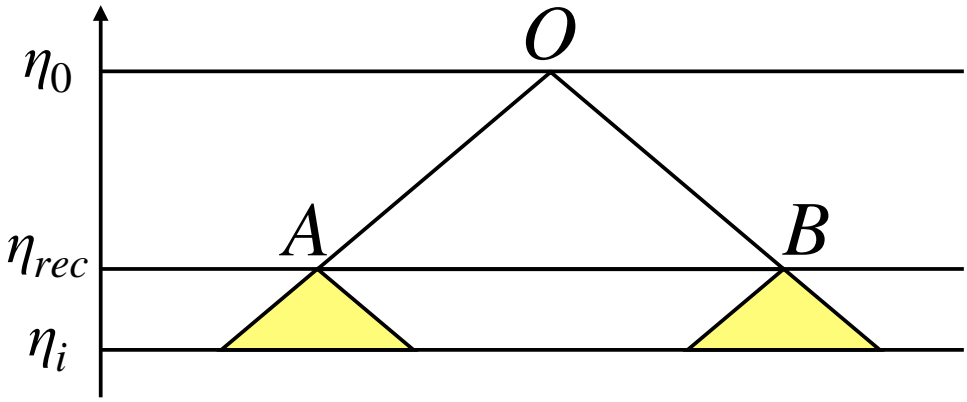

Figure 1.4: Spacetime diagram representing the past light-cones of two CMB photons, A and B, observed today at O. The horizontal and vertical axis display the comoving coordinate, r, and conformal time, η, respectively. This diagram visualises the horizon problem of the standard Big Bang theory, with the two CMB photons never been in causal contanct in the past, from the initial Big Bang singularity at η_i to recombination at $\eta_{\rm rec}$.

by more than 2 deg have never been in causal contact with each other, posing the pressing task to explain the homogeneity and isotropy of the CMB in absence of a common, causal process provided by the standard Big Bang theory.

In figure 1.4 we display a spacetime diagram illustrating the horizon problem. On the vertical axis conformal time is represented, with η_0, $\eta_{\rm rec}$ and η_i signalling respectively the present day, the time of recombination and an initial time when the universe started evolving from the Big Bang singularity. In this picture, two CMB photons, A and B, released at the time of recombination and detected today by an observer O, would have not been in causal contact in the past, i.e. their past light-cones, represented by the yellow triangles, do not overlap in the past.

In section 2.1 we show how an initial phase of accelerated expansion could solve the horizon problem.

1.2.4.2 Flatness and monopole problems

The flatness problem arises from the difficulty of reconciling the standard Big Bang theory with the fact that the universe is constrained to be extremely close to flatness today, see [14] for a review.

Let us consider the Friedmann equation (1.32) in presence of a fluid with energy density ρ and equation of state parameter w, and with $K \neq 0$,

$$H^2 = \frac{\rho}{3M_p^2} - \frac{K}{a^2}\,. \tag{1.51}$$

The time-dependent energy density parameter $\Omega(t)$, defined in eq.(1.36), reads

$$\Omega(t) \equiv \frac{\rho(t)}{3M_p^2 H(t)^2}\,. \tag{1.52}$$

Using eqs.(1.30) and (1.51), yields

$$\Omega(t) = \left(1 - \frac{3M_p^2 K}{\rho(t_0)} a(t)^{1+3w}\right)^{-1}\,. \tag{1.53}$$

By varying $\Omega(t)$ with respect to the scale factor, one obtains

$$\frac{d\Omega}{d\log(a)} = (1+3w)\Omega(\Omega-1)\,. \tag{1.54}$$

$|\Omega - 1|$ can be viewed as a measure of the curvature energy-density Ω_K, see eq.(1.39), and observations point to the value of Ω_K to be very small, or in other words Ω is measured to be very close to one, see the ΛCDM parameters in (1.40). Eq.(1.54) admits the solution $\Omega = 1$, in accordance with observations, but for fluids obeying the strong energy condition[6], i.e. $1 + 3w > 0$, this solution is unstable. While $\Omega_K = 0$ is a stable solution, to explain today's small value of Ω_K given by observations we need to fine-tune its initial value to be even smaller, and this is the reason why this is called the *flatness problem*. Adding a period of evolution before the standard Big Bang expansion where the dominant fluid violates the strong energy condition, $1 + 3w < 0$, would make the solution $\Omega = 1$ stable and solve this issue. We show in chapter 2 how inflation naturally drives the universe towards flatness.

The *monopole problem* arises in the context of grand unified theories [49, 50], high-energy theories based on gauge groups larger than the standard model one, proposed as possible extension of the standard model at energies larger than 10^{16} GeV. When the temperature of the universe drops, the GUT symmetries are broken into the standard model ones, and this process involves the creation of magnetic monopoles in large abundance [51–53]. Magnetic monopoles are not detected today [54], and this fact is not explained withing the standard Big Bang theory[7]. Nevertheless, an initial phase

[6] Clearly dark energy violates the strong energy condition, but we ignore here its effect as it came to dominate the universe energy budget only at late times.

[7] We note that, due to our limited knowledge about physical processes at such high energies, the monopole problem is not universally recognised as a serious issue for the Big Bang theory.

of accelerated expansion set to happen after the phase transition breaking the GUT symmetries would justify why magnetic monopoles are not detected, as their density would have been diluted by the accelerated expansion up to an unobservable level.

CHAPTER 2

COSMOLOGICAL INFLATION

First proposed by Alan Guth as a solution to the horizon and flatness problems [47], cosmological inflation is a period of accelerated expansion in the very early universe [55–57]. In the context of the simplest models, inflation is driven by a scalar field, the *inflaton* ϕ, minimally coupled to gravity and slowly rolling down its potential.

Shorty after the initial proposal, it was realised that inflation not only solves the three main problems of the Big Bang cosmology, but also provides the seeds for the large scale structure of the cosmic web [58–62]. The quantum fluctuations of the inflaton, $\delta\phi(t, \mathbf{x})$, are stretched to cosmological scales by the accelerated expansion and translated into the initial density perturbations that seed anisotropies in the CMB and the large-scale structure of the universe. For these reasons, cosmological inflation is generally accepted as part of the standard model of cosmology. In section 2.1, we show that a fluid violating the strong energy condition, associated with a shrinking Hubble radius and accelerated expansion, can solve the main puzzles of the Hot Big Bang theory. In section 2.2 we review the classical dynamics of a scalar field minimally coupled to gravity and show how a slowly-rolling scalar field violates the strong energy condition and causes an accelerated expansion of the universe. We discuss at length the slow-roll approximation in section 2.2.1, and review the dynamics at the end of inflation in section 2.2.2.

In section 2.3 we discuss the perturbations produced during inflation, in particular we analyse the scalar and tensor fluctuations around a single-field inflationary background in sections 2.3.1 and 2.3.2 respectively, and then present the scalar perturbations

associated with single-field inflation from a different perspective, applying an effective field theory treatment, in section 2.3.3.

In section 2.4 we review models of inflation comprising more than one scalar field.

2.1 Solving the horizon problem

In section 1.2.4.1 we have shown that cosmological fluids obeying the strong energy condition cause the comoving particle horizon to be finite, see eq.(1.47) for the case of CMB photons. In particular, the contribution from early times vanishes,

$$\eta_i = \frac{2}{1+3w}\left(H_{\rm rec}\, a_{\rm rec}{}^{\frac{3}{2}(1+w)}\right)^{-1} a^{\frac{1}{2}(1+3w)}\Big|_{a=0} = 0\,. \tag{2.1}$$

The result would be quite different if the universe was dominated by a fluid violating the strong energy condition, i.e. with equation of state parameter $w < -1/3$. In this case, the contribution from early times would be

$$\eta_i = \frac{2}{1+3w}\left(H_{\rm rec}\, a_{\rm rec}{}^{\frac{3}{2}(1+w)}\right)^{-1} a^{\frac{1}{2}(1+3w)}\Big|_{a\to 0} \to -\infty\,. \tag{2.2}$$

In other words, the comoving particle horizon, e.g. $\Delta\eta_{\rm rec} \equiv \eta_{\rm rec} - \eta_i$ for CMB photons at recombination, diverges with respect to the previous case. If the period characterised by $w < -1/3$ lasts sufficiently long[1], this modification to the expansion would allow all parts of our observed CMB sky to be causally connected, solving the horizon problem.

The scheme depicted in figure 1.4 is now different: η_i is pushed from 0 to $-\infty$, and before the evolution prescribed within the standard Big Bang theory there is a new phase. We represent the modified spacetime diagram in figure 2.1. The past light-cones of the photons A and B now extend back up to the initial singularity at $\eta_i = -\infty$, and they overlap in the region highlighted by the black star. A new phase, dominated by a fluid with $w < -1/3$, starts at η_{in} and stops at η_{end}, after which the standard Big Bang evolution begins.

A violation of the strong energy condition implies that the Hubble radius, defined in eq.(1.45), decreases with time,

$$\frac{d}{dt}(aH)^{-1} < 0\,. \tag{2.3}$$

Using the definition of the Hubble parameter, eq.(1.19), in eq.(2.3) yields

$$\frac{\ddot{a}}{\dot{a}^2} > 0\,, \tag{2.4}$$

implying that a shrinking Hubble radius is associated with accelerated expansion.

[1]The minimum duration of inflation required to solve the horizon problem is about 60 e-folds, see eq.(2.33) for the definition of the number of e-folds of accelerated expansion.

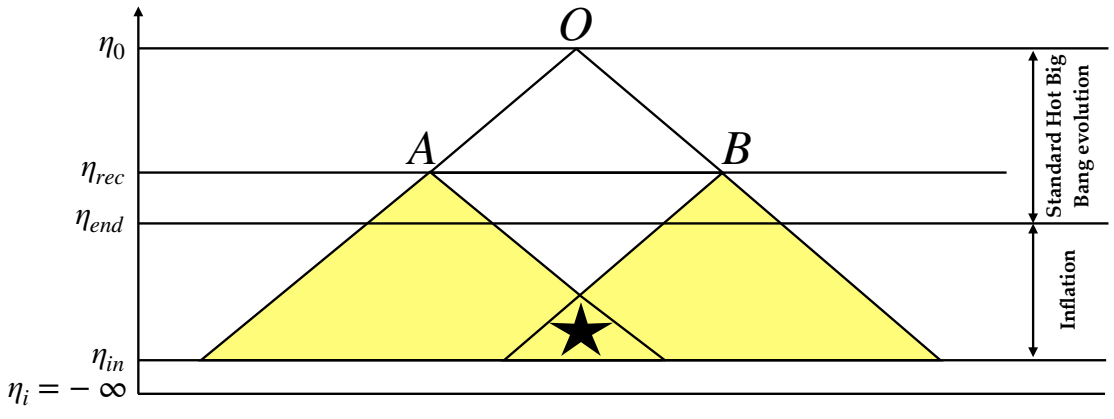

Figure 2.1: Spacetime diagram illustrating the solution of the horizon problem for two CMB photons emitted, or last-scattered, at A and B, and observed today at O, by means of the introduction of a new phase of evolution, with $w < -1/3$, between the initial singularity and the standard evolution prescribed by the Big Bang theory.

2.2 Classical dynamics of single-field slow-roll inflation

The action of a scalar field minimally coupled with gravity reads

$$S = \int d^4x \sqrt{-g} \left[\frac{M_p^2}{2} R - \frac{1}{2} g^{\mu\nu} \partial_\mu \phi \partial_\nu \phi - V(\phi) \right] , \tag{2.5}$$

where $V(\phi)$ is the inflaton potential and we assume for the moment that the inflaton field is homogeneous, $\phi(t)$. From this point on, we set ${M_p}^2 = 1$ unless otherwise stated.

The energy-momentum tensor associated with ϕ is

$$T_{\mu\nu} = \partial_\mu \phi \partial_\nu \phi - g_{\mu\nu} \left(\frac{1}{2} g_{\rho\sigma} \partial^\rho \phi \partial^\sigma \phi - V(\phi) \right) . \tag{2.6}$$

Contracting (2.6) with the inverse metric, ${T^\mu}_\nu = T_{\lambda\nu} g^{\lambda\mu}$, yields the energy density and pressure of the inflaton fluid,

$$T^0{}_0 = -\rho \qquad \text{with} \qquad \rho = \frac{1}{2}\dot{\phi}^2 + V(\phi) , \tag{2.7}$$

$$T^i{}_j = P \delta^i{}_j \qquad \text{with} \qquad P = \frac{1}{2}\dot{\phi}^2 - V(\phi) . \tag{2.8}$$

In particular, $\frac{1}{2}\dot{\phi}^2$ is the kinetic energy of ϕ, with a dot indicating a derivative with respect to cosmic time t. The potential $V(\phi)$ contributes with opposite signs to ρ and P. If the potential energy dominates over the kinetic energy,

$$\frac{1}{2}\dot{\phi}^2 \ll V(\phi)\,, \tag{2.9}$$

then the equation of state parameter of ϕ reads

$$w = \frac{P}{\rho} = \frac{\frac{1}{2}\dot{\phi}^2 - V(\phi)}{\frac{1}{2}\dot{\phi}^2 + V(\phi)} \simeq -1\,. \tag{2.10}$$

This goes to show that under the condition (2.9) the inflaton fluid violates the strong energy condition (1.28), and causes the universe to accelerate. The condition (2.9) means that the inflaton slowly rolls down the potential, and for this reason describing inflation assuming (2.9) goes by the name of *slow-roll inflation*. We explore more in details the slow-roll approximation in section 2.2.1.

The equation of state parameter (2.10) implies that $\dot{\rho} \simeq 0$, see eq.(1.29). Through eq.(1.32), a constant energy density, $\rho \simeq \text{const}$, leads to $H \equiv \dot{a}/a \simeq \text{const}$, which allows us to recover the evolution of the scale factor,

$$a(t) \simeq a_{\text{in}} \exp\left[H(t - t_{\text{in}})\right], \tag{2.11}$$

where a_{in} is the scale factor value at the initial time t_{in}. The background solution for slow-roll inflation is an *almost* de-Sitter spacetime, with the deviation from perfect de-Sitter expansion responsible for the end of inflation, i.e. in a perfectly de-Sitter universe eq.(2.11) is exact and the exponential accelerated expansion is eternal.

Substituting eq.(2.7) in the first Friedmann equation, eq.(1.32), leads

$$H^2 = \frac{1}{3}\left[\frac{1}{2}\dot{\phi}^2 + V(\phi)\right], \tag{2.12}$$

where we are working in flat space, $K = 0$, as the curvature energy-density decays in a universe dominated by a fluid with $w < -1/3$, see eq.(1.54). Noting that $\ddot{a}/a = \dot{H} + H^2$ and using eq.(2.12), allows us to rewrite the second Friedmann equation, eq.(1.33), as $\dot{H} = -(\rho + P)/2$. Using eqs.(2.7)-(2.8) in the latter yields

$$\dot{H} = -\frac{\dot{\phi}^2}{2}\,. \tag{2.13}$$

Taking a time derivative of eq.(2.12) and substituting eq.(2.13) yields the equation of motion for the inflaton field, also known as the *Klein–Gordon equation*,

$$\ddot{\phi} + 3H\dot{\phi} + V_\phi = 0\,, \tag{2.14}$$

where $V_\phi \equiv dV(\phi)/d\phi$. After specifying the inflationary potential and initial conditions for ϕ and $\dot{\phi}$, eqs.(2.13) and (2.14) can be numerically solved to obtain $\{\phi(t), H(t)\}$, specifying the inflationary dynamics. Inflation ends when the condition $w < -1/3$ is no longer met.

2.2.1 The slow-roll approximation

Studying the inflaton dynamics under the slow-roll condition (2.9) allows us to recover some analytical solutions. The slow-roll approximation is better described in terms of a hierarchical series of parameters, defined in terms of the inflaton potential, $V(\phi)$, or the Hubble rate during inflation, $H(\phi)$. We will refer to the two sets of slow-roll parameters as *potential slow-roll parameters* (PSRP) and *Hubble slow-roll parameters* (HSRP) respectively.

The first three PSRS parameters are

$$\epsilon_V \equiv \frac{1}{2}\left(\frac{V_\phi}{V}\right)^2, \quad \eta_V \equiv \frac{V_{\phi\phi}}{V}, \quad {\xi_V}^2 \equiv \frac{V_\phi V_{\phi\phi\phi}}{V^2}, \tag{2.15}$$

while the first three HSRP are

$$\epsilon_H \equiv 2\left(\frac{H_\phi}{H}\right)^2, \quad \eta_H \equiv 2\frac{H_{\phi\phi}}{H}, \quad {\xi_H}^2 \equiv 4\frac{H_\phi H_{\phi\phi\phi}}{H^2}. \tag{2.16}$$

In (2.15) and (2.16) the first two parameters are all that is required to obtain results at first order in the slow-roll approximation, but further parameters can be defined with increasing number of derivatives of $V(\phi)$ or $H(\phi)$. As an example of this progression, we have included in (2.15) and (2.16) also the second-order slow-roll parameters, ${\xi_V}^2$ and ${\xi_H}^2$ respectively.

The HSRP can also be expressed in terms of time derivatives of the inflaton field. By noting that eq.(2.13) can be rewritten as $\dot{\phi} = -2H_\phi$, we can derive the derivative transformation

$$\frac{d}{dt} = -2H_\phi \frac{d}{d\phi}, \tag{2.17}$$

which holds for *single-clock* theories, i.e. inflationary theories with only one relevant degree of freedom, the inflaton ϕ in this case. Eq.(2.17) allows us to transform the derivatives of H with respect to ϕ in (2.16) into derivatives with respect to t,

$$\epsilon_H \equiv -\frac{\dot{H}}{H^2}, \quad \eta_H \equiv -\frac{\ddot{H}}{2H\dot{H}}, \quad {\xi_H}^2 \equiv \frac{1}{2}\frac{\dddot{H}}{H^2\dot{H}} - 2\eta_H^2. \tag{2.18}$$

Eq.(2.13) relates the time derivative $\dot{H}$ to the inflaton velocity, $\dot{\phi}$. By differentiating eq.(2.13) one and two times one can obtain $\ddot{H}$ and $\dddot{H}$ in terms of $\dot{\phi}$, $\ddot{\phi}$ and $\dddot{\phi}$,

$$\frac{\ddot{H}}{\dot{H}} = 2\frac{\ddot{\phi}}{\dot{\phi}}\,, \quad \frac{\dddot{H}}{\ddot{H}} = 2\frac{\ddot{\phi}^2}{\dot{\phi}^2} + 2\frac{\dddot{\phi}}{\dot{\phi}}\,. \tag{2.19}$$

Substituting eqs.(2.13) and (2.19) into (2.18) one finds

$$\epsilon_H \equiv \frac{1}{2}\frac{\dot{\phi}^2}{H^2}\,, \quad \eta_H \equiv -\frac{\ddot{\phi}}{H\dot{\phi}}\,, \quad {\xi_H}^2 \equiv -\left(\frac{\ddot{\phi}}{H\dot{\phi}}\right)^2 + \frac{\dddot{\phi}}{H^2\dot{\phi}}\,. \tag{2.20}$$

The PSRP and the HSRP can be related to each other, e.g. substituting eq.(2.14) into ϵ_V in (2.15) and using (2.20) yields

$$\epsilon_V = \epsilon_H \left(\frac{3-\eta_H}{3-\epsilon_H}\right)^2\,. \tag{2.21}$$

A similar relation is found for η_V,

$$\eta_V = \frac{3\eta_H + 3\epsilon_H - {\eta_H}^2 - {\xi_H}^2}{3-\epsilon_H}\,. \tag{2.22}$$

Keeping only the contributions at first order in the slow-roll parameters, eqs.(2.21) and (2.22) become

$$\epsilon_V \simeq \epsilon_H \tag{2.23}$$

$$\eta_V \simeq \epsilon_H + \eta_H\,. \tag{2.24}$$

We introduce here another series of slow-roll paramaters, which will be used in chapters 4 and 5, defined by means of time-derivatives of the Hubble rate during inflation, H,

$$\epsilon_{i+1} \equiv \frac{\dot{\epsilon}_i}{H\epsilon_i} \quad \text{for}\, i \geq 0\,, \tag{2.25}$$

where a dot represents a derivative with respect to cosmic time, t, and $\epsilon_0 = H_{\rm in}/H$, with $H_{\rm in}$ the value of the Hubble rate at the initial time $t_{\rm in}$. Using (2.25) one can derive

$$\epsilon_1 = -\frac{\dot{H}}{H^2}\,, \quad \epsilon_2 = -2\frac{\dot{H}}{H^2} + \frac{\ddot{H}}{H\dot{H}}\,, \tag{2.26}$$

which can in turn be related to the HSRP, see eq.(2.18),

$$\epsilon_1 = \epsilon_H\,, \quad \epsilon_2 = 2\epsilon_H - 2\eta_H\,. \tag{2.27}$$

Let us now derive the conditions for the slow-roll parameters which realise an accelerated expansion of the background. By differentiating $H \equiv \dot{a}/a$ once with respect to t and substituting it in the definition of ϵ_H in eq.(2.18) yields

$$\epsilon_H = 1 - \frac{a\ddot{a}}{\dot{a}^2}\,, \tag{2.28}$$

which implies that for an accelerated expansion, $\ddot{a} > 0$, the slow-roll parameter has to be small $\epsilon_H < 1$. Additionally, substituting eq.(2.12) and (2.13) and applying the slow-roll condition (2.9) in the definition of ϵ_H in (2.20), yields $\epsilon_H \ll 1$. At leading order in slow-roll $\epsilon_H \simeq \epsilon_V$, see eq.(2.23), therefore the condition above implies $V_\phi \ll V$, i.e. a necessary condition for slow-roll inflation is the flatness of the inflaton potential.

In order for the condition $\epsilon_H \ll 1$ to persist during inflation, also the time-variation of ϵ_H has to remain small,

$$\frac{\dot{\epsilon}_H}{H\epsilon_H} = 2(\epsilon_H - \eta_H) \ll 1\,, \tag{2.29}$$

which implies $\eta_H \ll 1$. Slow-roll inflation is formally defined by requiring all the parameters in the slow-roll hierarchy to be small. Formally inflation ends when $\epsilon_H = 1$.

Eq.(2.12) can be rewritten exactly in terms of ϵ_H as

$$H^2 = \frac{V(\phi)}{3 - \epsilon_H}\,, \tag{2.30}$$

which at leading order in slow-roll simplifies to

$$H^2 \simeq V(\phi)/3\,. \tag{2.31}$$

Additionally, the smallness of η_H implies that the inflaton acceleration, $\ddot{\phi}$, is small, see eq.(2.20), and can therefore be neglected in eq.(2.14), reducing the equation of motion of the inflaton to

$$\dot{\phi} \simeq -\frac{V_\phi}{3H}\,. \tag{2.32}$$

By defining the number of e-folds of inflationary expansion as

$$N \equiv \log\frac{a_{\rm end}}{a_{\rm in}} = \int_{N_{\rm in}}^{N_{\rm end}} dN = \int_{t_{\rm in}}^{t_{\rm end}} H(t)\,dt\,, \tag{2.33}$$

eq.(2.32) becomes

$$\phi'(N) \simeq -\frac{V_\phi}{V}\,, \tag{2.34}$$

where $' \equiv d/dN$. At leading order in slow roll, the second-order differential Klein–Gordon equation becomes first order, no more dependent on the initial inflaton velocity. This means that, once inflation begins, different trajectories in phase space rapidly approach one another, all converging on the *attractor* solution (2.34) [63, 64]. So, as long as the solutions are given enough time to approach the attractor solution *before* inflation enters its observable window, different initial conditions in phase space (asymptotically) lead to the same dynamics.

Once $V(\phi)$ and the initial condition $\phi_{\rm in}$ are specified, eq.(2.34) can be solved analytically to derive $\phi(N)$. Using eq.(2.34), the duration of slow-roll inflation is

$$\Delta N_{\rm tot} \equiv N_{\rm end} - N_{\rm in} = -\int_{\phi_{\rm in}}^{\phi_{\rm end}} d\phi \, \frac{V}{V_\phi} \, . \tag{2.35}$$

Before closing this section, we note that having defined different series of slow-roll parameters is not simply a matter of aesthetics, and one should use the appropriate set depending on the purpose of the calculation. Let us consider for example the first slow-roll parameter, defined in terms of the potential, ϵ_V, or the Hubble rate, ϵ_H. They are related by eq.(2.21) and for most inflationary models their values are almost coincident at early times, e.g. when the CMB scale crossed the horizon, while they slightly deviate from each other towards the end of inflation. The end of inflation is defined as $\epsilon_H = 1$, and not $\epsilon_V = 1$, and using the latter would lead to different results. This is manifest for example in the calculation of the inflaton value at the end of inflation, $\phi_{\rm end}$. As demonstrated in [65], one should calculate $\phi_{\rm end}$ from solving $\left(1 + \sqrt{1 - \eta_V/2}\right)^2 = 1$ (as opposed to $\epsilon_V = 1$), which correctly takes into account the fact that $\epsilon_V = 1$ is only a first-order approximation at the end of inflation.

2.2.2 Reheating

At the end of inflation, the inflaton oscillates about the minimum of its potential $V(\phi)$ and its kinetic energy becomes comparable with its potential energy. During this phase, ϕ, and/or its decay products, must decay into Standard Model particles in order to recover Big Bang nucleosynthesis. The process describing the energy transfer from the inflaton sector to ordinary matter goes by the name of reheating [15].

During reheating the energy density decreases from its value at the end of inflation, $\rho_{\rm end}$, to $\rho_{\rm th}$, when the Standard Model particles are thermalised. Requiring that reheating is complete before the onset of Big Bang nucleosynthesis bounds the value of $\rho_{\rm th}$ from

below. In particular, $\rho_{\rm th}$ is in the range[2] $[(1\,{\rm TeV})^4, \rho_{\rm end}]$ [67], where the upper limit corresponds to the case of instant reheating.

The duration of reheating measured in terms of e-folds after the end of inflation, $\Delta\tilde{N}_{\rm rh} \equiv N_{\rm rh} - N_{\rm end}$, depends on the effective equation of state parameter, $w_{\rm rh}$, and the value of $\rho_{\rm th}$, and is given by

$$\Delta\tilde{N}_{\rm rh} \equiv \frac{1}{3(1+w_{\rm rh})} \log\left(\frac{\rho_{\rm end}}{\rho_{\rm th}}\right). \tag{2.36}$$

Usually reheating can be described as a matter-dominated phase, $w_{\rm rh} = 0$, as we demonstrate in the following for a specific case. When the inflaton starts oscillating around its minimum, the expansion time-scale, H^{-1}, quickly becomes much longer that the inflaton oscillation period. This implies that the drag term in the Klein–Gordon equation (2.14) due to the expansion can be neglected. Assuming that the inflaton potential can be approximated by a simple quadratic minimum, $V(\phi) = \frac{1}{2}m^2\phi^2$, the equation of motion for ϕ becomes that of an harmonic oscillator,

$$\ddot{\phi} + m^2\phi \simeq 0\,. \tag{2.37}$$

Solving eq.(2.37), together with the Friedmann equation (2.12), yields

$$\phi(t) = \sqrt{6}\,\frac{M_p}{m}\,H\cos(mt)\,. \tag{2.38}$$

The inflaton oscillates around its minimum, with a frequency set by the mass m. Substituting eq.(2.38) into the definition of the pressure of the inflaton fluid, P, and taking a time-average, leads

$$\langle P\rangle = 3M_p^2H^2\langle 1 - 2\cos^2(mt)\rangle \simeq 0\,, \tag{2.39}$$

showing that the inflaton behaves as non-relativisitic, pressureless matter, $w_{\rm rh} = 0$, when oscillating around a simple quadratic minimum of its potential.

2.3 Inflationary perturbations

We turn now to the study of quantum scalar and tensor fluctuations around the inflating background.

[2] Recalling that nuclei form at energies $\sim 100\,{\rm keV}$, the reheating temperature has to be larger than $\sim 1\,{\rm MeV}$ to allow for successful Big Bang nucleosynthesis, while being likely much higher to allow for baryogenesis after inflation [66].

In section 2.3.1 we derive the equation of motion for the scalar perturbation, we quantise it and calculate the 2-point correlation function, i.e. the dimensionless scalar power spectrum. We show that canonical single-field slow-roll inflation predicts an almost scale-invariant scalar power spectrum, decreasing towards smaller scales. By applying a similar procedure, we analyse the metric tensor fluctuations in section 2.3.2, derive the tensor power spectrum and show that the amplitude of primoridal gravitational waves generated during inflation is slow-roll-suppressed with respect to that of the scalar perturbations.

In section 2.3.3 we present a unifying perspective on the study of inflationary perturbations, based on an effective field theory (EFT) approach. We review the construction of the EFT of single-field inflation and re-derive the power spectrum of scalar perturbations.

2.3.1 Scalar perturbations

Let us start by perturbing the inflaton field and the spacetime metric,

$$\phi(t,\mathbf{x}) = \phi(t) + \delta\phi(t,\mathbf{x})\,, \tag{2.40}$$

$$ds^2 = -(1+\delta g_{00})dt^2 + 2a\,\delta g_{0i}dx^i dt + a^2(\delta_{ij}+\delta g_{ij})dx^i dx^j\,, \tag{2.41}$$

where $a(t)$ is the scale factor and the perturbations δg_{00}, δg_{0i} and δg_{ij} are functions of space and time. By applying the scalar-vector-tensor decomposition [68] and retaining only the scalar perturbations, we get

$$\phi(t,\mathbf{x}) = \phi(t) + \delta\phi(t,\mathbf{x})\,, \tag{2.42}$$

$$ds^2 = -(1+\delta g_{00})dt^2 + 2a\,\partial_i B dx^i dt + a^2\left[(1-2\zeta)\delta_{ij} + \partial_i\partial_j D\right]dx^i dx^j\,, \tag{2.43}$$

where we see that there is a total of 5 scalar perturbations, even if not all of them are physical, as discussed below.

Two scalar perturbations can be eliminated by using the energy and momentum constraints derived from the Einstein equations (1.12). This reduces the number of scalar perturbations to three,

$$\phi(t,\mathbf{x}) = \phi(t) + \delta\phi(t,\mathbf{x})\,, \tag{2.44}$$

$$ds^2 = -dt^2 + a^2\left[(1-2\zeta)\delta_{ij} + \partial_i\partial_j D\right]dx^i dx^j\,. \tag{2.45}$$

For the purpose of calculating the second-order action for the scalar perturbation, we choose to work in the comoving gauge [34], which for eqs.(2.44)-(2.45) implies

$$D(t,\mathbf{x}) = \delta\phi(t,\mathbf{x}) = 0\,. \tag{2.46}$$

The inflaton is now homogeneous, $\phi(t)$, and the metric (2.45) can be simplified to

$$ds^2 = -dt^2 + a^2(1-2\zeta)\delta_{ij}dx^i dx^j\,, \tag{2.47}$$

where ζ is known as the *curvature perturbation*, as its Laplacian corresponds to the spatial curvature of space-like slices at constant $\phi(t)$ [34]. After carefully removing the four non-physical scalar modes, we are left with one physical scalar perturbation, ζ.

After expanding the action (2.5) around the perturbed metric (2.47), one can derive the second-order action for the scalar perturbation ζ [34],

$$S = \frac{1}{2}\int dt\, d^3\mathbf{x}\, a^3\, \frac{\dot{\phi}^2}{H^2}\left[\dot{\zeta}^2 - \frac{1}{a^2}(\partial_i\zeta)^2\right]\,. \tag{2.48}$$

By defining

$$z \equiv a\frac{\dot{\phi}}{H} = a\sqrt{2\epsilon_H}\,, \tag{2.49}$$

and introducing the (canonically-normalised) Mukhanov–Sasaki variable [34, 69, 70]

$$v \equiv z\zeta\,, \tag{2.50}$$

the action (2.48) can be rewritten as

$$S = \frac{1}{2}\int d\eta\, d^3\mathbf{x}\left[(v')^2 - (\partial_i v)^2 + \frac{z''}{z}v^2\right]\,, \tag{2.51}$$

where we have also switched to conformal time, see eq.(1.17), and $' \equiv d/d\eta$.

By applying the principle of least action to (2.51) and transforming to Fourier space, $v(\eta,\mathbf{x}) = \int \frac{d^3\mathbf{k}}{(2\pi)^{3/2}}\, v_{\mathbf{k}}(\eta)e^{-i\mathbf{k}\cdot\mathbf{x}}$, the equation of motion for $v_{\mathbf{k}}(\eta)$, known as the *Mukhanov–Sasaki equation*, reads

$$v_{\mathbf{k}}{}'' + \left(k^2 - \frac{z''}{z}\right)v_{\mathbf{k}} = 0\,. \tag{2.52}$$

Eq.(2.52) is the equation of motion for an harmonic oscillator with time-dependent frequency, $\omega_k(\eta)^2 = k^2 - z''/z$, which only depends on the modulus k. By differentiating (2.49) twice with respect to conformal time, one obtains

$$\frac{z''}{z} = 2a^2H^2\left(1 + \epsilon_H - \frac{3}{2}\eta_H - 2\eta_H\epsilon_H + \epsilon_H{}^2 + \frac{1}{2}\xi_H{}^2 + \frac{1}{2}\eta_H{}^2\right)\,. \tag{2.53}$$

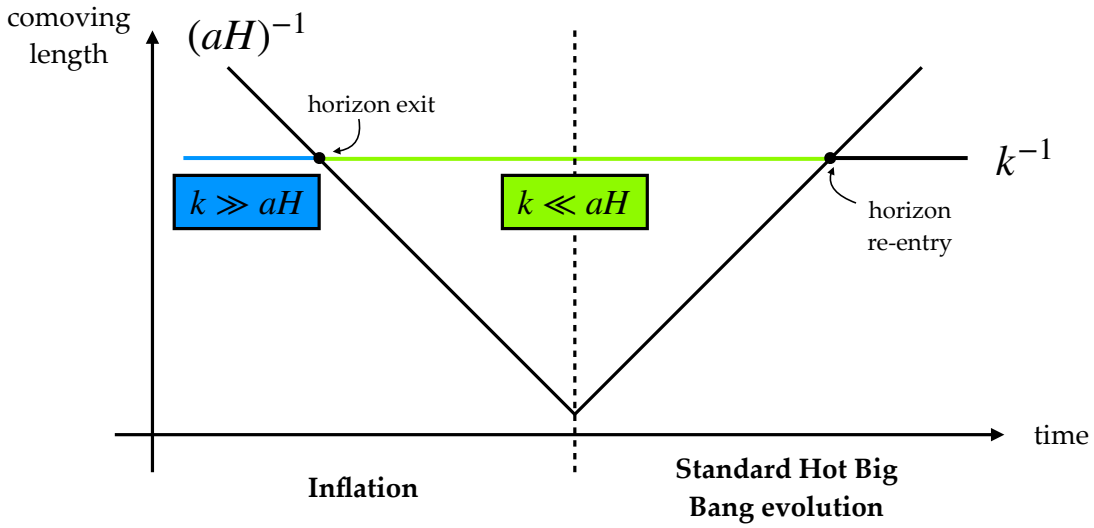

Figure 2.2: Schematic representation showing the horizon crossing of a mode with comoving wavenumber k during and after inflation. The sub-horizon ($k \gg aH$) and the super-horizon ($k \ll aH$) regimes are highlighted in blue and green respectively.

Solution in the de-Sitter limit and quantisation of the curvature perturbation

The inflationary background is *quasi* de-Sitter space, therefore we can study eq.(2.52) in the limit of a de-Sitter universe and gain insight into the behavior of ζ during inflation.

In de-Sitter space, $\epsilon_H = 0$ and $a = \exp(Ht) = -1/(H\eta)$. The size of the causal *Hubble horizon*, defined by the Hubble radius, is $(aH)^{-1} = -\eta$, which decreases for η ranging from $\eta = -\infty$ at very early times to $\eta = 0$. Using $a = -1/(H\eta)$ and the fact that ϵ_H is constant yields $\omega_k(\eta)^2 = k^2 - 2/\eta^2$,

$$v_{\mathbf{k}}'' + \left(k^2 - \frac{2}{\eta^2}\right) v_{\mathbf{k}} = 0\,. \tag{2.54}$$

Eq.(2.54) clearly points to the existence of two different regimes, $k \gg |\sqrt{2}/\eta| \simeq aH$ and $k \ll |\sqrt{2}/\eta| \simeq aH$. These respectively correspond to the *sub-horizon regime*, i.e. the wavelength of the mode k is smaller than the Hubble horizon, and the *super-horizon regime*, i.e. the wavelength of the mode k is larger than the Hubble horizon. We schematically summarise the different regimes of evolution in figure 2.2. Together with the horizontal line representing k^{-1}, the evolution of the Hubble horizon, $(aH)^{-1}$ is also displayed. The horizontal axis represents time, with inflation taking place before the standard evolution prescribed within the Big Bang model. The mode k starts off in the sub-horizon regime, $k \gg aH$, and, after crossing the horizon at $k \simeq aH$, becomes super-horizon, $k \ll aH$. We

highlight the sub-horizon and super-horizon regimes with blue and green colors respectively. The mode k later re-enters the horizon during the standard Big Bang evolution and sources the temperature anisotropies in the CMB.

For k modes that are sub-horizon ($k \gg aH$), eq.(2.52) reduces to $v_{\mathbf{k}}'' + k^2 v_{\mathbf{k}} = 0$, i.e. the equation of motion of an harmonic oscillator with constant frequency, with solution $v_{\mathbf{k}}(\eta) \simeq A\cos(k\eta) + B\sin(k\eta)$.

For k modes that are super-horizon ($k \ll aH$), eq.(2.52) reduces to $v_{\mathbf{k}}'' - 2/\eta^2\, v_{\mathbf{k}} = 0$, with solution $v_{\mathbf{k}}(\eta) \simeq A'\eta^{-1} + B'\eta^2$. By recalling the range of conformal time η, we see that the first solution grows, while the second one corresponds to a decaying mode. The evolution of the curvature perturbation $\zeta_{\mathbf{k}}(\eta)$ on super-horizon scales is therefore

$$\lim_{k\ll aH} \zeta_{\mathbf{k}}(\eta) = \lim_{k\ll aH} \frac{v_{\mathbf{k}}(\eta)}{z} \propto \frac{1}{\eta}\eta = \text{const}\,. \tag{2.55}$$

To summarise, during inflation the curvature perturbation $\zeta_{\mathbf{k}}(\eta)$ oscillates when sub-horizon and then freezes to a constant value after horizon crossing, $k \simeq aH$.

Whilst eq.(2.55) does apply during inflation, it is possible to demonstrate that the curvature perturbation generated within single-field canonical slow-roll inflation remains constant on super-horizon scales after inflation too [71]. This implies that, while perturbations are outside the horizon, we can neglect all the complex physical processes taking place at very high energies in the early universe after inflation is complete, and make a direct connection between the inflationary predictions and late time observables, e.g. the CMB.

We turn now to solving eq.(2.54). The frequency $\omega_k(\eta)^2$ only depends on the modulus k, therefore we can expand the solution, $v_{\mathbf{k}}(\eta)$, as

$$v_{\mathbf{k}}(\eta) = a_{\mathbf{k}}\, v_k(\eta) + a_{-\mathbf{k}}{}^{\dagger}\, v_k(\eta)^*\,, \tag{2.56}$$

where $v_k(\eta)$ and $v_k(\eta)^*$ are two linearly-independent solutions and $a_{\mathbf{k}}$ and $a^{\dagger}_{-\mathbf{k}}$ are two integration constants. By imposing the reality of $v_{\mathbf{k}}(\eta)$, it follows that $a^{\dagger}_{-\mathbf{k}} = (a_{-\mathbf{k}})^*$.

Promoting $a_{\mathbf{k}}$ and $a^{\dagger}_{-\mathbf{k}}$ to quantum operators, we can quantise the field $v_{\mathbf{k}}(\eta)$,

$$\hat{v}_{\mathbf{k}}(\eta) = \hat{a}_{\mathbf{k}}\, v_k(\eta) + \hat{a}^{\dagger}_{-\mathbf{k}}\, v_k(\eta)^*\,, \tag{2.57}$$

with

$$[\hat{a}_{\mathbf{k_1}}, \hat{a}^{\dagger}_{-\mathbf{k_2}}] = \delta^3(\mathbf{k_1} + \mathbf{k_2}) \quad \text{and} \quad [\hat{a}_{\mathbf{k_1}}, \hat{a}_{-\mathbf{k_2}}] = [\hat{a}^{\dagger}_{\mathbf{k_1}}, \hat{a}^{\dagger}_{-\mathbf{k_2}}] = 0\,. \tag{2.58}$$

For the mode $v_k(\eta)$ in (2.57), eq.(2.54) becomes

$$v_k'' + \left(k^2 - \frac{2}{\eta^2}\right) v_k = 0\,, \tag{2.59}$$

with solution

$$v_k(\eta) = c_1\sqrt{\frac{2}{\pi k}}\left(-\frac{\cos(k\eta)}{k\eta} - \sin(k\eta)\right) + c_2\sqrt{\frac{2}{\pi k}}\left(-\cos(k\eta) + \frac{\sin(k\eta)}{k\eta}\right). \tag{2.60}$$

We rewrite the solution (2.60) in a more illuminating fashion,

$$v_k(\eta) = \alpha\frac{e^{-ik\eta}}{\sqrt{2k}}\left(1 - \frac{i}{k\eta}\right) + \beta\frac{e^{ik\eta}}{\sqrt{2k}}\left(1 + \frac{i}{k\eta}\right), \tag{2.61}$$

where the constants $\alpha = -c_2 - ic_1$ and $\beta = -c_2 + ic_1$ are fixed by using the initial condition for $v_k(\eta)$.

The definition of the vacuum associated with the Mukhanov–Sasaki equation in the limit of de-Sitter space in ambiguous. Indeed, by looking at eq.(2.57) we can see that $\hat{v}_{\mathbf{k}}(\eta)$ is left unchanged if $\hat{a}_{\mathbf{k}}$ and $v_k(\eta)$ are both suitably changed. Since $\hat{a}_{\mathbf{k}}$ defines the vacuum of the theory, $\hat{a}_{\mathbf{k}}|0\rangle = 0$, an additional input is required to completely fix $v_k(\eta)$, such that the vacuum state $|0\rangle$ is unambiguously defined. To this end, we note that at sufficiently early times all the modes $v_k(\eta)$ were sub-horizon, $k \gg aH$, obeying eq.(2.59) with $k \gg 2/\eta^2$,

$$v_k''(\eta) + k^2 v_k(\eta) = 0\,. \tag{2.62}$$

This is the equation of motion for an harmonic oscillator with constant frequency, i.e. the Mukhanov–Sasaki equation in the limit of Minkowski space. The modes $v_k(\eta)$ are not affected by gravity and the mode

$$v_k(\eta) = \frac{1}{\sqrt{2k}}\,e^{-ik\eta} \tag{2.63}$$

is the Minkowski vacuum state.

By identifying the initial condition for $v_k(\eta)$ with the Minkowski vacuum (2.63), we can solve the Mukhanov–Sasaki equation in the limit of de-Sitter space, see eq.(2.59), with the initial condition

$$\lim_{\eta\to-\infty} v_k(\eta) = \frac{1}{\sqrt{2k}}\,e^{-ik\eta}\,, \tag{2.64}$$

also known at the *Bunch–Davies vacuum*[3].

[3]Requiring that the initial state correspond to the vacuum, i.e. that the average occupation number of states with momentum k is much less than 1, is ensured by having enough inflation before the observable universe left the horizon. This is realised when the mild requirement $2\Delta N \gtrsim \log M_p/H$ holds, where ΔN here is the number of e-folds already occurred before the observable window of inflation [72].

Taking the $\eta \to -\infty$ limit of (2.61), we can compare it with (2.64) and get $\alpha = 1$ and $\beta = 0$, yielding

$$v_k(\eta) = \frac{e^{-ik\eta}}{\sqrt{2k}}\left(1 - \frac{i}{k\eta}\right). \tag{2.65}$$

The super-horizon limit of $v_k(\eta)$ in eq.(2.65) determines the super-horizon, constant behavior of the curvature perturbation $\zeta_k(\eta)$, see eq.(2.50). Taking the super-horizon limit of $v_k(\eta)$, i.e. $k \ll aH \Rightarrow -k\eta \ll 1$, yields

$$\lim_{-k\eta\to 0} v_k(\eta) = \frac{1}{i\sqrt{2}k^{3/2}}\frac{1}{\eta}. \tag{2.66}$$

Substituting eq.(2.66) into eq.(2.50) and using (2.49), yields the curvature perturbation $\zeta_k(\eta)$ in the super-horizon regime,

$$\zeta_k(\eta) = \frac{i}{\sqrt{2}k^{3/2}}\frac{H}{\sqrt{2\epsilon_H}}\Big|_{k=aH}, \tag{2.67}$$

where the expression is evaluated at $k = aH$ since $\zeta_k(\eta)$ freezes after horizon crossing.

The scalar power spectrum

The quantum fluctuations produced during inflation can be characterised by the correlation functions $\langle\hat{\zeta}(\mathbf{x_1})\hat{\zeta}(\mathbf{x_2})\cdots\rangle$, or equivalently in terms of their Fourier transforms $\langle\hat{\zeta}_{\mathbf{k_1}}\hat{\zeta}_{\mathbf{k_2}}\cdots\rangle$. Quantum Gaussian fields are completely characterised by the 2-point correlation function, $\langle\hat{\zeta}_{\mathbf{k_1}}\hat{\zeta}_{\mathbf{k_2}}\rangle$, while non-zero higher-order correlations contain information about deviations from Gaussianity. The 2-point correlation function for the quantum vacuum curvature fluctuation $\zeta_{\mathbf{k}}(\eta)$ is

$$\langle\hat{\zeta}_{\mathbf{k_1}}\hat{\zeta}_{\mathbf{k_2}}\rangle \equiv \langle 0|\hat{\zeta}_{\mathbf{k_1}}\hat{\zeta}_{\mathbf{k_2}}|0\rangle = |\zeta_k(\eta)|^2\,\delta(\mathbf{k_1}+\mathbf{k_2}), \tag{2.68}$$

which is obtained using eqs.(2.50), (2.57), the commutation relations (2.58) and the vacuum normalisation $\langle 0|0\rangle = 1$. In eq.(2.68), we identify $|\zeta_k(\eta)|^2 \equiv \mathscr{P}_\zeta(k)$ and define the dimensionless power spectrum of the curvature perturbation as

$$P_\zeta(k) \equiv \frac{k^3}{2\pi^2}\mathscr{P}_\zeta(k) = \frac{H^2}{8\pi^2\epsilon_H}\Big|_{k=aH}, \tag{2.69}$$

where eq.(2.67) has been used.

At leading order in slow-roll, $H^2 \simeq V/3$, see eq.(2.31), and $\epsilon_H \simeq \epsilon_V$, see eq.(2.23), therefore $P_\zeta(k)$ can be equivalently written in terms of the inflaton potential $V(\phi)$ and the first PSRP ϵ_V as

$$P_\zeta(k) = \frac{V}{24\pi^2\epsilon_V}\Big|_{k=aH}. \tag{2.70}$$

It is costumary to parametrise the scalar power spectrum on large scales with a simple power-law expression,

$$P_\zeta(k) = \mathscr{A}_s \left(\frac{k}{k_{\rm CMB}}\right)^{n_s - 1 + \frac{\alpha_s}{2}\log(k/k_{\rm CMB}) + \cdots}, \tag{2.71}$$

where $\mathscr{A}_s$ and $n_s - 1$ are the *amplitude* and *spectral tilt* of $P_\zeta(k)$ respectively, defined at the scale $k_{\rm CMB} = 0.05{\rm Mpc}^{-1}$ (chosen as pivot scale as it is best constrained by CMB measurements, and to conform with most of analyses, including *Planck*), and α_s measures the scale-dependence of the tilt. The further $P_\zeta(k)$ is evaluated from $k_{\rm CMB}$, the more we expect the power spectrum to deviate from a simple power law with constant tilt, e.g. the running of the tilt and higher order terms become important.

Assuming $\alpha_s = 0$, $n_s - 1$ quantifies the deviation of the scalar power spectrum from perfect scale-invariance, $P_\zeta(k) \propto k^0$. Considering the expression (2.69) and the fact that in canonical single-field slow-roll inflation H and possibly ϵ_H are time-dependent, e.g. $\eta_H \neq 0$, $P_\zeta(k)$ is expected to be almost scale-invariant, with n_s very close to one, but different from it. Using eq.(2.71), $n_s - 1$ is defined as

$$n_s - 1 \equiv \frac{d\log\left(P_\zeta(k)\right)}{d\log(k)}, \tag{2.72}$$

which is evaluated at horizon crossing $k = aH$. We can transform the derivative with respect to $\log(k)$ into a derivative with respect to the number of e-folds N,

$$\frac{d}{d\log(k)} = \frac{dN}{d\log(k)}\frac{d}{dN}. \tag{2.73}$$

Considering that $\log(k) = \log(a_{\rm in}\exp(N)) + \log(H)$, we get

$$\frac{dN}{d\log(k)} = \left(\frac{d\log(k)}{d\log(N)}\right)^{-1} = (1-\epsilon_H)^{-1} \simeq 1 + \epsilon_H, \tag{2.74}$$

where we have used the fact that $\epsilon_H \equiv -H'/H$ in terms of N. By differentiating $\log\left(P_\zeta(k)\right)$ with respect to N we get

$$\frac{d\log\left(P_\zeta(k)\right)}{dN} = -2\epsilon_H - \frac{\epsilon_H'}{\epsilon_H} = -4\epsilon_H + 2\eta_H, \tag{2.75}$$

where we have used (2.29). Putting eqs.(2.74) and (2.75) together yields

$$n_s - 1 = \left(-4\epsilon_H + 2\eta_H\right)(1+\epsilon_H) \simeq -4\epsilon_H + 2\eta_H \tag{2.76}$$

at first order in slow-roll. In a similar way, one can also calculate

$$\alpha_s \equiv \frac{d^2\log\left(P_\zeta(k)\right)}{d\log(k)^2} = -2\xi_H + 10\epsilon_H\eta_H - 8{\epsilon_H}^2, \tag{2.77}$$

where we have used eq.(2.29) and $\eta_H' = \epsilon_H \eta_H - \xi_H$. The expressions (2.76) and (2.77) are to be evaluated when the CMB scale, $k_{\rm CMB}$, crossed the horizon during inflation. From (2.76) and (2.77), one realises that α_s is slow-roll suppressed with respect to the tilt, n_s, and therefore we expect the power law expansion given in eq.(2.71) to be accurate in single-field slow-roll inflation.

Neglecting the effect of the running of the tilt for the reason above, we see from eq.(2.76) that $P_\zeta(k)$ is predicted to be slightly deviating from scale-invariance, $n_s \neq 1$, in single-field slow-roll inflation, since ϵ_H and η_H are non-zero and small. As we will describe in section 3.1, measurements of the CMB anisotropies are consistent with an almost scale-invariant primordial scalar power spectrum, see (3.5), in perfect agreement with what predicted within single-field slow-roll inflation. Besides resolving the main issues related to the Hot Big Bang cosmology, inflation also provides the seeds for the large-scale structure of the cosmic web.

Let us pause here for a moment to remind the reader that, despite being the leading paradigm describing the very early universe, cosmological inflation faces some criticisms. One of the main challenges for inflation relies with its initial conditions. For cosmological inflation to be considered as a really successful theory, it should arise from generic initial conditions. A lot of work has been done to assess whether the inflationary spacetime is robust against homogeneous and inhomogeneous initial conditions, with some works pointing to problems with the naturalness of the initial conditions [73], and others supporting that the inflationary spacetime arises very naturally [74, 75]. For more details on recent developments see the review [76] and [77] (and references therein). Another issue related to inflation is the so-called *Trans-Planckian problem* [78, 79]. Most models involve a period of inflation that lasts much longer than the number of e-folds required to solve the horizon problem, and therefore the comoving scales which correspond to the present large-scale structure of the universe were smaller than the Planck length at the beginning of inflation. For this reason, the usual computations of the inflationary fluctuations inevitably rely on hidden assumptions about physics at energies above the Planck scale [78, 79]. This poses questions as to whether the current predictions of inflationary cosmology might need to be revisited taking into account our ignorance about super-Planckian physics, but also opens up the possibility of testing the imprints of such high-energy physics with current observations [80].

2.3.1.1 Ultra-slow-roll inflation

In section 2.3.1 we have shown that single-field slow-roll inflation leads to an almost scale-invariant scalar power spectrum. On the other hand, it is interesting to explore under which conditions the scalar power spectrum can become large. By inspecting eq.(2.69) we see that this could happen when the inflaton velocity drops substantially, $\dot{\phi} \to 0$, corresponding to $\epsilon_H \to 0$, see eq.(2.20). Equivalently, this is realised when the gradient of the potential gets extremely small, $V_\phi \to 0$, corresponding to $\epsilon_V \to 0$ in eq.(2.70).

Cases where the gradient of the potential becomes extremely small can coincide with violations of the slow-roll approximation [81], and potentially realise a phase of *ultra-slow-roll* dynamics [82–84]. Indeed, neglecting the gradient of the potential in the Klein–Gordon equation (2.14) yields

$$\ddot{\phi} + 3H\dot{\phi} \simeq 0 \,, \tag{2.78}$$

signalling a break-down of the slow-roll approximation, see eq.(2.32) where the acceleration of the inflaton field is neglected instead. This can be implemented by having an almost stationary inflection point in the potential [85–90].

More formally, one can show under which conditions the scalar perturbation is no longer constant on super-horizon scales and potentially become large. By rewriting the Mukhanov–Sasaki equation (2.52) in terms of the scalar perturbation ζ and transforming the time variable to the number of e-folds N, see eq. (2.33), one gets [91]

$$\frac{d^2\zeta(N,\mathbf{k})}{dN^2} + \left(3 + \epsilon_H - 2\eta_H\right)\frac{d\zeta(N,\mathbf{k})}{dN} + \left(\frac{k}{aH}\right)^2 \zeta(N,\mathbf{k}) = 0 \,. \tag{2.79}$$

On super-horizon scales, $k \ll aH$, this equation admits the solution

$$\zeta(N,\mathbf{k})_{k\ll aH} = c_1 + c_2 \int dN\, e^{-\int dN' \left(3+\epsilon_H - 2\eta_H\right)} \,. \tag{2.80}$$

On super-horizon scales the scalar perturbation receives two contributions, a constant *adiabatic* mode, and a second term whose magnitude depends on the sign of the quantity $3 + \epsilon_H - 2\eta_H$ and is usually referred to as the *entropic* perturbation. During slow-roll inflation $\epsilon_H, \eta_H \ll 1$, therefore the second contribution in eq.(2.80) is approximately proportional to $\exp(-3N)$ and quickly decays, i.e. the scalar perturbation is constant in the super-horizon regime, see eq.(2.55). On the other hand, when $3 + \epsilon_H - 2\eta_H < 0$, the second contribution grows and ζ is no longer constant on super-horizon. This is realised during ultra-slow-roll inflation when the gradient term V_ϕ can be neglected and typically $\eta_H \sim 3$ (or equivalently $\epsilon_2 \simeq -6$, see eq.(2.27), where we have assumed $\epsilon_H \ll \eta_H$).

2.3.2 Primordial gravitational waves

The tensor perturbation to the space-like part of the metric g_{ij} is $\delta g_{ij} = \gamma_{ij}$, where γ_{ij} is a symmetric, transverse and traceless tensor, $\partial_i \gamma^{ij} = \gamma_i{}^i = 0$. This implies that it has only two degrees of freedom, or polarisations, which in the chiral basis are L and R.

At linear order, the scalar, vector and tensor perturbations are decoupled, therefore we can consider only the metric tensor perturbation, $\gamma_{ij}(\eta, \mathbf{x})$, and derive its second order action by expanding the Einstein–Hilber term in the action (2.5) at second order,

$$S = \frac{1}{8} \int d\eta d^3\mathbf{x}\, a^2 \left[\left(\gamma'_{ij}\right)^2 - \left(\partial_l \gamma_{ij}\right)^2 \right] , \tag{2.81}$$

analogous to eq.(2.51) for the scalar mode $v(\eta, \mathbf{x})$.

Proceeding in a similar fashion with respect to what was done in section 2.3.1 for the scalar perturbation, we expand the tensor modes in Fourier components as $\gamma_{ij}(\eta, \mathbf{x}) = \int \frac{d^3k}{(2\pi)^{3/2}} \gamma_{\mathbf{k},ij}(\eta)\, \mathrm{e}^{-i\mathbf{k}\cdot\mathbf{x}}$. The modes $\gamma_{\mathbf{k},ij}(\eta)$ can be decomposed using the transverse and traceless polarization tensors $\epsilon^{\lambda}_{ij}\left(\hat{\mathbf{k}}\right)$,

$$\gamma_{\mathbf{k},ij}(\eta) = \sum_{\lambda=L,R} \epsilon^{\lambda}_{ij}\left(\hat{\mathbf{k}}\right)\, \gamma^{\lambda}_{\mathbf{k}}(\eta) \, . \tag{2.82}$$

We quantise the tensor modes by setting

$$\hat{\gamma}^{\lambda}_{\mathbf{k}}(\eta) = \hat{a}^{\lambda}_{\mathbf{k}} \gamma^{\lambda}_{k}(\eta) + \hat{a}^{\lambda\,\dagger}_{-\mathbf{k}} \gamma^{\lambda *}_{k}(\eta) \, , \tag{2.83}$$

where the creation and annihilation operators satisfy $[\hat{a}^{\lambda}_{\mathbf{k}}, \hat{a}^{\lambda'\,\dagger}_{-\mathbf{k_2}}] = (2\pi)^3\, \delta^{\lambda\lambda'}\, \delta^{(3)}(\mathbf{k_1} + \mathbf{k_2})$.

If there is no evidence for parity violating terms in the universe, the two polarisations behave in the same way and they contribute equally to the tensor power spectrum. For this reason, we first solve eq.(2.81) for a single polarisation and then add the second polarisation contribution to the final result. For this reason we drop the superscript λ in the following.

By defining the canonically-normalised variable

$$w_k(\eta) \equiv \frac{a}{2} \gamma_k(\eta) \, , \tag{2.84}$$

one can show from the action (2.81) that it obeys the equation

$$w_k{}'' + \left(k^2 - \frac{a''}{a} \right) w_k = 0 \, . \tag{2.85}$$

In the limit of de-Sitter space, $a''/a = 2/\eta^2$, which makes eq.(2.85) the same as eq.(2.59) for $v_k(\eta)$. By using the results found in section 2.3.1, we get

$$P_{\gamma}(k) = \frac{2H^2}{\pi^2}\Big|_{k=aH} \, , \tag{2.86}$$

where the difference with respect to $P_\zeta(k)$ is due to the different canonical normalisation (2.84) and a factor 2 accounting for the contribution of both polarisations.

Similarly to eq.(2.71), the tensor power spectrum (2.86) is usually parametrised with a power-law centered around $k_{\rm CMB}$, with amplitude $\mathscr{A}_t = 2H^2/\pi^2$ and spectral tilt $n_t = -2\epsilon_H$. Usually the amplitude of the tensor power spectrum is discussed in terms of the *tensor-to-scalar ratio*,

$$r \equiv \frac{\mathscr{A}_t}{\mathscr{A}_s} \simeq 16\epsilon_H \,, \tag{2.87}$$

where the second equality applies to canonical single-field slow-roll inflation, see eqs.(2.69) and (2.86).

Tensor fluctuations of primordial origin contribute to the present GWs energy density, $\Omega_{\rm GW}$,

$$\Omega_{\rm GW}(k,\eta_0) = \frac{1}{12}\left(\frac{k}{a_0 H_0}\right)^2 P_\gamma(k)\, T^2(k,\eta_0)\,, \tag{2.88}$$

where $P_\gamma(k)$ here stands for the generic primordial tensor power spectrum including all early-universe contributions. In eq.(2.88) quantities with the label "0" are evaluated at present time, η is the conformal time, see eq.(1.17), $H_0 = 100h$ km/s/Mpc is the Hubble rate today (we use $h = 0.674$ [29]), and $T(k,\eta_0)$ the transfer function. By considering a standard reheating scenario where inflation is initially followed by a matter-dominated phase, see section 2.2.2, and then by a radiation-dominated era, the transfer function is given by (see e.g. [92, 93])

$$T(k,\eta_0) = \frac{3\,\Omega_m\, j_1(k\eta_0)}{k\eta_0}\sqrt{1.0 + 1.36\left(\frac{k}{k_{\rm eq}}\right) + 2.50\left(\frac{k}{k_{\rm eq}}\right)^2}\,. \tag{2.89}$$

In the equation above, $\Omega_m = 0.315$ [29] is the matter energy-density today, $j_1(k\eta_0)$ is the first spherical Bessel function and $k_{\rm eq} = 7.1\times10^{-2}\,\Omega_m h^2\,{\rm Mpc}^{-1}$ is the comoving wavenumber that crossed the horizon at radiation-matter equality. By assuming the standard ΛCDM cosmological model, Ω_K and Ω_r are negligible and

$$\eta_0 = \int_0^\infty \frac{dz}{H_0\sqrt{\Omega_\Lambda + \Omega_m(1+z)^3}}\,. \tag{2.90}$$

We note that in eq.(2.88) there might be other sources of GWs from the early universe other than those predicted by quantuum vacuum fluctuations during single-field slow-roll inflation. These include GWs from other inflationary models, non-perturbative effects during preheating, first-order phase transitions, topological defects such as cosmic strings. For a complete review of early universe sources see [94].

In general, it is important to stress that sources in the early universe give rise to a stochastic background of GWs [94], i.e. the amplitude of $\gamma_{ij}(\eta, \mathbf{x})$ is a random variable and can be characterised only statistically. GWs generated during inflation are intrinsically stochastic, as they are generated by quantum vacuum fluctuations of the metric, and the transition from quantum to classical regime[4] due to the exponential expansion of the background makes the random, quantum, tensor fluctuation an effectively classical stochastic variable. Stochastic GWs backgrounds from the early universe are assumed to be [94] statistically (i) homogeneous and isotropic, as the background is; (ii) unpolarised, as there is no evidence of a parity violating source in the universe; (iii) Gaussian, as gravitons are only very weakly interacting.

2.3.3 The effective field theory approach

We discuss here a unifying approach for the study of inflationary perturbations for general single-field models. This is based on an effective field theory (EFT) approach and has the advantage of systematically including all possible deviations from the vanilla single-field slow-roll scenario due to the effect of high energy operators. This approach was pioneered in [96] for single-field inflation, and later extended to the case of multi-field inflation [97], light spinning fields [98], and also to the study of dark energy [99]. In the following we review the results of [96] and explore in chapter 4 the case of light spinning fields during inflation.

EFT of single-field inflation

The EFT provides a systematic way of parametrising our ignorance about the microphysical description of a physical system when describing some of its macroscopic properties [100]. One needs to first identify the relevant degrees of freedom for the physical process of interest. For instance, for a specific experiment in particle physics, one can distinguish between light particles, ϕ_l, which can be produced on shell at the energies available to the experiment, and heavy particles, ϕ_h, too heavy to be produced at these energies. If the full action for heavy and light fields is $S(\phi_\mathrm{h}, \phi_\mathrm{l})$, the effective action for the light fields is obtained by integrating out the heavy fields,

$$e^{iS_{\mathrm{EFT}}(\phi_\mathrm{l})} \equiv \int \mathscr{D}\phi_\mathrm{h}\, e^{iS(\phi_\mathrm{h}, \phi_\mathrm{l})} \,. \tag{2.91}$$

[4] While before horizon crossing the field $\hat{v}_{\mathbf{k}}(\eta, \mathbf{x})$ and its conjugate momentum $\hat{\pi}_{\mathbf{k}}(\eta, \mathbf{x})$ do not commute, on super-horizon scales $\hat{\pi}_{\mathbf{k}}(\eta, \mathbf{x}) \propto \hat{v}_{\mathbf{k}}(\eta, \mathbf{x})$, and they therefore commute. This implies that a state with definite field value has definite momentum, signalling a transition from the quantum to classical regime, see e.g. [66, 95] and references therein.

As a result, the effective Lagrangian for the light fields includes an infinite number of operators, $\mathcal{O}_i(\phi_\mathrm{l})$, with dimension Δ_i higher than 4,

$$\mathscr{L}_\mathrm{EFT} \supset \sum_i m_i \frac{\mathcal{O}_i(\phi_\mathrm{l})}{\Lambda^{\Delta_i-4}} \,. \tag{2.92}$$

In other words, the effects of high-energy degrees of freedom (dof) are included as higher-dimension operators in the effective Lagrangian. In the schematic expression (2.92), operators appear suppressed by the energy scale Λ, also known as the cut-off of the EFT, i.e. the energy scale that signals the break down of the EFT and above which one should not trust the EFT results.

In principle, one should take into account the complete series of operators in (2.92), but in practice only few terms need to be considered. This is because the effect of higher energies operators on low-energy physics is suppressed by powers of $E_\mathrm{l}/E_\mathrm{h} \ll 1$, where the energies E_l and E_h identify the characteristic scales of the low- and high-energy dof. The higher the energy associated with one operator, the more its effect on the low-energy physics will be suppressed.

An EFT approach is particularly useful for the study of those systems whose UV-complete theory is not known. If the symmetries of the low-energy theory are known, one considers an effective, low-energy, theory that contains all the operators that are compatible with these symmetries. In this way, all the possible effects of the high-energy dof are systematically taken into account. In the context of theories of gravity, for example, general relativity is the EFT of the complete (and unknown) theory of quantum gravity, valid at scales $E \ll M_p$ [101].

Let us first identify the symmetries relevant for the inflationary scalar perturbation. Unlike a perfectly de-Sitter universe, inflation has to end and the inflaton field $\phi(t)$ acts as a clock, measuring the time left to the end of inflation [96]. The time-dependent background, $\bar{\phi}(t)$, breaks the time diffeomorphism (diffs)

$$t \to t + \xi^0(t, \mathbf{x}) \,, \tag{2.93}$$

with the inflationary perturbation transforming non-linearly under (2.93), i.e. $\delta\phi' \neq (1+\alpha)\delta\phi$ with α small, but instead

$$\delta\phi' = \delta\phi + \dot{\bar{\phi}}(t)\xi^0 \,. \tag{2.94}$$

While space diffs are still an explicit symmetry of the system, the symmetry associated with the time diffs (2.93) is linearly broken.

By choosing $\xi^0 = -\delta\phi/\dot{\bar{\phi}}$ in eq.(2.94), one can choose to work in the comoving (or unitary) gauge [96], with $\delta\phi = 0$ and $\phi(t) = \bar{\phi}(t)$. In this gauge, the scalar degree of freedom is contained in the metric and the most generic action including all the terms compatible with the (unbroken) space diffs $x^i \to x^i + \xi^i(t, \mathbf{x})$ is [96]

$$S = \int d^4x \sqrt{-g}\Big[\frac{1}{2}{M_p}^2 R - c(t)g^{00} - \Lambda(t) + \frac{M_2(t)^4}{2!}(g^{00}+1)^2 + \frac{M_3(t)^4}{3!}(g^{00}+1)^3 + \\ - \frac{\bar{M}_1(t)^3}{2}(g^{00}+1)\delta K_\mu{}^\mu - \frac{\bar{M}_2(t)^2}{2}\delta K_\mu{}^{\mu 2} - \frac{\bar{M}_3(t)^2}{2}\delta K_\mu{}^\nu \delta K_\nu{}^\mu + \cdots\Big] \tag{2.95}$$

where $\delta K_{\mu\nu} \equiv K_{\mu\nu} - a^2 H h_{\mu\nu}$ is the variation of the extrinsic three-curvature of constant time hypersurfaces, $K_{\mu\nu}$, and $h_{\mu\nu}$ is the induced three-metric. These are defined in terms of the unit vector n_μ, which is perpendicular to hypersurfaces at constant time, $t = \tilde{t}$,

$$n_\mu \equiv \frac{\partial_\mu \tilde{t}}{\sqrt{-g^{\rho\sigma}\partial_\rho\tilde{t}\partial_\sigma\tilde{t}}}\,. \tag{2.96}$$

The induced three-metric is $h_{\mu\nu} \equiv g_{\mu\nu} + n_\mu n_\nu$ and the extrinsic three-curvature of constant time hypersurfaces is $K_{\mu\nu} \equiv h_\mu^\rho \nabla_\rho n_\nu$.

The coefficients $M_i(t)$ and $\bar{M}_i(t)$ in the action (2.95) may have a generic time dependence, as the inflaton breaks time-reparametrisation invariance, and keep track of the energy scales above which the EFT treatment cannot be trusted, in analogy with the (unique) scale Λ introduced in the schematic effective Lagrangian in eq.(2.92).

The first and third terms in eq.(2.95) are background quantities, and the second term is explicitly linearly-dependent on the perturbations, while all the other terms contain quadratic perturbations or higher. For this reason, the part of action

$$S = \int d^4x \sqrt{-g}\left[\frac{1}{2}{M_p}^2 R - c(t)g^{00} - \Lambda(t)\right] \tag{2.97}$$

can be used to fix the background, i.e. a FLRW universe [96]. Using eq.(1.14) at zeroth order in the metric perturbations, one can calculate the density ρ and pressure P associated with the action (2.97),

$$\rho = c(t) + \Lambda(t)\,, \quad P = c(t) - \Lambda(t)\,. \tag{2.98}$$

Substituting the above in the Friedmann equations (1.32) and (1.33) (with no cosmological constant) and solving for $c(t)$ and $\Lambda(t)$ yields

$$c(t) = -{M_p}^2 \dot{H}\,, \quad \Lambda(t) = {M_p}^2(3H^2 + \dot{H})\,. \tag{2.99}$$

Substituting eq.(2.99) back in the action (2.95) yields

$$S = \int d^4x\sqrt{-g}\Big[\frac{1}{2}M_p{}^2R + M_p{}^2\dot{H}g^{00} - M_p{}^2(3H^2+\dot{H}) + \\ + \frac{M_2(t)^4}{2!}(g^{00}+1)^2 + \frac{M_3(t)^4}{3!}(g^{00}+1)^3 + \cdots\Big], \tag{2.100}$$

where for simplicity we drop the terms containing $\delta K_\mu{}^\nu$, not relevant for the purposes of this review.

Even if eq.(2.100) might seem a bit obscure, it is possible to write the inflationary single-field models we are familiar with in the language of (2.100). Let us consider the case of single-field slow-roll inflation. In the comoving gauge, $\delta\phi(t,\mathbf{x}) = 0$ and $\phi = \bar{\phi}(t)$, the action (2.5) becomes

$$S = \int d^4x\sqrt{-g}\left[\frac{1}{2}M_p{}^2R - \frac{\dot{\bar{\phi}}^2}{2}g^{00} - V(\bar{\phi})\right]. \tag{2.101}$$

Using eqs.(2.12) and (2.13) to write $\dot{\bar{\phi}}^2$ and $V(\bar{\phi})$ in terms of $\dot{H}$ and H^2, eq.(2.101) can be rewritten as eq.(2.100) with $M_2 = M_3 = 0$. We note here that there is an advantage in using the action (2.100) rather than the single-field slow-roll action (2.5): the former carries more information about the system, containing all the terms that could possibly be generated by loop corrections, i.e. it systematically includes the effects of high-energy physics [96].

The action (2.100) is not invariant under the time diffs (2.93), but it is possible to restore the full gauge symmetries by employing a technique known in standard gauge theory as the *Stückelberg trick* [102]. This effectively mimics a gauge transformation, after which the scalar mode explicitely appears as the *Goldstone boson*. To this end, let us consider the simplified action (2.97) and the transformations

$$t \to \tilde{t} = t + \xi^0(x) \quad \text{and} \quad x^i \to \tilde{x}^i = x^i\,. \tag{2.102}$$

Under (2.102) the term g^{00} transforms as

$$g^{00} \to \tilde{g}^{00}(\tilde{x}(x)) = \frac{\partial\tilde{x}^0}{\partial x^\mu}\frac{\partial\tilde{x}^0}{\partial x^\nu}g^{\mu\nu}(x)\,, \tag{2.103}$$

with the inverse transformation being

$$g^{00}(x) = \frac{\partial x^0}{\partial\tilde{x}^\mu}\frac{\partial x^0}{\partial\tilde{x}^\nu}\tilde{g}^{\mu\nu}(\tilde{x})\,. \tag{2.104}$$

The inverse tranformation for $\sqrt{-g}$ is

$$\sqrt{-g} = \left|\frac{\partial x}{\partial\tilde{x}}\right|\sqrt{-\tilde{g}}\,, \tag{2.105}$$

where $\left|\frac{\partial x}{\partial \tilde{x}}\right|$ is the Jacobian of the inverse coordinate transformation. Substituting eqs.(2.104) and (2.105) in the action (2.97) yields

$$S = \int d^4x \left|\frac{\partial x}{\partial \tilde{x}}\right| \sqrt{-\tilde{g}} \left[-c(t) \frac{\partial x^0}{\partial \tilde{x}^\mu} \frac{\partial x^0}{\partial \tilde{x}^\nu} \tilde{g}^{\mu\nu}(\tilde{x}) - \Lambda(t) \right] , \tag{2.106}$$

where we have dropped for the moment the Einstein-Hilbert term. Recognising that $d^4x \left|\frac{\partial x}{\partial \tilde{x}}\right| = d^4\tilde{x}$ and using the time diffs (2.102) yields

$$S = \int d^4\tilde{x} \sqrt{-\tilde{g}} \left[-c\left(\tilde{t} - \xi^0\right) \frac{\partial\left(\tilde{t} - \xi^0\right)}{\partial \tilde{x}^\mu} \frac{\partial\left(\tilde{t} - \xi^0\right)}{\partial \tilde{x}^\nu} \tilde{g}^{\mu\nu}(\tilde{x}) - \Lambda\left(\tilde{t} - \xi^0\right) \right] . \tag{2.107}$$

If we promote the parameter $\xi^0(x)$ to being a field, $\xi^0(x(\tilde{x})) \to -\tilde{\pi}(\tilde{x})$, eq.(2.107) becomes

$$S = \int d^4\tilde{x} \sqrt{-\tilde{g}} \left[-c\left(\tilde{t} + \tilde{\pi}(\tilde{x})\right) \frac{\partial\left(\tilde{t} + \tilde{\pi}(\tilde{x})\right)}{\partial \tilde{x}^\mu} \frac{\partial\left(\tilde{t} + \tilde{\pi}(\tilde{x})\right)}{\partial \tilde{x}^\nu} \tilde{g}^{\mu\nu}(\tilde{x}) - \Lambda\left(\tilde{t} + \tilde{\pi}(\tilde{x})\right) \right] . \tag{2.108}$$

The field $\tilde{\pi}(\tilde{x})$ is the Goldstone boson, and provided it transforms as

$$\pi(x) \to \tilde{\pi}\left(\tilde{x}(x)\right) = \pi(x) - \xi^0(x) \tag{2.109}$$

under diffs (2.102), the action (2.97) is now invariant under space *and* time diffs.

Applying this transformations to the full action (2.100) and dropping the tilde symbol for simplicity, we obtain [96]

(2.110)

$$\begin{aligned} S = \int d^4x \sqrt{-g} \Big\{ & \frac{1}{2} {M_p}^2 R + {M_p}^2 \dot{H}(t+\pi) \left((1+\dot{\pi})^2 g^{00} + 2(1+\dot{\pi}) \partial_i \pi g^{0i} + \partial_i \pi \partial_j \pi g^{ij} \right) + \\ & - {M_p}^2 \left[3H(t+\pi)^2 + \dot{H}(t+\pi) \right] + \frac{M_2(t+\pi)^4}{2!} \left[(1+\dot{\pi})^2 g^{00} + 2(1+\dot{\pi}) \partial_i \pi g^{0i} + \partial_i \pi \partial_j \pi g^{ij} + 1 \right]^2 + \\ & + \frac{M_3(t+\pi)^4}{3!} \left[(1+\dot{\pi})^2 g^{00} + 2(1+\dot{\pi}) \partial_i \pi g^{0i} + \partial_i \pi \partial_j \pi g^{ij} + 1 \right]^3 + \cdots \Big\} , \end{aligned}$$

where we have used

$$\frac{\partial(t+\pi)}{\partial x^\mu} \frac{\partial(t+\pi)}{\partial x^\nu} g^{\mu\nu}(x) = (1+\dot{\pi})^2 g^{00} + 2(1+\dot{\pi}) \partial_i \pi g^{0i} + \partial_i \pi \partial_j \pi g^{ij} . \tag{2.111}$$

We are interested in slow-roll solutions where H and $\dot{H}$ do not vary significantly in one Hubble time, and we assume the same also for the other time-dependent coefficients M_2 and M_3. For this reason, the time-dependence of all these functions is slow-roll suppressed, and we can safely assume $H(t+\pi) \simeq H(t)$ and so on in eq.(2.110).

In the action (2.110) the metric components are perturbed, e.g. $g^{00} = -1 + \delta g^{00}$, so in principle the scalar field π couples with the metric fluctuations. This can be seen for

example from one of the terms in (2.110) proportional to $\dot{H}$, $M_p{}^2\dot{H}\,(1+\dot{\pi})^2\,g^{00}$. Expanding it yields

$$M_p{}^2\dot{H}\,(1+\dot{\pi})^2\,g^{00} \supset -M_p{}^2\dot{H}\,\dot{\pi}^2 + 2M_p{}^2\dot{H}\,\dot{\pi}\,\delta g^{00}\,, \tag{2.112}$$

where we can see that, besides the usual kinetic term $\propto \dot{\pi}^2$, there is also a term coupling $\dot{\pi}$ and the perturbation δg^{00}. Nevertheless, by working in the regime where this term is suppressed, also known as the *decoupling limit*, we can safely neglect the mixing between the Goldstone and gravity [96]. The decoupling energy scale can be estimated by looking at the second term in eq.(2.112) for the canonically normalised fields[5] $\delta g_c^{00} \simeq M_p \delta g_c^{00}$ and $\pi_c \simeq M_p \dot{H}^{1/2}\pi$,

$$2\dot{H}^{1/2}\dot{\pi}_c\delta g_c^{00}\,. \tag{2.113}$$

For energies $E \gg E_{\rm mix} = \dot{H}^{1/2} = \sqrt{\epsilon_H H}$, the mixing with gravity can be neglected.

In the decoupling limit, we can study the action (2.110) with the unperturbed metric

$$g^{00} = -1\,, \quad g^{0i} = 0\,, \quad g^{ij} = \delta^{ij}/a^2\,, \tag{2.114}$$

yielding up to third order [96]

$$S = \int d^4x\sqrt{-g}\,\left[\frac{1}{2}M_p{}^2R - M_p{}^2\dot{H}\left(\dot{\pi}^2 - \frac{(\partial\pi)^2}{a^2}\right) + 2M_2^4\left(\dot{\pi}^2 + \dot{\pi}^3 - \dot{\pi}\frac{(\partial\pi)^2}{a^2}\right) - \frac{4}{3}M_3^4\dot{\pi}^3 + \cdots\right]\,, \tag{2.115}$$

where we do not include the terms linear in π because they do not contribute to the second-order action, and the equation of motion therefore.

The Goldstone boson described by the action (2.115) can be related to the the curvature perturbation, ζ. In particular, ζ is defined in the comoving gauge as the scalar perturbation to the three-metric g_{ij}, see eq.(2.47). When the Goldstone boson is on stage instead, time is transformed according to $t \to \tilde{t} = t - \pi$ and the metric is unperturbed, see eq.(2.114). By simply comparing these two different pictures,

$$g_{ij} = a(t)^2(1+2\zeta)\delta_{ij} \Longleftrightarrow g_{ij} = a(t-\pi)^2\delta_{ij} \simeq a(t)^2\,(1-2H\pi)\delta_{ij}\,, \tag{2.116}$$

we can derive the first-order relation between π and ζ [96]

$$\zeta = -H\pi\,. \tag{2.117}$$

[5]The canonical normalisation for π is obtained for $M_2 = 0$, in which case the dominant $\dot{\pi}^2$ term is the first term in eq.(2.112). For a theory where $M_2 \neq 0$, the canonically normalised π_c is determined by the coefficient of the dominating $\dot{\pi}^2$ term.

Eq.(2.117) implies that, up to a factor of H, the Goldstone action (2.115) describes the scalar fluctuations around an inflating background up to third order in the perturbations.

Using eq.(2.117) allows us to connect the 2-point correlation function of the curvature perturbation with that of the Goldstone boson,

$$P_\zeta(k) \simeq \frac{k^3}{2\pi^2}\langle \zeta_{\mathbf{k_1}}\zeta_{\mathbf{k_2}}\rangle = \frac{k^3}{2\pi^2}H^2\langle \pi_{\mathbf{k_1}}\pi_{\mathbf{k_2}}\rangle\,, \tag{2.118}$$

where we use the symbol $\simeq$ as we are not including the delta function $\delta^3(\mathbf{k_1}+\mathbf{k_2})$. To calculate the 2-point correlation function of the Goldstone boson, let us consider for the moment the slow-roll case, e.g. we set $M_2 = M_3 = 0$ in eq.(2.115). The quadratic action for the canonical field π_c then is

$$S = \int d^4x\sqrt{-g}\left[\frac{1}{2}{M_p}^2 R + \left(\dot{\pi}_c^2 - \frac{(\partial\pi_c)^2}{a^2}\right)\right]\,, \tag{2.119}$$

which is the quadratic action for scalar perturbations on de-Sitter space. By using the results obtained in section 2.3.1, the two-point correlation function for the field $\pi_{c\mathbf{k}}$ is

$$\langle \pi_{c\mathbf{k_1}}\pi_{c\mathbf{k_2}}\rangle = \delta^3(\mathbf{k_1}+\mathbf{k_2})\frac{H^2}{4k^3}\Big|_{k=aH}\,, \tag{2.120}$$

where the expression above is evaluated at horizon crossing. Transforming to the non-canonical field, $\pi = \pi_c \Big/ \left(M_p \dot{H}^{1/2}\right)$, and inserting the resulting expression in eq.(2.118) yields

$$P_\zeta(k) \simeq \frac{k^3}{2\pi^2{M_p}^2}\frac{H^2}{\dot{H}}\langle \pi_{c\mathbf{k_1}}\pi_{c\mathbf{k_2}}\rangle = \frac{H^2}{8\pi^2{M_p}^2\epsilon_H}\Big|_{k=aH}\,, \tag{2.121}$$

which is the same result obtained in section 2.3.1 in the context of the standard perturbation theory calculation.

Another interesting consequence of the action (2.115) is that, in principle, the coefficient of the time kinetic term, $\dot{\pi}^2$, is different from that of the spatial kinetic term, $(\partial\pi)^2$,

$$\left(-{M_p}^2\dot{H} + 2M_2^4\right)\dot{\pi}^2 \quad \text{vs} \quad {M_p}^2\dot{H}(\partial\pi)^2\,. \tag{2.122}$$

To avoid ghost and gradient[6] instabilities, it must be that $-{M_p}^2\dot{H} + 2M_2^4 > 0$ and $\dot{H} < 0$ respectively. Moreover, if $M_2 \neq 0$ the sound speed of π would be different from one [96],

$$c_s^2 \equiv \frac{-{M_p}^2\dot{H}}{2M_2^4 - {M_p}^2\dot{H}}\,. \tag{2.123}$$

[6]Having a ghost in the theory implies that the energy of the system is unbounded from below and unitarity is broken, while in presence of a gradient instability the field modes grow exponentially.

If $\dot{H} < 0$ and $M_2^4 > 0$, then the propagation of π is sub-luminal, $c_s < 1$. A reduced sound speed is natural in this context, as the background evolution breaks Lorentz invariance, so that $c_s = 1$ is not protected by any symmetry.

By inspecting the action (2.115) one can see that the same operator which leads to a reduced speed of sound also induces cubic couplings of π, see e.g. the terms $\dot{\pi}^3$ and $\dot{\pi}(\partial\pi)^2$. These terms induce primordial 3-point correlations for the scalar perturbation, $\langle\zeta_{\mathbf{k_1}}\zeta_{\mathbf{k_2}}\zeta_{\mathbf{k_3}}\rangle$, which constitute the leading non-Gaussian signature for inflationary perturbations. In other words, a reduced sound speed for the scalar perturbations in single-field inflation is always associated with enhanced non-Gaussianities [96].

We conclude this section with a comment on the cut-off of the EFT of single-field inflation. While the theory (2.115) makes sense and can be used at energies $E \simeq H \gg E_{\rm mix}$, at high energies we expect the Goldstone boson to become strongly coupled, e.g. its cubic self-interactions induce loop corrections to the 2-point correlation function. By calculating the energy at which these corrections become important, we can evaluate [96] the cutoff of the theory (2.115),

$$\Lambda^4 \simeq 16\pi^2 {M_p}^2 |\dot{H}| \frac{c_s^5}{1-c_s^2} \,. \tag{2.124}$$

We note that the cutoff of the theory is higher in case $c_s \simeq 1$, while it decreases for sub-luminal propagation, which again manifests the connection between a reduced sound speed and enhanced effects of 3-point interactions.

2.4 Multi-field inflation

Despite the great success of single-field inflaton in solving the puzzles within the standard Big Bang cosmology and explaining the origin of structure formation, it is more natural to embed in high-energy theories inflationary models comprising multiple fields.

A straightforward example of the UV-sensitivity of single-field inflation is the η *problem*. In order to solve the horizon problem, inflation has to last at least (approximately) 60 e-folds. To this end, not only the first PSRP has to be small, $\epsilon_V \ll 1$, but also $\eta_V \ll 1$ for at least 60 e-folds. If we consider the EFT of single-field inflation, we have to include in the effective Lagrangian, $\mathscr{L}_{\rm eff}$, an infinite number of non-renormalisable terms with dimension $\Delta > 4$, each one suppressed by powers of the cutoff of the theory, $\Lambda^{\Delta-4}$. Amongst these, there is the dimension six operator

$$\mathscr{L}_{\rm eff} \supset cV(\phi)\frac{\phi^2}{\Lambda^2} = \frac{1}{2}cm^2\frac{\phi^4}{\Lambda^2} \,, \tag{2.125}$$

where c is a coupling constant of $\mathcal{O}(1)$ and in the second equality we assumed a quadratic $V(\phi)$. The operator above induces a modification to the inflaton potential, which in terms causes η_V to change,

$$\Delta\eta_V = \mathcal{O}\left(c\frac{{M_p}^2}{\Lambda^2}\right). \tag{2.126}$$

For $c = \mathcal{O}(1)$ and $\Lambda \lesssim M_p$, the correction above is $\Delta\eta_V \gtrsim 1$, pointing to the fact that the small value of η_V is not protected from the effect of high-energy physics. The sensitivity of inflation to Planck-scale physics motivates the study of inflation in the context of higher energy theories, e.g. string theory, which usually accommodate a rich(er) inflationary particle content, including compactification moduli, axions, gauge fields, Kaluza-Klein modes [103].

For these reasons, inflationary models comprising multiple fields have been extensively studied in the last 20 years. We devote the rest of this section to reviewing the basic formalism of multi-field inflation, where multiple scalar fields are considered, and the interesting effects of the multi-field dynamics.

When considering the extension from single-field inflation into a multi-field scenario, there are two novel ingredients which enter the inflationary evolution: the field-space geometry and the multi-field potential. The action of the multi-field model can be written as

$$S = \int d^4x\sqrt{-g}\left[-\frac{1}{2}\mathcal{G}_{IJ}\left(\phi^K\right)\partial_\mu\phi^I\partial^\mu\phi^J - V\left(\phi^K\right)\right], \tag{2.127}$$

where $\mathcal{G}_{IJ}\left(\phi^K\right)$ is the metric on the field space and $V\left(\phi^K\right)$ is the multi-field potential. For simplicity, let us consider the case of two-field models, $K = \{1, 2\}$.

In a FLRW universe, the equations of motion for the evolution of the background fields read (see e.g. [104])

$$3H^2 = \frac{1}{2}\dot{\sigma}^2 + V\,, \tag{2.128}$$

$$\dot{H} = -\frac{1}{2}\dot{\sigma}^2\,, \tag{2.129}$$

$$\mathcal{D}_t\dot{\phi}^I + 3H\dot{\phi}^I + \mathcal{G}^{IJ}V_{,J} = 0\,, \tag{2.130}$$

where $V_{,J} \equiv dV/d\phi^J$, $\dot{\sigma}^2 \equiv \mathcal{G}_{IJ}\dot{\phi}^I\dot{\phi}^J$ is the kinetic energy of the fields, $\mathcal{D}_t A^I = \dot{A}^I + \Gamma^I_{JK}\dot{\phi}^J A^K$ and Γ^I_{JK} are the Christoffel symbols on the field space. After some manipulation, eq. (2.130) can be rewritten as [105]

$$\ddot{\sigma} + 3H\dot{\sigma} + V_{,\sigma} = 0\,, \tag{2.131}$$

where $V_{,\sigma} \equiv \dot{\phi}^I V_{,I} \Big/ \dot{\sigma}$.

In order to ensure that the study of scalar field fluctuations relies on quantities which are covariant under field-space transformations, the covariant perturbation in the spatially-flat gauge, Q^I, is used [106]. The equations of motion for the linear perturbations are then [107–109] (see also the review [110])

$$\mathscr{D}_t\mathscr{D}_t Q^I + 3H\mathscr{D}_t Q^I + \frac{k^2}{a^2}Q^I + M^I{}_J Q^J = 0\,, \tag{2.132}$$

where the mass matrix, $M^I{}_J$, is defined as

$$M^I{}_J \equiv V^I_{;\,J} - \mathscr{R}^I{}_{KLJ}\dot{\phi}^K\dot{\phi}^L - \frac{1}{a^3}\mathscr{D}_t\left(\frac{a^3}{H}\dot{\phi}^I\dot{\phi}_J\right). \tag{2.133}$$

The first component of $M^I{}_J$ is the Hessian of the multi-field potential $V_{;IJ} \equiv V_{,IJ} - \Gamma^K_{IJ}V_{,K}$, defined by means of a covariant derivative in field space in order to take into account the non-trivial geometry. The second term also depends on the geometry of the field space, whose Riemann tensor is $\mathscr{R}^I{}_{KLJ}$. For a two-dimensional field space, the Riemann tensor is $\mathscr{R}_{IJKL} = \frac{1}{2}\mathscr{R}_{\rm fs}(\mathscr{G}_{IK}\mathscr{G}_{JL} - \mathscr{G}_{IL}\mathscr{G}_{JK})$, where $\mathscr{R}_{\rm fs}$ is the intrinsic scalar curvature of the field space. The third term encodes the gravitational backreaction due to spacetime metric perturbations induced by the field fluctuations at first order.

When studying the dynamics of the perturbations, instead of directly using the variables Q^I it is often convenient to project the fluctuations along the instantaneous adiabatic and entropic directions [108, 111]. The adiabatic direction follows the background trajectory in field space and the entropic direction is orthogonal to it. More precisely, the new basis is described by the unit vectors $(\hat{\sigma}^I, \hat{s}^I)$, where

$$\hat{\sigma}^I \equiv \frac{\dot{\phi}^I}{\dot{\sigma}}\,, \tag{2.134}$$

$$\hat{s}^I \equiv \frac{\omega^I}{\omega} \text{ where } \omega^I \equiv \mathscr{D}_t\hat{\sigma}^I\,, \tag{2.135}$$

$$\hat{\sigma}^I\hat{s}_I = 0\,,\ \ \hat{\sigma}^I\hat{\sigma}_I = \hat{s}^I\hat{s}_I = 1\,. \tag{2.136}$$

Usually ω is referred to as the turn rate in field space, while the dimensionless bending parameter

$$\eta_\perp \equiv \frac{\omega}{H} \tag{2.137}$$

measures the deviation of the background trajectory from a geodesic in field space. Using eqs. (2.130) and (2.131), the components of the turn rate can be expressed as

$$\omega^I = -\frac{\mathscr{G}^{IJ}V_{,J}}{\dot{\sigma}} + \frac{\dot{\phi}^I}{\dot{\sigma}^2}V_{,\sigma} \tag{2.138}$$

and

$$\omega^2 \equiv \mathcal{G}_{IJ}\omega^I\omega^J = \frac{\mathcal{G}^{KM}V_{,K}V_{,M}}{\dot\sigma^2} - \frac{(V_{,\sigma})^2}{\dot\sigma^2}\,. \tag{2.139}$$

Projecting the perturbations Q^I in the adiabatic and entropic directions allows us to define the adiabatic and entropic perturbations as $Q_\sigma \equiv \hat\sigma_I Q^I$ and $Q_s \equiv \hat s_I Q^I$ respectively. From these, the dimensionless comoving curvature and isocurvature perturbations are given by

$$\zeta \equiv \frac{H}{\dot\sigma}Q_\sigma, \quad S \equiv \frac{H}{\dot\sigma}Q_s\,. \tag{2.140}$$

The presence of isocurvature perturbations, S, gives rise to multi-field effects. The equations of motion for Q_σ and Q_s are [107–109]

$$\ddot Q_\sigma + 3H\dot Q_\sigma + \left(\frac{k^2}{a^2} + {m_\sigma}^2\right)Q_\sigma = \left(2H\eta_\perp Q_s\right)^{\cdot} - \left(\frac{\dot H}{H} + \frac{V_{,\sigma}}{\dot\sigma}\right)2H\eta_\perp Q_s\,, \tag{2.141}$$

$$\ddot Q_s + 3H\dot Q_s + \left(\frac{k^2}{a^2} + {m_s}^2\right)Q_s = -2\dot\sigma\eta_\perp\dot\zeta\,. \tag{2.142}$$

These equations show that the adiabatic and entropic perturbations are coupled in the presence of a non-zero bending of the trajectory ($\eta_\perp \neq 0$), i.e., non-geodesic motion in field space [111]. The squared-masses of the adiabatic and isocurvature fluctuations are ${m_\sigma}^2$ and ${m_s}^2$ respectively. At leading order in slow roll the adiabatic squared-mass is ${m_\sigma}^2 = -\frac{3}{2}\epsilon_2 + \mathcal{O}(\epsilon^2)$, while the entropic squared-mass is

$$\frac{{m_s}^2}{H^2} \equiv \frac{V_{;ss}}{H^2} + \epsilon_1\mathcal{R}_{\rm fs} - \eta_\perp^2\,, \tag{2.143}$$

where $V_{;ss} \equiv \hat s^I\hat s^J V_{;IJ}$.

In the super-horizon regime ($k \ll aH$) the curvature perturbation obeys

$$\dot\zeta \simeq 2\eta_\perp\frac{H^2}{\dot\sigma}Q_s\,, \tag{2.144}$$

which demonstrates that in multi-field inflation the curvature perturbation, ζ, is not constant in the super-horizon regime for non-geodesic trajectories, in contrast to what found in section 2.3.1 for single-field inflation. Substituting this expression into eq. (2.142) for Q_s we obtain

$$\ddot Q_s + 3H\dot Q_s + {m_{s,\rm eff}}^2 Q_s \simeq 0\,, \tag{2.145}$$

where the entropic effective squared-mass in the super-horizon regime is [112]

$$\frac{{m_{s,\rm eff}}^2}{H^2} \equiv \frac{V_{;ss}}{H^2} + \epsilon_1\mathcal{R}_{\rm fs} + 3\eta_\perp^2\,. \tag{2.146}$$

For reasons which will become clear in chapter 6, we focus on the case of hyperbolic field space, $\mathscr{R}_{\rm fs} < 0$. From the equations above one can identify two important regimes characterising the multi-field dynamics in a hyperbolic field space:

(i) geometrical destabilisation: the effective squared-mass of the isocurvature perturbation (2.146) receives a contribution from the curvature of the field space, $\mathscr{R}_{\rm fs}$, which on a hyperbolic geometry is negative. If the combination $\epsilon_1 \mathscr{R}_{\rm fs}$ is large enough to overcome the other contributions in (2.146), this can lead to geometrical destabilisation [112, 113]. In this case, the entropic fluctuation is tachyonic and renders the background trajectory unstable. As a consequence, inflation might end prematurely, affecting the inflationary observables [114], or the geometrical instability drives the system away from its original trajectory into a new, side-tracked, field-space trajectory [105, 115, 116];

(ii) strongly non-geodesic motion: a large bending of the background trajectory ($\eta_\perp \gg 1$) could drive the entropic squared-mass, ${m_s}^2$ in eq. (2.143), to negative values. In this case the entropic fluctuation may undergo a transient instability in the sub-horizon regime where it is exponentially amplified. However, while contributing negatively to the squared-mass on sub-horizon scales, ${m_s}^2$ in eq. (2.143), a large bend in the trajectory contributes positively to the effective squared-mass on super-horizon scales, ${m_{s,\rm eff}}^2$ in eq. (2.146), therefore keeping the background trajectory stable. As a consequence of the transfer between the entropic and adiabatic modes (whose efficiency is set by $\eta_\perp$), the exponentially-enhanced isocurvature fluctuations can source curvature perturbations [117–119]. In this case, the scalar power spectrum can grow faster than would be allowed in single-field ultra-slow-roll inflation [120]. Depending on the duration of the turn in field space, it can be classified as broad (taking several e-folds) or sharp (less than one e-fold), as will be discussed in chapter 6. In the case of sharp turns $P_\zeta(k)$ exhibits characteristic oscillatory patterns [117–119, 121], see also [122, 123] for earlier works on features in $P_\zeta(k)$ produced by sudden turns of the inflationary trajectory.

In summary, multi-field dynamics in a hyperbolic field-space geometry can lead to a very rich phenomenology, because of geometrical effects and non-geodesic motion. This has been studied in the context of the generation of features in the primordial power spectrum on large scales, primordial black hole production production [4, 117, 118], and second-order gravitational waves generation [119, 121, 124–126]. We go back to these topics in chapter 3 when discussing observational tests of inflation and in chapter 6, where we explore multi-field effects in the context of cosmological α-attractor models of inflation [127–134].

CHAPTER 3

OBSERVATIONAL TESTS OF INFLATION

In this section we discuss observational tests of inflation. We present large-scale CMB observations of the primordial scalar power spectrum and current upper bounds on primordial GWs from observations of the CMB polarisation map in sections 3.1 and 3.2 respectively. In sections 3.3 and 3.4 we define the scalar and tensor 3-point correlation functions for the scalar and tensor perturbations, and discuss current upper bounds from CMB observations. In section 3.5 we focus on inflationary models that support large scalar fluctuations on small scales, which could potentially lead to primordial black hole formation, see section 3.5.1, and detectable second-order GWs at high frequencies, see section 3.5.2.

3.1 CMB temperature anisotropies

In section 2.3.1 we demonstrate that the scalar perturbation is conserved on super-horizon scales within canonical single-field inflation, see eq.(2.55). Weinberg [71] formally showed that the adiabatic mode of the curvature fluctuation is excited during inflation and that it has a physical non-zero constant solution on super-horizon scales, regardless of the equation of state of the constituents of the universe. Importantly, this result allows us to neglect the complicated high-energy processes taking place at the end of inflation and connect directly inflationary predictions to observables quantities at later times. Some years before, a similar result was derived in [135], where the separate-universe argument is used to prove the conservation of ζ for adiabatic perturbations.

In this section we focus on the CMB anisotropies, see section 1.2.4.1, which are mainly seeded by scalar quantum vacuum fluctuations produced during inflation [14, 33].

When studying the phenomenology of an inflationary potential, in order to compare it with CMB observations it is of key importance to calculate the number of e-folds before the end of inflation when the CMB scale, defined by the comoving wavenumber $k_{\rm CMB} = 0.05\,{\rm Mpc}^{-1}$, crossed the horizon ($k = aH$) during inflation [67]

$$\begin{aligned}\Delta N_{\rm CMB} &\equiv N_{\rm end} - N_{\rm CMB} \\ &\simeq 67 - \ln\left(\frac{k_{\rm CMB}}{a_0 H_0}\right) + \frac{1}{4}\ln\left(\frac{V_{\rm CMB}^2}{\rho_{\rm end}}\right) + \frac{1-3w_{\rm r}}{12(1+w_{\rm r})}\ln\left(\frac{\rho_{\rm th}}{\rho_{\rm end}}\right) - \frac{1}{12}\ln(g_{\rm th}).\end{aligned} \tag{3.1}$$

In this expression $(a_0 H_0)^{-1}$ is the comoving current size of the universe, $\rho_{\rm end}$ is the energy density at the end of inflation, $V_{\rm CMB}$ is the value of the potential when the comoving wavenumber $k_{\rm CMB}$ crossed the horizon during inflation, $w_{\rm r}$ is the equation of state parameter describing reheating, see section 2.2.2, $\rho_{\rm th}$ is the energy scale and $g_{\rm th}$ is the number of effective bosonic degrees of freedom at the completion of reheating. Following [67], we fix $g_{\rm th} = 10^3$.

The precise value of $\Delta N_{\rm CMB}$ depends on the inflationary potential and the details of reheating [136]. For matter-dominated rehating, $w_{\rm r} = 0$, and more in general for reheating scenarios with equation of state $-1 < w_{\rm r} < 1/3$, one can obtain the maximum value which $\Delta N_{\rm CMB}$ can take by assuming instant reheating, $\rho_{\rm th} = \rho_{\rm end}$.

In single-field slow-roll inflation, the inflationary predictions for scalar fluctuations on large scales can be calculated by evaluating the corresponding slow-roll expressions $\Delta N_{\rm CMB}$ e-folds before the end of inflation. In particular, the slow-roll expressions for the scalar spectral tilt, $n_s - 1$, the running of the spectral tilt, α_s and the tensor-to-scalar ratio, r, are in eqs. (2.76), (2.77) and (2.87) respectively. These predictions should then be compared with the observational constraints from the latest *Planck* data release [67]. In this section we present current measurements of the spectral tilt and its running, and leave for section 3.2 the discussion of bounds on primordial GWs.

By fitting the *Planck* temperature, polarisation and lensing, plus BICEP2/Keck Array BK15 data with the $\Lambda{\rm CDM} + r + \alpha_s$ model, the amplitude, the tilt and its running are [67]

$$\mathscr{A}_s = 2.1 \times 10^{-9} \ \ (68\,\%\,{\rm C.L.})\,, \tag{3.2}$$

$$n_s = 0.9639 \pm 0.0044 \ \ (68\,\%\,{\rm C.L.})\,, \tag{3.3}$$

$$\alpha_s = -0.0069 \pm 0.0069 \ \ (68\,\%\,{\rm C.L.})\,, \tag{3.4}$$

where we leave the discussion of the upper bound on r to section 3.2.

Observational bounds on the scalar spectral index at CMB scales using the baseline ΛCDM cosmology, i.e. excluding both α_s and r, with *Planck* temperature, polarisation and lensing data, are [67]

$$n_s = 0.9649 \pm 0.0042 \ \ (68\%\text{C.L.})\,. \tag{3.5}$$

3.2 CMB polarisation and primordial gravitational waves

As shown in section 2.3.2, inflation predicts the existence of a stochastic background of gravitational waves (GWs) [137]. These primordial GWs are too faint to be directly detected at CMB scales. Nevertheless, it is possible to *indirectly* probe them by detecting a specific pattern in the CMB polarisation map [138].

The CMB photons are polarised due to *Thompson scattering*, in this case elastic scattering off the free electrons in the primordial plasma just before decoupling [138]. The outgoing radiation is polarised only when the incoming radiation is anisotropic, in particular with a quadrupolar pattern [138].

To demonstrate this, let us start from the simplest case and consider an electron, sitting in the origin of the (x, y, z) space, and incoming radiation in the $\hat{x}$ direction, see the top-left panel in figure 3.1. This corresponds to electric and magnetic fields oscillating perpendicularly to the direction of propagation, i.e. in the $\hat{y}$ and $\hat{z}$ directions. If the intensity along the $\hat{y}$ and $\hat{z}$ directions is equal, then the incident light is *unpolarized*, which is the case depicted in the top-left panel in figure 3.1, where the thickness of lines representing the incoming radiation is the same in the $\hat{y}$ and $\hat{z}$ directions. The electric field of the incident wave accelerates the electron, causing it to emit radiation at the same frequency as the incident wave, i.e. the electron scatters the wave. In particular, the radiation component parallel to the incoming ($\hat{x}$) and outgoing ($\hat{z}$) directions is blocked, while the perpendicular one passes through unchanged. In this case, the result is radiation polarised in the $\hat{y}$ direction.

This very simple cartoon does not describe the primordial plasma case, where incident light is coming from all directions. So, let us now consider the case of isotropic radiation incident on the electron, where for simplicity we consider two photons travelling from perpendicular directions. In addition to the photon travelling along the $\hat{x}$ direction as before there is also one, with same intensity, incoming from the $\hat{y}$ direction. This

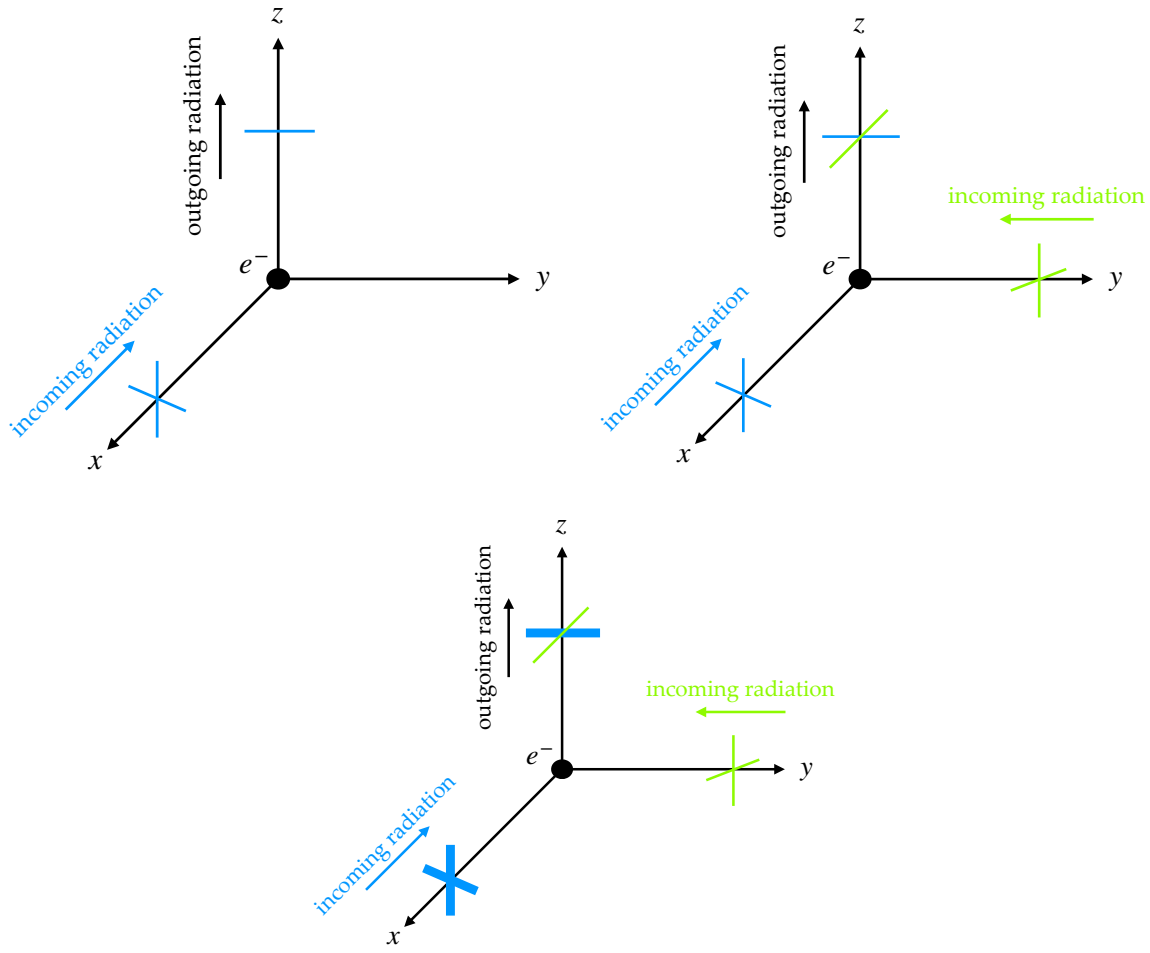

Figure 3.1: Schematic representation of different Thompson scattering processes. We display the scattering off an electron placed in the origin of unpolarised light incoming from the $\hat{x}$ direction (top-left panel), unpolarised light incoming from two perpendicular directions (top-right panel) and light with a quadrupolar anisotropy pattern (bottom panel).

case is represented in the top-right panel of figure 3.1. The second photon induces an additional polarisation to the light emitted by the electron, this time in the $\hat{x}$ direction. This, combined with the one from the first photon, makes the light emitted from the electron unpolarised, i.e. in presence of isotropic radiation Thompson scattering leads to unpolarised light.

The same mechanism of cancellations happens also for the case of anisotropic light with a dipole pattern, with overall unpolarised outgoing radiation.

The case of incoming radiation with a quadrupolar anisotropy is different. This corresponds to a set-up in which the free electron sees, e.g., two hot spots in the $\hat{x}$ and $-\hat{x}$ directions and two cold spots in the $\hat{y}$ and $-\hat{y}$ directions, where hot (cold) means more (less) intense radiation. This situation is represented in the bottom panel of figure 3.1, where the thicker lines indicate more intense radiation. The outgoing light in this case is linearly polarised in the $\hat{y}$ direction. As anticipated, incoming radiation with a quadrupolar anisotropy induces a net linear polarisation of the CMB photons.

The polarisation field can be described in terms of two components, the *E*- and *B-modes*. While scalar perturbations can induce only E-modes, tensor perturbations produce both E- and B-modes[1] [138]. E-modes in the CMB have already been detected [139], while the search for primordial B-modes is ongoing[2].

Detecting B-mode polarisation patterns in the CMB would be an indirect detection of primordial gravitational waves, i.e. would be the smoking gun for inflation[3]. It would also determine a specific value of the tensor-to-scalar ratio, see eq.(2.87), which would allow us to measure the energy scale of inflation, H, for single-field slow-roll models.

In the absence of a detection, using *Planck*, WMAP and the latest BICEP/Keck data to constrain the tensor-to-scalar ratio at $k = 0.05\,\mathrm{Mpc}^{-1}$ for the $\Lambda\mathrm{CDM}+r$ cosmological model yields the upper bound [142]

$$r < 0.036 \quad (95\,\%\,\mathrm{C.L.})\,. \tag{3.6}$$

Space- and Earth-based observatories proposed as future CMB surveys, such as CMB-S4 [143, 144], Simons Observatory [145], LiteBIRD [146] and PICO [147] will continue

[1] Primordial vector modes can also give rise to B-mode polarisation, but vector perturbations decay with the expansion of the universe [13], therefore their contributions is expected to be subdominant at recombination and can be neglected.

[2] B-modes have also been observed in the CMB, but are consistent with being caused by gravitational lensing of E-modes, see e.g. [140].

[3] This is because alternatives to inflation do not generate a detectable signal, see e.g. [141], but this is also true of many inflationary models, e.g. single-field α-attractor models, see chapter 6, with $\alpha < \mathcal{O}(10^{-2})$ would lead to a signal that is out of reach for detection with current and planned CMB polarisation observatories.

the hunt for B-modes, reaching a designed sensitivity, e.g. for the case of PICO, up to $\sigma(r) = 10^{-4}$ [147].

We note here that single-field slow-roll inflation predicts a red-tilted tensor power spectrum, see section 2.3.2, therefore the direct detection of primoridal GWs on small scales is not expected before the launch of dedicated space-based detectors such as DECIGO/BBO [148, 149]. On the other hand, a direct detection of GWs of primordial origin on small scale could point to different inflationary scenarios, possibly comprising additional fields, see e.g. the review [93]. We explore this possibility in chapter 4 for the case of additional light spin-2 fields.

Coherent phases: two striking pieces of evidence for inflation

While inflation was motivated in the first place as a solution to the main problems of the Hot Big Bang cosmology, see section 2.1, we presented in section 3.1 observations of the CMB temperature anisotropies that point to an almost scale-invariant power spectrum of primordial scalar fluctuations that is in perfect agreement with the predictions of single-field slow-roll inflation, see eq.(2.76).

On top of these remarkable successes of cosmological inflation, there is another characteristic of CMB primordial fluctuations, namely their *phase coherence*, that constitute strong evidence for inflation, see [138]. Inflation causes the modes of a single wavelength to oscillate with the same phase, i.e. all modes reach the maximum amplitude (or cross zero) at the same time. Coherent phases (as opposite to random initial phases) are therefore responsible for the coherent interference which produces the typical peaks and troughs observed in the CMB temperature power spectrum at multipoles $l > 200$ (see e.g. figure 1 of [29]). If the modes were oscillating with random phases, the CMB power spectrum would look like white noise instead. The multipoles involved ($l > 200$) correspond to scales that were sub-horizon at recombination, so one might think about other causal processes that could have been responsible for coherent phases. Given this, an even more striking observation is the (anti-)cross-correlation between the CMB temperature fluctuations and E-modes polarization on large scales, $50 < l < 200$ [150]. This is again the result of coherent phases, but now the scales involved were on super-horizon at recombination, meaning that no causal process can explain these observations.

3.3 Scalar non-Gaussianities

For a Gaussian quantity the 2-point correlation function is sufficient to statistically characterise its distribution. Observations of the CMB anisotropies point to scalar fluctuations with a nearly Gaussian distribution. The leading deviation from the Gaussian distribution is given by the 3-point correlation function, $\langle\zeta(\mathbf{x_1})\zeta(\mathbf{x_2})\zeta(\mathbf{x_3})\rangle$.

There are several sources of non-Gaussianities in the CMB [151], and in the following we focus on the description of primordial non-Gaussianities produced during inflation.

The Fourier transform of the 3-point correlation function of ζ is the *bispectrum* [14, 152],

$$\langle\zeta_{\mathbf{k_1}}\zeta_{\mathbf{k_2}}\zeta_{\mathbf{k_3}}\rangle \equiv (2\pi)^3\,\delta^3(\mathbf{k_1}+\mathbf{k_2}+\mathbf{k_3})\,B(k_1,k_2,k_3)\,. \tag{3.7}$$

Here the delta-function is due to the statistical homogeneity, or translation invariance[4], of the background, and it implies that the three momenta must form a closed triangle. Isotropy, or rotational invariance, implies that the bispectrum only depends on the magnitude of the momenta, $B(k_1,k_2,k_3)$.

The bispectrum is usually written as [152]

$$B(k_1,k_2,k_3) = f_{\rm NL}F(k_1,k_2,k_3)\,, \tag{3.8}$$

where $f_{\rm NL}$ is the dimensionless non-linearity parameter[5] which measures the *amplitude* of the bispectrum, and $F(k_1,k_2,k_3)$ describes the *shape* and *scale dependence* of it. Possible configurations for the momenta include the *squeezed* one[6], $k_1 \ll k_2 \sim k_3$, and the *equilateral* one, $k_1 = k_2 = k_3$. The value of the bispectrum varies as we change the momenta configuration, and the shape of the bispectrum is defined by the configuration of the triangle which contributes the most to the signal. Importantly, the shape of the bispectrum carries a lot of information about the ζ interactions that produced the 3-point correlation in the first place. For example, derivative interactions typically lead to an equilateral shape as the correlation is mainly imprinted on modes with similar k, due to the suppression of the interactions after horizon crossing.

Maldacena [153] showed that non-Gaussianities produced in single-field slow-roll inflation are slow-roll suppressed, $f_{\rm NL} = \mathcal{O}(\epsilon,\eta)$, and that the squeezed limit of the

[4] Spatial translation invariance leads to momentum conservation.

[5] Note that the parameter $f_{\rm NL}$ is shape-dependent, i.e. there will be a specific amplitude for each shape.

[6] The momenta k_2 and k_3 in the squeezed configuration are nearly equal because of momentum conservation, e.g. the squeezed triangle is closed.

bispectrum[7] can be related to the power spectrum through the consistency relation

$$\lim_{k_1 \ll k_2 \sim k_3} B(k_1, k_2, k_3) \propto (1 - n_s) P_\zeta(k_1) P_\zeta(k_2)\,, \tag{3.9}$$

where n_s is the spectral tilt of the scalar power spectrum. In other words, for an almost scale-invariant $P_\zeta(k)$, non-Gaussianities with a large squeezed limit are suppressed, and this applies in general to all single-field slow-roll inflation models, regardless of details of the inflaton potential. These results imply that detecting large squeezed non-Gaussianities would potentially rule out single-field slow-roll inflation [153, 157].

Using an EFT approach, see section 2.3.3, it is possible to show that single-field inflation supports in general non-Gaussianities in the equilateral and orthogonal shapes [158, 159], where the latter is orthogonal to the local and equilateral shapes. Examples of single-field models different from the vanilla slow-roll scenario include models with non-standard kinetic terms [160], $\mathscr{L} = P\left(X, \phi\right)$, where $X = \partial_\mu \phi \partial^\mu \phi$, or models with higer-derivative interactions, such as ghost inflation [161].

Multi-field models typically support non-Gaussianities of the squeezed type, see the reviews [157, 162, 163]. When the field-space geometry is hyperbolic and the trajectories strongly deviate from geodesic motion the bispectrum can be enhanced in the *flat* configuration, $k_1 + k_2 \sim k_3$, [164], see section 2.4.

Measurements from the *Planck* satellite lead to the current bounds at 68% C.L. [151]

$$f_{\rm NL}^{sq} = -0.9 \pm 5.1\,, \quad f_{\rm NL}^{eq} = -26 \pm 47\,, \tag{3.10}$$

consistent with single-field slow-roll inflation.

3.4 Tensor non-Gaussianities

Whilst in the previous section we have focused on the bispectrum of the scalar perturbation, there could be sources in the early universe leading to tensor non-Gaussianities [165].

Similarly to what was done in eq.(3.7) for the scalar 3-point correlation function, we define the tensor bispectrum as

$$\langle \gamma^{\lambda_1}_{\mathbf{k_1}} \gamma^{\lambda_2}_{\mathbf{k_2}} \gamma^{\lambda_3}_{\mathbf{k_3}} \rangle \equiv (2\pi)^3 \delta^3(\mathbf{k_1} + \mathbf{k_2} + \mathbf{k_3})\, \mathscr{A}^{\lambda_1 \lambda_2 \lambda_3}\, B_\gamma(k_1, k_2, k_3)\,, \tag{3.11}$$

[7] Whether the squeezed bispectrum corresponds to a physical observable effect, or can be cancelled by a suitable coordinates tranformation is still a matter of discussion, see e.g. [154–156].

where the function $\mathscr{A}^{\lambda_1\lambda_2\lambda_3}$ accounts for the different polarizations. Current bounds at 68% C.L. on the amplitude of tensor non-Gaussianities in the squeezed and equilateral limits are [151, 165]

$$f^{sq}_{\rm NL,\,tens} = 290 \pm 180\,, \quad f^{eq}_{\rm NL,\,tens} = 600 \pm 1600\,, \tag{3.12}$$

where the non-linearity parameters in (3.12) are defined as

$$f^{sq}_{\rm NL,\,tens} \equiv \lim_{k_1 \ll k_2 \sim k_3} \frac{B_\gamma^{+++}(k_1,k_2,k_3)}{S^{sq}(k_1,k_2,k_3)}\,, \tag{3.13}$$

$$f^{eq}_{\rm NL,\,tens} \equiv \frac{B_\gamma^{+++}(k,k,k)}{\frac{18}{5}\mathscr{P}_\zeta(k)^2}\,. \tag{3.14}$$

To connect with the bispectrum definition given in eq. (3.11), we identify $B_\gamma^{+++}(k_1,k_2,k_3) \equiv \mathscr{A}^{RRR} B_\gamma(k_1,k_2,k_3)\Big/2\sqrt{2}$. The numerical factor $\mathscr{A}^{RRR}$ is equal to 27/64 and 1/4 in the equilateral and squeezed shapes respectively [166]. In the squeezed limit, the bispectrum shape template S^{sq} reduces to

$$S^{sq}(k_L,k_S) = \frac{12}{5}\left(2\pi^2 P_\zeta(k)\right)^2 \frac{1}{k_L^3 k_S^3}\,, \tag{3.15}$$

where we have identified $k_L = k_1$ and $k_S = k_2 \sim k_3$, with $k_L \ll k_S$. The scalar power spectrum in eq.(3.14) can be related to the dimensionless scalar power spectrum $P_\zeta(k)$ using eq.(2.69).

Sizeable non-Gaussianities in the tensor sector are typically produced when additional fields source primordial GWs. This is the case, for example, for inflationary models with an additional spectator sector comprising a pseudo-scalar axion field and gauge fields [167–169]. Whilst the gauge fields are directly coupled with the axion spectator, the spectator sector is coupled only gravitationally with the inflaton.

Cook and Sorbo [167, 168] considered the case of $U(1)$ gauge fields and showed that the rolling of the axion amplifies the vacuum fluctuations of the gauge fields, which in turn can source primordial GWs and lead to an amplified tensor bispectrum signal. Only one polarisation of the gauge fields is excited and therefore the induced tensor bispectrum is parity-odd [168]. The $U(1)$ fields also source scalar perturbations, and current tight constraints on the scalar power spectrum and bispectrum severly restrict the parameter space of these models [170].

If the gauge fields have an $SU(2)$ symmetry instead, the sourcing of scalar modes is negligible and the model is shown to support enhanced primordial GWs [169], as well as amplified (equilateral) tensor non-Gaussianities at CMB scales [171].

We explore tensor non-Gaussianities sourced by light spin-2 fields during inflation in chapter 5.

3.5 Testing models predicting large fluctuations on small scales

As discussed in section 3.1, CMB observations tightly constrain the power spectrum of scalar fluctuations produced during inflation on large scales. On the other hand, the primordial power spectrum is much less constrained on smaller scales, i.e. $k \gg k_{\rm CMB}$. An intriguing possibility is that, on small scales, the statistics of the curvature perturbation deviates strongly from the large-scale behaviour, for example displaying a significant enhancement in the scalar power spectrum.

A sudden growth of the scalar power spectrum is usually associated with departures from single-field slow-roll inflation [81], for example in cases when a transient ultra-slow-roll phase is realised, see section 2.3.1.1. In single-field inflation this can be realised by a local feature in the inflaton potential, e.g., an inflection point [85–90, 172]. Other mechanisms associated with multi-field models have been proposed, such as a strongly non-geodesic motion [117, 118] and/or a large and negative curvature of the field space [4, 173]. These could cause a transient instability of the isocurvature perturbation, then transferred to the curvature fluctuation, leading to a peak in the scalar power spectrum, see section 2.4.

Enhanced scalar perturbations can lead to primordial black hole (PBH) production and potentially detectable second-order GWs, which we review in sections 3.5.1 and 3.5.2 respectively. These provide appealing ways of testing on small scales models of inflation beyond the vanilla single-field slow-roll one. In chapter 6, we study small-scale enhancements of the scalar fluctuations in the context of cosmological α-attractors [127–134], and explore their phenomenology in light of CMB large-scale constraints.

3.5.1 Primordial black hole formation

Very large amplitude scalar fluctuations produced during inflation give rise to large density perturbations when they re-enter the horizon after inflation, which can collapse to form primordial black holes [174] (see the review [175] for other formation mechanisms).

Interestingly, PBHs formed in the early universe could potentially constitute cold dark matter (or a fraction of it) [176–178], or could explain some of the events detected by the LIGO-Virgo collaboration [179–182].

The mass of the PBHs formed is related to the mass contained within the Hubble

horizon at the time of formation [175]

$$M_{\rm PBH} \equiv \gamma M_{\rm H} = \gamma \frac{4\pi\rho}{3H^3}\,, \tag{3.16}$$

where ρ is the energy density at the time of formation and γ is a dimensionless coefficient describing the fraction of the Hubble horizon mass which collapses into the PBH. The parameter γ is a numerical factor (somewhat below 1) [183] that depends on details of the gravitational collapse; for illustration we use the benchmark value $\gamma = 0.2$ [184]. For simplicity, we assume that there is a one-to-one correspondence between the mass of the PBH formed and the comoving scale of the scalar perturbations which produced it, $M(k) \equiv M_k$. In practice the spectrum of enhanced scalar perturbations will span a range of scales, and the process of critical collapse [185] will then lead to a spectrum of PBH masses [186, 187]. Nonetheless the Hubble mass (3.16) provides an upper limit on the PBH masses formed.

The mass fraction at formation of PBHs with mass M_k is given by

$$\beta(M_k) \equiv \left.\frac{\rho_{\rm PBH}}{\rho_{\rm tot}}\right|_{\rm at\ formation}\,. \tag{3.17}$$

This is commonly estimated using the Press–Schechter formalism [188], but we note that the peak theory approach [189–191] can also be used. In the Press-Schechter approach the PBH abundance is determined by the probability that some coarse-grained random field, δ, related to the comoving density perturbation (e.g., the compaction function [192, 193]) exceeds some critical threshold value, $\delta \geq \delta_c$:

$$\beta(M_k) = 2\gamma \int_{\delta_{\rm c}}^{\infty} \frac{{\rm d}\delta}{\sqrt{2\pi\sigma^2(M_k)}} {\rm e}^{-\frac{1}{2}\frac{\delta^2}{\sigma^2(M_k)}}\,. \tag{3.18}$$

The PBH mass fraction, $\beta(M_k)$, is exponentially sensitive to the variance of the coarse-grained density field, $\sigma^2(M_k)$, and thus to the peak of the primordial power spectrum on small scales [187, 194, 195]. In eq. (3.18) we assume that the probability distribution of the coarse-grained scalar perturbations, δ, is well-described by a Gaussian distribution, while noting that the abundance of very large density fluctuations could be very sensitive to any non-Gaussian tail of the probability distribution function [196–200].

The abundance of PBHs is constrained by several observations, with different masses leading to different types of constraints [175, 183]. PBHs with masses $M < 10^{15}$g [183] evaporate within the current age of the Universe due to Hawking radiation [201]. PBHs with smaller masses, $10^9{\rm g} < M < 10^{15}{\rm g}$, are mainly constrained by the effects that the radiation they emit would have on Big Bang nucleosynthesis [202] and CMB anisotropies

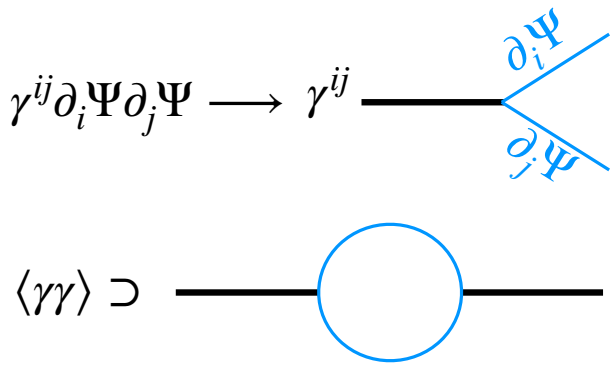

Figure 3.2: Diagrammatic representation of the interaction between a tensor mode, γ^{ij}, and the density perturbation, Ψ, at second order. We depict a representative interaction vertex, $\gamma^{ij}\partial_i\Psi\partial_j\Psi$, and the resulting 1-loop contribution to the tensor power spectrum in the top and bottom sections of the figure respectively.

[203], see figure 4 in [183]. PBHs with masses $M > 10^{15}$g are constrained e.g. by (i) the amount of radiation they emit [202]; (ii) the lensing they would induce in the light from sources of known redshift, e.g. gamma-ray bursts events [204], near stars [205], stars in Large and Small Magellanic Clouds [206], stars in Messier 31 [207]; (iii) the dynamical interaction they could have with astrophysical objects [183]. For a summary of these constraints see figure 10 in [183] or figure 1 in [208].

3.5.2 Second-order gravitational waves generation

First-order primordial scalar fluctuations produced during inflation induce a stochastic background of primordial GWs at second order in perturbation theory [209–213] (see also the review [214]).

After reheating is complete, primordial perturbations from inflation, $\zeta(\eta, \mathbf{k})$ in the language of section 2.3.1, re-enter the horizon during the radiation-dominated era and are transferred to the density perturbation, $\Psi(\eta, \mathbf{k})$, where $\Psi(\eta, \mathbf{k}) \equiv 2/3\, T(k\eta)\zeta(\mathbf{k})$ and $T(k\eta)$ is the transfer function in the radiation-dominated era [215]. In the Newtonian gauge, $\Psi(\eta, \mathbf{k})$ coincides with the Bardeen potential and it plays the role of the gravitational potential. The scalar perturbation sources at second-order the tensor fluctuations $\gamma_{ij}(\eta, \mathbf{k})$ [216]. As an example, we schematically represent in figure 3.2 one of the source terms, in the form $\partial_i\Psi\partial_j\Psi$. This type of interaction, depicted in the upper part of figure 3.2, in turn induces a 1-loop contribution to the tensor power spectrum, as represented in the lower section of figure 3.2.

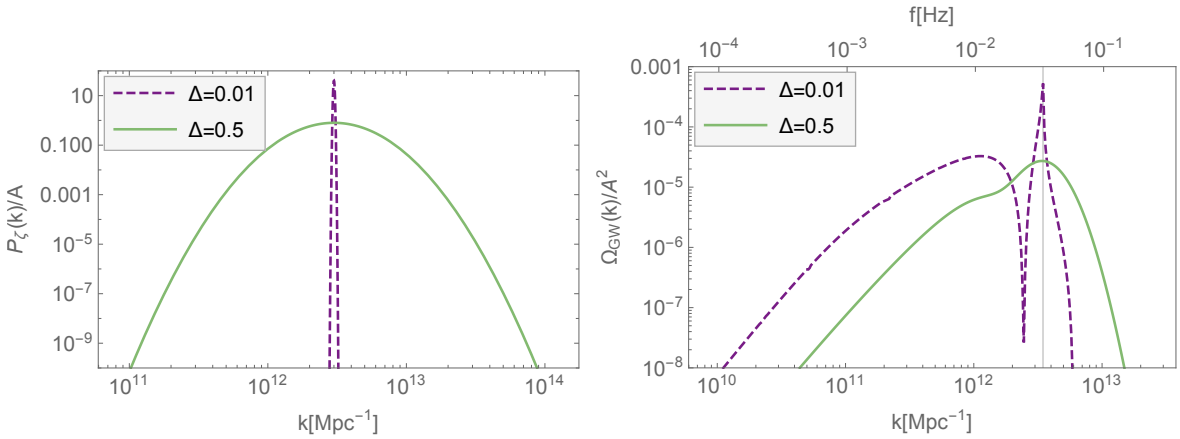

Figure 3.3: *Left panel:* two examples of a scalar power spectrum with a log-normal peak, see eq.(3.20), with parameters $\{k_{\rm peak} = 3\times 10^{12}\,{\rm Mpc}^{-1}, \Delta = 0.01\}$ (dashed-purple line) and $\{k_{\rm peak} = 3\times 10^{12}\,{\rm Mpc}^{-1}, \Delta = 0.5\}$ (green line) respectively. *Right panel:* $\Omega_{\rm GW}(k)$ of the second-order GWs induced by the primordial scalar power spectra displayed on the left. The vertical gray line signals the scale $k = 2/\sqrt{3}\,k_{\rm peak}$, where resonant amplification produces a peak in the induced GWs [211].

GWs induced at second order contribute to the stochastic background of GWs, see eq.(2.88). In particular, the present-day energy density associated with the second-order GWs is [212, 217]

$$\Omega_{\rm GW}(k) = \frac{\Omega_{\rm r,0}}{36}\int_0^{1/\sqrt{3}} {\rm d}d \int_{1/\sqrt{3}}^{\infty} {\rm d}s \left[\frac{(d^2-1/3)(s^3-1/3)}{s^2-d^2}\right]^2 P_\zeta\left(\frac{k\sqrt{3}}{2}(s+d)\right) \times P_\zeta\left(\frac{k\sqrt{3}}{2}(s-d)\right)\left[\mathscr{I}_c(d,s)^2+\mathscr{I}_s(d,s)^2\right], \tag{3.19}$$

where $\Omega_{\rm r,0} = 8.6\times 10^{-5}$ and the functions $\mathscr{I}_c$ and $\mathscr{I}_s$ are defined in eq. (D.8) in [217]. We note that the expression above is derived assuming a ΛCDM evolution, see [218, 219] for details on how the induced GWs could be used to probe the thermal history of the universe.

The amplitude and scale-dependence of the second-order GWs depends on the overall shape and amplitude of the primordial scalar power spectrum, see $P_\zeta(k)$ appearing twice in eq.(3.19). In single-field slow-roll inflation, $P_\zeta(k)$ has amplitude $\mathscr{A}_s \simeq 10^{-9}$ at CMB scales and is red-tilted, see sections 2.3.1 and 3.1, therefore the induced GW signal is expected to be small in amplitude, decreasing towards small scales, and in general beyond the reach of GWs detectors in the near future.

On the other hand, a large peak in the scalar power spectrum could lead to a potentially detectable second-order GW signal. As an example, in figure 3.3 we illustrate the

(idealised) case of a log-normal peak in the scalar power spectrum [220],

$$P_\zeta(k) = \frac{A}{\sqrt{2\pi\Delta^2}} \exp\left(-\log\left(k/k_{\rm peak}\right)\Big/ 2\Delta^2\right), \tag{3.20}$$

where $k_{\rm peak}$ is the position of the peak, Δ controls the width of the scalar power spectrum and A its amplitude. In the left panel we display $P_\zeta(k)/A$ for two models with $k_{\rm peak} = 3\times 10^{12}\,{\rm Mpc}^{-1}$ and $\Delta = 0.01$ (dashed-purple line) and $\Delta = 0.5$ (green line). The resulting spectrum of the second-order GWs is plotted in the right panel, and it is produced by numerically evaluating eq.(3.19). Both spectra display a two-peak structure, with a principal peak from resonant amplification located at $k = 2/\sqrt{3}\,k_{\rm peak}$ [211]. The two-peak structure is more evident for narrow peaks, in this case $\Delta = 0.01$, while it gets smoothed away for broader peaks, $\Delta = 0.5$.

Because of their primordial origin, the detection and characterisation of the second-order GWs signal could provide an indirect way of probing the scalar power spectrum on scales much smaller than those where the CMB constraints apply, see section 3.1, and in turn constrain the physics of inflation. From 2035 a series of space- and Earth-based GWs observatories will be searching for GWs on small scales, $10^6\,{\rm Mpc}^{-1} \lesssim k \lesssim 10^{18}\,{\rm Mpc}^{-1}$, potentially able to detect GWs of primordial origin, including the stochastic background induced at second-order from inflationary perturbations. We represent in figure 3.4 the sensitivity curves of present and upcoming GWs observatories, including the Square Kilometer Array (SKA) [221], Laser Interferometer Space Antenna (LISA) [222], Einstein Telescope (ET) [223], DECIGO/BBO [149], Cosmic Explorer (CE) [224] and Advanced LIGO-Virgo (aLV) [225].

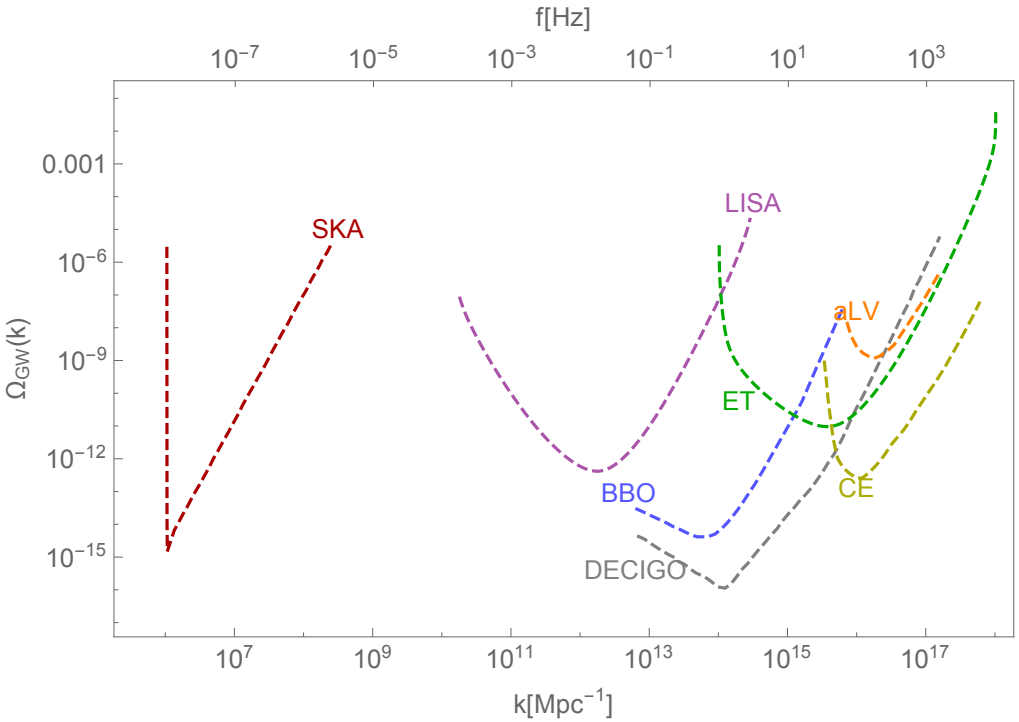

Figure 3.4: Sensitivity curves of present and future space- and Earth-based GWs observatories, operating up to frequencies in the kHz.

CHAPTER 4

PRIMORDIAL GWS FROM LIGHT SPIN-2 FIELDS

As discussed in chapter 3, the detection on small scales of a stochastic background of GWs with cosmological origin could point to inflationary scenarios different from canonical single-field slow-roll inflation. In this sense, present and future GWs interferometers, see figure 3.4, directly probe inflationary physics that deviates from the minimal scenario. In this chapter, we adopt an EFT description, see section 2.3.3, of extra spin-2 fields, where we dub the spin-2 as "extra" to underline the fact that it is distinguished from the standard massless spin-2 particle, the graviton, of general relativity. We demonstrate that time-dependent sound speed for the helicity-2 modes can generate primordial GWs with a blue-tilted spectrum, potentially detectable at interferometer scales. In particular, we focus here on the capability of the Laser Interferometer Space Antenna (LISA) [222] to constrain the parameter space of the spin-2 fields.

This chapter is based on the publication [1], and is arranged as follows. After motivating our work in section 4.1, in section 4.2 we briefly review the EFT approach and derive the scalar and tensor spectral indices in the case of time-dependent sound speeds for the helicity modes of an extra spin-2 field. In section 4.3 we discuss the theoretical requirements on the EFT Lagrangian parameters alongside current experimental constraints. These are later employed in section 4.4 to define current exclusion limits on the parameter space and to explore LISA detection and constraining power on this very general set-up. We discuss our results in section 4.5.

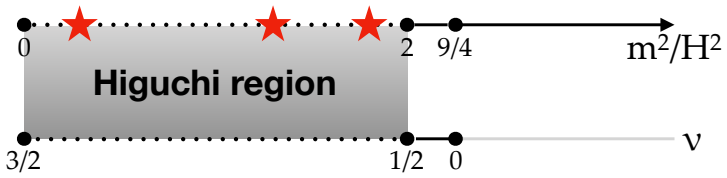

Figure 4.1: *Upper line:* mass spectrum the spin-2 field in case of coupling through gravity; the dotted region is excluded by the Higuchi bound [236] and red stars represent the (light) masses tested in this work, see section 4.4.1, which cover most of the Higuchi region without going to the massless limit. *Lower line:* values of $\nu \equiv \sqrt{9/4-(m/H)^2}$ corresponding to the masses above.

4.1 Motivation

Single-field slow-roll inflation is just one of several scenarios compatible with current observations and plenty of multi-field realizations can be found in the literature, see section 2.4. Upon requiring that the mass of the main field driving inflation is small enough to guarantee about 60 e-folds of expansion, any extra particle content can in principle cover a wide mass range. Very massive fields, $m \gg H$, are typically integrated out, although one may look for remnants of such fields in late-time observables [105, 122, 164, 226–232]. For example, inflaton trajectories that display fast turns might lead to effects of heavy physics in the primordial fluctuations, such as oscillatory features in the scalar power spectrum and related non-Gaussian signatures [122]. Cosmological probes are more sensitive to lighter, i.e. more long-lived, particles, satisfying $m \lesssim H$. Light extra particles will be the main focus of this chapter.

It proves useful to organize any extra content according to the *mass* and the *spin* of each given particle. Primordial correlators such as the bispectrum, see section 3.3, in their squeezed (and generalizations thereof) configuration, store key information about the mass and the spin of particles that mediate the corresponding interactions. Intriguingly, spinning fields generate a richer dynamics, including for example an extra angular dependence [233–235] that may be searched for by current and up-coming experiments.

As one considers the requirement of a consistent and predictive theory of spinning fields in de-Sitter space, the allowed mass range is dramatically reduced. Starting with $s = 2$, unitarity bounds [236] force massive particles to satisfy inequalities of the schematic form $m \gtrsim H$, to the detriment of the observational prospects for signatures corresponding to spinning fields. For spin-2 fields this takes the form of the so-called *Higuchi bound* on the graviton [236], $m^2 > 2H^2$, see figure 4.1.

Given that the inflationary background is not exactly de-Sitter, one may hope that unitarity is less demanding on an FLRW background. This specific question has been addressed, for the case of extra spin-2 fields, in [237]: although weakened in FLRW, a consistent cosmological evolution leads to a unitarity bound of the same form. In the absence of fine-tuning, the bound is no weaker than about one order of magnitude with respect to the pure de-Sitter case. Intuitively, this is expected in view of the fact that one can continuously go from FLRW to de-Sitter.

The one implicit assumption in the above results is that the extra fields are *minimally* coupled, i.e. only coupled through gravity to the inflaton field. Therein lies the key for drastically weaken unitarity bounds. Indeed, the latter stem from identifying unitary representations of the de-Sitter isometry group [238]. However, the inflationary background breaks de-Sitter isometries, see section 2.3.3, the very same isometries at the heart of unitarity requirements, and so will any field with sizable coupling to the inflaton. Unitarity bounds are much weakened as a result of such *non-minimal* couplings[1] and a much more interesting phenomenology ensues. This is not surprising: direct coupling to a light field, in this case the inflaton, makes much more efficient the energy exchange and enables heavier modes to become effectively lighter and considerably more long-lived.

When considering extra fields non-minimally coupled with the inflaton, it is important to first verify that the direct coupling does not lead to instabilities, or ghostly degrees of freedom, see e.g. [239]. There is an extra difficulty when it comes to higher spin ($s > 2$) theories in that a fully non-linear Lagrangian formulation is still missing [240, 241]. The massive $s = 2$ case is special in that a ghost-free fully non-linear formulation exists [242, 243] and has been used in the context of inflation [244–247] (see also [248] and references therein for an approach with a related model).

Here we shall adopt a specific approach [98] to non-minimal coupling during inflation which is the natural generalization of the EFT of single field inflation of [96], see section 2.3.3. The advantage intrinsic to this formalism is that the EFT will span almost the entire space of possible signatures. It is nevertheless possible to implement some consistency checks so that the theory is free of well-known pathologies, such as e.g. gradient instabilities [98].

We will focus in particular on the gravity sector of an inflationary theory with extra spinning fields. The degrees of freedom associated to spinning particles can source GWs

[1] For the spin-2 field with non-minimal coupling described in [98], the unitarity bound is derived by imposing the positivity of the coefficient of the helicity-0 mode kinetic term. The non-minimal coupling modifies (more precisely, it increases the number of) the parameters that affect the bound, and therefore one has more freedom to relax it with respect to the minimal-coupling case.

already at linear order, and the fact that these extra modes can be light enhances their effect on late-time observables. Remarkably, the sourced contribution can be the leading one and may dramatically alter the properties of the signal with respect to the vacuum dominated scenario, see eq.(2.86). Indeed, in contrast to the slightly red-tilted GW signal of single-field slow-roll models, multi-field set-ups enable a (strong) scale dependence in the tensor power spectrum, spanning from bump-like features to a purely blue-tilted signal, see e.g. [169, 249–256].

In the following sections, we first review how an extra spin-2 field can source the GW spectrum at tree level [98] and then show how a time-dependent speed of sound for the extra modes delivers a blue-tilted spectrum within reach of LISA. We combine bounds from the model self-consistency checks with those originating from (i) measurements of the primordial scalar power spectrum on large scales; (ii) the upper limit on the tensor-to-scalar ratio r at CMB scales and scalar/mixed non-Gaussianities in the same regime; (iii) ultracompact minihalos and primordial black holes; (iv) big bang nucleosynthesis; (v) the Laser Interferometer Gravitational-Wave Observatory (LIGO) and the Pulsar Timing Arrays (PTA).

4.2 EFT of light spin-2 fields during inflation

The unitarity bounds that prohibit a large fraction of the mass range for fields with spin $s \geq 2$ stem from the common notion of particles as unitary irreducible representations of the spacetime isometry group [238]. The fact that inflation does not correspond to de-Sitter, but rather to *quasi* de-Sitter background, points to a natural way around stringent unitarity requirements. The inflaton itself breaks de-Sitter isometries for the simple reason that inflation needs a "clock" for the accelerated expansion to eventually come to an end, see section 2.3.3. Demanding unitarity on extra fields in *quasi* de-Sitter space turns out to enforce qualitatively similar constraints to the de-Sitter case as long as the extra content is only *minimally*, i.e. gravitationally, coupled to the inflaton field. The key step is then to *directly* couple spinning particles to the inflaton.

Given a specific set-up one can then work out the corresponding effects of non-minimal coupling on late-time observables. In this work we shall adopt a different perspective, namely that of [98], which is an extension of the works in [96, 97] on the EFT of inflation. As reviewed in section 2.3.3, the set-up of [96] uses the Stueckleberg trick to make manifest the Goldstone boson of the (spontaneously) broken time-reparametrization invariance. At sufficiently high energies, i.e. in the decoupling limit, the dynamics of the

system if fully captured by the Goldstone boson π, which can be related to the curvature fluctuations ζ, see eq.(2.117). It is then natural to consider extra fields in this framework [97].

The extension to extra spinning fields is somewhat more complex. It relies on the fact that one can classify the extra field content, as is typical in the case of non-linearly realised symmetries, as representations of the unbroken group. The unbroken symmetries being rotations, it is straightforward that particles of different spin will have a different description (as a three-vector, a three-tensor and so on). In the case of interest for us, that of an extra spin-2, the five propagating degrees of freedom are described by the traceless symmetric tensor Σ^{ij} which is "embedded" as the four-tensor $\Sigma^{\mu\nu}$, whose $(0,0)$ and $(0,i)$ components are:

$$\Sigma^{00} = \frac{\partial_i\pi\partial_j\pi}{(1+\dot\pi)^2}\Sigma^{ij}\,, \qquad \Sigma^{0j} = -\frac{\partial_i\pi}{1+\dot\pi}\Sigma^{ij}\,. \tag{4.1}$$

The effectively light states described by Σ have their couplings with the inflaton prescribed by the fact that broken symmetries are non-linearly realized. An explicit example is provided in the quadratic and cubic interactions for $\sigma^{ij} = a^2\Sigma^{ij}$ [98],

$$\begin{aligned} S \supseteq\, & S^{(2)}_{\rm free} + S^{(2)}_{\rm int} + S^{(3)}_{\rm int} \\ =\, & \frac{1}{4}\int dt\, d^3\mathbf{x}\, a^3 \left[\left(\dot\sigma^{ij}\right)^2 - c_2^2 a^{-2}\left(\partial_i\sigma^{jk}\right)^2 - \frac{3}{2}\left(c_0^2-c_2^2\right)a^{-2}\left(\partial_i\sigma^{ij}\right)^2 - m^2\left(\sigma^{ij}\right)^2\right] \\ & + \int dt\, d^3\mathbf{x}\, a^3\left[-\frac{\rho}{\sqrt{2\epsilon_1}H}a^{-2}\partial_i\partial_j\pi_c\sigma^{ij} + \frac{1}{2}\rho\dot\gamma_{c\,ij}\sigma^{ij}\right] \\ & - \int dt\, d^3\mathbf{x}\, a^3\left[\frac{\rho}{2\epsilon_1 H^2 M_p}a^{-2}\left(\partial_i\pi_c\partial_j\pi_c\dot\sigma^{ij} + 2H\partial_i\pi_c\partial_j\pi_c\sigma^{ij}\right) + \mu\left(\sigma^{ij}\right)^3 + \dots\right] \end{aligned} \tag{4.2}$$

where ϵ_1 is defined in eq.(2.26), m is the mass of the spin-2 field and $\pi_c \equiv \sqrt{2\epsilon_1}HM_p\,\pi$ and $\gamma^c{}_{ij} \equiv M_p\gamma_{ij}$ are the canonically normalized Goldstone boson and tensor fluctuations respectively, see section 2.3.3. The quantities ρ and μ are coupling constants with mass dimension one.

The quadratic interactions in the action (4.2) are obtained in the decoupling limit from a term $\propto \rho\,\delta K_{\mu\nu}\Sigma^{\mu\nu}$ [98], coupling the spin-2 tensor with the fluctuation of the extrinsic curvature of hypersurfaces at constant time, see below eq.(2.100); the cubic self-interaction of the spin-2 derives from a term $\propto \mu\,\Sigma_{\mu\nu}\Sigma^\mu_\rho\Sigma^{\rho\nu}$ [98].

In eq.(4.2), the sound speeds for the 0, 1 and 2-helicity components of σ are indicated as c_0, c_1 and c_2, and they satisfy the relation [98]

$$c_1^2 = \frac{1}{4}c_2^2 + \frac{3}{4}c_0^2\,. \tag{4.3}$$

The interactions in $S^{(2)}_{\rm int}$ generate tree-level contributions to the scalar and tensor power spectra, whose amplitudes are sensitive to the sound speeds (c_0, c_2), and to the magnitude of the ρ/H coupling. In this work, we shall allow for a time-dependence in the sound speeds and explore its implications at the level of the power spectra. For simplicity, we take the parameter ρ to be a constant.

The scalar and tensor power spectra and their scale-dependence[2] is given by

$$P_\zeta(k) = \frac{H^2}{8\pi^2 M_p^2 \epsilon_1}\left(\frac{k}{k_{\rm CMB}}\right)^{n_s^{(v)}-1} + \frac{H^2}{8\pi^2 M_p^2 \epsilon_1^2}\frac{C_\zeta(\nu)}{{c_0}^{2\nu}}\left(\frac{\rho}{H}\right)^2\left(\frac{k}{k_{\rm CMB}}\right)^{n_s^{(\sigma)}-1}, \tag{4.4a}$$

$$P_\gamma(k) = \frac{2H^2}{\pi^2 M_p^2}\left(\frac{k}{k_{\rm CMB}}\right)^{n_t^{(v)}} + \frac{2H^2}{\pi^2 M_p^2}\frac{C_\gamma(\nu)}{{c_2}^{2\nu}}\left(\frac{\rho}{H}\right)^2\left(\frac{k}{k_{\rm CMB}}\right)^{n_t^{(\sigma)}}, \tag{4.4b}$$

where $k_{\rm CMB}$ is the CMB pivot scale, $k_{\rm CMB} = 0.05\,{\rm Mpc}^{-1}$. The first contribution on the right-hand side of eq.(4.4a) is due to vacuum fluctuations, see eq.(2.69), while the second one is sourced by σ. The same holds for the tensor power spectrum in eq.(4.4b). The scalar and tensor spectral indices are given by

$$n_s^{(v)} - 1 = -2\epsilon_1 - \epsilon_2\,, \tag{4.5a}$$

$$n_s^{(\sigma)} - 1 = -2\epsilon_2 - 2\nu s_0 - \frac{m^2}{H^2}\epsilon_1\frac{1}{\nu}\left(\frac{\partial}{\partial\nu}\ln C_\zeta(\nu) - 2\ln c_0\right), \tag{4.5b}$$

$$n_t^{(v)} = -2\epsilon_1\,, \tag{4.5c}$$

$$n_t^{(\sigma)} = -2\nu s_2 - \frac{m^2}{H^2}\epsilon_1\frac{1}{\nu}\left(\frac{\partial}{\partial\nu}\ln C_\gamma(\nu) - 2\ln c_2\right). \tag{4.5d}$$

In the above, $\nu \equiv \sqrt{9/4 - (m/H)^2}$, ϵ_1 and ϵ_2 are defined in eq.(2.26) and the time-dependence of the sound speeds is described in terms of the parameters $s_n \equiv \dot{c}_n \big/ (H c_n)$, with $n = 0, 1, 2$. The functions $C_\zeta(\nu)$ and $C_\gamma(\nu)$ can be computed analytically for $c_0 \ll 1$ and $c_2 \ll 1$ [98] and are represented in figure 4.2 in the mass range $3/5 < \nu < 7/5$.

When discussing the phenomenology of the EFT and comparing it with observations, one needs to connect comoving scales corresponding to specific observations with the dynamics of inflation, see the discussion around eq.(3.1). This is achieved by employing the number of e-folds of inflationary expansion as defined in eq.(2.33). We refer to the number of e-folds elapsed between the horizon crossing of the comoving wavenumber

[2]While the validity of the power law expansion is ensured around the pivot scale, $k_{\rm CMB}$, higher-order corrections might become relevant on scales $k \gg k_{\rm CMB}$. To systematically take these into account, one should include the running of the spectral tilt and higher-order derivatives, see e.g. eq.(2.71). For the present analysis, we choose to cut the power law expansions in eqs.(4.4a) and (4.4b) at the level of the spectral tilt.

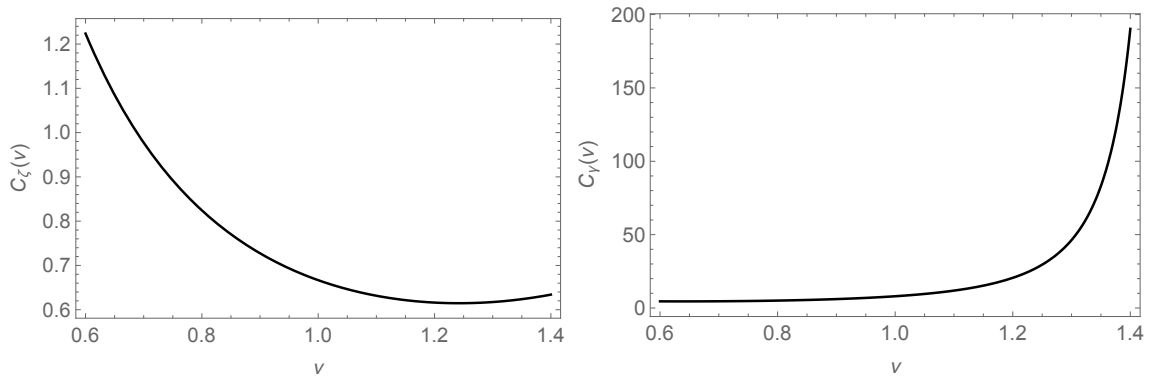

Figure 4.2: $C_\zeta(\nu)$ (left panel) [98] and $C_\gamma(\nu)$ (right panel) [98] plotted over the range $3/5 < \nu < 7/5$, corresponding to spin-2 masses $0.54 \lesssim m/H \lesssim 1.37$.

$k_0 = a_0 H_0 \simeq 10^{-4}\,\mathrm{Mpc}^{-1}$, corresponding to the current comoving size of the universe, and the end of inflation as $\Delta N_{\rm tot}$, which is defined in a way similar to eq.(3.1) [67, 257], where $k_{\rm CMB}$ is now substituted by k_0. By considering no significant energy drops at the end of inflation, so that $\rho_{\rm end} \simeq V$, instant reheating, $\rho_{\rm th} = \rho_{\rm end}$ and $g_{th} = 10^3$, eq.(3.1) becomes

$$\Delta N_{\rm tot} \simeq 67 + \frac{1}{4} \ln \frac{3H^2}{M_p^2}\,, \tag{4.6}$$

where we have used the Friedmann equation during slow-roll inflation (2.31). Once $\Delta N_{\rm tot}$ is given, we define the number of e-folds elapsed between the horizon crossing of a mode k and the end of inflation, $\Delta N(k)$, as

$$\Delta N(k) \equiv \Delta N_{\rm tot} - \ln \frac{k}{a_0 H_0}\,. \tag{4.7}$$

4.3 Current and future bounds

Let us elaborate on the bounds on the scalar and tensor power spectra that are employed in section 4.4 to constrain the parameter space of the effective Lagrangian. We refer the interested reader to a similar analysis carried out in [93]. There, the starting point is the specific model in [258] (see also [259, 260]), with an additional feature: the time-dependence of the speed of sound for the scalar spectator field has been switched on. In what follows, theoretical requirements and experimental constraints will be combined to draw the current exclusion regions in the $\left(\rho/H, |s_2|\right)$ plane of the EFT Lagrangian parameter space and to identify LISA's constraining power.

4.3.1 Consistency requirements

Besides being generally defined in the $(0,1]$ interval[3], the sound speeds in the EFT framework are subject to additional theoretical (and observational) constraints. One such bound, $c_n \gtrsim 10^{-3}$, arises from perturbativity requirements, in particular from requiring that the one loop σ-sourced corrections are smaller than the tree-level power spectra [98]. In the following we relax this bound, and consider $c_n \gtrsim 10^{-4}$ throughout the EFT validity.

General consistency of the perturbative treatment also translates into bounds on the coupling constants, $\rho/H \ll \sqrt{\epsilon_1}$ and $\rho/H \ll 1$, which define the weak-mixing regime. These ensure that $S^{(2)}_{\rm int}$ can be treated as a (small) correction to the kinetic Lagrangian, see eq.(4.2).

An additional constraint on ρ/H is imposed in order to avoid gradient instabilities,

$$\frac{\rho}{H} \ll \sqrt{\epsilon_1 c_0^2}\,. \tag{4.8}$$

In presence of a time-dependent sound speed c_0, we always make sure that the constraint above is satisfied at all times, by using the minimum value that c_0 acquires throughout the evolution. Eq.(4.8) automatically ensures that also the previous two conditions on ρ/H are satisfied, given that $c_0 \leq 1$ and $\epsilon_1 \ll 1$.

We point out here that the expressions of the power spectra reported in eqs. (4.4) are accurate only in the regime [98]

$$\rho \ll m\,, \tag{4.9a}$$

$$\Delta N(k) \gg \left(\frac{m}{H}\right)^{-2} \equiv \Delta N_{\rm EFT}\,, \tag{4.9b}$$

where $\Delta N(k)$ is defined in eq.(4.7). For the mass values considered here, see section 4.4.1, we calculate the corresponding $\Delta N_{\rm EFT}$ by using (4.9b),

$$\{(m/H, \Delta N_{\rm EFT})\} = \{(1.37, 0.53), (1.12, 0.80), (0.54, 3.45)\}\,. \tag{4.10}$$

The conditions in (4.9) ensure that the perturbative result for the tensor power spectrum coincides with the one derived from a non-perturbative treatment of the $(\gamma - \sigma)$ mixing [98].

[3]For a Lorentz-invariant quantum field theory, the requirement $c_s \leq 1$ ensures causality is preserved; for a recent discussion about superluminality and causality see e.g. [261].

4.3.2 Observational bounds on the scalar sector

The 2- and 3-point statistics of scalar perturbations are constrained on large scales by measurement of CMB anisotropies, see sections 3.1 and 3.3. Constraints on scalar non-Gaussianities on these scales give rise to a lower bound on the sound speeds of the order $c_n \gtrsim 10^{-2}$ [98]. As to the 2-point statistics, *Planck* data constrain the amplitude and the tilt of the primordial scalar power spectrum for the ΛCDM model [67]. Using the power-law parameterisation in eq.(2.71) yields the measurements (3.2) for the amplitude and (3.5) for the tilt. In the following, we use the central value of the tilt, $n_s = 0.9649$ [67].

For simplicity, we assume that on large scales the scalar power spectrum (4.4a) is dominated by the vacuum contribution which implies

$$\frac{\rho}{H} \ll \sqrt{\frac{\epsilon_1 c_0^{2\nu}}{C_\zeta(\nu)}}\Big|_{k=k_{\rm CMB}} . \tag{4.11}$$

As it will become clearer in the next section, within the spin-2 field mass range considered in this work, eq. (4.11) and the gradient instability condition (4.8) are nearly equivalent. When eq.(4.11) holds, ϵ_1 can be deduced from the measurement of $\mathscr{A}_s$ upon fixing the Hubble rate, H.

One can further verify that, given the above conditions, *Planck* constraints on the spectral tilt, n_s, are easily satisfied. To this aim, we compute the EFT Lagrangian prediction for the parameters in the power-law parametrisation (2.71),

$$P_\zeta(k) = \frac{H^2}{8\pi^2 M_p^2 \epsilon_1}\left[1 + \frac{C_\zeta(\nu)}{{c_0}^{2\nu}\epsilon_1}\left(\frac{\rho}{H}\right)^2\right]\left(\frac{k}{k_{\rm CMB}}\right)^{n_s^{\rm tot}} , \tag{4.12}$$

where $n_s^{\rm tot} = (-2\epsilon_1 - \epsilon_2 + \delta)\Big|_{k=k_{\rm CMB}}$, with

$$\delta = \frac{\frac{C_\zeta(\nu)}{{c_0}^{2\nu}\epsilon_1}\left(\frac{\rho}{H}\right)^2}{1 + \frac{C_\zeta(\nu)}{{c_0}^{2\nu}\epsilon_1}\left(\frac{\rho}{H}\right)^2}\left[-\epsilon_2 + 2\epsilon_1 - 2\nu s_0 - \frac{m^2}{H^2}\epsilon_1\frac{1}{\nu}\left(\frac{\partial}{\partial\nu}\ln C_\zeta(\nu) - 2\ln c_0\right)\right] . \tag{4.13}$$

Using the observed value of the tilt to fix $\epsilon_2 = -2\epsilon_1 - (n_s - 1)$, one concludes that the condition $\delta \ll -2\epsilon_1 - \epsilon_2$ puts a bound on the parameter space which is automatically satisfied if eq.(4.11) holds, and provided we span the range of masses and sound speeds used throughout our analysis.

The amplitude of the scalar fluctuations is constrained on small scales by CMB spectral distortions, primordial black holes and ultra-compact mini-halos (UCMH). Spectral

distortions can be generated by dissipation of primordial perturbations through photon diffusion and are relevant in the $1 \lesssim k/\mathrm{Mpc}^{-1} \lesssim 10^4$ range [262]. We apply spectral distortions bounds on the scalar power spectrum at $k_{\rm SD} = 3 \times 10^2\,\mathrm{Mpc}^{-1}$, in particular $P_\zeta(k_{\rm SD}) < 4 \times 10^{-5}$ [120].

PBH may have formed from the collapse of large density perturbations, see section 3.5.1, and therefore constraints on their abundance result into bounds on the primordial scalar power spectrum [202, 263, 264]. These are several orders of magnitude weaker compared with CMB bounds, however they are important in that they span significantly more orders of magnitude in scales, see [186] for an updated analysis. We apply the bound at the scale $k_{\rm PBH} = 10^{14}\,\mathrm{Mpc}^{-1}$, in particular $P_\zeta(k_{\rm PBH}) < 10^{-2}$ [265]. This corresponds to PBH masses $\simeq 10^{-12}\,M_\odot$, whose Schwartzshild radius is $R_{\rm s} \simeq 10^{-9}\,\mathrm{m}$. They can affect the path of photons with $\lambda \simeq R_{\rm s}$, introducing an interference pattern in their energy spectrum. This effect goes by the name of *femptolensing*[4]. The non-detection of femptolensing from PBHs with these masses in turn constrains the scalar power spectrum [265].

We verified that both spectral distortions and PBH constraints produce less stringent bounds on the parameter space of our EFT Lagrangian than those obtained by implementing the gradient instability condition. These will therefore not be included in the final plots.

UCMH are dense dark matter structures that can form from large density perturbations right after matter-radiation equality [266]. While many of the constraints on their abundance depend on assumptions regarding the nature of the dark matter particles, more general constraints can be obtained by accounting for gravitational effects, in particular lensing time-delay in pulsar timing [265]. For this reason we apply UCMH constraints at a scale $k_{\rm UCMH} = 3 \times 10^5\,\mathrm{Mpc}^{-1}$. The value of the bound depends on whether one assumes a constant or a scale- and redshift-dependent value of the density contrast that is required to form the UCMH structure. In the scale-independent case the bound is given by $P_\zeta(k_{\rm UCMH}) < 2 \times 10^{-8}$[265]. If instead a scale-dependence is allowed the corresponding bound is $P_\zeta(k_{\rm UCMH}) < 3 \times 10^{-7}$ [265]. In section 4.4 we implement both and refer to them as “UCMHconst” and “UCMHsc”.

[4]The name comes from the angular separation of the two images (of the photon), which is of the order of 10^{-15} arcsecs.

4.3.3 Observational bounds on the tensor sector

Taking the upper limit[5] on the tensor-to-scalar ratio $r < 0.056$, at a pivot scale $k_r = 0.002\,\mathrm{Mpc}^{-1}$ [67], implies that

$$P_\gamma^{(v)}(k_r) + P_\gamma^{(\sigma)}(k_r) < 1.3 \times 10^{-10}\,, \tag{4.14}$$

where the superscripts (v) and (σ) indicate respectively the vacuum and sourced contributions in eq. (4.4b). For each configuration analyzed in section 4.4, characterized by fixed values of $\{H, m\}$ and initial conditions for the sound speeds, eq. (4.14) will generate an exclusion line in the $\left(\rho/H, |s_2|\right)$ plane. In the case of a tensor power spectrum dominated by vacuum fluctuations on large scales, the constraint on r corresponds to a maximum value $H_{\rm max} = 6.13 \times 10^{13}\,\mathrm{GeV}$ for the Hubble rate during inflation. In section 4.4 we will derive exclusion limits on the parameter space for the following values of the Hubble rate, $H = \{10^{12}\,\mathrm{GeV}, 10^{13}\,\mathrm{GeV}, 6.1 \times 10^{13}\,\mathrm{GeV}\}$.

In addition to constraints on the tensor power spectrum, measurements of CMB anisotropies reflect on equilateral and squeezed tensor non-Gaussianity in the form of a lower bound on the helicity-2 sound speed, $c_2 \gtrsim 10^{-2}$ [166]. This bound will restrict the range of possible values for the initial, $c_{2\mathrm{i}}$, i.e. the value that the helicity-2 sound speed has on large scales.

Inflationary tensor fluctuations contribute to the present GW energy density, $\Omega_{\rm GW}(k)$, see eq.(2.88). Existing bounds on $\Omega_{\rm GW}(k)$, besides those from CMB anisotropies, are provided by (i) advanced LIGO-Virgo; (ii) Big Bang nucleosynthesis (BBN); and (iii) pulsar timing arrays (PTA).

Data from the second observing run of advanced LIGO, combined with the results of the first run, can be used to place upper limits on $\Omega_{\rm GW}$ for a background which is frequency-independent in the LIGO frequency band. The bound is given by [267]

$$\Omega_{\rm GW} < 6.0 \times 10^{-8}\,, \tag{4.15}$$

and it applies at scales comparable to those probed by LIGO, $k_{\rm LIGO} \simeq 10^{16}\,\mathrm{Mpc}^{-1}$. As for all bounds listed in this section, we translate this limit into a constraint in the $\left(\rho/H, |s_2|\right)$ space. In particular, for each configuration tested in section 4.4, we replace the expression of the tensor power spectrum (4.4b) into eq.(2.88), and derive the LIGO exclusion line from (4.15)[6].

[5] The bound presented in section 3.2, see eq.(3.6), appeared after this work was published.

[6] In principle, we should use a bound from a specific search for the spin−2 signal in LIGO data. However, as shown in section 4.4, the LIGO bound is never the strongest one in the parameter space, hence we find it safe to use the constraint given on a flat signal.

Measurements of the abundance of the primordial light elements constrain the number of effective massless degrees of freedom at the onset of nucleosynthesis [268]. This bound is weaker than the LIGO constraint (4.15). Pulsars, or "cosmic lighthouses", are rotating neutron stars that emit a beam of electromagnetic radiation, observed on Earth as a regular train of radiation pulses [269]. In presence of a stochastic background of GWs, the arrival times of the electromagnetic pulses are shifted, and therefore PTA provide a way of constraining $\Omega_{\rm GW}$. We apply constraints from PTA at the scale $k_{\rm PTA} \simeq 10^6\,{\rm Mpc}^{-1}$, in particular $\Omega_{\rm GW}(k_{\rm PTA}) < 2.7 \times 10^{-9}$ [94]. It can be verified that for a monotonically growing primordial power spectrum as $P_\gamma^{(\sigma)}$, the BBN and PTA exclusion lines always sit above the LIGO line in the $\left(\rho/H, |s_2|\right)$ plane. For this reason they are not represented in the plots of section 4.4.

Besides existing observational bounds on $\Omega_{\rm GW}$, we also consider LISA [222] expected sensitivity limits. The duration of the mission will be 4 years, with a possible 6-year extension, and LISA arms will be $2.5 \times 10^6\,{\rm Km}$ long. The data taking efficiency of the mission is expected to be $\sim 75\%$ of the nominal time, because of operations needed for the antenna maintenance. As a result, the 4-year mission will effectively produce 3 years of data. The most updated LISA strain sensitivity curve can be found in [270] (see also [271]), where the power law sensitivity curve is derived following [272], for a signal-to-noise ratio SNR = 10. In the following, we pick as reference scale for LISA the one that minimizes the sensitivity curve calculated in [270], $k_{\rm LISA} \simeq 1.79 \times 10^{12}\,{\rm Mpc}^{-1}$, which corresponds to a sensitivity value $\Omega_{\rm LISA} \simeq 4.12 \times 10^{-13}$. In order to be detectable by LISA, the energy-density associated with a gravitational wave mode must overcome LISA's sensitivity curve at the same scale, $\Omega_{\rm GW}(k_{\rm LISA}) > \Omega_{\rm LISA}$. This condition is used to generate the LISA line in $\left(\rho/H, |s_2|\right)$ plane, see plots in section 4.4.

We provide in figure 4.3 a pictorial representation of $\Delta N_{\rm tot} \simeq 60$ e-folds of inflationary expansion for $H = 10^{12}\,{\rm GeV}$, see eq.(4.6), and highlight the stages at which the relevant scales discussed above left the horizon.

4.4 Examples of time-dependent sound speeds

The parameters $s_n \equiv \dot{c}_n/(H c_n)$, where $n = 0, 1, 2$ for the helicity 0, 1 and 2 of σ, quantify the time-dependence of the sound speeds. From eq.(4.3) one finds

$$s_0 = \frac{4}{3}\frac{c_1^2}{c_0^2} s_1 - \frac{1}{3}\frac{c_2^2}{c_0^2} s_2 \,. \tag{4.16}$$

In table 4.1, we report some of the solutions to (4.16). A negative (positive) s_n produces

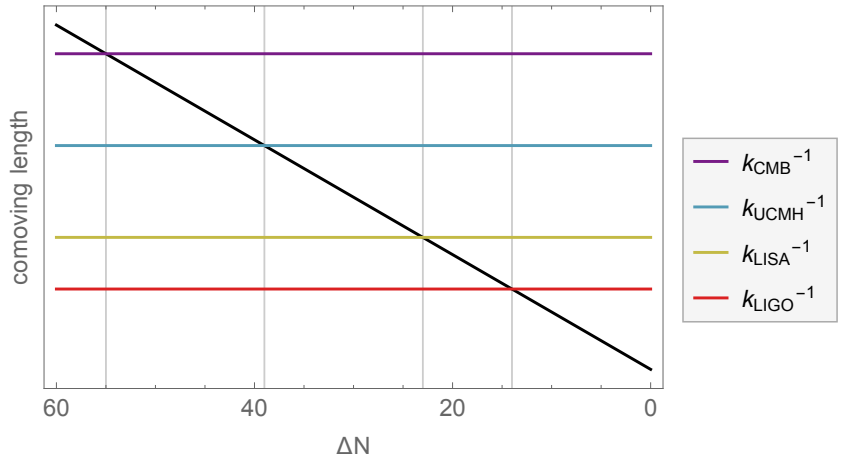

Figure 4.3: Sketch of the evolution of the horizon size, $(aH)^{-1}$, (black line), together with the comoving lengths associated with experimental bounds discussed in section 4.3. Here we fix for illustration $\Delta N_{\rm total} \simeq 60$ e-folds of inflationary expansion, which is obtained from eq.(4.6) for $H = 10^{12}\,$GeV. The gray vertical lines highlight the values $\Delta N = \{55, 39, 23, 14\}$, which is when the modes $k_{\rm CMB}$, $k_{\rm UCMH}$, $k_{\rm LISA}$ and $k_{\rm LIGO}$ left the horizon respectively. Here inflation ends at $\Delta N = 0$.

s_0	s_1	s_2		case
$s_0 = -\frac{1}{3}\frac{c_2^2}{c_0^2}s_2$	$s_1 = 0$	s_2	$s_2 < 0, s_0 > 0$	(1.a)
			$s_2 > 0, s_0 < 0$	(1.b)
$s_0 = 0$	$s_1 = \frac{1}{4}\frac{c_2^2}{c_1^2}s_2$	s_2	$s_2 < 0, s_1 < 0$	(2.a)
			$s_2 > 0, s_1 > 0$	(2.b)
s	s	s	$s < 0$	(3.a)
			$s > 0$	(3.b)

Table 4.1: Some of the phenomenologically interesting solutions of eq. (4.16). The fourth column indicates the signs of the solutions. The cases highlighted in yellow are analysed in sections 4.4.1, 4.4.2 and 4.4.3.

a decreasing (increasing) sound speed for the corresponding helicity, hence a power spectrum that grows (decreases) towards small scales, see the signs of the terms including s_0 and s_2 in eqs.(4.5b) and (4.5d). For tensor perturbations, this implies the existence of a GW signal potentially detectable with interferometers. The solutions with $s_2 < 0$, which we shall refer to as (1.a), (2.a), and (3.a), are highlighted in yellow in table 4.1. Naturally, we anticipate that the region of parameter space corresponding instead to an enhanced scalar power spectrum at small scales, $s_0 < 0$, will be more constrained, given also the absence of gradient instabilities enforced by eq. (4.8).

4.4.1 Case (1.a): constant c_1

Let us consider the solution $\{s_0 = -\frac{1}{3}c_2^2/c_0^2 s_2 > 0, s_1 = 0, s_2 < 0\}$. In addition, let us assume $s_2 =$ constant for simplicity. The time evolution of c_2 is obtained by solving the differential equation $s_2 = \dot{c}_2/(Hc_2)$ and reads

$$c_2(t) = c_{2\mathrm{i}}\, e^{s_2 \int_{t_\mathrm{i}}^{t} dt' H(t')} = c_{2\mathrm{i}}\, e^{s_2(\Delta N_{\mathrm{tot}} - \Delta N(t))}\,, \tag{4.17}$$

where we have used the definition of the number of e-folds elapsed between a given reference time t_i and t, see eq.(2.33). We take t_i to be the time at which our current observable universe exited the horizon, corresponding to modes with comoving wavenumber $k_0 = a_0 H_0$ that crossed the horizon ΔN_{tot} e-folds before the end of inflation, and $c_{2\mathrm{i}} \equiv c_2(t_i)$. From eq.(4.17) one can equivalently write the sound speed evolution in terms of k,

$$c_2(k) = c_{2\mathrm{i}} \left(\frac{k}{a_0 H_0}\right)^{s_2}\,, \tag{4.18}$$

where the k-dependence is obtained by virtue of the fact that cosmological correlators give the leading contribution at horizon crossing, i.e. when a precise relation is in place between k and t.

We consider benchmark values $c_{2i} = \{10^{-2}, 10^{-1}, 1\}$. This set of initial conditions lies comfortably within the range allowed by perturbativity requirements ($c_2 \gtrsim 10^{-4}$) and CMB constraints on non-Gaussianity ($c_2 \gtrsim 10^{-2}$). Enforcing perturbativity throughout the scales of validity of the EFT treatment results in a lower limit for s_2. In particular, using eq.(4.17) and requiring that the sound speed saturates the perturbativity bound at the scale k_F, $c_2(k_\mathrm{F}) \gtrsim 10^{-4}$, yields

$$s_2 \geq \frac{1}{\log(k_\mathrm{F}/(a_0 H_0)) + (m/H)^{-2}} \log\left(\frac{10^{-4}}{c_{2\mathrm{i}}}\right). \tag{4.19}$$

The factor $(m/H)^{-2}$ in the denominator is due to the condition (4.9b), stating that scales must cross the horizon $\Delta N_{\mathrm{EFT}} = (m/H)^{-2}$ e-folds before the end of validity of the EFT[7]. For the EFT perturbative results (4.4) to be valid up until the scale k_F crossed the horizon, the EFT treatment must be valid for a little more, i.e. up until the scale $k_{\mathrm{end}} = a_0 H_0 \exp\left(\log(k_\mathrm{F}/a_0 H_0) + (m/H)^{-2}\right)$, such that the bound (4.9b) is satisfied for the scale k_F. In the following we identify $k_\mathrm{F} = k_{\mathrm{LIGO}}$, i.e. we assume the spin-2 fields can be described within the EFT treatment up until LIGO scales crossed the horizon. This

[7] Or before the end of inflation if the EFT treatment is valid up until the end of inflation.

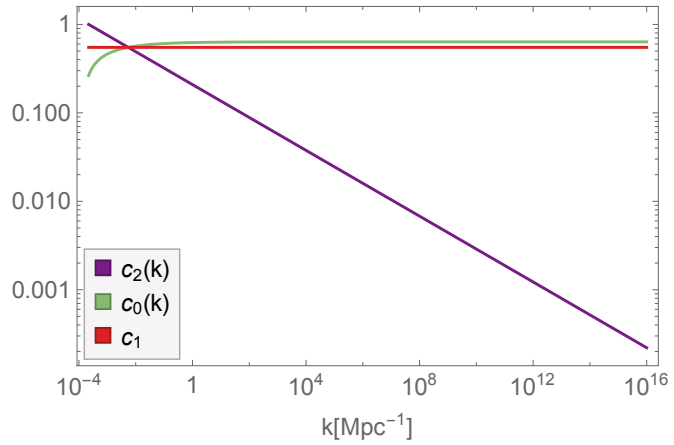

Figure 4.4: Example for the evolution of $c_2(k)$, $c_0(k)$ and c_1, see eqs.(4.18) and (4.20) with parameters $\{c_{2\mathrm{i}} = 1, c_1 = 0.55, s_2 = -0.186\}$. On the horizontal axis comoving wavenumbers ranging from $k_0 = a_0 H_0$ up to $k_{\mathrm{LIGO}} = 10^{16}\,\mathrm{Mpc}^{-1}$ have been displayed. The value of s_2 chosen saturates the perturbativity bound at k_{LIGO}, $c_2(k_{\mathrm{LIGO}}) \simeq 10^{-4}$, see eq.(4.19).

choice is supported by the fact that the EFT theory does not describe the background, i.e. the EFT describes the fluctuations around a quasi de-Sitter spacetime and details of the fields background evolution are not included, and it is reasonable to consider the possibility that the spin-2 fields decay during inflation.

In the configuration (1.a), c_1 is constant and c_0 increases as inflation proceeds. Using eq. (4.3) one obtains the time-evolution of c_0

$$c_0(k) = \sqrt{\frac{4}{3}c_1^2 - \frac{1}{3}c_2(k)^2}\,. \tag{4.20}$$

Requiring c_0 to be a real quantity, alongside the perturbativity and subluminality conditions on the sound speeds throughout their evolution, defines, for each c_{2i} value, the corresponding range for c_1. One can easily verify that values $0.55 < c_1 < 0.85$ are allowed for all chosen c_{2i} values. Let us point out that, rather than describing the time-evolution of $c_0(k)$ using the leading-order term in its Taylor expansion, as would be the case for the expression in (4.4a), we derive the exact scale dependence of the power spectrum by using eq.(4.20) directly.

As an example, we show in figure 4.4 the evolution of the sound speeds $c_2(k)$, $c_0(k)$ and c_1, where we use eqs.(4.18) and (4.20) with the parameters $\{c_{2\mathrm{i}} = 1, c_1 = 0.55, s_2 = -0.186\}$.

We proceed by selecting a number of sample values for the set $\{H, m/H, c_1, c_{2i}\}$ and applying the constraints described in section 4.3 to obtain (current and future) exclusion lines in the $\left(\rho/H, |s_2|\right)$ plane. We consider the masses $m/H = \{1.37, 1.12, 0.54\}$, identify in

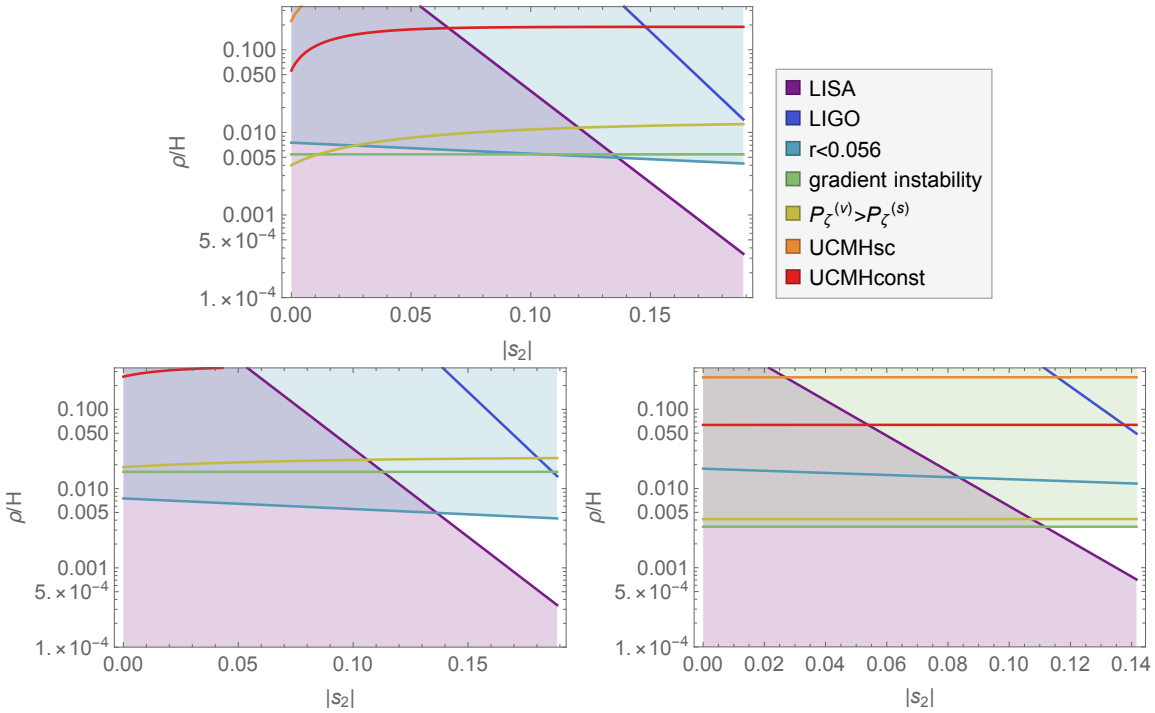

Figure 4.5: Case (1.a). We consider the $(\rho/H, |s_2|)$ plane of the effective theory parameter space for some of the configurations that can be probed with LISA. We identify the strongest bounds among those considered and shade with the corresponding color the area of parameter space that is (or would be, in the case of detection by LISA) excluded. *Top:* the configuration $\{H = 6.1 \times 10^{13}\,\text{GeV}, m/H = 0.54, c_1 = 0.55, c_{2i} = 1\}$ is displayed. *Bottom-left:* $\{H = 6.1 \times 10^{13}\,\text{GeV}, m/H = 0.54, c_1 = 0.85, c_{2i} = 1\}$. *Bottom-right:* $\{H = 10^{13}\,\text{GeV}, m/H = 0.54, c_1 = 0.85, c_{2i} = 0.1\}$. Bounds discussed in section 4.3 that are weaker than $\rho/H < 1/3$ are not captured by figure 4.5 or the following plots, but they have been taken into account in our analysis.

each plot the strongest among all the bounds and shade with its corresponding color the area of parameter space that is excluded. We also shade in purple the area which would be excluded by LISA in case of detection.

We show in figure 4.5 the parameter space associated with configurations that are within reach for LISA. Among the mass values of the spin-2 particle which we test, the lowest, $m/H = 0.54$, allows for a detectable signal. This reflects the fact that, the lighter the spin-2, the stronger its effect on the tensor power spectrum at small scales.

For illustration, we consider one of the EFT models such that it is currently unconstrained by existing bounds and it is within reach for LISA, i.e. one of the points in the white triangles in the parameter spaces of figure 4.5. In particular, we select the parameters $\{H = 6.1 \times 10^{13}\,\text{GeV}, m/H = 0.54, c_1 = 0.55, c_{2\text{i}} = 1, s_2 = -0.186, \rho/H = 2 \times 10^{-3}\}$, see the parameter space in the top of figure 4.5. By means of eqs.(4.4a) and (4.4b) we

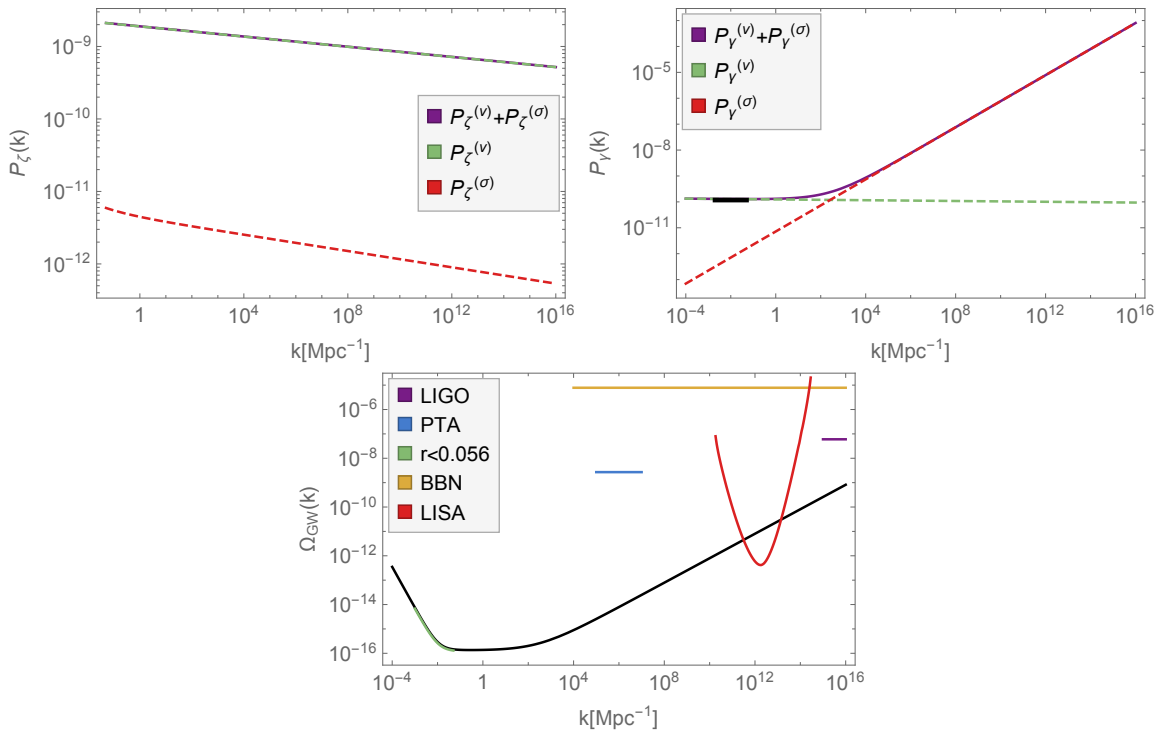

Figure 4.6: *Top row:* total scalar and tensor power spectra for an EFT model with parameters $\{H = 6.1 \times 10^{13}\,\text{GeV}, m/H = 0.54, c_1 = 0.55, c_{2\text{i}} = 1, s_2 = -0.186, \rho/H = 2 \times 10^{-3}\}$, together with the single contributions from quantum vacuum fluctuations and light spin-2 fields, see the legends. *Bottom row:* GW signal $\Omega_{\text{GW}}(k)$ corresponding to the tensor power spectrum plotted in the top-right panel, together with LISA sensitivity curve [270], and upper limits from LIGO, PTA and BBN, see section 4.3.3.

represent the scalar and tensor power spectra, $P_\zeta(k)$ and $P_\gamma(k)$, in the top of figure 4.6. The scalar power spectrum is completely dominated by the vacuum contribution, as expected from enforcing the bounds (4.8) and (4.11). On the other hand, the tensor power spectrum receives the largest contribution from the quantum vacuum fluctuations on large scales, and is then dominated by the sourced contribution on smaller scales. We note here that the value of H selected saturates the bound on the tensor-to-scalar ratio at k_r, see section 4.3.3, as illustrated by the black bar in the right panel, representing $\mathscr{A}_s \times 0.056$ on large scales.

In the bottom line of figure 4.6 we display the energy density in GWs, $\Omega_{\text{GW}}(k)$, associated with $P_\gamma(k)$ plotted in the top-right panel. The signal is blue-tilted and within reach for LISA, whose sensitivity curve is plotted in red [270]. The upper limits on Ω_{GW} at LIGO and PTA scales and the upper bound from BBN physics, see section 4.3.3, are also represented.

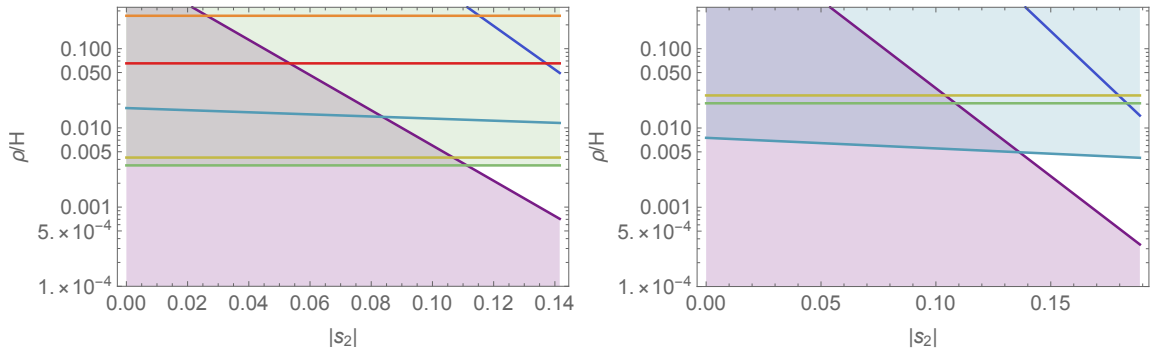

Figure 4.7: Case (2.a). The $(\rho/H, |s_2|)$ plane for configurations at reach with LISA. In the left panel, the EFT model $\{H = 10^{13}\,\text{GeV}, m/H = 0.54, c_0 = 1, c_{2i} = 0.1\}$ is displayed; in the right panel we show the plot corresponding to $\{H = 6.1 \times 10^{13}\,\text{GeV}, m/H = 0.54, c_0 = 1, c_{2i} = 1\}$. Conventions for colors and line codes are as in figure 4.5.

4.4.2 Case (2.a): constant c_0

Let us now consider the solution $\{s_0 = 0, s_1 = \frac{1}{4}c_2^2/c_1^2 s_2 < 0, s_2 < 0\}$, where again we consider $s_2 =$ constant. The time-evolution of c_2 is similar to case (1.a), c_0 is constant and c_1 decreases in time as

$$c_1(k) = \sqrt{\frac{3}{4}c_0^2 + \frac{1}{4}c_2(k)^2}\,. \tag{4.21}$$

One can verify that values $c_0 = \{10^{-2}, 10^{-1}, 1\}$ and $c_{2i} = \{10^{-2}, 10^{-1}, 1\}$ guarantee subluminal propagation also for the helicity-1 mode, in addition to preserving perturbativity bounds. We consider a number of sample configurations $\{H, m/H, c_0, c_{2i}\}$ and represent in figure 4.7 the constraints on the parameter space for those that are potentially observable with LISA.

4.4.3 Case (3.a): monotonically decreasing sound speeds

We explore here the solution $\{s_0 = s_1 = s_2 = s < 0\}$: in this case all the sound speeds decrease over time, and we capture their dynamics by means of eq. (4.17). For simplicity, we focus on the initial conditions $c_{0i} = c_{1i} = c_{2i} = 1$. In this case also the scalar power spectrum is blue-tilted. It is straightforward to conclude that none of the configurations $\{H, m/H\}$ tested corresponds to a signal above the sensitivity limits of LISA. What is behind the most stringent constraints in this case is the fact that c_0 decreases with time. As a consequence, the line representing the gradient instabilities bound (4.8) bends downwards, i.e. the bound gets stronger, in the $(\rho/H, |s_2|)$ plane as $|s_2| = |s_0|$ increases, preventing any crossing with the LISA curve.

Case (1.a), figure 4.5	Case (2.a), figure 4.7
(b)$\{H = 6.1 \times 10^{13}\,\text{GeV}, c_1 = 0.85, c_{2i} = 1\}$	(b) $\{H = 6.1 \times 10^{13}\,\text{GeV}, c_0 = 1, c_{2i} = 1\}$
(c) $\{H = 10^{13}\,\text{GeV}, c_1 = 0.85, c_{2i} = 0.1\}$	(a) $\{H = 10^{13}\,\text{GeV}, c_0 = 1, c_{2i} = 0.1\}$

Table 4.2: Configurations that select a similar portion of parameter space are listed on the same row of the table; all the samples are characterized by the choice $m/H = 0.54$.

4.4.4 Additional remarks

Before drawing our conclusions, we remind the reader that an upper bound is imposed on $|s_2|$ in each configuration from theoretical consistency, see eq.(4.19). This limits the region accessible to interferometers: while the lines representing LIGO and LISA bounds bend downwards as $|s_2|$ increases, the upper bound on $|s_2|$ limits the area accessible.

It is also worth remarking that the parameter space of some of the configurations analyzed for cases (1.a) and (2.a) ends up being rather similar, see table 4.2. This should not come as a surprise in light of eq.(4.3).

We also stress that we have focused our analysis mainly (i) on two specific observables, namely scalar and tensor power spectra, and (ii) considered a bi-dimensional sub-region of the entire parameter space, the $\left(\rho/H, |s_2|\right)$ plane. Extending the dimensionality of the parameter space that is being probed and exploring the non-Gaussian profile of scalar/mixed/tensor interactions will enhance the characterization of the extra particle content in the EFT Lagrangian. We consider tensor non-Gaussianities mediated by the light spin-2 fields in chapter 5.

As for the $s_0 < 0 < s_2$ scenario, which corresponds to a blue- (red-)tilted scalar (tensor) power spectrum, the growth of the scalar spectrum on small scales is reduced upon demanding the absence of gradient instabilities and complying with the bound on the tensor-to-scalar ratio $r < 0.056$. These limits turn out to be stronger than those that arise from PBH and UCMH.

Besides the configurations plotted in figure 4.5 and 4.7, there are other models whose parameter space can only be marginally surveyed by LISA. We do not include here details and plots about these models, but refer the interested reader to [1].

4.5 Discussion

In this chapter we have explored the possibility of a GW signal at interferometer scales due to the presence of extra fields during inflation. The existence of content beyond the minimal single-field scenario is well-motivated from the top-down perspective [103],

see section 2.4. Within this set, are there compelling models supporting in particular a tensor signal detectable at small scales? One interesting example is provided by so-called axion-inflation models [273]. The appeal of such set-ups lies in their ability to solve the η-problem, see section 2.4: an approximate shift symmetry, for example in the "natural inflation" model of [274], protects the inflaton mass from large quantum corrections. Extensions of the set-up in [274] have been motivated by the need to accommodate a sub-Planckian[8] axion decay constant f. Among the most interesting proposals to emerge from these efforts are those *non-minimally* coupling the axion-inflaton with gauge fields without losing the naturalness of the original proposal. As a result of the direct coupling, the GW spectrum can be blue or exhibit bump-like features that peak at small scales [169, 249–256, 275, 276].

Having identified a class of models that delivers a signal detectable by LIGO-Virgo and/or, in the near future, LISA, it is natural to ask whether several more multi-field set-ups, sharing this very same property, await discovery. One proven way to scan all that is possible, at least from the late-time signatures perspective, is to employ an EFT approach, see section 2.3.3 and 4.2. We have done so by adopting the approach of [98] and focusing on the phenomenology of an extra spin-2 field. The key to a sufficiently large signal at small scales is choosing an appropriate time-dependence for the sound speed of the helicity-2 mode, $c_2(t)$. The existence of a time-dependence may be interpreted as due to a departure, in field space, from the adiabatic trajectory [226]. We have shown that a small and constant $s_2 \equiv \dot{c}_2/(Hc_2)$ corresponds to a signal to which LISA would be sensitive and that, at the same time, cannot be ruled out by LIGO-Virgo. It would be interesting to explore other possibilities for the functional form of c_2; we leave this to future work. It is important to stress that a considerable region of parameter space has not been ruled out by existing data, but by the requirement that the dynamics does not run into a gradient instability [98]. This goes to show that it is the interplay between model building and observational requirements to act as the most powerful filter towards a viable cosmology.

The potential to detect a primordial signal must be confronted with our ability to (i) distinguish it from astrophysical sources [277]; (ii) identify signatures that are specific to certain (classes of) inflationary models. To address such issues one ought to characterize as much as possible the signal at small scales, and also consider cross-correlations with other cosmological probes. Given our results on the power spectrum, it is natural to

[8]The reasons [273] for why this is desirable are manifold: (i) the expectation that all global symmetries (including the aforementioned shift symmetry) are broken at the Planck scale; (ii) the near-absence of string theory constructions accommodating axions with a (super-)Planckian decay constant.

think of non-Gaussianities as the next logical step. It has recently been shown that crucial information on the strength of primordial interactions is (at least) indirectly accessible at small scales [278], and even once propagation effects are taken into account [279]. A necessary ingredient to access the information via the quadrupolar anisotropies of [278] is a non-zero, and ideally large, component of the tensor bispectrum in the squeezed configuration. The presence of light extra fields in the inflationary set-up we have been studying supports precisely such a scenario. Furthermore, the contribution in the squeezed configuration mediated by the extra content will break consistency relations and therefore deliver a signal that is immediately physical. We shall elaborate more on the subject in chapter 5.

CHAPTER 5

TENSOR BISPECTRUM MEDIATED BY LIGHT SPIN-2 FIELDS

Building on the findings presented in chapter 4, we consider here primordial tensor non-Gaussianities mediated by light spin-2 fields with time-dependent sound speed for the helicity-2 mode. After characterising the bispectrum amplitude and shape-function at CMB scales, we move on to smaller scales where anisotropies induced in the tensor power spectrum by long-short modes coupling become the key observable potentially constraining (squeezed) primordial non-Gaussianities. We identify the parameter space generating percent level anisotropies at scales to be probed by SKA [221] and LISA [222].

This chapter is based on the publication [2], and is organised as follows. In section 5.1 we discuss the importance of non-Gaussianities in characterising the inflationary field content and briefly review the results from chapter 4 that will be our starting point. In section 5.2 we calculate the tensor bispectrum mediated by light spin-2 fields and study its amplitude and shape-function. In section 5.3 we focus on the GW observables at large scales, while in section 5.4 we show how the squeezed bispectrum may be tested in the small-scale regime. We summarise our findings and point to future research in section 5.5. Additional details of the bispectrum calculation may be found in appendices A and B.

5.1 Motivation

In chapter 4 we presented an extension of the EFT of light spinning fields during inflation [98], allowing for sub-luminal sound speeds [1]. When the helicity-2 component has a decreasing sound-speed, the spin-2 sources blue-tilted GWs, potentially detectable on small scales [1].

As there are several other realisations that may lead to a sizable GW production on small scales, see e.g. [93], it is important to further explore the observational consequences of the set-up in [1] in order to distinguish it from other inflationary mechanisms. In this chapter we characterise the higher-point statistics of GWs by calculating the tensor 3-point correlation function[1], as primordial non-Gaussianities are a very efficient probe of inflationary interactions, see sections 3.3 and 3.4.

A direct detection of the tensor bispectrum on small scales is in general not expected given the suppression of higher-point functions due to propagation effects [178]. Interestingly, the *ultra-squeezed* bispectrum does not suffer from the same suppression [278]. The long mode in this configuration is horizon size (or larger). Two immediate consequences are that (i) the bispectrum cannot be accessed directly given that short modes are e.g. at interferometer scales and the long mode is horizon size; (ii) the long mode and its correlation with two nearly identical short modes is not dampened by propagation effects, much as is the case for the GW power spectrum [278, 280]. The effect of the long wavelength is best probed by the anisotropies it induces on the power spectrum of the two small-wavelength modes [235, 281–284]. This configuration has been recently studied in [278]: a primordial ultra-squeezed tensor bispectrum induces a modulation of the corresponding power spectrum. In this context, anisotropies represents our best handle on inflationary GW interactions. For this reason, in section 5.4 we explore the ability of SKA and LISA to indirectly probe non-Gaussianities in the ultra-squeezed configuration by testing anisotropies of the GW power spectrum.

Before diving into the bispectrum calculation, let us review some key findings of [98] and [1] that will be our starting point for the following analysis.

EFT warm up

As a consequence of the non-minimal coupling between the inflaton and the spin-2 field, the EFT quadratic Lagrangian includes terms linearly coupling the spin-2 fluctuations,

[1] We note here that the present analysis goes beyond the study in [166] in several directions, one being that we are no longer bound by the assumption of a *constant* sub-luminal sound speed.

$\sigma_{ij}(\mathbf{x}, t)$, and the scalar and tensor metric perturbations, $\pi(\mathbf{x}, t)$ and $\gamma_{ij}(\mathbf{x}, t)$ respectively, see eq.(4.2).

To ensure that the interaction Lagrangian can be treated perturbatively and to avoid gradient instabilities, the coupling must satisfy $\rho/H \ll \sqrt{\epsilon_1 c_0^2}$ [98], see section 4.3.1. While in general one should find a new basis where the degrees of freedom are decoupled, this is not necessary here as the perturbativity requirement above ensures we are working in the *weak-mixing* regime for the spin-2 field, where the mode function of the ith-helicity component is well-described by the solution to the free-field equation,

$$\sigma_k(\eta) = \sqrt{\frac{\pi}{2}}\, H (-\eta)^{3/2}\, H_\nu^{(1)}(-c_i k \eta)\,, \tag{5.1}$$

with $H_\nu^{(1)}$ the Hankel function of the first kind.

As a result of the linear coupling between $\sigma_{ij}(\mathbf{x}, t)$ and the metric perturbations, the spin-2 field sources both scalar and tensor power spectra, see eqs.(4.4),

$$P_\zeta(k) = \frac{H^2}{8\pi^2 M_p^2 \epsilon_1}\left[1 + \frac{C_\zeta(\nu)}{\epsilon_1 c_0^{2\nu}}\left(\frac{\rho}{H}\right)^2\right], \tag{5.2}$$

$$P_\gamma(k) = \frac{2H^2}{\pi^2 M_p^2}\left[1 + \frac{C_\gamma(\nu)}{c_2^{2\nu}}\left(\frac{\rho}{H}\right)^2\right], \tag{5.3}$$

We represent the functions $C_\zeta(\nu)$ and $C_\gamma(\nu)$ in figure 4.2.

As shown in [1], there are phenomenologically interesting ansatze according to which one can safely assume that the scalar power spectrum is dominated by the vacuum contribution across all scales of interest, see eq.(4.11) and the related discussion.

As done in [1], we will employ the expression for the helicity-2 sound speed as a function of k, see eq.(4.18),

$$c_2(k) = c_{2\mathrm{i}}\left(\frac{k}{a_0 H_0}\right)^{s_2}, \tag{5.4}$$

where we assume $s_2 \equiv \dot{c}_2 \Big/ (H c_2)$ to be constant for simplicity, and we take the comoving size of the universe today as the pivot scale (one could alternatively use k_{CMB}, as done in [93]). Such k dependence is obtained by virtue of the fact that cosmological correlators give the leading contribution at horizon crossing, where a precise relation is in place between wavenumber and conformal time, e.g. $-c_s k\eta \simeq 1$.

The sound speed $c_2(k)$ is assumed to be slowly varying, $|s_2| \ll 1$, therefore the next-to-leading corrections to the mode function in eq.(5.1) can be safely neglected [285]. The resulting scaling of the tensor power spectrum is given by

$$P_\gamma(k) \propto \frac{1}{{c_{2\mathrm{i}}}^{2\nu}}\left(\frac{k}{a_0 H_0}\right)^{-2\nu s_2}. \tag{5.5}$$

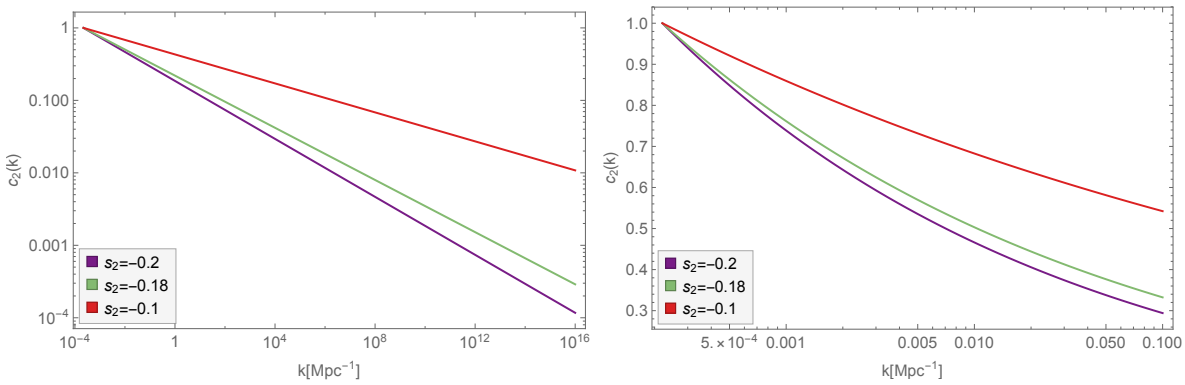

Figure 5.1: Working example for the evolution of $c_2(k)$. In both panels the function (5.4) is plotted, with $c_{2\mathrm{i}} = 1$ and different lines representing different choices of $s_2 < 0$. On the left, the evolution of $c_2(k)$ is shown over a range of comoving scales which spans from the size of the observable horizon, $a_0 H_0$, to LIGO scales, $k_{\mathrm{LIGO}} \simeq 10^{16}\,\mathrm{Mpc}^{-1}$. On the right, the focus is on the large scale behavior of $c_2(k)$.

For a decreasing sound speed, $s_2 < 0$, and an appropriate choice of the other parameters, the GW signal is detectable at interferometer scales by upcoming probes, including LISA [1]. One such configuration is

$$\left\{H = 6.1 \times 10^{13}\mathrm{GeV},\, \nu = 1.4,\, c_{2\mathrm{i}} = 1\right\}, \tag{5.6}$$

whose parameter space is represented in the bottom-left panel of figure 4.5. We stress that this is just one example in a wide region of parameter space that would generate a detectable signal.

In figure 5.1, the function (5.4) is plotted with initial condition $c_{2\mathrm{i}} = 1$ for three different values of s_2. In particular, an upper bound $|s_2|_{\mathrm{max}}$ is identified to ensure we stay within the perturbative regime [1], see section 4.4.1. On the left panel the evolution over a large range of scales is displayed, while in the right panel the focus is on the large scale behavior.

The EFT Lagrangian (4.2) also includes cubic self-interactions for the σ field,

$$\mathscr{L}^{(3)} = -a^3 \mu \left(\sigma_{ij}\right)^3, \tag{5.7}$$

where $\mu/H \ll 1$ to ensure perturbativity. As pointed out in [166], the structure of the interaction sector of the theory closely resembles the one in quasi-single field inflation [286]. In particular, the 3-point correlation function of tensor perturbations receives a contribution mediated by the light spin-2 field, as shown in figure 5.2.

In section 5.2 we shall investigate the tensor bispectrum, its amplitude and shape dependence.

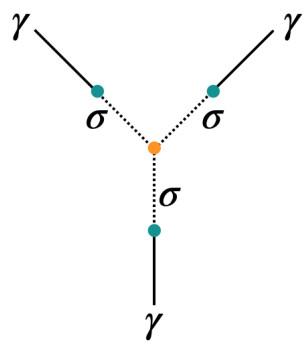

Figure 5.2: Diagrammatic contribution to the tensor bispectrum mediated by a light spin-2 field. The vertices making up the diagram correspond to the quadratic interaction $\mathscr{L}^{(2)} \sim \rho\, \sigma^{ij} \dot{\gamma}_{ij}$ (green) and the cubic self-interaction $\mathscr{L}^{(3)} \sim \mu (\sigma_{ij})^3$ (orange).

5.2 Tensor bispectrum

A key observable when it comes to testing inflationary interactions, (tensor) non-Gaussianities are typically more constrained at CMB scales, e.g. by data from the *Planck* mission [151], than in the complementary high-frequency regime. With the advent of new, more sensitive, GW probes we can aim also at testing those inflationary scenarios that support a large signal at small scales. The set-up we are considering here is one such example and the EFT approach we adopt is the ideal framework to expand our analysis. Our current focus is on a spin-2 field, σ_{ij}, directly coupled with the standard tensor degrees of freedom field and mediating their interactions. We organise the various contributions to the tensor 3-point correlation function in the following fashion

$$\langle \gamma^{\lambda_1}_{\mathbf{k_1}} \gamma^{\lambda_2}_{\mathbf{k_2}} \gamma^{\lambda_3}_{\mathbf{k_3}} \rangle = (2\pi)^3 \delta^{(3)}(\mathbf{k_1}+\mathbf{k_2}+\mathbf{k_3})\, \mathscr{A}^{\lambda_1\lambda_2\lambda_3}\, B_\sigma(k_1,k_2,k_3)\,, \tag{5.8}$$

see eq.(3.11), where the function $\mathscr{A}^{\lambda_1\lambda_2\lambda_3}$ accounts for the different polarizations. The quantity B_σ is given by

$$B_\sigma(k_1,k_2,k_3) = \frac{12\pi^3}{k_1^4 k_2 k_3} \frac{\mu}{H} \left(\frac{\rho}{M_p}\right)^3 [\mathscr{M}_A + \mathscr{M}_B + \mathscr{M}_C] + 5 \text{ perms}\,, \tag{5.9}$$

where

(5.10)

$$\begin{aligned}\mathscr{M}_A(\nu,k_1,k_2,k_3) = &\int_{-\infty}^{0} dx_1 \int_{-\infty}^{x_1} dx_2 \int_{-\infty}^{x_2} dx_3 \int_{-\infty}^{x_3} dx_4 \sqrt{\frac{x_2}{x_1 x_3 x_4}}\, \sin(-x_1) \\ &\Im\left[H^{(1)}_\nu(-c_2(k_1)x_1) H^{(2)}_\nu(-c_2(k_1)x_2)\right] \Im\left[e^{-ik_3/k_1 x_4} H^{(1)}_\nu\left(-c_2(k_3)\frac{k_3}{k_1}x_4\right) H^{(2)}_\nu\left(-c_2(k_3)\frac{k_3}{k_1}x_2\right)\right] \\ &\Im\left[e^{ik_2/k_1 x_3} H^{(1)}_\nu\left(-c_2(k_2)\frac{k_2}{k_1}x_2\right) H^{(2)}_\nu\left(-c_2(k_2)\frac{k_2}{k_1}x_3\right)\right]\,,\end{aligned}$$

(5.11)
$$\mathcal{M}_B(\nu,k_1,k_2,k_3)=\int_{-\infty}^{0}dx_1\int_{-\infty}^{x_1}dx_2\int_{-\infty}^{x_2}dx_3\int_{-\infty}^{x_3}dx_4\sqrt{\frac{x_3}{x_1x_2x_4}}\sin(-x_1)\sin\left(-\frac{k_2}{k_1}x_2\right)$$
$$\Im\left[H_\nu^{(1)}(-c_2(k_1)x_3)H_\nu^{(1)}\left(-c_2(k_2)\frac{k_2}{k_1}x_3\right)H_\nu^{(2)}(-c_2(k_1)x_1)H_\nu^{(2)}\left(-c_2(k_2)\frac{k_2}{k_1}x_2\right)\right]$$
$$\Im\left[\mathrm{e}^{-ik_3/k_1x_4}H_\nu^{(1)}\left(-c_2(k_3)\frac{k_3}{k_1}x_4\right)H_\nu^{(2)}\left(-c_2(k_3)\frac{k_3}{k_1}x_3\right)\right],$$

(5.12)
$$\mathcal{M}_C(\nu,k_1,k_2,k_3)=\int_{-\infty}^{0}dx_1\int_{-\infty}^{x_1}dx_2\int_{-\infty}^{x_2}dx_3\int_{-\infty}^{x_3}dx_4\sqrt{\frac{x_4}{x_1x_2x_3}}\sin(-x_1)\sin\left(-\frac{k_2}{k_1}x_2\right)$$
$$\sin\left(-\frac{k_3}{k_1}x_3\right)\Im\Big[H_\nu^{(1)}(-c_2(k_1)x_4)H_\nu^{(1)}\left(-c_2(k_2)\frac{k_2}{k_1}x_4\right)H_\nu^{(1)}\left(-c_2(k_3)\frac{k_3}{k_1}x_4\right)$$
$$\times H_\nu^{(2)}(-c_2(k_1)x_1)H_\nu^{(2)}\left(-c_2(k_2)\frac{k_2}{k_1}x_2\right)H_\nu^{(2)}\left(-c_2(k_3)\frac{k_3}{k_1}x_3\right)\Big],$$

where $\Im[x]$ is the imaginary part of x and $c_2(k)$ is given in eq.(5.4). The structure of the integrals is due to the use of the nested commutator form in the *in-in formalism* computation, see e.g. [286, 287]. The dimensionless integration variables are defined as $x_i\equiv k_1\eta_i$. Let us now focus on the bispectrum in two specific limits, the equilateral and squeezed ones.

5.2.1 Equilateral configuration

In the equilateral configuration, $k_1=k_2=k_3\equiv k$, the bispectrum reads

(5.13)
$$B_{\sigma,\mathrm{eq}}(k)=\frac{72\pi^3}{k^6}\frac{\mu}{H}\left(\frac{\rho}{M_p}\right)^3 s_{\mathrm{eq}}(\nu,k),$$

where

(5.14)
$$s_{\mathrm{eq}}(\nu,k)=\int_{-\infty}^{0}dx_1\int_{-\infty}^{x_1}dx_2\int_{-\infty}^{x_2}dx_3\int_{-\infty}^{x_3}dx_4\Big\{\sqrt{\frac{x_2}{x_1x_3x_4}}\sin(-x_1)\times$$
$$\Im\left[H_\nu^{(1)}(-c_2(k)x_1)H_\nu^{(2)}(-c_2(k)x_2)\right]\Im\left[\mathrm{e}^{-ix_4}H_\nu^{(1)}(-c_2(k)x_4)H_\nu^{(2)}(-c_2(k)x_2)\right]\times$$
$$\Im\left[\mathrm{e}^{ix_3}H_\nu^{(1)}(-c_2(k)x_2)H_\nu^{(2)}(-c_2(k)x_3)\right]+\sqrt{\frac{x_3}{x_1x_2x_4}}\sin(-x_1)\sin(-x_2)\times$$
$$\Im\left[H_\nu^{(1)}(-c_2(k)x_3)H_\nu^{(1)}(-c_2(k)x_3)H_\nu^{(2)}(-c_2(k)x_1)H_\nu^{(2)}(-c_2(k)x_2)\right]\times$$
$$\Im\left[\mathrm{e}^{-ix_4}H_\nu^{(1)}(-c_2(k)x_4)H_\nu^{(2)}(-c_2(k)x_3)\right]+\sqrt{\frac{x_4}{x_1x_2x_3}}\sin(-x_1)\sin(-x_2)\sin(-x_3)\times$$
$$\Im\left[H_\nu^{(1)}(-c_2(k)x_4)H_\nu^{(1)}(-c_2(k)x_4)H_\nu^{(1)}(-c_2(k)x_4)H_\nu^{(2)}(-c_2(k)x_1)H_\nu^{(2)}(-c_2(k)x_2)H_\nu^{(2)}(-c_2(k)x_3)\right]\Big\}.$$

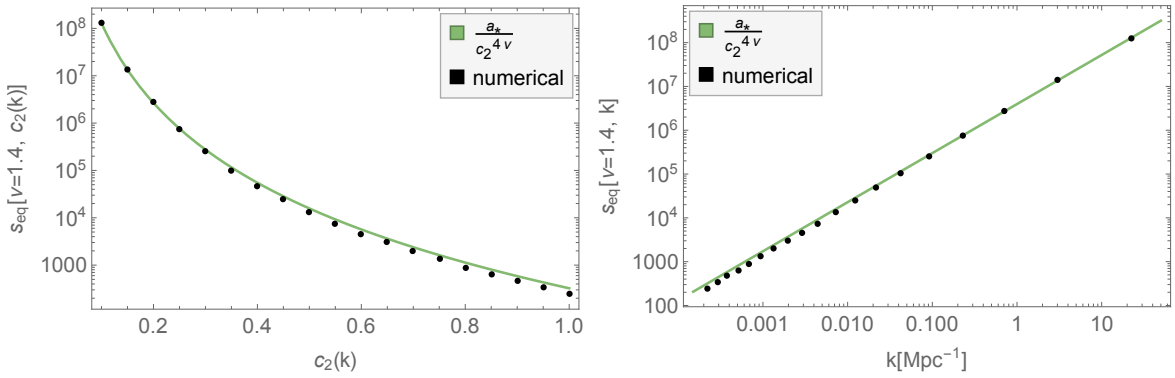

Figure 5.3: Results for $s_{\rm eq}(\nu = 1.4)$. On the left panel we represent the results as a function of $c_2(k)$, keeping the k-dependence implicit, whereas on the right we replace eq.(5.4) and make explicit the dependence on the scale. In both plots, black dots represent numerical results and the green line the fitting functions (5.16) (left) and (5.17) (right).

The integrals in eq.(5.14) need to be evaluated numerically. In figure 5.3, black dots represent the numerical values of eq.(5.14) computed for $\nu = 1.4$, which corresponds to $m \simeq 0.54H$, and different values of $c_2(k)$. As expected, $s_{\rm eq}$ increases for small values of the sound speed, enhancing the resulting bispectrum. The numerical results are fitted with the power law

$$s_{\rm eq}[\nu, c_2(k)] = \frac{a_\star}{c_2(k)^{4\nu}} \,. \tag{5.15}$$

The validity of the approximation with a power law is, of course, not surprising considering the usual scaling $B_\sigma(k) \propto f_{\rm NL,\,tens}\,\mathscr{P}_\gamma(k)^2$. For $\nu = 1.4$, the fit produces

$$s_{\rm eq}[\nu = 1.4, c_2(k)] \simeq \frac{324.4}{c_2(k)^{5.6}} \,, \tag{5.16}$$

which is plotted in green on the left panel of figure 5.3. One can write explicitly the k-dependence, to obtain

$$s_{\rm eq}[\nu = 1.4, k] \simeq 324.4 \left(\frac{k}{a_0 H_0}\right)^{-5.6 s_2} \,, \tag{5.17}$$

as displayed in the right panel of figure 5.3 for $s_2 = -0.2$. The value of $s_{\rm eq}$ increases on small scales as the sound speed c_2 decreases. In figure 5.4, the fit in (5.17) is shown for different values of s_2. Similar plots for different mass values, $\nu = \{0.4, 0.8, 1.1, 1.48\}$ are included in Appendix A. Our analysis shows that the lighter the spin-2 is, the greater is the size of $s_{\rm eq}$. This is intuitively clear given the suppression effect of a heavy mass on cosmological correlators. We shall now consider the squeezed limit.

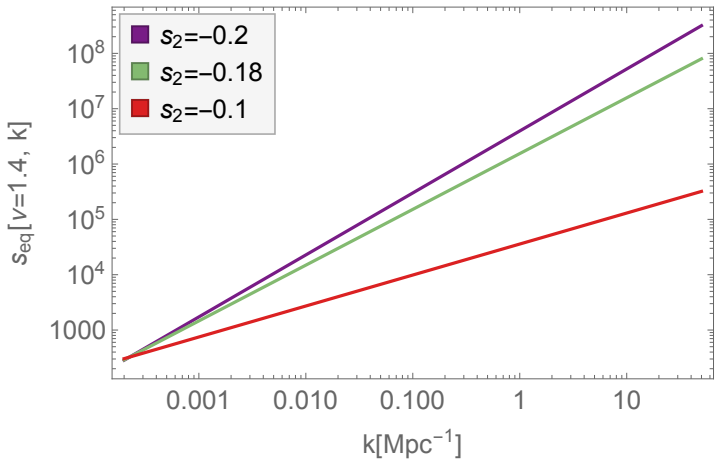

Figure 5.4: Investigating the effect of s_2 on $s_{\rm eq}(\nu = 1.4, k)$. The larger $|s_2|$ is, the faster the sound speed decreases, see figure 5.1, amplifying the magnitude of the sourced bispectrum at a given scale.

5.2.2 Squeezed configuration

We now evaluate the bispectrum in the squeezed limit $k_3 \ll k_1 \sim k_2$ and, for practical purposes, identify $k_3 \equiv k_L$ and $k_1 \sim k_2 \equiv k_S$. We find that the leading contributions to the bispectrum are given by (5.10) and (5.11), while the other permutations, as well as the C term (5.12), are sub-leading. Details on the derivation are included in Appendix B. Our findings on tensor non-Gaussianities are somewhat reminiscent of the analysis performed in [286] for (the scalar sector of) quasi-single field inflation and in [166] for (the tensor sector of) the EFT set-up. The bispectrum in the squeezed configuration reads

$$B_{\sigma,\rm sq}(k_L,k_S) = \frac{24\times 2^\nu \pi^2}{k_S^{9/2-\nu}\, k_L^{3/2+\nu}}\, \frac{\mu}{H}\left(\frac{\rho}{M_p}\right)^3 s_{\rm sq}(\nu,k_L,k_S)\,, \tag{5.18}$$

where

$$\begin{aligned} s_{\rm sq}(\nu,k_L,k_S) = {}& \frac{\Gamma(\nu)}{c_2(k_L)^\nu}\int_{-\infty}^{0} dx_1 \int_{-\infty}^{x_1} dx_2 \int_{-\infty}^{x_2} dx_3 \times \\ & \Big\{(-x_2)^{1/2-\nu}(-x_1)^{-1/2}(-x_3)^{-1/2}\,\sin(-x_1)\,\Im\left[H_\nu^{(1)}(-c_2(k_S)x_1)H_\nu^{(2)}(-c_2(k_S)x_2)\right] \\ & \Im\left[e^{ix_3}H_\nu^{(1)}(-c_2(k_S)x_2)H_\nu^{(2)}(-c_2(k_S)x_3)\right] + (-x_1)^{-1/2}(-x_2)^{-1/2}(-x_3)^{1/2-\nu} \\ & \times \Im\left[H_\nu^{(1)}(-c_2(k_S)x_3)H_\nu^{(1)}(-c_2(k_S)x_3)H_\nu^{(2)}(-c_2(k_S)x_1)H_\nu^{(2)}(-c_2(k_S)x_2)\right]\,\sin(-x_1)\,\sin(-x_2)\Big\} \\ & \times \int_{-\infty}^{0} dy_4\,(-y_4)^{-1/2}\,\Re\left[e^{-iy_4}H_\nu^{(1)}(-c_2(k_L)y_4)\right]\,. \end{aligned} \tag{5.19}$$

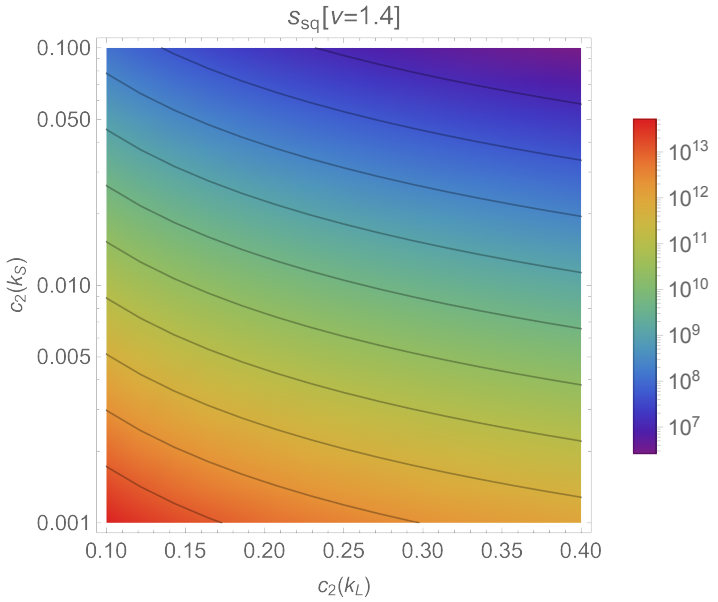

Figure 5.5: Fit of the numerical results obtained for $s_{sq}[\nu = 1.4]$ as a function of $c_2(k_S)$ and $c_2(k_L)$, the sound speeds of the short- and long-scale modes respectively.

Similarly to what has been done for the equilateral configuration, the numerical results can be fitted with a power law

$$s_{sq}[\nu, c_2(k_L), c_2(k_S)] = \frac{b_\star}{c_2(k_L)^{2\nu} c_2(k_S)^{2\nu}} , \tag{5.20}$$

which is used to arrive at figure 5.5, where setting $\nu = 1.4$ gives

$$s_{sq}[\nu = 1.4, c_2(k_L), c_2(k_S)] \simeq \frac{482.8}{c_2(k_L)^{2.8} c_2(k_S)^{2.8}} . \tag{5.21}$$

In order to visualize our findings in a different fashion, we provide in the left panel of figure 5.6 the numerical results and the fit (5.21) with fixed $c_2(k_L) = 0.346$. The explicit scale dependence is given by

$$s_{sq}[\nu = 1.4, k_L, k_S] \simeq 482.8 \left(\frac{k_L}{a_0 H_0}\right)^{-2.8 s_2} \left(\frac{k_S}{a_0 H_0}\right)^{-2.8 s_2} , \tag{5.22}$$

which is plotted on the right in figure 5.6 with $k_L \simeq 0.05\,\mathrm{Mpc}^{-1}$ and $s_2 = -0.2$. Just as for the equilateral configuration, a smaller c_2 enhances the amplitude of non-Gaussianities. In Appendix A, a similar analysis is performed for mass values $\nu = \{0.4, 0.8, 1.1, 1.48\}$. The lighter the spin-2 field is ($\nu \to 3/2$), the greater the amplitude of $s_{sq}(\nu)$.

5.2.3 Shape

We move now to study the shape function of the bispectrum, i.e. the dependence on the configuration of the momenta (k_1, k_2, k_3). We expect it to interpolate between the

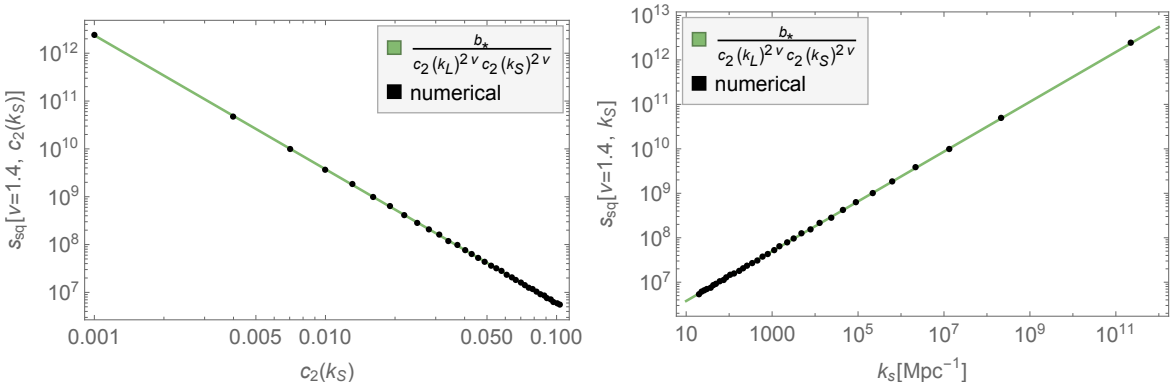

Figure 5.6: Results for $s_{\rm sq}(\nu = 1.4)$. On the left panel eq.(5.21) with $c_2(k_L) = 0.346$ is displayed as a function of the value of the sound speed on small scales $c_2(k_S)$, while on the right eq.(5.22) is plotted, with the long mode fixed at CMB scales and $s_2 = -0.2$. In both plots, black dots represent numerical results.

local and equilateral configurations depending on the mass of the spin-2 field mediating the interaction in the diagram of figure 5.2. This expectation stems from the analogous interactions one finds in the scalar sector of quasi-single field inflation [286]. In particular, for a lighter particle, $\nu \gtrsim 1$, the signal peaks in the local[2] configuration, while for smaller values $\nu \ll 1$, i.e. for a heavier field, the bispectrum displays a momentum dependence akin to the equilateral template. As an example, we study the shape-functions for $\nu = 0$ and $\nu = 1$ in presence of k-dependent sound speed c_2 (5.4), with initial condition $c_{2\rm i} = 1$ and $s_2 = -0.2$. These are plotted in figure 5.7, where the case $\nu = 0$ is represented on the left and $\nu = 1$ on the right. The plots are produced numerically, after applying a Wick rotation to the mixed-form of the bispectrum.

The fact that the shape-function tends towards the equilateral template for interactions mediated by massive particles (as opposed to the light and/or massless fields) has a simple explanation as clear already in the scalar case. The (*quasi* de-Sitter) wavefunction for massive fields has approximately a non-zero $(-k\eta)^{3/2-\nu}$ factor in front of what would be the massless solution. This term suppresses the wavefunction (and, in turn, the bispectrum) after horizon crossing especially for small wavenumber values, so that the signal in the squeezed configuration is suppressed, to the advantage of the equilateral one. For massless (scalar) fields, $\nu = 3/2$, the same factor is instead equal to unity and therefore inconsequential for the shape. We also note that, despite c_2 not being

[2]Strictly speaking, it would be more appropriate to say that the bispectrum peaks in the squeezed limit and that its shape-function is very similar to that obtained by employing the local template. One may define a scalar product between shape functions (see e.g. [288]) and quantify precisely their overlap. It is usually assumed in the literature that an overlap above 75% would make two templates difficult to distinguish from each other via CMB probes.

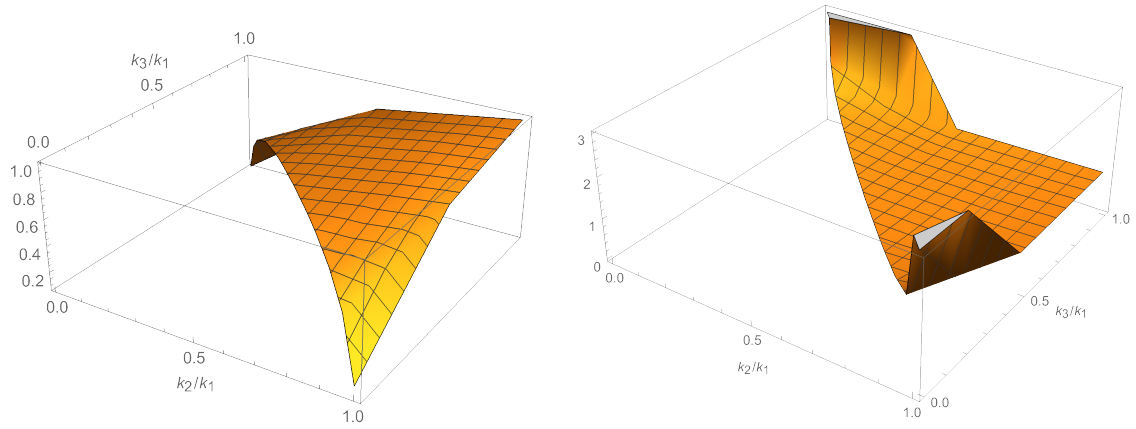

Figure 5.7: Shape-function for $\nu = 0$ (left) and $\nu = 1$ (right). To conform with the literature convention, the bispectrum has been multiplied by $(k_1 k_2 k_3)^2$ and the weight $\mathscr{A}^{\lambda_1\lambda_2\lambda_3}$ is not included. The shape values are normalised with respect to the value in the equilateral point $k_1 = k_2 = k_3$.

constant in our set-up, the shape-function does not noticeably change with respect to the constant case [166], unlike the bispectrum amplitude.

5.3 Bounds on tensor non-Gaussianities at CMB scales

We now explore the consequences of current bounds on tensor non-Gaussianities at CMB scales, see section 3.4 where we defined $f^{eq}_{\text{NL, tens}}$ and $f^{sq}_{\text{NL, tens}}$. We consider the configuration described by the parameters in (5.6). As anticipated in section 5.1, this choice is interesting as it is potentially testable at interferometer scales. The latest CMB bounds on tensor non-Gaussianities in the squeezed and equilateral configurations are given in eq.(3.12), and the non-linearity parameters are defined in eqs.(3.14) and (3.13). To connect with the bispectrum definition given in eq.(5.8), we identify $B_\gamma^{+++}(k_1, k_2, k_3) \equiv \mathscr{A}^{RRR} B_\sigma(k_1, k_2, k_3) \Big/ 2\sqrt{2}$, where the numerical factor $\mathscr{A}^{RRR}$ is equal to 27/64 and 1/4 in the equilateral and squeezed configuration respectively [166]. Equipped with these definitions and by using (5.13) and (5.18), one can calculate the values of $f^{eq}_{\text{NL, tens}}$ and $f^{sq}_{\text{NL, tens}}$ within the EFT.

In figure 5.8 the bounds at large scales (3.12) are displayed on the parameter space $\left(s_2, \rho/H\right)$ of the configuration (5.6). The additional green and purple lines in the plot represent the constraint stemming from the bound on the tensor-to-scalar ratio at CMB scales, $r < 0.056$ [67], and LISA sensitivity, with the area above the purple line surveyable

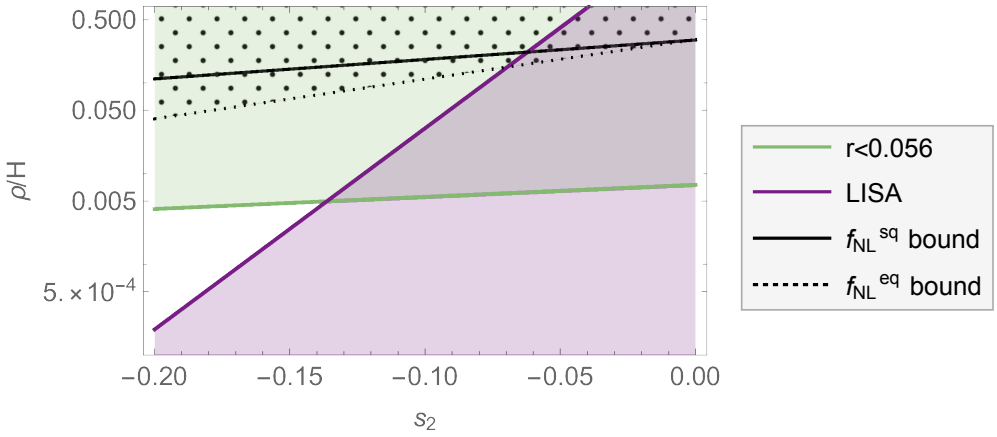

Figure 5.8: Effective theory parameter space $(s_2, \rho/H)$ of the configuration $\{H = 6.1 \times 10^{13}\,\text{GeV}, v = 1.4, c_{2i} = 1, \mu/H = 0.5\}$. Bounds in (3.12) are plotted with black lines. The region highlighted with black dots is excluded by the bound on $f^{eq}_{\text{NL, tens}}$, the strongest among the two. The black lines lie in the green-shaded region, which is excluded already by the bound on the tensor-to-scalar ratio r [67]. The area above the purple line will be surveyed by LISA. For more details on the construction of the parameter space see chapter 4.

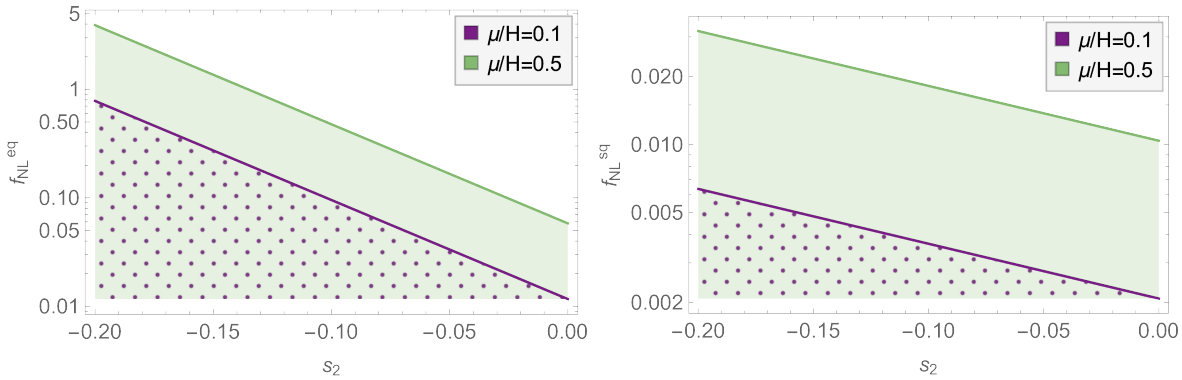

Figure 5.9: Maximum level of tensor non-Gaussianities produced at $k_{\text{CMB}} = 0.05\,\text{Mpc}^{-1}$ in the set-up $\{H = 6.1 \times 10^{13}\text{GeV}, v = 1.4, c_{2i} = 1\}$. $f^{eq}_{\text{NL, tens}}$ and $f^{sq}_{\text{NL, tens}}$ are represented on the left and right panels respectively, for different values of the cubic self-interaction coupling μ/H. The shaded areas correspond to values of ρ/H smaller than that obtained from saturating the value of r to the current upper limit [67].

by LISA [1]. The bounds from eq.(3.12) are weaker on the parameter space than the constraint coming from the current upper limit on r.

Given an upper bound on ρ/H as a function of s_2 obtained by requiring $r < 0.056$, it is possible to maximize the level of tensor non-Gaussianities produced at CMB scales for the configuration under scrutiny. The corresponding amplitudes $f^{eq}_{\text{NL, tens}}$ and $f^{sq}_{\text{NL, tens}}$ are given in figure 5.9. The behavior with respect to s_2 is clear: the greater $|s_2|$ is, the

faster c_2 decreases, see figure 5.1, and a smaller sound speed enhances the level of non-Gaussianities, as shown in section 5.2.

For the configuration described by the parameters (5.6), we conclude that that the present bound on r is more constraining on the region of parameter space we are probing than existing bounds on non-Gaussianities. This finding is specific to our starting point in terms of the chosen parameters as well as the role played by the helicity-0 mode in sourcing the scalar signal (which is negligible by choice, see eq.(4.11)), therefore we expect the impact of current constraints on tensor non-Gaussianities at CMB scales to depend on the chosen EFT configuration. Discussing these constraints for the full range of EFT configurations is beyond the scope of the current analysis, where our choice of parameters has been guided by its testability at small scales by upcoming probes.

5.4 Testing squeezed tensor non-Gaussianities on small scales

As shown in the last section, tensor non-Gaussianities produced within the configuration in (5.6) are well-below current bounds at CMB scales. When it comes to testing inflationary GW higher-point correlators at small scales, one should be aware that these are not directly testable: de-correlation sets in as a result of the propagation through structure that GWs undergo on their way to the detector [178].

Nonetheless, it is possible to test non-Gaussianities in a specific configuration, namely the *ultra-squeezed* one. Such nomenclature refers to the case where the long wavenumber is (nearly) horizon size or larger, so that it avoids propagation effects whilst still correlating with short, well-inside-the-horizon, modes. In the presence of non-trivial[3] ultra-squeezed tensor non-Gaussianities, the specific effect of a long tensor fluctuation is to induce a quadrupolar anisotropy on the power spectrum of the short modes [235, 281–284]. This idea has been explored in the context of inflationary GW at small scales in [248, 278, 290]. One should also keep in mind that, next to the cosmological SGWB we

[3]Here "non-trivial" does not mean merely non-zero. The squeezed limit of the 3-point function is directly physical whenever so-called consistency relations (CRs) are broken [289] , i.e. whenever the squeezed 3-point function cannot be expressed as the action of a gauge transformation on the corresponding power spectrum. The prototypical case of broken CRs is that of multi-field inflation. However, a multi-field scenario does not by itself guarantee CRs breaking. A quick route to see that CRs are indeed broken in our set-up when the bispectrum contribution is mediated by σ is to notice that such interactions are regulated by the parameter μ (see eq. (5.7)), which does not appear in the quadratic Lagrangian. The reader familiar with quasi-single field inflation may take another path to the same conclusions by noticing the analogies between the quantity μ here and (the third derivative of) the potential $V(\sigma)$ of the extra field σ in [286].

want to probe, there is an astrophysical SGWB whose signal we need to disentangle from the primordial one. For a comprehensive account on how to characterise the anisotropies of the stochastic GWs background, we refer the interested reader to e.g. [279, 291, 292]. It suffices here to say that a sufficiently large primordial signal at small scales may dominate the anisotropic component [278].

We briefly review here the results of [278] and then explore their consequences for the EFT set-up at hand. This is appropriate given that the EFT bispectrum has a significant squeezed component for sufficiently light σ, such as is the case for e.g. $\nu = 1$ and $\nu = 1.4$. In the presence of a non-trivial ultra-squeezed primordial tensor bispectrum, a long tensor mode k_L induces a quadrupolar modulation on the tensor power spectrum evaluated locally at $\mathbf{x_c}$,

$$\mathscr{P}_\gamma(\mathbf{k_S}, \mathbf{x_c})\Big|_{k_L} = \mathscr{P}_\gamma(k_S)\left(1 + \mathscr{Q}_{lm}(\mathbf{k_S}, \mathbf{x_c})\hat{k}_{S\,l}\hat{k}_{S\,m}\right), \tag{5.23}$$

where $\mathscr{P}_\gamma(k)$ is the standard isotropic component of the (dimensionful) power spectrum, k_S stands for a generic small wavelength such that $k_S \gg k_L$, and $\mathscr{Q}_{lm}$ is the anisotropy parameter defined as

$$\mathscr{Q}_{lm}(\mathbf{k_S}, \mathbf{x_c}) \equiv \int \frac{d^3k_L}{(2\pi)^3}\, e^{i\,\mathbf{k_L}\cdot\mathbf{x_c}}\, F_{\rm NL}(k_L, k_S) \sum_{\lambda_3} \epsilon^{\lambda_3}_{lm}\left(-\hat{k}_L\right) \gamma^{*\,\lambda_3}_{-\mathbf{k_L}}\,. \tag{5.24}$$

The quantity $F_{\rm NL}(k_L, k_S)$ is the non-Gaussianity parameter in the squeezed configuration, defined as[4]

$$F_{\rm NL}(k_L, k_S) \equiv \frac{B_{\rm sq}(k_L, k_S)}{\mathscr{P}_\gamma(k_L)\mathscr{P}_\gamma(k_S)}\,, \tag{5.25}$$

where $\mathscr{P}_\gamma(k) = 2\pi^2 P_\gamma(k)\Big/k^3$ and the quantities $P_\gamma(k)$ and $B_{\rm sq}(k_L, k_S)$ are spelled out in eqs.(5.3) and (5.18) respectively. One can characterize the quadrupolar tensor anisotropy by computing its variance [235],

$$\bar{\mathscr{Q}}^2 \equiv \langle \sum_{m=-2}^{+2} |\mathscr{Q}_{2m}|^2 \rangle = \frac{8\pi}{15}\langle \mathscr{Q}_{ij}\mathscr{Q}^{*\,ij}\rangle\,, \tag{5.26}$$

with

$$\langle \mathscr{Q}_{ij}\mathscr{Q}^{*\,ij}\rangle = 16 \int \frac{d^2\hat{k}_L}{4\pi} \int_{k_L^{\rm min}}^{k_L^{\rm max}} \frac{dk_L}{k_L} F^2_{\rm NL}(k_L, k_S) P_\gamma(k_L)\,, \tag{5.27}$$

[4] As mentioned in chapter 3, whether the squeezed bispectrum corresponds to a physical observable effect, or can be cancelled by a suitable coordinates tranformation is still a matter of discussion, see e.g. [154–156]. If the latter holds, one might need to apply the same coordinate transformation mentioned above when connecting the primordial bispectrum to late-time observables, e.g. the quadrupolar modulation of $\mathscr{P}_\gamma$. Here we choose to directly employ the primordial, non-trivial, bispectrum.

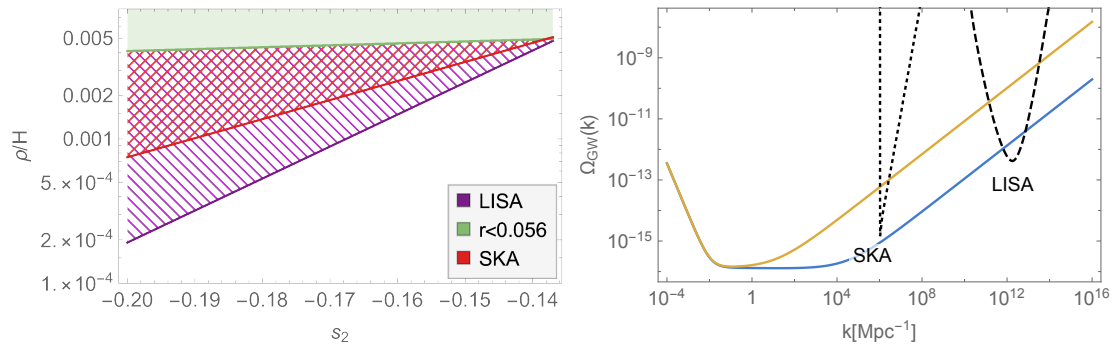

Figure 5.10: *Left panel:* effective theory parameter space $(s_2, \rho/H)$ of the configuration $\{H = 6.1 \times 10^{13}\,\text{GeV}, \nu = 1.4, c_{2i} = 1\}$. The green-shaded area is excluded by the bound on the tensor-to-scalar ratio r. The purple-hatch-shaded area is surveyable by LISA, on top of which the region highlighted with red hatch-shading is also visible to SKA. *Right panel:* examples of two tensor signals sourced within the theory. The orange line corresponds to $(s_2 = -0.2, \rho/H = 0.0035)$ and is visible both to LISA and SKA, while the blue line corresponds to $(s_2 = -0.2, \rho/H = 0.0004)$ and might be detected by LISA only.

where $P_\gamma(k)$ is the dimensionless tensor power spectrum.

We now use the results in section 5.2 to explore small-scale signatures associated to the presence of an extra spin-2 field during inflation with parameters (5.6). From eq.(5.26) we compute $\sqrt{\bar{\mathcal{Q}}^2}$ and identify in the EFT parameter space areas that (i) support a detectable tensor power spectrum and (ii) whose squeezed tensor bispectrum produces a quadrupolar modulation with $\sqrt{\bar{\mathcal{Q}}^2} \gtrsim 0.01$. We use the percent value for anisotropies as a benchmark point. There is ongoing research focussed on establishing whether this will be attainable with upcoming probes, see [293, 294] and references therein.

We should stress at this stage that, although our analysis has been mainly motivated by the possibility to explore the capability of laser interferometers to detect inflationary signatures, our results apply equally well to pulsar timing arrays. In the left panel of figure 5.10 we plot the EFT parameter space $(s_2, \rho/H)$ and highlight with purple hatch-shading the area delivering a GW signal testable by LISA. The red-hatch-shaded area in instead at reach for SKA [221]. The region above the green line is off-limits as it correspond to a tensor to scalar ratio already excluded by CMB data. The right side of figure 5.10 illustrates how two points in the EFT parameter space engender a GW signal that is sufficiently large to be detected by SKA and LISA (orange line) or by LISA only (blue line). In order to generate the plot, we have used $k_{\text{SKA}} = 6.5 \times 10^5\,\text{Mpc}^{-1}$ and $k_{\text{LISA}} = 10^{12}\,\text{Mpc}^{-1}$ and eq.(2.88) as the definition of today's energy density in GWs. For studies on reconstructing the tensor power spectrum with LISA and PTA see [270, 271]

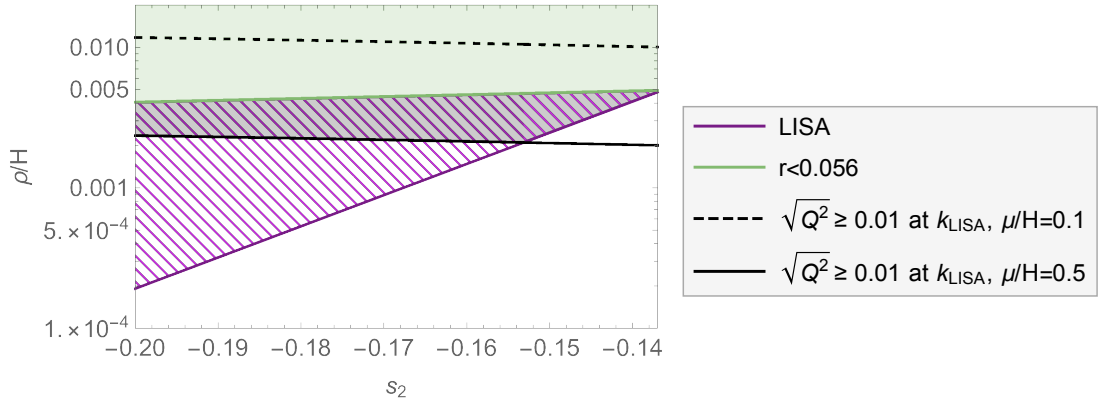

Figure 5.11: Effective Theory parameter space $(s_2, \rho/H)$ of the configuration $\{H = 6.1 \times 10^{13}\,\text{GeV}, \nu = 1.4, c_{2\text{i}} = 1\}$. The purple-hatch-shaded area delivers a tensor power spectrum detectable by LISA. The region above the black lines corresponds to parameter values which produce a quadrupolar modulation of the tensor power spectrum with standard deviation $\sqrt{\bar{\mathcal{Q}}^2} \geq 0.01$ at LISA scales, with $\mu/H = 0.1$ (dashed line) and $\mu/H = 0.5$ (continuous line). If LISA will be able to detect quadrupolar modulations with standard deviation ≥ 0.01, the squeezed bispectrum can be indirectly tested in the parameter space area which is shaded in gray, corresponding to $\mu/H = 0.5$. On the other hand, the parameter choice $\mu/H = 0.1$ lies in a region which is already excluded by the bound on the tensor-to-scalar ratio.

and [295] respectively.

Let us now turn to identifying the area of the parameter space delivering a tensor quadrupolar anisotropy with standard deviation of the order of a few percent. We focus on LISA first. Using eqs. (5.3), (5.18) and (5.25) in eq.(5.27), one arrives at the value of $\sqrt{\bar{\mathcal{Q}}^2}$. In figure 5.11, the area above the black lines produces a signal with $\sqrt{\bar{\mathcal{Q}}^2} \geq 0.01$; the continuous and dashed lines correspond to $\mu/H = 0.5$ and $\mu/H = 0.1$ respectively. The overlap with the purple-hatch-shaded area, highlighted in gray, selects the parameter values in the $(s_2, \rho/H)$ plane that deliver a detectable tensor power spectrum with a quadrupolar modulation characterised by $\sqrt{\bar{\mathcal{Q}}^2} \geq 0.01$. Depending on the configuration parameters, the F_{NL} values needed to produce a quadrupolar modulation at the percent level are of order $10^3 - 10^4$. This goes to show how probes such as LISA will access information on (the size of) squeezed tensor non-Gaussianities and, in turn, the inflationary particle content, by testing anisotropies.

We have stressed throughout this paper that the EFT of inflation framework is ideal for capturing the full spectrum of possible signatures of inflationary models. On the other hand, it may be difficult, once a specific observational feature has been identified, to map it back all the way to a precise model of inflation. Indeed, the EFT enables

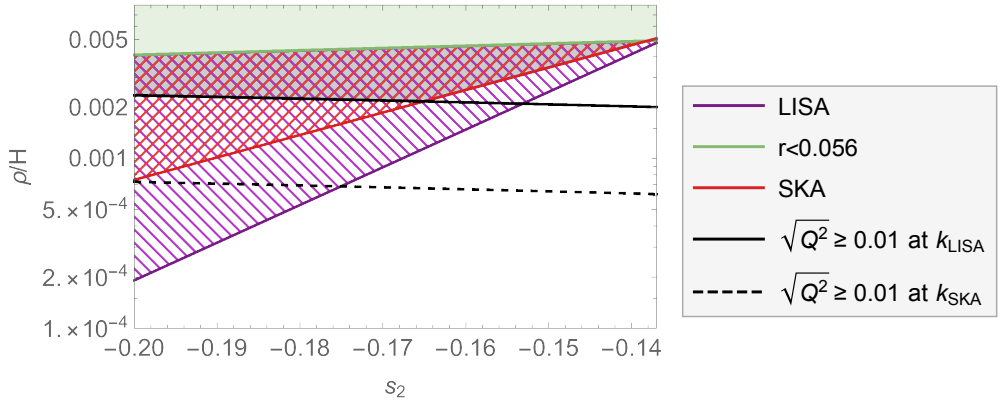

Figure 5.12: Effective Theory parameter space $(s_2, \rho/H)$ of the configuration $\{H = 6.1 \times 10^{13}\,\text{GeV}, \nu = 1.4, c_{2\text{i}} = 1, \mu/H = 0.5\}$. The hatch-shaded areas deliver a tensor power spectrum detectable by the corresponding probe, where the purple and red colors correspond to LISA [222] and SKA [221] respectively. The green area is already excluded by current upper bounds on primordial GWs on large scales [1]. The parameter space areas above the black lines delivers a quadrupolar modulation of the tensor power spectrum induced by squeezed tensor non-Gaussianities with standard deviation $\sqrt{\bar{\mathcal{Q}}^2} \geq 0.01$. The gray area highlights the parameter space delivering a tensor power spectrum detectable by LISA and SKA with a quadrupolar modulation such that $\sqrt{\bar{\mathcal{Q}}^2} \geq 0.01$ at both probes.

one to associate signatures with specific operators in the Lagrangian of the effective theory of fluctuations around an FLRW solution, but it is less illuminating in identifying the complete theory (both background and fluctuations) supporting the acceleration mechanism. These considerations apply to the use of the EFT of inflation both in the single-field [96] as well as in the multi-field [97, 98] context. In the latter case however, especially as particles of increasing spin are considered, it is sometimes difficult to arrive at a fully non-linear Lagrangian formulation of the theory[5]. We should nevertheless be aware of the crucial extra step necessary to build a clear-cut signature-to-theory dictionary.

In figure 5.12, an analysis similar to the one done for LISA is performed for SKA. The area highlighted in gray delivers a tensor power spectrum detectable by LISA and SKA with a quadrupolar modulation such that $\sqrt{\bar{\mathcal{Q}}^2} \geq 0.01$ at both probes. At this stage it is important to point out the following fact: very recent work [296] suggests that, in order to be able to detect anisotropies, the monopole signal should be above the instrument (e.g. LISA) sensitivity curve of about one order of magnitude. A similar analysis exists

[5]This is the case for higher spin fields, while we refer the interested reader to [244, 245, 247] for an explicit embedding in the inflationary context of a fully non-linear theory [242, 243] comprising a massive spin-2 field.

also for PTAs [297]. While the parameter space on the left half of the plot in figure 5.12 can satisfy this condition, this is not the case towards smaller values of $|s_2|$.

Our analysis underscores the possibility of testing the same signal with different probes and on different scales. The multi-probe characterisation of the GW signal is a crucial steps towards solving the cosmological *vs* astrophysical sources dichotomy, see e.g. [298].

5.5 Discussion

In this chapter we studied the signature of an inflationary scenario equipped with a particle content that goes beyond that of the minimal single-field slow-roll paradigm. By employing an EFT approach, we accounted for an extra spin-2 field non-minimally coupled to the inflaton [1, 98]. The focus of our analysis has been on gauging the capability of small-scale probes of gravity, such as SKA [221] and LISA [222], to uncover signatures of inflationary dynamics in the gravitational waves spectrum we may observe today.

After reviewing how the EFT parameter space supports a detectable GW signal at small scales once we allow time-dependence for the sound speed of helicity-2 fluctuations [1], we studied the tensor 3-point correlation function. Its amplitude and, most importantly, its shape dependence contain tell-tale signs of the mass and the couplings of the extra spin-2 field. We showed how a decreasing helicity-2 sound speed is connected with enhanced tensor non-Gaussianities, and derived explicit expressions for the equilateral and squeezed configurations, see eqs.(5.13) and (5.18). We found that the shape of the bispectrum interpolates between the equilateral and local templates, depending on the mass of the spin-2 mediator. In particular, lighter particles are associated with bispectra peaking in the squeezed limit. We showed that the EFT supports a non-trivial bispectrum signal in the *ultra-squeezed* configuration and showed how this may be indirectly tested at small scales by the anisotropies induced in the GW power spectrum. The amount of tensor non-Gaussianities needed to generate a percent level anisotropy in the GW signal within reach of SKA and LISA is $F_{\rm NL} \simeq \mathcal{O}(10^3 - 10^4)$. These large tensor non-Gaussianities could potentially lead to large one-loop corrections to the tensor 2-point correlation function; while the validity of the perturbative expansion needs to be checked, this goes beyond the scope of this work.

CHAPTER 6

TESTING THE SCALAR SECTOR

Cosmological α–attractors [127–134] stand out as particularly compelling models to describe inflation in the very early universe, naturally meeting tight observational bounds from CMB experiments [67]. In this chapter we investigate α–attractor potentials in the presence of an inflection point, leading to enhanced curvature perturbations on small scales. We study both single- and multi-field models, driven by scalar fields living on a hyperbolic field space. In the single-field case, ultra-slow-roll dynamics at the inflection point is responsible for the growth of the power spectrum, while in the multi-field set-up we study the effect of geometrical destabilisation and non-geodesic motion in field space. As discussed in section 3.5, models displaying a significant enhancement in the scalar power spectrum can lead to primordial black hole (PBH) production and potentially detectable second-order GWs. We show that, due to the existence of *universal predictions* in α–attractors, consistency with current CMB constraints on the large-scale spectral tilt implies that PBHs can only be produced with masses smaller than $10^8\,\mathrm{g}$ and are accompanied by ultra-high frequency GWs, with a peak expected to be at frequencies of order $10\,\mathrm{kHz}$ or above.

This chapter is based on the publication [3], and is organised as follows. After reviewing α–attractor models in section 6.1, we analyse in section 6.2 single-field α–attractor models featuring an inflection-point potential and discuss the models' predictions for large-scale observables. In section 6.3 we discuss the single-field model phenomenology, focusing on PBH production and second-order GW generation. In section 6.4 we describe the multi-field extension of the single-field inflection-point model, discuss its dynamics,

large-scale predictions and small-scale phenomenology. We discuss our findings in section 6.5. For completeness, we provide additional material in a series of appendices. In appendix C we review how the universal predictions of α–attractors models are derived. In appendix D we illustrate how the numerical computation of the single-field scalar power spectrum is performed. In appendix E we study the limiting behaviour of the single-field potential. In appendix F we provide a parameter study of the multi-field potential. In appendix G we discuss the two-field model of [4] in terms of polar coordinates mapping of the hyperbolic field space, clarifying its relationship with α–attractors models.

6.1 Cosmological α–attractors

Cosmological α–attractors [127–134] stand out as particularly compelling models to describe inflation in the very early universe. On the theoretical side they can be embedded in supergravity theories, while leading to universal predictions for large-scale observables that are independent of the detailed form of the scalar field potential [127], and which at the same time provide an excellent fit to current observational constraints on the primordial power spectra [67].

Usually α–attractors are formulated in terms of a complex field Z belonging to the Poincaré hyperbolic disc [299, 300], with potential energy $V(Z,\bar{Z})$ which is regular everywhere in the disc. The corresponding kinetic Lagrangian reads

$$\mathscr{L}_{\rm kin} = -3\alpha \frac{\partial_\mu Z \partial^\mu \overline{Z}}{(1-Z\overline{Z})^2}\,, \tag{6.1}$$

where the curvature of the hyperbolic field space is constant and negative, $\mathscr{R}_{\rm fs} = -4/(3\alpha)$. The complex field Z can be parameterized by

$$Z \equiv r\, e^{i\theta}\,, \tag{6.2}$$

where $r \equiv |Z| < 1$, and eq.(6.1) can then be rewritten in terms of the fields r and θ as

$$\mathscr{L}_{\rm kin} = -\frac{3\alpha}{(1-r^2)^2}\left[(\partial r)^2 + r^2(\partial\theta)^2\right]\,. \tag{6.3}$$

As neither of the fields r and θ are canonically normalised, it is often useful to transform to the canonically normalised radial field ϕ, defined as

$$r \equiv \tanh\left(\frac{\phi}{\sqrt{6\alpha}}\right). \tag{6.4}$$

In terms of ϕ and θ, the kinetic Lagrangian in eq.(6.3) reads

$$\mathscr{L}_{\rm kin} = -\frac{1}{2}(\partial\phi)^2 - \frac{3\alpha}{4}\sinh^2\left(\frac{2\phi}{\sqrt{6\alpha}}\right)(\partial\theta)^2 \,. \tag{6.5}$$

Usually it is assumed that the angular field θ is strongly stabilised during inflation, in which case ϕ is the only dynamical field and plays the role of the inflaton [300]. This leads to an effective single-field description of α–attractor models of inflation, characterised by *universal predictions* for the large-scale cosmological observables which are stable against different choices of the inflaton potential [127, 301, 302]. In particular, the scalar spectral tilt, $n_s - 1$, and the tensor-to-scalar ratio, $r_{\rm CMB}$[1], are given at leading order in $(\Delta N_{\rm CMB})^{-1}$ as

$$n_s \simeq 1 - \frac{2}{\Delta N_{\rm CMB}} \,, \tag{6.6}$$

$$r_{\rm CMB} \simeq 12\frac{\alpha}{\Delta N_{\rm CMB}{}^2} \,, \tag{6.7}$$

where $\Delta N_{\rm CMB}$ is the number of e-folds that separate the horizon crossing of the CMB comoving scale from the end of inflation, see eq.(3.1). See appendix C for a derivation of eqs.(6.6) and (6.7). For $50 \lesssim \Delta N_{\rm CMB} \lesssim 60$ and $\alpha \lesssim \mathscr{O}(1)$ the predictions above sit comfortably within the bounds from the latest CMB observations [67, 142].

In some cases both ϕ and θ are light during inflation, implying that the angular field θ cannot be integrated out and the full multi-field dynamics has to be taken into account. Effects associated with the dynamics of the angular field have been investigated in the context of cosmological inflation [303–305][2]. In particular, in [303] the authors consider a multi-field α–attractor model with $\alpha = 1/3$ and whose potential depends also on the angular field θ. Under slow-roll and slow-turn approximations, and considering a background evolution close to the boundary of the Poincaré disc, the authors demonstrate that the fields "roll on the ridge", evolving almost entirely along the radial direction, and the single-field predictions, eqs. (6.6) and (6.7), are stable against the effect of the light angular field. The impact of a strongly-curved hyperbolic field space ($\alpha \ll 1$) has been investigated in [305], showing that for small α the background trajectory could display a phase of angular inflation, a regime in which the fields' evolution is mostly along the angular direction. For the models considered in [305], the phase of angular inflation

[1] Here the subscript CMB indicates the tensor-to-scalar ratio is evaluated when the comoving scale $k_{\rm CMB}$ crossed the horizon, while usually r is quoted at $k = 0.002\,{\rm Mpc}^{-1}$, as using the *Planck* plus BK15 data the tensor perturbations are best constrained at $k = 0.002\,{\rm Mpc}^{-1}$, while the scalar perturbations, and hence the scalar spectral index and its running, are best constrained at $k_{\rm CMB} = 0.05\,{\rm Mpc}^{-1}$ [67].

[2] See [306–308] for implications of multi-field α–attractors for preheating.

shifts the universal predictions (6.6) and (6.7), whilst it does not lead to an enhancement of the scalar perturbations.

In this chapter we investigate inflationary models that can support a large enhancement of the scalar power spectrum on small scales and belong to the class of α–attractors. Building on the work [89], we focus on single-field potentials which feature an inflection point, proposing a potential parametrisation which has a clear physical interpretation. The ultra-slow-roll dynamics associated with non-stationary inflection points can enhance the scalar power spectrum on small scales. We then assess the impact of a light angular direction on the single-field potential, suggesting a simple multi-field extension of the inflection-point model. Within this set-up, the inflationary evolution is realised in two phases, the transition between them being caused by a geometrical destabilisation of the background trajectory and characterised by a deviation from geodesic motion in field space. At the transition the combined effect of a strongly-curved field space and non-geodesic motion could trigger a tachyonic instability in the isocurvature perturbation. The enhanced isocurvature mode couples with and sources the curvature perturbation, delivering a peak in the scalar power spectrum on small scales whose amplitude is set by the curvature of field space and the angular field initial condition. Even if the mechanisms enhancing the scalar perturbations differ between the single- and multi-field models, we find that the predicted large-scale observables can be described in both cases by a modified version of the universal predictions for α–attractor models, eqs. (6.6) and (6.7).

6.2 Single-field inflection-point model

We will first consider α–attractor models where the angular field θ is stabilised, leading to an effective single-field model. We take the potential to be a non-negative function of the modulus of the original complex field, $f^2(r)$, where $r = |Z|$. The Lagrangian in terms of the canonically normalised radial field ϕ, defined in eq.(6.4), is

$$\mathscr{L} = \frac{1}{2}R - \frac{1}{2}(\partial\phi)^2 - f^2\left(\tanh\frac{\phi}{\sqrt{6\alpha}}\right), \tag{6.8}$$

where f is an arbitrary analytic function.

We will consider models which can successfully support an inflationary stage generating an almost scale-invariant power spectrum of primordial curvature perturbations on large scales, compatible with CMB constraints, and can also amplify scalar curvature

fluctuations on smaller scales, potentially producing PBHs and/or significant primordial GWs. To do so, the potential $f^2(r)$ must have some characteristics:

(i) at large field values ($\phi \gg 1, r \to 1$), the potential has to be flat enough to support slow-roll inflation and satisfy the large-scale bounds on the CMB observables. In α–attractor models, the flatness of the potential is naturally achieved at the boundary ($r \to 1$) by the stretching induced by the transformation (6.4) so long as $f(r)$ remains finite;

(ii) in single-field inflation, a significant amplification of scalar fluctuations on small scales can be achieved by deviations from slow roll [81]. In particular, this may be realised with a transient ultra-slow-roll phase [82–84], see section 2.3.1.1, where the gradient of the potential becomes extremely small at intermediate field values. This can be implemented by having an almost-stationary inflection point in the potential [85–90];

(iii) at the end of inflation, the condition $V(\phi_{\rm end}) = 0$ ensures that inflation can end without giving rise to a cosmological constant at late times.

In the following, we outline a procedure to fix the potential profile in a way that addresses all the requirements listed above. The potential is constructed in a way similar to [89], but our analysis differs in that we present a simplified potential, with a reduced number of parameters and we give a clear dynamical interpretation of each parameter. Furthermore, while in [89] cases with $\alpha = \mathcal{O}(1)$ have been studied extensively, we will consider configurations with $\alpha < 1$, which will enhance the role of the hyperbolic geometry in the model's multi-field extension.

6.2.1 Parameterising the inflection-point potential

Given the single-field Lagrangian (6.8), the easiest way to implement an almost-stationary inflection point in the potential, $V(\phi)$, is to consider a function $f(r)$ which itself has an almost-stationary inflection point. The inflection-point structure of $f(r)$ is then transmitted to the potential

$$V(\phi) = f^2\left(r(\phi)\right) . \tag{6.9}$$

The lowest order polynomial that allows the presence of a single inflection point is of

order three[3],

$$f(r) = f_0 + f_1 r + f_2 r^2 + f_3 r^3 \,. \tag{6.10}$$

From condition (iii) above we require $V(\phi_{\rm end}) = 0$ at the end of inflation. Here, for simplicity, we set $\phi_{\rm end} = 0$, which together with (6.9) and (6.10) implies

$$f_0 = 0 \,. \tag{6.11}$$

We require $f_1 \neq 0$ so that $\phi = 0$ is a simple minimum with $V''(0) > 0$, and given that the potential (6.9) is symmetric under $f \to -f$ we then pick $f_1 > 0$ without loss of generality.

An inflection point in $f(r)$ at $r = r_{\rm infl}$, where $0 < r_{\rm infl} < 1$, is defined by the condition $f''(r_{\rm infl}) = 0$. For the function in eq.(6.10), this translates into the condition

$$f_3 = -\frac{f_2}{3 r_{\rm infl}} \,, \tag{6.12}$$

where the positivity of $r_{\rm infl}$ implies that f_2 and f_3 have opposite signs.

The first derivative of the function (6.10) calculated at the inflection point is then

$$f'(r_{\rm infl}) = f_1 + f_2 r_{\rm infl} \,. \tag{6.13}$$

In order for $r_{\rm infl}$ to be a stationary ($f'(r_{\rm infl}) = 0$) or almost-stationary ($f'(r_{\rm infl}) \simeq 0$) inflection point, we require $f_2 < 0$, which follows from the positivity of f_1 and $r_{\rm infl}$. From (6.12), this implies that $f_3 > 0$.

In order to achieve a significant amplification of the scalar power spectrum on small scales, we will consider models with an approximately stationary inflection point where the first derivative at $r_{\rm infl}$ is slightly negative, $f'(r_{\rm infl}) < 0$. As the inflaton rolls from $r > r_{\rm infl}$ down towards $r = 0$ this acts to further slow the inflaton as it passes through the inflection point, realising an ultra-slow-roll phase. In this case the inflection point is then preceded by a local minimum (for $r > r_{\rm infl}$) and followed by a local maximum (for $r < r_{\rm infl}$). Using (6.13), both stationary and almost-stationary configurations can be described by the condition

$$f_1 = -f_2 (r_{\rm infl} - \xi) \,, \tag{6.14}$$

where $\xi = 0$ corresponds to the case of a stationary inflection point and an approximate stationary inflection point is realised if $0 < \xi \ll r_{\rm infl}$.

[3]While setting the (arbitrary) function $f(r)$ to be a cubic polynomial is a pretty generic choice, (some of) the coefficients need to be fine-tuned to produce a stationary/non-stationary inflection point. We note here that there are no symmetries protecting the fine-tuned coefficients from radiative corrections (see e.g. [309] for the role played by radiative corrections during inflation).

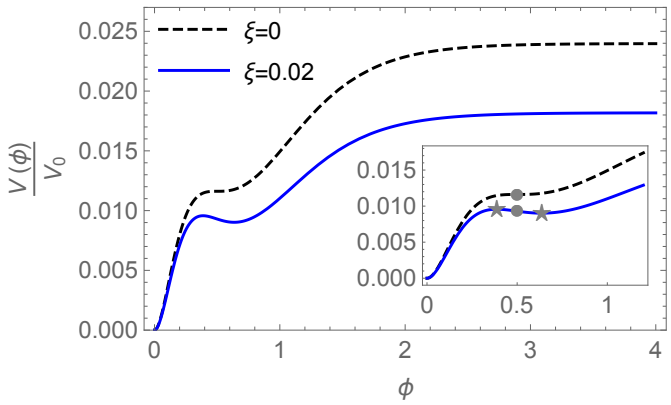

Figure 6.1: Structure of the potential (6.15) with $\alpha = 0.1$ and $\phi_{\rm infl} = 0.5$. The inset zooms around the inflection point. If $\xi = 0$ the inflection point is stationary. The case $\xi \neq 0$ corresponds to an approximate stationary inflection point, where $\phi_{\rm infl}$ (grey dot) is accompanied by a local minimum and a local maximum (grey stars).

Finally, by substituting (6.10) into (6.9) subject to the conditions (6.11), (6.12) and (6.14), and transforming to the canonical field ϕ defined in eq.(6.4), the potential can be written as

$$V(\phi) = V_0 \left\{ (r_{\rm infl} - \xi) \tanh\left(\frac{\phi}{\sqrt{6\alpha}}\right) - \tanh^2\left(\frac{\phi}{\sqrt{6\alpha}}\right) + \frac{1}{3r_{\rm infl}} \tanh^3\left(\frac{\phi}{\sqrt{6\alpha}}\right) \right\}^2 , \tag{6.15}$$

where we have defined $V_0 \equiv {f_2}^2$. For $\xi = 0$ we have a stationary inflection point at $\phi = \phi_{\rm infl}$, where we define $\tanh\left(\phi_{\rm infl}/\sqrt{6\alpha}\right) \equiv r_{\rm infl}$. More generally we have an approximately-stationary inflation point, with $V'(\phi_{\rm infl}) = \mathcal{O}(\xi/r_{\rm infl})$ and $V''(\phi_{\rm infl}) = \mathcal{O}(\xi/r_{\rm infl})$ for $0 < \xi \ll r_{\rm infl}$.

Starting from an initial set of free parameters $\{f_0, f_1, f_2, f_3\}$ for a fixed value of α, we have reduced it to the set $\{V_0, r_{\rm infl}, \xi\}$. The normalisation of the potential V_0 is fixed at CMB scales in order to reproduce the right amplitude of the scalar fluctuations, see (3.2), leaving only two free parameters to describe the shape of the potential, $\{r_{\rm infl}, \xi\}$, for a given α. In figure 6.1, two configurations of $V(\phi)$ are shown in order to illustrate a stationary inflection point ($\xi = 0$) and an approximately stationary inflection point ($0 < \xi \ll r_{\rm infl}$).

6.2.2 Background evolution

The equations of motion for the homogenous field $\phi(t)$ in an FLRW cosmology are given by the Klein–Gordon and evolution equations, see eqs.(2.14) and (2.13) respectively. These are subject to the Friedmann constraint (2.12).

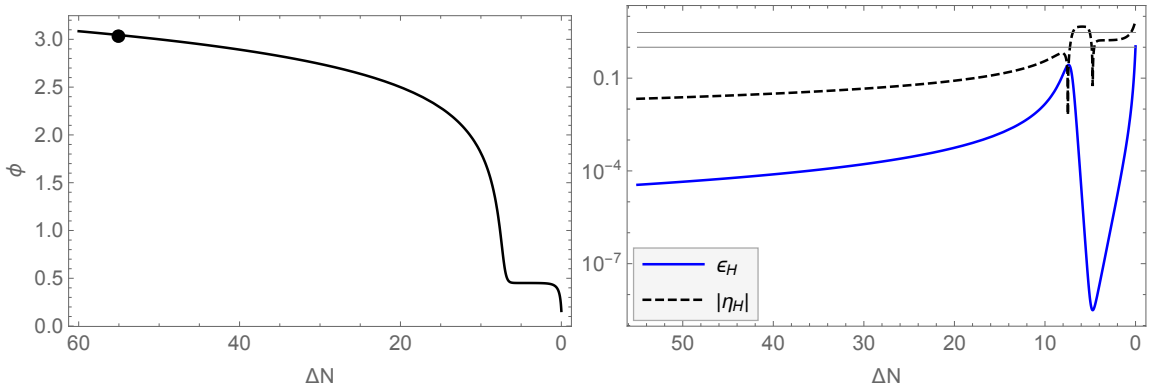

Figure 6.2: *Left panel:* the inflaton evolution $\phi(N)$, for a single-field α–attractor model with potential $V(\phi)$ given in (6.15), where we set $\alpha = 0.1$, $\phi_{\rm infl} = 0.5$ and $\xi = 0.0035108$. The black dot marks the field value when the CMB scale, $k_{\rm CMB} = 0.05\,{\rm Mpc}^{-1}$, exits the horizon, taking $\Delta N_{\rm CMB} = 55$. *Right panel:* the corresponding evolution of the first two Hubble slow-roll parameters ϵ_H and $|\eta_H|$. The two horizontal grey lines correspond to 1 and 3 respectively. Inflation ends when $\epsilon_H = 1$ and $\eta_H \approx 3$ signals the ultra-slow-roll regime.

As an example, in figure 6.2 we display the evolution of the scalar field, ϕ, and the first two slow-roll parameters, ϵ_H and η_H, see (2.18), for the case of a single-field α–attractor potential, eq.(6.15), with $\alpha = 0.1$ and an almost-stationary inflection point, given by $\{\phi_{\rm infl} = 0.5, \xi = 0.0035108\}$. The time evolution is represented in terms of the number of e-folds to the end of inflation, $\Delta N \equiv N_{\rm end} - N$, see eq.(2.33) for the definition of the integrated expansion or e-folds N. The early evolution corresponds to a typical α–attractor slow-roll phase with $\epsilon_H \ll |\eta_H| \ll 1$. The inflaton slows down as it approaches the inflection point and enters an ultra-slow-roll regime with ϵ_H small and rapidly decreasing, such that[4] $\eta_H \gtrsim 3$, almost coming to a stop momentarily. After it passes the potential barrier, caused by the local maximum of $V(\phi)$ following the inflection point at $\phi < \phi_{\rm infl}$, the inflaton rolls towards the minimum of the potential at $\phi = 0$ and inflation ends when $\epsilon_H = 1$.

6.2.3 CMB constraints

As discussed in section 3.1, in order to connect predictions from an inflationary model with late-time observables, e.g. the CMB, one has to compute the number of e-folds elapsed between the horizon crossing of the comoving scale relevant for the specific observable

[4] In terms of the Hubble-flow parameter ϵ_2, the ultra-slow-roll regime is described by $\epsilon_2 \lesssim -6$. Given that $\epsilon_2 = 2\epsilon_H - 2\eta_H$, the latter becomes $\eta_H \gtrsim 3$ in the limit $\epsilon_H \ll |\eta_H|$ [83], see section 2.3.1.1.

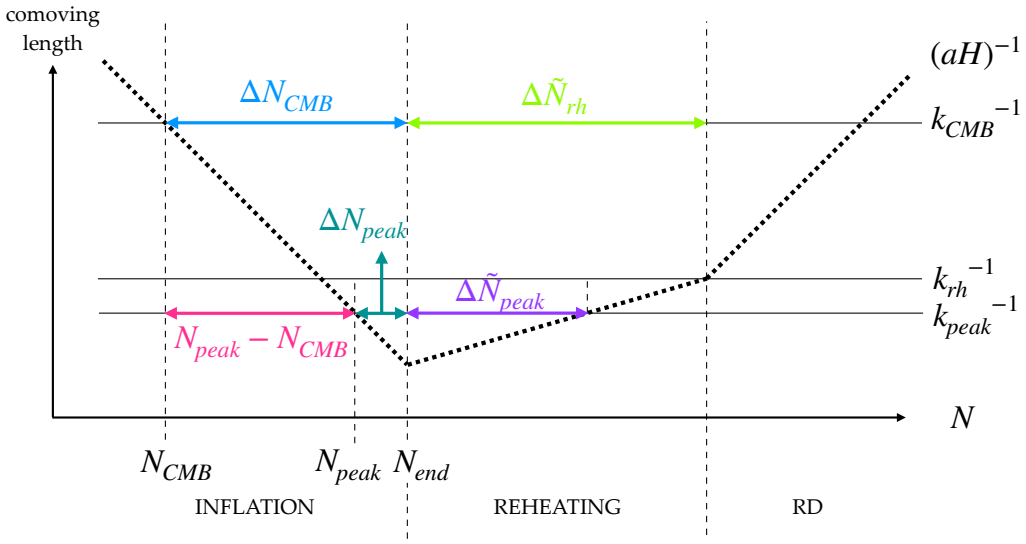

Figure 6.3: Schematic representation showing the horizon crossing of modes with comoving wavenumber k during and after inflation. We use the expression $\Delta N \equiv N_{\rm end} - N$ when referring to e-folds elapsed during inflation, and $\Delta\tilde{N} \equiv N - N_{\rm end}$ when referring to e-folds elapsed after inflation. RD stands for radiation domination.

and the end of inflation, e.g. $\Delta N_{\rm CMB}$ for the CMB comoving scale, $k_{\rm CMB} = 0.05\,{\rm Mpc}^{-1}$, see eq.(3.1).

The precise value of $\Delta N_{\rm CMB}$ depends on the inflationary potential and the details of reheating [136], as illustrated in figure 6.3. By assuming instant reheating, $\rho_{\rm th} = \rho_{\rm end}$, one can obtain the maximum value which $\Delta N_{\rm CMB}$ can take (assuming the reheating equation of state $-1 < w < 1/3$). For α–attractor potentials of the type considered here we (numerically) obtain $\Delta N_{\rm CMB,\,max} \approx 55$ by iteratively solving (3.1) for values of V_0 compatible with CMB observations. In particular, we start by substituting on the right hand side of (3.1) an initial guess for the value of $\Delta N_{\rm CMB}$, $\Delta N_{\rm CMB}{}^{(0)}$, and use the numerical solution for background quantities to calculate the resulting $\Delta N_{\rm CMB}{}^{(1)}$, as dictated by (3.1). We then substitute the new value, $\Delta N_{\rm CMB}{}^{(1)}$, and calculate the resulting $\Delta N_{\rm CMB}{}^{(2)}$. We proceed in the same fashion until convergence is reached, $\Delta N_{\rm CMB}{}^{(i+1)} \simeq \Delta N_{\rm CMB}{}^{(i)}$ and assign the last value to $\Delta N_{\rm CMB,\,max}$.

In the following sections, 6.2.4–6.2.6, we will present results assuming that reheating is instantaneous, bearing in mind that in order to describe a complete inflationary scenario it is necessary to include the details and duration of the reheating phase and understand how it impacts the predictions for observable quantities. We will address this topic in section 6.3.1.

Once $\Delta N_{\rm CMB}$ is fixed, it is possible to derive the model's predictions for the CMB observables $n_s - 1$, α_s and r using the slow-roll expressions (2.76), (2.77) and (2.87). A full numerical computation of the scalar power spectrum (see appendix D) confirms that the slow-roll approximation describes well the behaviour on large scales, i.e. far from the inflection point and the end of inflation.

Model predictions can then be compared with the observational constraints from the latest *Planck* data release [67], see section 3.1. For the α–attractor potentials under consideration, we will show that α_s and n_s are not independent parameters, but rather are related by eq.(6.25). In particular, the lower observational bound $n_s > 0.9551$ (95 % C.L.) from (3.3) implies that $-0.001 \lesssim \alpha_s < 0$ at 95 % C.L., about an order of magnitude smaller than the observational uncertainty in eq.(3.4). For these reasons, we neglect the effect of the running when considering bounds on n_s and r in the following. We comment further on this topic in section 6.2.7.

The upper bound on the tensor-to-scalar ratio at $k_{\rm CMB} = 0.05\,{\rm Mpc}^{-1}$ in the absence of running (i.e., for the $\Lambda{\rm CDM} + r_{\rm CMB}$ cosmological model) is $r_{\rm CMB} < 0.036$ (95 % C.L.) [142], see eq.(3.6). The predicted value of the tensor-to-scalar ratio changes by about 10% if evaluated at $k_{\rm CMB} = 0.05\,{\rm Mpc}^{-1}$ instead of $k = 0.002\,{\rm Mpc}^{-1}$. For $\alpha \leq 1$, this is irrelevant as the predicted values of the tensor-to-scalar ratio in our model will be at least an order of magnitude below this observational bound.

For the reasons outlined above, in the following we will impose observational bounds on the scalar spectral index at CMB scales using the baseline ΛCDM cosmology, excluding both α_s and $r_{\rm CMB}$. *Planck* temperature, polarisation and lensing data yield $n_s = 0.9649 \pm 0.0042$ (68 % C.L.) [67], see eq.(3.5). In particular this gives a lower bound on the spectral index

$$n_s > 0.9565 \ \ (95\,\%\,{\rm C.L.})\,, \tag{6.16}$$

which provides the strongest constraint on our models, and hence their small-scale phenomenology.

6.2.4 $\xi = 0$: stationary inflection point

In the case of a stationary inflection point, the only free parameter specifying the shape of the function $f(r)$ in the simple cubic polynomial (6.10) is the position of the inflection point $r_{\rm infl}$. Along with the hyperbolic curvature parameter, α, this then determines the field value at the inflection point, $\phi_{\rm infl}$, in the potential, $V(\phi)$ in (6.15).

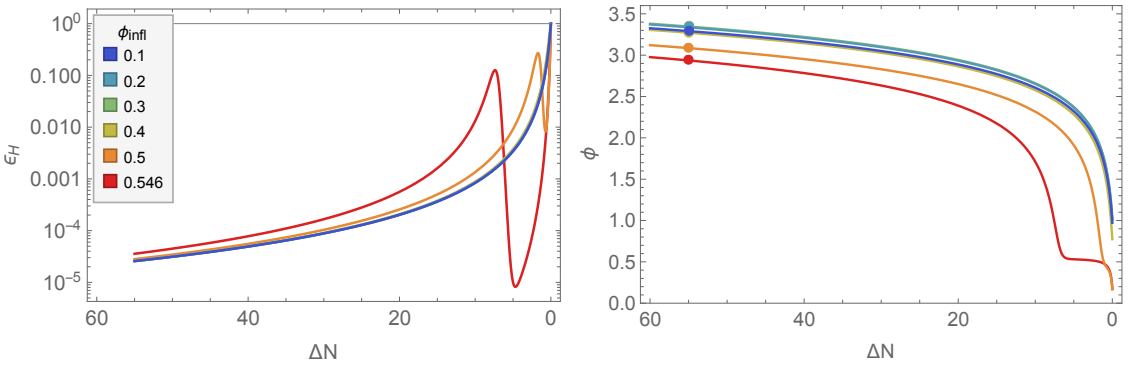

Figure 6.4: Background evolution of the first slow-roll parameter ϵ_H (left panel) and of the inflaton field (right panel) for the stationary inflection-point model, $\xi = 0$. Different lines correspond to different locations of the inflection point $\phi_{\rm infl}$, as displayed in the legend. In the right panel, the points represented on top of $\phi(N)$ signal the field value at which the CMB scale leave the horizon, $\phi_{\rm CMB}$. All the configurations represented produce $\Delta N_{\rm CMB} \simeq 55$.

For our fiducial value of $\alpha = 0.1$, we find that when $\phi_{\rm infl} \geq 0.56$ the inflaton, after a brief ultra-slow-roll phase, settles back down into slow roll towards the inflection point and takes an infinite time to reach it. We therefore exclude that portion of the model's parameter space. We study configurations with $0.1 \leq \phi_{\rm infl} \leq 0.5465$ and plot the resulting background evolution in figure 6.4. The limiting behaviour at large or small values of $\phi_{\rm infl}$ are explored in appendix E.

Let us first discuss the configurations with $0.1 \leq \phi_{\rm infl} \leq 0.5$. When the inflection point is located at small field values, for $0.1 \leq \phi_{\rm infl} \leq 0.4$, inflation ends even before the inflaton reaches $\phi_{\rm infl}$, making the background evolution effectively indistinguishable between those configurations. The case $\phi_{\rm infl} = 0.5$ is slightly different, as seen from the corresponding ϵ_H profile in the left panel of figure 6.4; the inflaton does slow down as it approaches the inflection point and its velocity drops, but only briefly before it passes through the inflection point.

Using eqs.(2.76), (2.77) and (2.87) we find $0.961 \lesssim n_s \lesssim 0.963$, $\alpha_s \sim -0.0007$ and $r_{0.002} \sim 4 \times 10^{-4}$, for $\{\xi = 0, 0.1 \leq \phi_{\rm infl} \leq 0.5\}$, showing that this parameter space is compatible with the CMB bounds given in (3.5) and (3.6). However we find that larger values of $\phi_{\rm infl}$, corresponding to a longer persistence of the inflaton around the inflection point (see the left panel of figure 6.4), lead to smaller values for n_s, making the scalar power spectrum more red on CMB scales. This is due to the fact that the large-scale CMB measurements test a steeper portion of the inflaton potential as a consequence of the persistence at the inflection point. We will return this topic in more detail in section 6.2.7

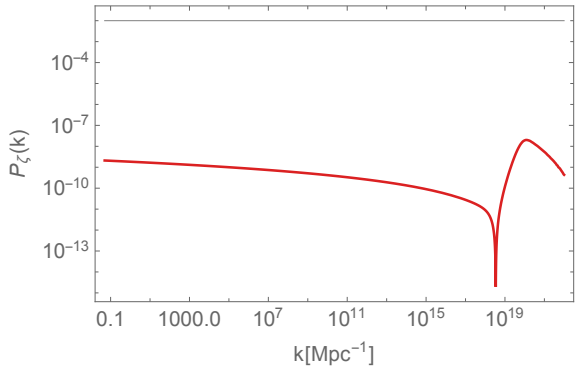

Figure 6.5: Numerical scalar power spectrum for the single-field inflection-point model (6.15) with parameters $\{\alpha = 0.1, \phi_{\rm infl} = 0.5465, \xi = 0\}$, plotted against the comoving scale k.

and give a simple explanation of the connection between the large-scale observations and the inflection-point location.

The largest value of $\phi_{\rm infl}$ which we find is compatible with the lower limit of the observational bound on the scalar spectral tilt, eq.(6.16), is $\phi_{\rm infl} = 0.5465$. The corresponding background evolution is displayed in figure 6.4. The inflection point does slow down the inflaton field, but without realising a sustained ultra-slow-roll phase. We therefore expect only a limited enhancement of the scalar fluctuations on small scales, which is confirmed by an exact computation of the scalar power spectrum (see appendix D for a detailed description of the computational strategy). In figure 6.5, we display $P_\zeta(k)$ obtained numerically for this configuration. The power spectrum does exhibit a peak located at $k_{\rm peak} = 1.3 \times 10^{20}\,{\rm Mpc}^{-1}$, whose amplitude is only one order of magnitude larger with respect to the large-scale power spectrum, $P_\zeta(k_{\rm peak}) = 2 \times 10^{-8}$. It is useful to characterise the position of the inflection point through the parametrisation

$$\Delta N_{\rm CMB} \equiv \left(N_{\rm peak} - N_{\rm CMB}\right) + \Delta N_{\rm peak}\,, \tag{6.17}$$

which implies that the number of e-folds elapsed between the horizon crossing of the CMB scale and the moment in which $k_{\rm peak}$ left the horizon can be expressed as $\Delta N_{\rm CMB} - \Delta N_{\rm peak}$, see figure 6.3. For the configuration plotted in figure 6.5 its value is $\Delta N_{\rm CMB} - \Delta N_{\rm peak} \simeq 49.5$.

Surveying the parameter space with $\xi = 0$ shows that potentials with a stationary inflection point do not produce a large enhancement of the scalar fluctuations on small scales. In order for inflection-point α–attractor models to display an interesting phenomenology on small scales, such as primordial black hole formation and/or significant

	$\phi_{\rm infl}$	ξ	$\Delta N_{\rm CMB} - \Delta N_{\rm peak}$	$k_{\rm peak}/{\rm Mpc}^{-1}$	n_s	$r_{0.002}$
(I)	0.51	0.0023495	47.8	2.2×10^{19}	0.9555	5.3×10^{-4}
(II)	0.5	0.0035108	49.3	9×10^{19}	0.9569	4.9×10^{-4}
(III)	0.49	0.0049575	50.4	2.7×10^{20}	0.9579	4.7×10^{-4}

Table 6.1: Details of three potentials with $\alpha = 0.1$ and approximate stationary inflection points, $\xi \neq 0$. The value $\Delta N_{\rm CMB} - \Delta N_{\rm peak}$ refers to the parametrisation (6.17). All the potentials lead to inflation with $\Delta N_{\rm CMB} \sim 55$, $V_0 \sim 10^{-10}$ and $\alpha_s \sim -9 \times 10^{-4}$.

production of gravitational waves induced at second order, it is necessary to turn to the approximate inflection-point case, $\xi \neq 0$.

6.2.5 $\xi \neq 0$: approximate stationary inflection point

It is possible to obtain a large enhancement of the scalar power spectrum on small scales, $P_\zeta(k_{\rm peak}) \simeq 10^{-2}$, necessary for PBH production after inflation, in simple cubic-polynomial α–attractor models with $\xi \neq 0$ in eq.(6.15).

In table 6.1 we display a selection of configurations for our fiducial curvature parameter of $\alpha = 0.1$ which produce a peak $P_\zeta(k_{\rm peak}) \simeq 10^{-2}$. We see that the field value at the inflection point, $\phi_{\rm infl}$, determines both the location of the peak, $k_{\rm peak}$, and the predicted value of the scalar spectral index, n_s, on CMB scales. The correspondence between $\phi_{\rm infl}$ and n_s holds regardless of the amplitude of the power spectrum peak. In particular, the larger $\phi_{\rm infl}$, the smaller $k_{\rm peak}$ and n_s, as we saw for the case $\xi = 0$. For the configurations listed in table 6.1, the inflection-point field value is selected in order to have the power spectrum peak on the largest scale possible, with predicted values for the tilt n_s around the CMB observational lower bound (6.16). The parameter ξ has then been adjusted to obtain $P_\zeta(k_{\rm peak}) \simeq 10^{-2}$. Configuration (I) in table 6.1 lies slightly outside the 95% C.L. observational bound on n_s, while (II) and (III) are within the 95% C.L. bound. In figure 6.6 numerical results for the power spectra corresponding to these three configurations are displayed.

6.2.6 Changing α

In the preceding sections the parameter space $\{\phi_{\rm infl}, \xi\}$ has been studied for a fixed fiducial value of the hyperbolic field-space curvature, corresponding to $\alpha = 0.1$. In this section we consider the effect of varying α.

We select five different values of $\alpha \in \{0.01, 0.1, 1, 5, 10\}$, and for simplicity restrict our attention to the case of a stationary inflection point, $\xi = 0$. This avoids any numerical

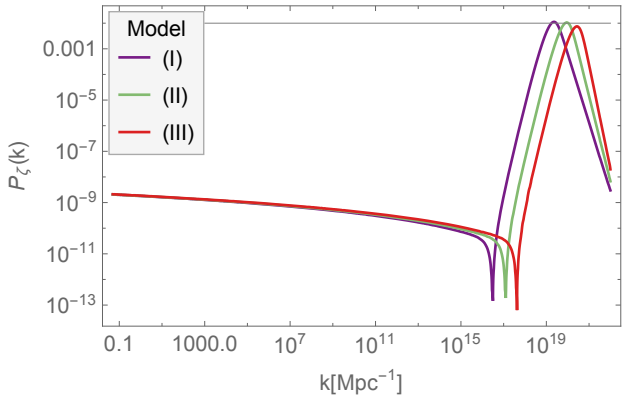

Figure 6.6: Numerical results for the scalar power spectrum $P_\zeta(k)$ for three single-field models with $\alpha = 0.1$ and $\xi \neq 0$. The values of $\phi_{\rm infl}$ and ξ corresponding to each line are listed in table 6.1.

α	$\phi_{\rm infl}$	$\Delta N_{\rm CMB}$	$\Delta N_{\rm CMB} - \Delta N_{\rm peak}$	$k_{\rm peak}/{\rm Mpc}^{-1}$	n_s	$r_{0.002}$
0.01	0.255	54.3	49	10^{20}	0.9565	5×10^{-5}
0.1	0.5465	55	49.5	1.3×10^{20}	0.9565	5×10^{-4}
1	1.009	56.3	49.4	3×10^{19}	0.9565	4.9×10^{-3}
5	1.313	57.6	49.3	4×10^{18}	0.9565	0.0217
10	1.39	58.3	48.3	8×10^{18}	0.9565	0.0385

Table 6.2: Table of parameters for each of the single-field inflection-point models used to generate the scalar power spectra shown in figure 6.7.

instabilities, possible when $\alpha > 1$ due to fine-tuning of the inflection point when $\xi \neq 0$. For each case, the value of $\phi_{\rm infl}$ is chosen such that the predicted scalar spectral index, n_s, is close to the lower observational bound in (6.16). The key parameters for each model are listed in table 6.2 and the numerically computed scalar power spectra are displayed in figure 6.7.

The peak positions for $\alpha < 1$ are very close to each other, while for larger α the peak moves, not following a specific trend and always on scales smaller than $10^{18}\,{\rm Mpc}^{-1}$. The peak magnitudes vary depending on α, whilst being fairly similar for $\alpha < 1$.

The potential normalisation, V_0, and hence the values of $r_{0.002}$ differ from each other by roughly one order of magnitude. This is as expected in α–attractor models [127] where the universal predictions relate the level of primordial gravitational waves at CMB scales to α, as shown in eq.(6.7). Smaller α values are associated with a smaller predicted tensor-to-scalar ratio, as seen in table 6.2. Note that the predicted value of $r_{0.002}$ for $\alpha = 10$ is in tension with the upper bound (3.6), hence we do not explore $\alpha > 10$ (see also [310]).

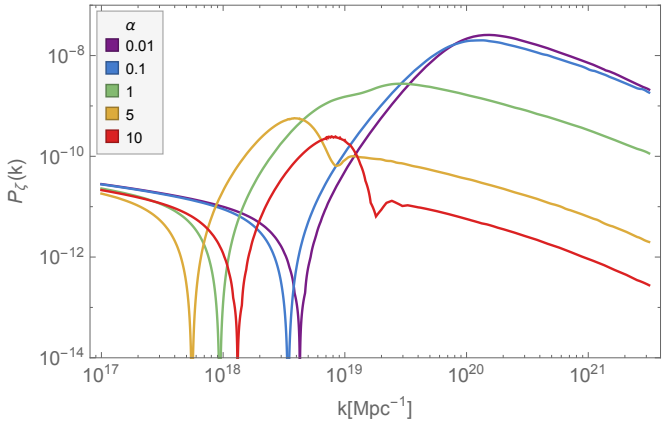

Figure 6.7: Scalar power spectra obtained numerically for the single-field inflection-point models listed in table 6.2. Each line corresponds to a different choice of α, as detailed in the legend.

The fact that the results for $k_{\rm peak}$, $P_\zeta(k_{\rm peak})$ and $r_{0.002}$ are fairly consistent for small α is consistent with the expected α–attractor behaviour. On the other hand the characteristic behaviour of α–attractors, formulated on a hyperbolic field space, gets washed away for large α, where these models approach the simple chaotic inflation behaviour [299].

6.2.7 Modified universal predictions

The numerical results that we have found for observables on CMB scales from single-field models including an inflection point suggest a simple modification of the α–attractors universal predictions for n_s and r given in eqs.(6.6) and (6.7), as previously noted in [89]. In the presence of an inflection point at smaller field values (after CMB scales exit the horizon), the α–attractors universal predictions still hold if we replace $N_{\rm end}$ with $N_{\rm peak}$, and hence $\Delta N_{\rm CMB} \to \Delta N_{\rm CMB} - \Delta N_{\rm peak}$, such that (6.6) and (6.7) are modified for $\Delta N_{\rm peak} > 0$ to become

$$n_s \approx 1 - \frac{2}{\Delta N_{\rm CMB} - \Delta N_{\rm peak}}\,, \tag{6.18}$$

$$r_{\rm CMB} \approx 12 \frac{\alpha}{\left(\Delta N_{\rm CMB} - \Delta N_{\rm peak}\right)^2}\,. \tag{6.19}$$

In figure 6.8 we plot the approximations (6.18) and (6.19) together with our numerical results for a number of selected configurations which lie close to the lower bound on n_s. The coloured points are centered around values $47 \lesssim \Delta N_{\rm CMB} - \Delta N_{\rm peak} \lesssim 51$ which, while being compatible with CMB measurements, produce a peak in $P_\zeta(k)$ on the largest

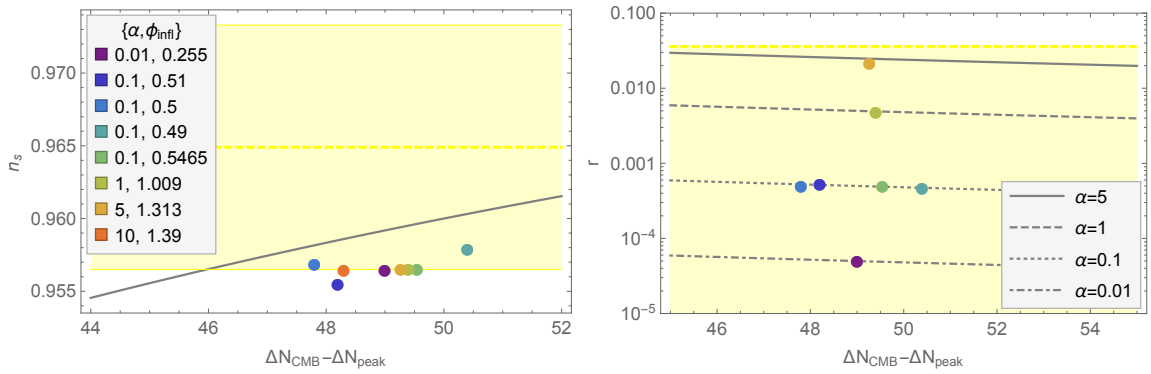

Figure 6.8: *Left panel:* the approximation (6.18) (grey line) is plotted against numerical results (coloured points) for the scalar spectral index on CMB scale, n_s. Each point corresponds to a specific configurations discussed in sections 6.2.4 and 6.2.5. The yellow-shaded area highlights the *Planck* 95% C.L. region, see (3.5), with the dashed line representing the central value. *Right panel:* the approximation (6.19) is plotted against the numerical results for the tensor-to-scalar ratio, $r_{\rm CMB}$. Each line corresponds to a different value of α. See the left panel for the legend illustrating the coloured points. The yellow-dashed line signals the 95% C.L. upper limit (3.6). We do not include the point corresponding to the model with $\alpha = 10$, as the predicted value for $r_{\rm CMB}$ puts the model in tension with the bound (3.6).

scales possible. We see that the modified universal predictions describe quite well the numerical points, with a small offset observed in the left panel in figure 6.8. We will investigate this further within the multi-field analysis in section 6.4.4 and show a simple way of moving the numerical results even closer to the modified universal predictions.

In the following we will use eqs.(6.18) and (6.19) to explore in a simple and straightforward way the phenomenology of the inflection-point potential (6.15). Rather than considering all the possibilities, we will focus on configurations that are consistent with the large-scale CMB observational constraints, eqs.(3.5) and (3.6). Using eq.(6.18), the observational bounds on n_s given in (3.5) translate into

$$46 \lesssim \Delta N_{\rm CMB} - \Delta N_{\rm peak} \lesssim 75\,. \tag{6.20}$$

A lower limit on $\Delta N_{\rm CMB} - \Delta N_{\rm peak}$ can also be obtained by substituting the upper bound on the tensor-to-scalar ratio (3.6) in eq.(6.19), but for $\alpha \leq 1$ it is always weaker than the one given in eq.(6.20). The lower bounds become comparable only when $\alpha \gtrsim 10$.

During inflation there is a one-to-one correspondence between a scale k and the number of e-folds, N, when that scale crosses the horizon, $k = aH$. Calibrating this relation using the values corresponding to the CMB scale yields

$$k(N) = \frac{a(N)}{a_{\rm CMB}}\frac{H(N)}{H_{\rm CMB}} \times 0.05\,{\rm Mpc}^{-1}\,, \tag{6.21}$$

where $a(N)\Big/a_{\rm CMB} = \mathrm{e}^{N-N_{\rm CMB}}$. For the scale corresponding to the peak in the scalar power spectrum eq.(6.21) is

$$k_{\rm peak} \simeq \mathrm{e}^{\Delta N_{\rm CMB}-\Delta N_{\rm peak}} \times 0.05\,{\rm Mpc}^{-1}\,, \tag{6.22}$$

where we simplify the expression by assuming that the Hubble rate is almost constant during inflation. This equation shows that the largest scale, i.e., the lowest $k_{\rm peak}$, corresponds to the lowest allowed value of $\Delta N_{\rm CMB} - \Delta N_{\rm peak}$. The lower limit in (6.20) can therefore be used in eq.(6.22) to derive an estimate of the lowest scale $k_{\rm peak}$ for configurations which are not in tension with the CMB observations,

$$k_{\rm peak} \gtrsim 4.7 \times 10^{18}\,{\rm Mpc}^{-1}\,, \tag{6.23}$$

which is valid regardless of the enhancement of the scalar power spectrum, $P_\zeta(k_{\rm peak})$. Conversely, using eqs.(6.23) and (6.18) one can show that a peak at, for example, LISA ($k_{\rm peak} \simeq 10^{12}\,{\rm Mpc}^{-1}$) or LIGO ($k_{\rm peak} \simeq 10^{16}\,{\rm Mpc}^{-1}$) scales would lead to the large-scale spectral tilt values $n_s = 0.9333$ and $n_s = 0.9498$ respectively, well outside of the 95% C.L. lower end of the *Planck* measurement (6.16).

Eq.(6.23) has important implications for the phenomenology of the model under analysis[5] and is confirmed by the results obtained numerically and presented in tables 6.1 and 6.2.

Modifying the universal prediction for the running of the tilt, eq.(C.14), with $\Delta N_{\rm CMB} \to \Delta N_{\rm CMB} - \Delta N_{\rm peak}$ gives the approximation

$$\alpha_s \approx -\frac{2}{\left(\Delta N_{\rm CMB} - \Delta N_{\rm peak}\right)^2}\,. \tag{6.24}$$

The numerical results for α_s can be well-approximated by the expression above, with a small offset similar to that seen for n_s in the left panel of figure 6.8. We show in appendix C that in fact the values of α_s and n_s are well-described the consistency relation

$$\alpha_s \approx -\frac{(n_s-1)^2}{2}\,. \tag{6.25}$$

In figure 6.9 we plot our numerical results for (n_s, α_s), and show that they are well-described by the consistency relation (6.25). In particular, even if we allow for non-zero running, using the lower observational bound on n_s given in eq.(3.3), the consistency relation (6.25) implies that $\alpha_s > -1.01 \times 10^{-3}$ at 95% C.L., about an order of magnitude

[5] For a counter example see, e.g., [311], where a localised feature is superimposed on the original global potential.

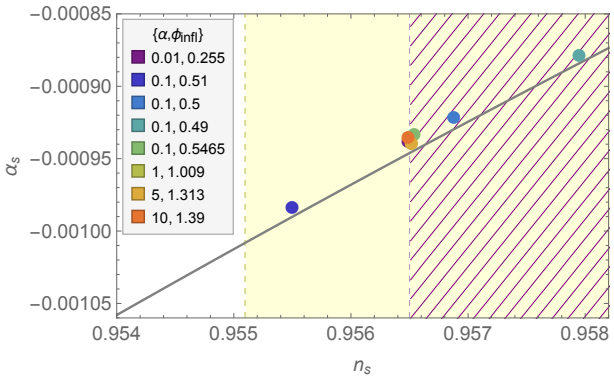

Figure 6.9: Points representing our numerical results for the spectral index and its running, (n_s, α_s). The consistency relation (6.25) is plotted as a solid-grey diagonal line. The yellow area represents part the 95% C.L. region for n_s when *Planck* data are compared with the $\Lambda\text{CDM} + r_{\text{CMB}} + \alpha_s$ model, (3.3), and the hatch-shaded area to the right represents the 95% C.L. region for n_s for the ΛCDM model neglecting running and r_{CMB}. The range of α_s shown is within the observational bound (3.4).

smaller than the observational uncertainty in eq.(3.4). This justifies what was already anticipated in section 6.2.3, that we can in practice neglect the running when comparing the model predictions with CMB bounds on the tilt, n_s. Thus in the following we will apply the more stringent lower bound on n_s, eq.(6.16), derived for the ΛCDM model without running, in contrast to the approach taken in [89].

6.3 Extended phenomenology of single-field models

Building on the numerical results presented in section 6.2, we extend here our considerations to the phenomenology of inflection-point models on scales much smaller than those probed by the CMB. In section 6.3.1 we consider the implications of a reheating phase at the end of inflation. In sections 6.3.2 and 6.3.3 we review some aspects of the formation of PBHs and the production of second-order GWs in presence of large scalar perturbations. Using the modified universal predictions appropriate for inflection-point models, we restrict our analysis to configurations of the inflection-point potential (6.15) which are not in tension with the large-scale CMB measurements and explore the implications for the masses of the PBHs generated and the wavelengths of the second-order GWs.

6.3.1 Reheating

Thus far we have worked under the assumption of instant reheating. Next we will take into account the presence of a reheating stage with finite duration, see section 2.2.2 for a review of the process of reheating after the end of inflation.

The duration of reheating measured in terms of e-folds is given in eq.(2.36). We will consider a matter-dominated reheating phase ($w_{\rm rh} = 0$), as the inflaton behaves as non-relativisitic, pressureless matter[6] when oscillating around a simple quadratic minimum of its potential, eq.(6.15), for all configurations with $\xi \neq r_{\rm infl}$.

The exact duration of reheating depends on the efficiency of the energy transfer process. In order to be as general as possible, we estimate first the maximum duration of reheating and then, within the allowed range, consider the impact of a reheating phase on observable quantities.

Requiring that reheating is complete before the onset of big bang nucleosynthesis yields $\rho_{\rm th} \in \left[(1\,\text{TeV})^4, \rho_{\rm end}\right]$ [67], where the upper limit corresponds to the case of instant reheating. Substituting the lower limit for $\rho_{\rm th}$ into eq.(2.36) allows us to estimate the maximum duration of reheating as

$$\Delta\tilde{N}_{\rm rh} \leq \frac{1}{3}\ln\left(\frac{\rho_{\rm end}}{(1\,\text{TeV})^4}\right). \tag{6.26}$$

The inflection-point potential (6.15) predicts $\rho_{\rm end} \sim 10^{-12}\, {M_{\rm Pl}}^4$, with only a weak dependence on α, which by means of eq.(6.26) yields

$$0 \leq \Delta\tilde{N}_{\rm rh} \lesssim 38\,. \tag{6.27}$$

It is instructive to isolate the reheating contribution to the value of $\Delta N_{\rm CMB}$ given in eq.(3.1). For example, for our α–attractor models with $\alpha = 0.1$ eq.(3.1) gives

$$\Delta N_{\rm CMB} \simeq 55 - \frac{1}{4}\Delta\tilde{N}_{\rm rh}\,. \tag{6.28}$$

Different values of $\Delta\tilde{N}_{\rm rh}$, and hence $\Delta N_{\rm CMB}$, can shift the observational predictions for a given inflationary model [136]. CMB constraints, combined with the standard universal predictions for n_s and r in α–attractor models, eqs.(6.6) and (6.7), already have implications for the duration of reheating in these models. Substituting (6.28) in (6.6) and requiring that the duration of reheating does not put the model in tension with the CMB measurement (3.5), yields the observational bound

$$0 \leq \Delta\tilde{N}_{\rm rh} \lesssim 36\,. \tag{6.29}$$

[6] See section 2.2.2 where we demonstrate that $w_{\rm rh} = 0$ in the case of a quadratic minimum.

This restricts the maximum duration of reheating allowed compared with the theoretical range given in eq.(6.27) and implies $\rho_{\rm th} \gtrsim (4.5\,{\rm TeV})^4$.

If we now generalise this to include inflection-point α–attractor models, giving rise to a peak in the power spectrum on small scales, $k_{\rm peak}$ given in eq.(6.22), then substituting eq.(6.28) in eq.(6.18) and imposing the bound on the CMB spectral index (3.5), yields a stronger bound on the duration of reheating

$$0 \leq \Delta\tilde{N}_{\rm rh} \lesssim 36 - 4\Delta N_{\rm peak}\,. \tag{6.30}$$

This in turn puts a lower bound on the the thermal energy at the end of reheating

$$\rho_{\rm th}^{1/4} \gtrsim 4.5\,{\rm TeV} \times e^{3\Delta N_{\rm peak}}\,. \tag{6.31}$$

In practice, eq.(6.30) will determine the maximum range for the duration of reheating which we consider in the following.

6.3.2 Primordial black hole formation

Very large amplitude scalar fluctuations produced during inflation give rise to large density perturbations when they re-enter the horizon after inflation, which can collapse to form primordial black holes [174]. We reviewed the PBH formation process in section 3.5.1.

The masses and abundance of the PBHs formed differ according to whether the scale corresponding to the peak in the scalar power spectrum re-enters the horizon ($k_{\rm peak} = aH$) during reheating or during radiation domination after reheating. If $k_{\rm peak}$ exits the horizon $\Delta N_{\rm peak}$ e-folds before the end of inflation, it re-enters the horizon $\Delta\tilde{N}_{\rm peak}$ e-folds after the end of inflation (see figure 6.3), where

$$\Delta\tilde{N}_{\rm peak} = \frac{2}{(1+3w)}\Delta N_{\rm peak}\,. \tag{6.32}$$

In the expression above w is the equation of state parameter describing the background evolution when $k_{\rm peak}$ re-enters the horizon. Under the assumption of instant reheating ($\Delta\tilde{N}_{\rm rh} = 0$), $k_{\rm peak}$ always re-enters the horizon during radiation domination ($w = 1/3$), which from eq.(6.32) implies that $\Delta\tilde{N}_{\rm peak} = \Delta N_{\rm peak}$. If instead $\Delta\tilde{N}_{\rm rh} \neq 0$, then $k_{\rm peak}$ re-enters the horizon during reheating if $\Delta\tilde{N}_{\rm rh} > \Delta\tilde{N}_{\rm peak} = 2\Delta N_{\rm peak}$, where we take $w = 0$ in eq.(6.32).

6.3.2.1 PBH formation during radiation domination

For modes that re-enter the horizon during the radiation-dominated era after reheating, eq.(3.16), assuming conservation of entropy between the epoch of black hole formation and matter-radiation equality, yields [312]

$$\frac{M(k)}{M_\odot} \simeq 10^{-16}\left(\frac{\gamma}{0.2}\right)\left(\frac{g(T_k)}{106.75}\right)^{-1/6}\left(\frac{k}{10^{14}\,\mathrm{Mpc}^{-1}}\right)^{-2}, \tag{6.33}$$

where $g(T_k)$ is the effective number of degrees of freedom at the time of formation. Assuming the Standard Model particle content, we take $g(T_k) = 106.75$ and $g(T_{\rm eq}) = 3.38$.

If we consider the non-stationary inflection-point models presented in section 6.2.5 where we calculated the CMB constraints assuming instant reheating, the PBHs are formed from the collapse of large scalar fluctuations at $k = k_{\rm peak}$ which re-enter the horizon during radiation domination. Substituting the numerical values of $k_{\rm peak}$ listed in table 6.1 in eq.(6.33) leads to PBH masses $M_{\rm PBH}\Big/g \simeq 4.2\times10^6, 2.6\times10^5, 2.8\times10^4$ for configurations (I), (II) and (III) respectively. Thus PBHs resulting from these inflection-point α–attractor models would have evaporated before primordial nucleosynthesis [313, 314].

In section 6.3.2.3 we will argue that this is a general result which applies to all α–attractor inflection-point models which are not in tension with the CMB measurements on large scales and extends beyond the instant reheating assumption. In particular, the black-dashed line in figure 6.10 shows the range of PBH masses formed when the peak of the power spectrum on small comoving scales re-enters the horizon during the radiation-dominated era after reheating, over the range (6.23) consistent with CMB constraints on large scales.

6.3.2.2 PBH formation during matter domination

As discussed above, it is possible that large scalar perturbations which collapse to form PBHs re-enter the horizon during reheating, corresponding to a transient matter-dominated stage after inflation. The different background evolution during reheating modifies PBH formation; intuitively the collapse is easier in a matter-dominated epoch than in the presence of radiation pressure. Another consequence is that the correspondence between the scale of the perturbation that collapses to form the PBH and its mass is modified. In particular, following a procedure similar to the one illustrated for eq.(6.33) and taking into account the different background evolution yields [89]

$$\frac{M(k)}{M_\odot} \simeq 10^{-16}\left(\frac{\gamma}{0.2}\right)\left(\frac{g(T_{\rm rh})}{106.75}\right)^{-1/6}\left(\frac{k_{\rm rh}}{10^{14}\,\mathrm{Mpc}^{-1}}\right)^{-2}\left(\frac{k}{k_{\rm rh}}\right)^{-3}, \tag{6.34}$$

where the scale

$$k_{\rm rh} = e^{-3\Delta\tilde{N}_{\rm rh}/4} \times 3.8 \times 10^{22}\,{\rm Mpc}^{-1} \tag{6.35}$$

re-enters the horizon at the end of reheating. For perturbations that re-enter the horizon during reheating we have $k > k_{\rm rh}$, as sketched in figure 6.3. The coloured diagonal lines in figure 6.10 show the range of PBH masses formed when the peak of the power spectrum on small comoving scales re-enters the horizon during reheating for models which are in accordance with CMB constraints on large scales.

6.3.2.3 Implications of reheating and modified universal predictions for PBH formation

In the following we examine the implications for the allowed PBHs masses of the modified universal predictions presented in section 6.2.7 and the resulting constraints from CMB measurements of the spectral tilt on large scales. We consider inflection-point potentials (6.15) with parameters, $\{\alpha, \phi_{\rm infl}, \xi\}$, which generate significant enhancements of the scalar power spectrum on small scales, as we have done for the specific cases discussed in section 6.2. We take into account the fact that inflation could be followed by a reheating stage, whose duration is bounded by (6.30) for $\alpha = 0.1$. We discuss the effect of varying α at the end of this section.

As already discussed, it is the hierarchy between $k_{\rm peak}$ and $k_{\rm rh}$ in the presence of reheating that determines the setting for PBH formation, during either radiation or matter domination. Equivalently one can consider the hierarchy between $\Delta N_{\rm peak}$ and $\Delta N_{\rm rh} = \Delta\tilde{N}_{\rm rh}/2$. The bound (6.30) can be written as

$$\Delta N_{\rm rh} + 2\Delta N_{\rm peak} \lesssim 18\,. \tag{6.36}$$

and we discuss here the implications of the expression above for the mass of the PBHs formed within three different scenarios.

(i) Instantaneous reheating ($\Delta N_{\rm rh} = 0$): In this case $k_{\rm peak}$ always re-enters the horizon during radiation domination and it is bounded by (6.23). In figure 6.10 the black-dashed line represents $M_{\rm PBH}$ against $k_{\rm peak}$ over the range $4.7 \times 10^{18}\,{\rm Mpc}^{-1} < k_{\rm peak} < k_{\rm end}$, compatible with (6.23), where $k_{\rm end} \simeq 4 \times 10^{22}\,{\rm Mpc}^{-1}$ for models with $\alpha = 0.1$ and instantaneous reheating. The modified universal predictions therefore imply that the mass is maximised for the smallest $k_{\rm peak}$ and in general

$$M_{\rm PBH} < 10^{8}\,{\rm g}\,, \tag{6.37}$$

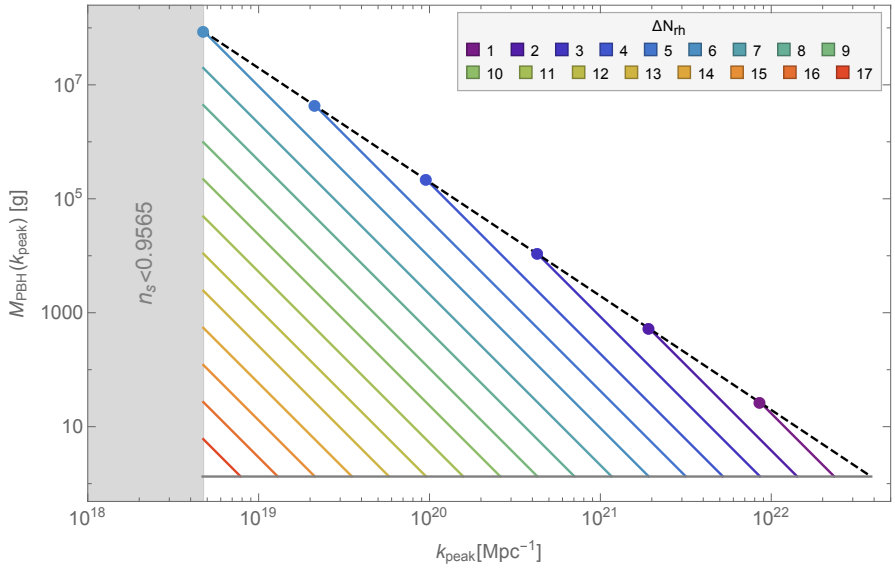

Figure 6.10: Masses of PBHs generated during or after reheating as a function of $k_{\rm peak}$ for models with $\alpha = 0.1$. Diagonal coloured lines correspond to PBHs produced by modes re-entering the horizon during a period of reheating ($w = 0$), where each coloured line corresponds to a given duration of reheating, $\Delta N_{\rm rh}$. The region on the left highlighted in grey is excluded by the 95% C.L. lower bound on n_s, eq.(6.16). The black-dashed line corresponds to PBHs produced during radiation domination. The lower horizontal grey line corresponds to scales that re-enter the horizon at the start of reheating, immediately after the end of inflation.

which means that PBHs produced in this case have evaporated before primordial nucleosynthesis and are not a candidate for dark matter. Explicit realisations of this scenario have been discussed in section 6.3.2.1.

(ii) PBH formation after reheating is complete ($\Delta N_{\rm peak} > \Delta N_{\rm rh}$): In this case the PBHs form during radiation domination. The requirement that scales $k_{\rm peak}$ re-enter the horizon after reheating together with (6.36) implies that

$$0 < \Delta N_{\rm rh} < 6 \quad \text{and} \quad \Delta N_{\rm rh} < \Delta N_{\rm peak} \lesssim 9 - \frac{1}{2}\Delta N_{\rm rh} \,. \tag{6.38}$$

For fixed $\Delta N_{\rm rh}$, using (6.21) in the expression above gives a range of possible scales

$$4.7 \times 10^{18}\,{\rm Mpc}^{-1} \lesssim k_{\rm peak} < k_{\rm rh} \,, \tag{6.39}$$

where the reheating scale is given by eq.(6.35).

The mass of the PBHs formed is still set by (6.33), corresponding to the black-dashed line in figure 6.10 for $M_{\rm PBH}(k_{\rm peak})$, but in contrast to the case of instant reheating, $k_{\rm peak}$ can now only run up to $k_{\rm rh}$. This means that only part of the black-dashed line in figure

6.10 for $M_{\rm PBH}(k_{\rm peak})$ is accessible for a given value of $\Delta N_{\rm rh}$. In particular, the coloured points on the black-dashed line signal the largest allowed value of $k_{\rm peak} = k_{\rm rh}$ for a fixed $\Delta N_{\rm rh} < 6$. In this case the largest PBH mass produced is again $M_{\rm PBH} \sim 10^8\,{\rm g}$ and it corresponds to $k_{\rm peak} = 4.7 \times 10^{18}\,{\rm Mpc}^{-1}$.

(iii) PBH formation during reheating ($\Delta N_{\rm peak} \leq \Delta N_{\rm rh}$): In this case the PBHs form before reheating is complete, i.e., during a matter-dominated era. This implies a hierachy, $k_{\rm peak} \geq k_{\rm rh}$, which together with (6.36) results in either

$$0 < \Delta N_{\rm peak} \leq \Delta N_{\rm rh} \leq 6\,, \tag{6.40}$$

or

$$6 < \Delta N_{\rm rh} < 18 \quad \text{and} \quad 0 < \Delta N_{\rm peak} \leq 9 - \frac{1}{2}\Delta N_{\rm rh}\,. \tag{6.41}$$

For a given value of $\Delta N_{\rm rh}$ and hence a given value of $k_{\rm rh}$, see eq.(6.35), we have

$$k_{\rm rh} \leq k_{\rm peak} < e^{\Delta N_{\rm rh}} k_{\rm rh} \quad \text{if} \quad 0 < \Delta N_{\rm rh} \leq 6\,, \tag{6.42}$$

$$4.7 \times 10^{18}\,{\rm Mpc}^{-1} \leq k_{\rm peak} < e^{\Delta N_{\rm rh}} k_{\rm rh} \quad \text{if} \quad 6 < \Delta N_{\rm rh} < 18\,. \tag{6.43}$$

The masses of the PBHs produced is set by (6.34) and it is shown as a function of $k_{\rm peak}$ in figure 6.10. For a given $k_{\rm peak}$, the masses produced during a matter-dominated ($w = 0$) reheating stage are all below the corresponding masses produced during radiation domination, because $k_{\rm peak}$ re-enters the horizon before the onset of radiation domination and this suppresses the PBH mass by a factor $\left(k_{\rm rh}\Big/k_{\rm peak}\right)^3$, see eq.(6.34). The PBH masses approach those generated in radiation domination in the limit $\Delta N_{\rm peak} \to \Delta N_{\rm rh}$. In this case $k_{\rm peak} \to k_{\rm rh}$ and therefore the formula (6.34) coincides with (6.33). The cases representing $\Delta N_{\rm peak} = \Delta N_{\rm rh}$ are plotted in figure 6.10 with the coloured points, which mark the intersection between the coloured lines and the black-dashed line. The case $\Delta N_{\rm rh} = \Delta N_{\rm peak} = 6$ maximises the PBH mass which could be produced in this scenario, $M_{\rm PBH} \sim 10^8\,{\rm g}$.

For any duration of reheating, $\Delta N_{\rm rh}$, substituting the upper value $k_{\rm peak} = e^{\Delta N_{\rm rh}} k_{\rm rh}$ in (6.34) results in a PBH mass independent of $\Delta N_{\rm rh}$, which justifies why all the coloured lines lie above the horizontal grey line in figure 6.10 corresponding to $M_{\rm PBH} \sim 1\,{\rm g}$.

The right vertex of allowed values in figure 6.10 corresponds to the case $\Delta N_{\rm rh} = 0$ and $k_{\rm peak} = k_{\rm end}$. This is the limiting case where the peak is produced at the very end of inflation. While it may be possible to have configurations which produce a peak a few e-folds before the end of inflation, the limited growth of the scalar power spectrum in

single-field models [120] would not allow the 7 orders of magnitude enhancement with respect to the CMB scales which is necessary for significant production of PBHs.

The analysis above is performed for our fiducial value $\alpha = 0.1$. The parameter α sets the maximum value of $\Delta N_{\rm CMB}$ (corresponding to $\Delta N_{\rm rh} = 0$) as illustrated in table 6.2. Thus the expression (6.28) gets modified for different α, which in turns changes the scales involved, see eq.(6.21). In particular, the lower bound on the PBH mass that can be produced during reheating corresponds to $k_{\rm peak} = \mathrm{e}^{\Delta N_{\rm CMB,\,max} - \frac{1}{2}\Delta N_{\rm rh}} \times 0.05\,{\rm Mpc}^{-1}$, moving the horizontal grey line in figure 6.10 up for $\alpha < 0.1$ and down for $\alpha > 0.1$. On the other hand it is the lower bound on n_s (6.16) that bounds $k_{\rm peak}$ from below and the modified universal prediction for n_s, eq.(6.18), does not depend on the parameter α. This implies that the largest PBH mass that can be produced is the same for all α.

In summary the maximum PBH mass that can be produced in any of these scenarios is $M_{\rm PBH} \simeq 10^8\,{\rm g}$ which corresponds to a peak on scales $k_{\rm peak} = 4.7 \times 10^{18}\,{\rm Mpc}^{-1}$ which re-enter the horizon during radiation domination, after reheating. PBHs with this mass would have evaporated by today and cannot constitute a candidate for dark matter. This strong constraint on $M_{\rm PBH}(k_{\rm peak})$ comes from the CMB observational lower bound on n_s, eq.(6.16), in these α–attractor models.

PBHs with masses $M_{\rm PBH} \lesssim 10^8\,{\rm g}$ would have evaporated before the onset of big bang nucleosynthesis and cannot therefore be directly constrained. Nevertheless, it is possible that these ultra-light PBHs are produced with such a large abundance that they come to dominate the cosmological density before they evaporate, giving rise to a period of early black hole domination [313, 315–318]. In this scenario, there are various sources of GW production (see e.g., recent work [314, 319, 320]), which open up the possibility of constraining ultra-light PBHs using GW observatories, see also the discussion in section 6.3.3.

Another possibility is that primordial black holes could leave behind stable relics. When the mass of an evaporating black hole becomes comparable to the Planck scale, quantum gravitational effects become relevant, such that a complete evaporation could be prevented, leaving stable PBHs relics with masses $M \sim M_p$ [321–323]. Interestingly, they could account for the totality of dark matter, a possibility that has been investigated in the context of different inflationary models, see e.g. [324] where an α–attractor single-field inflationary model is considered. PBHs relics might be tested (and their abundance constrained) because of their gravitational effects, or with terrestrial detectors if the carry a charge [325].

We leave for future work the exploration of early PBH domination or stable PBH

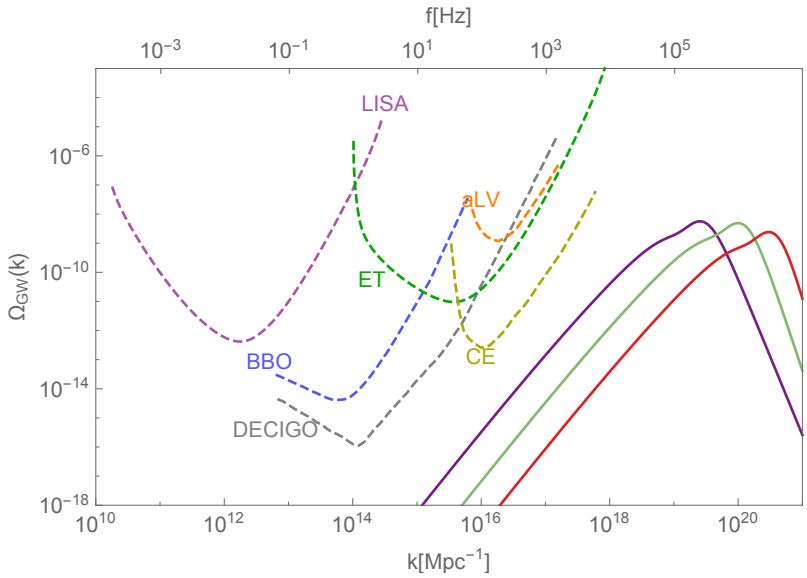

Figure 6.11: GWs produced at second order by the large scalar perturbations generated in single-field inflection-point models with $\xi \neq 0$. The legend is the same as in figure 6.6 and details about the parameters $\{\phi_{\rm infl}, \xi\}$ are listed in table 6.1.

relics in the context of α–attractor models of inflation.

6.3.3 Induced gravitational waves at second order

6.3.3.1 Induced GWs after reheating

First-order scalar perturbations produced during inflation can source a stochastic background of primordial gravitational waves at second order from density perturbations that re-enter the horizon and oscillate during the radiation-dominated era after reheating [209–214].

We reviewed second-order GWs in section 3.5.2; in particular the present-day energy density associated with these second-order GWs is given in eq.(3.19).

We numerically evaluate $\Omega_{\rm GW}(k)$ for the gravitational waves induced from the peak in the scalar power spectrum on small scales in the inflection-point models with $\xi \neq 0$ discussed in section 6.2.5. In figure 6.11 the results are represented together with the sensitivity curves of upcoming Earth- and space-based GW observatories, operating up to frequencies in the kHz.

The spectral shape of the GW signal for the non-stationary inflection-point models can be understood in terms of the infrared ($k \ll k_{\rm peak}$) and ultraviolet ($k \gg k_{\rm peak}$) tilt of the peak in $P_\zeta(k)$ [214, 326]. To demonstrate this, we select configuration (III), see table 6.1

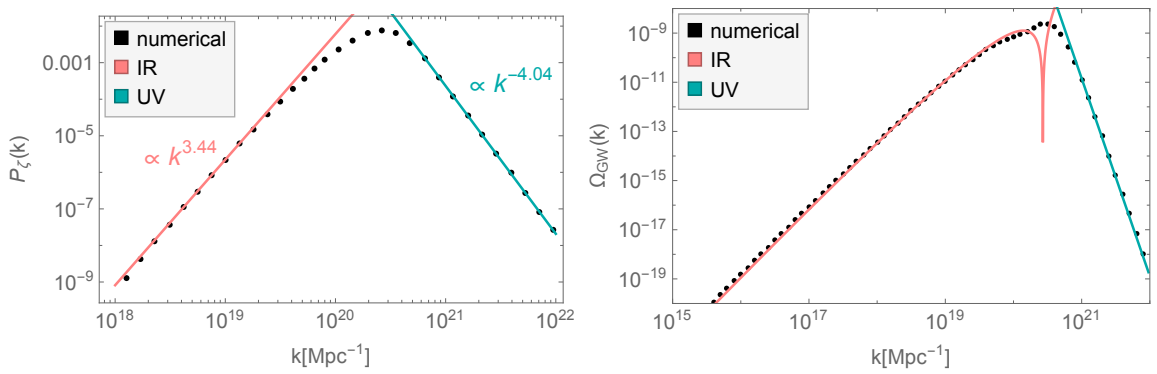

Figure 6.12: Spectral shape of the scalar power spectrum (left) and second-order GWs (right) for a non-stationary inflection-point model with $\{\alpha = 0.1, \phi_{\rm infl} = 0.49, \xi = 0.0049575\}$. The scalar power spectrum is well approximated by a broken power-law and the IR and UV scaling of $P_\zeta(k)$ explain the IR and UV tails of the GW numerical results. In both plots, the black dots represent numerical results.

for the model's parameters, and represent in the left panel of figure 6.12 the approximate IR and UV scaling of $P_\zeta(k)$ around the peak on top of the numerical results (black dots). We note that the IR tilt is in accordance with the estimate of the maximum growth of the scalar perturbations for single-field inflationary models, $n_{\rm IR} \leq 4$ [120]. The IR and UV scaling of $P_\zeta(k)$ determine the IR and UV tails of the second-order GWs, see eqs. (5.16) and (5.20) in [214]. In the right panel of figure 6.12, we represent the numerical results for $\Omega_{\rm GW}(k)$ together with the IR and UV approximations aforementioned, which well describe the numerical IR and UV tails.

The principal peak of $\Omega_{\rm GW}(k)$ is located at very small scales, as a consequence of the position of the peak in the scalar power spectrum. In particular, the lower bound (6.23) on $k_{\rm peak}$ implies that the GWs produced at second order exhibit a principal peak at $k \gtrsim 6 \times 10^{18}\,{\rm Mpc}^{-1}$, see section 3.5.2. This equivalently implies that the GW signal peaks at frequencies $f \gtrsim 10^5\,{\rm Hz}$, as confirmed by the numerical results plotted in figure 6.11. Configurations which are in accordance with CMB measurements on large scales cannot be probed on small scales by currently planned GW observatories.

6.3.3.2 Induced GWs during reheating

Second-order GWs resulting from first-order scalar perturbations that re-enter the horizon during reheating are in general suppressed [214, 327]. First-order scalar metric perturbations, in the longitudinal gauge for example, on sub-Hubble scales during a matter-dominated era, remain constant rather than oscillating as they do in a radiation-dominated universe. While these scalar perturbations support second-order tensor metric

perturbations in the longitudinal gauge during the matter era [210, 212, 328], these tensor perturbations are not freely-propagating gravitational waves and indeed they are gauge-dependent[7] [331, 332]. At the end of the reheating epoch, when the Hubble rate drops below the decay rate of the inflaton ($\Gamma \approx H$), the scalar metric perturbations decay slowly with respect to the oscillation time for sub-horizon GWs ($k/a \gg \Gamma$). Thus the tensor metric perturbations that they support also decay adiabatically on sub-horizon scales. The resulting power spectrum for freely propagating second-order GWs in the subsequent radiation-dominated era is therefore strongly suppressed on scales that re-enter the horizon during reheating. This gives an upper bound on the comoving wavenumber of any second-order GWs produced by modes re-entering the horizon after inflation, $k \lesssim k_{\rm rh}$.

The only exception could be if there is a sudden transition from matter domination to radiation domination (rapid with respect the oscillation time, a/k) [327, 333]. This could indeed occur in an early pressureless era dominated by light PBHs which decay and reheat the universe before primordial nucleosynthesis, as mentioned in section 6.3.2.3. For a sufficiently narrow range of PBH masses and therefore lifetimes, the final evaporation of PBHs would be an explosive event and could lead to a sudden transition from an early PBH-dominated era after inflation to the conventional radiation-dominated era, leading to an enhancement of the spectrum of induced GWs from first-order scalar perturbations on sub-horizon scales at the transition [318]. We leave the study of GWs from a possible early PBH-dominated era for future work.

6.4 Multi-field extension

Cosmological α–attractor models are naturally formulated in terms of two fields living in a hyperbolic field space, see section 6.1, therefore we explore here the consequences of embedding in a multi-field setting the single-field inflection-point model studied in the preceding sections. Our aim is to establish whether the single-field predictions are robust against multi-field effects and under which conditions it may be possible to enhance the scalar power spectrum through inherently multi-field effects.

[7] In contrast to the linear perturbation theory, the second-order (induced) tensor perturbations are known to have gauge dependence. For the GWs produced in a radiation-dominated era, the observable (late-time) GWs in the transverse-traceless (synchronous) gauge and in the Newtonian gauge are the same [329], while more care needs to be taken in the matter-dominated era, as the scalar perturbations continue to couple with the tensor perturbations on subhorizon scales even in the Newtonian gauge because of the growing matter perturbations [329]. See also [330] for further discussions about the second-order gauge-invariant formalism for the cosmological observables.

We reviewed the dynamics of multi-field inflation in section 2.4, and we focus here on the multi-field set-up of α–attractor models, with $\phi^I = \{\phi, \theta\}$. The geometry of field space is hyperbolic, with curvature $\mathscr{R}_{\rm fs} = -4/(3\alpha)$. The kinetic Lagrangian for the fields ϕ and θ is given in eq.(6.5). The Christoffel symbols associated with the hyperbolic metric are

$$\Gamma^{\phi}_{\theta\theta} = -\frac{1}{2}\sqrt{\frac{3}{2}\alpha}\,\sinh\left(2\sqrt{\frac{2}{3\alpha}}\,\phi\right),\quad \Gamma^{\theta}_{\phi\theta} = \frac{2}{\sqrt{6\alpha}}\tanh^{-1}\left(\sqrt{\frac{2}{3\alpha}}\,\phi\right). \tag{6.44}$$

In this way the equations of motion for the background evolution (2.129)–(2.130) can be written explicitly for the fields ϕ and θ as

$$-\frac{H'}{H} = \frac{1}{2}\left(\phi'^2 + \frac{3\alpha}{2}\sinh^2\left(\sqrt{\frac{2}{3\alpha}}\,\phi\right)\theta'^2\right), \tag{6.45}$$

$$H^2\phi'' + HH'\phi' + 3H^2\phi' + \Gamma^{\phi}_{\theta\theta}H^2\theta'^2 + U_{,\phi} = 0\,, \tag{6.46}$$

$$H^2\theta'' + HH'\theta' + 3H^2\theta' + 2\Gamma^{\theta}_{\phi\theta}H^2\theta'\phi' + \left[\frac{3\alpha}{2}\sinh^2\left(\sqrt{\frac{2}{3\alpha}}\,\phi\right)\right]^{-1} U_{,\theta} = 0\,, \tag{6.47}$$

where a prime denotes a derivative with respect to the number of e-folds, N.

In section 6.4.1 we illustrate one possible multi-field embedding of the single-field inflection-point potential and discuss its phenomenology in sections 6.4.2 and 6.4.3. In section 6.4.4 we establish the robustness of the modified universal predictions given in eqs.(6.18)–(6.19) for single-field models against multi-field effects, and consider the small-scale phenomenology of multi-field models which are compatible with CMB measurements.

6.4.1 Multi-field embedding of the single-field inflection-point potential

In section 6.2 we outlined the construction of an inflection-point potential in the context of single-field α–attractor models, where the building block is the cubic function $f(r)$. This construction can easily be extended to a multi-field set-up. In analogy with the single-field case, let us consider a function $F(r,\theta)$ cubic in r, in terms of which the multi-field potential is

$$U(\phi,\theta) \equiv F^2(r(\phi),\theta)\,. \tag{6.48}$$

In constructing a cubic function of r, we have at our disposal the complex field Z, as defined in (6.2), its complex conjugate $\bar{Z}$ and their combinations

$$Z\bar{Z} = r^2 \,, \tag{6.49}$$

$$\frac{Z+\bar{Z}}{2} = r\cos\theta \,. \tag{6.50}$$

In particular, the former is symmetric under a phase-shift while the latter depends on θ explicitly. The general form of $F(r,\theta)$ arising from terms proportional to $(Z\bar{Z})^{n/2}(Z+\bar{Z})^m \propto \cos^m(\theta) r^{n+m}$ is

$$F(r,\theta) = \sum_{m,n} F_{n+m,m}\cos^m(\theta) r^{n+m} \,. \tag{6.51}$$

We note that our potential will thus be symmetric under the reflection $\theta \to -\theta$.

As in the single-field case, we set $F_{0,0} = 0$ such that the potential (6.48) has a minimum at $U(0,\theta) = 0$. For $F(r,\theta)$ to be a cubic function of r, there are potentially nine terms contributing in (6.51). For simplicity we select just the 3 remaining phase-independent terms to be non-zero and one θ-dependent term, such that

$$F(r,\theta) = F_{1,0}r + F_{2,0}(1+\gamma\cos(\theta))r^2 + F_{3,0}r^3 \,, \tag{6.52}$$

where $\gamma \equiv F_{2,1}\Big/F_{2,0}$.

Identifying the potential $U(r,0) \equiv F^2(r,0)$ along the direction $\theta = 0$ with the single-field potential in (6.15), with an inflection point in the radial direction located at $r = r_{\rm infl}$, gives the coefficients

$$F_{1,0} = r_{\rm infl} - \xi \,, \quad F_{2,0} = -1/(1+\gamma) \,, \quad F_{3,0} = 1/(3r_{\rm infl}) \,. \tag{6.53}$$

Substituting these coefficients into eq.(6.52) yields

$$F(r,\theta) = (r_{\rm infl}-\xi)r - \frac{1+\gamma\cos(\theta)}{1+\gamma}r^2 + \frac{1}{3r_{\rm infl}}r^3 \,. \tag{6.54}$$

Away from the particular direction $\theta = 0$ the function (6.54) has an inflection point in the radial direction at

$$\tilde{r}_{\rm infl}(\theta) = \left(\frac{1+\gamma\cos(\theta)}{1+\gamma}\right) r_{\rm infl} \,. \tag{6.55}$$

For $-(1-r_{\rm infl}^2)\Big/r_{\rm infl} < \xi < r_{\rm infl}$ there is a stationary inflection point (where $\partial F/\partial r = 0$) when

$$\cos(\theta_{\rm st}) = \frac{(1+\gamma)(r_{\rm infl}-\xi)^{1/2} - r_{\rm infl}^{1/2}}{\gamma r_{\rm infl}^{1/2}} \,. \tag{6.56}$$

and

$$\tilde{r}_{\rm infl}(\theta_{\rm st}) = r_{\rm infl}^{1/2}(r_{\rm infl}-\xi)^{1/2}\,. \tag{6.57}$$

If $\xi = 0$ then $F(r,\theta)$ has only one inflection point in the radial direction, located at $r = r_{\rm infl}$ along $\theta = 0$, and it is stationary. This property simplifies the form of the potential and it is for this reason that in the following we consider two-field models with $\xi = 0$ and leave the analysis of the non-stationary inflection-point case, or a stationary inflection point away from the symmetric $\theta = 0$ direction, to future work.

Substituting (6.54) with $\xi = 0$ in (6.48) yields

$$U(\phi,\theta) = U_0\left\{r_{\rm infl}\tanh\left(\frac{\phi}{\sqrt{6\alpha}}\right) - \frac{1+\gamma\cos(\theta)}{1+\gamma}\tanh^2\left(\frac{\phi}{\sqrt{6\alpha}}\right) + \frac{1}{3r_{\rm infl}}\tanh^3\left(\frac{\phi}{\sqrt{6\alpha}}\right)\right\}^2\,, \tag{6.58}$$

which is written in terms of the canonical field ϕ, defined in eq.(6.4). The profile of the multi-field potential along the direction $\theta = 0$ is represented by the black-dashed line in figure 6.1 for a configuration with $\{\alpha = 0.1, \phi_{\rm infl} = 0.5\}$.

Once the field-space curvature, α, and the position of the inflection point along $\theta = 0$, $r_{\rm infl}$, are fixed, the only remaining free parameter in the potential (6.58) is γ. We impose some simple conditions on $U(\phi,\theta)$ to ensure a successful inflationary scenario, which will restrict the allowed range of γ. In particular, we require that the potential has a non-negative derivative in the radial direction, a condition which forbids the radial field, ϕ, from running back towards larger (radial) field values at late times. Thus we require

$$\frac{\partial F(r,\theta)}{\partial r} \geq 0 \quad \forall\, r,\theta\,, \tag{6.59}$$

which one can show implies

$$-1 \leq \frac{1+\gamma\cos(\theta)}{1+\gamma} \leq 1\,. \tag{6.60}$$

Thus we will restrict our analysis to the case $\gamma > 0$ where the condition that the potential has a non-negative derivative in the radial direction holds for any angle θ. In addition, we can see from eq.(6.58) that the effective squared-mass of the angular field, θ, is non-negative along $\theta = 0$ for $\gamma > 0$ (see also the discussion in appendix F). Thus we expect to recover the single-field behaviour for evolution along the symmetric direction, $\theta = 0$, while the potential can exhibit a richer phenomenology in the two-dimensional field space for $\theta \neq 0$.

We plot the profile of the multi-field potential (6.58) with $\{\alpha = 0.1, \phi_{\rm infl} = 0.542, \gamma = 10\}$ in figure 6.13. The direction $\theta = 0$ corresponds to a minimum of the potential in the angular direction, as expected for $\gamma > 0$.

An interesting comparison can be made between multi-field α–attractor potentials, which remain non-singular throughout the hyperbolic field space, and other inflation models discussed in the literature which employ a different coordinate chart in the hyperbolic field space. In particular, the two-field model of [4] is formulated in terms of planar coordinates on the hyperbolic field space and supports a strong enhancement of the scalar power spectrum on small scales. We show in appendix G that the multi-field potential in [4] diverges at a point on the boundary of the hyperbolic disc. At this point, the potential shares the same singularity as the kinetic Lagrangian, and initial conditions which support a small-scale peak in the scalar power spectrum are close to the singularity. In this case, the large-scale observables are then sensitive to characteristics of the potential and initial conditions, as already noted in [105] in the context of side-tracked inflation. The model in [4], while being of interest in its own right, lies outside the class of α–attractors that we consider here.

6.4.2 Exploring the multi-field potential: turning trajectories and geometry at play

In the following we perform a numerical analysis of the background evolution stemming from the multi-field potential (6.58). Initially we will explore a range of possibilities which follow from the form of the potential and the consequences of different choices of parameters and initial conditions. Later, in section 6.4.4, we will restrict our attention to configurations which have been specifically selected to be consistent with CMB measurements on large scales and explore the consequences that CMB observations have for this model.

The first parameter we fix is α, which determines the Ricci curvature of the field space, $\mathscr{R}_{\rm fs} = -4/(3\alpha)$. As we did in the single-field case, we start by considering $\alpha = 0.1$, which corresponds to $\mathscr{R}_{\rm fs} \simeq -13.3$. The profile of the potential is then parametrised by $\{\phi_{\rm infl}, \gamma\}$, and here we select $\{\phi_{\rm infl} = 0.542, \gamma = 10\}$, as shown in figure 6.13. The effect of different choices for γ and $\phi_{\rm infl}$ is discussed in appendix F. The background evolution is derived by numerically solving the differential equations (6.45)–(6.47). We consider vanishing initial velocities for the fields, but in practice the fields rapidly settle into single-field, slow-roll attractor solution at early times. We select $\phi_{\rm in}$ such that the model supports at least 55 e-folds[8] before the end of inflation after the background evolution reaches the attractor solution.

[8]This choice is made in analogy with the single-field case, where $\Delta N_{\rm CMB} \simeq 55$ for models with $\alpha = 0.1$ and assuming instant reheating.

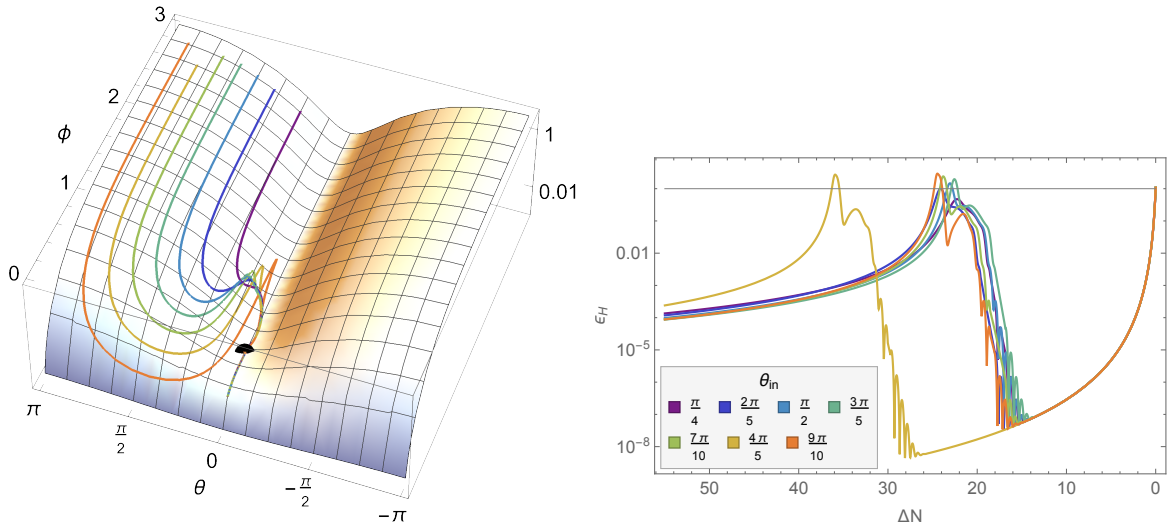

Figure 6.13: Background evolution obtained numerically for the potential (6.58) with model parameters $\{\alpha = 0.1, \phi_{\rm infl} = 0.542, \gamma = 10\}$ and different initial conditions $\theta_{\rm in}$. On the left the fields trajectories are represented on top of the potential profile, with different colours corresponding to different $\theta_{\rm in}$, see the right panel for the legend. The black point located at $\theta = 0$ and $\phi = \phi_{\rm infl}$ highlights the position of the inflection point. On the right we display the evolution of the slow-roll parameter ϵ_H against $\Delta N \equiv N_{\rm end} - N$.

In figure 6.13 we show the field evolution (left panel) and first slow-roll parameter (right panel) for several initial conditions for the angular field in the range $\pi/4 \leq \theta_{\rm in} \leq 9\pi/10$. All the trajectories share some common features. Initially, the angular field, θ, is frozen and only the radial field, ϕ, is evolving. This is a well known effect in hyperbolic field space, referred to as "rolling on the ridge" [303], where the geometry is responsible for suppressing the potential gradient in the equation of motion for θ, see the term $2/(3\alpha)\sinh^{-2}\phi/\sqrt{3\alpha/2}$ multiplying $U_{,\theta}$ in eq.(6.47). As long as $\phi \gg \sqrt{3\alpha/2}$, this term is suppressed, effectively freezing θ at its initial value during the early stages of inflation.

When $\phi \sim \sqrt{3\alpha/2}$, the angular field θ starts evolving and there is a turn in the trajectory, which is shallower or sharper depending on $\theta_{\rm in}$. During the turn, the field ϕ can be driven back towards larger values, this effect being more or less pronounced depending again on $\theta_{\rm in}$. The change of sign of $\phi'(N)$ is due to the motion of θ, which switches on the geometrical contribution, $\Gamma^{\phi}_{\theta\theta}H^2\theta'^2$, in the equation of motion for ϕ, eq.(6.46). This effect also appears in other multi-field α–attractor models, e.g., angular inflation [305]. Once θ starts oscillating around its minimum, $\theta = 0$, the fields cross the radial inflection point and inflation comes to an end soon afterwards. In the right panel of figure 6.13 we display $\epsilon_H \equiv -H'/H$ (see eq.(6.45)) against $\Delta N \equiv N_{\rm end} - N$, where each coloured line corresponds to a different $\theta_{\rm in}$. Depending on $\theta_{\rm in}$ the profile of ϵ_H changes,

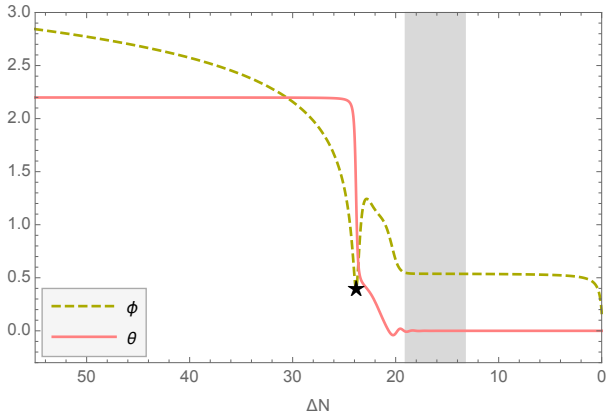

Figure 6.14: Numerical evolution of the fields for the multi-field model with parameters $\{\alpha = 0.1, \phi_{\text{infl}} = 0.542, \gamma = 10\}$ and $\theta_{\text{in}} = 7\pi/10$. The black star signals the moment when $\phi = \sqrt{3\alpha/2}$ and the grey area corresponds to the radial field being within 1% of the inflection point, $\left|\left(\phi - \phi_{\text{infl}}\right)\Big/\phi_{\text{infl}}\right| \leq 0.01$.

with some trajectories temporarily violating slow roll and ending inflation ($\epsilon_H \gtrsim 1$). Despite these differences, all trajectories end up on the same attractor after crossing the inflection point, due to the 'levelling' effect of the inflection point, suppressing the inflaton velocity regardless of the preceding dynamics.

To get a better understanding of the background evolution we will focus on a single case. We select $\theta_{\text{in}} = 7\pi/10$ and represent the evolution of ϕ and θ against ΔN in figure 6.14. When ϕ becomes comparable with the curvature length of the field space, $\sqrt{3\alpha/2}$, signaled by the black star in the plot, the angular field, θ, which was previously frozen, starts evolving. The plot shows the transient change of direction of ϕ and its subsequent persistence at the inflection point before finally rolling down to the global minimum, ending inflation. In particular, the grey region highlights the phase of the evolution when the radial field, ϕ, is within 1% of the inflection point, ϕ_{infl}.

In the left panel of figure 6.15 ϵ_H is plotted for this case, together with its two component parts coming from the evolution of ϕ (green-dashed) and θ (pink-dotted), see eq.(6.45). At the beginning, ϵ_H is dominated by the kinetic energy of ϕ, which is slowly rolling towards smaller values. Then, when $\phi \approx \sqrt{3\alpha/2}$, θ gets released, its kinetic energy becomes comparable to that of ϕ, and ϕ changes direction. The simple ultra-slow-roll behaviour of ϵ_H observed in the single-field case (see e.g., figure 6.2) is modified due to the change of direction of ϕ and the contribution of θ, which oscillates around its minimum. Overall ϵ_H decreases, until ϕ crosses the inflection point and rolls away from it towards the global minimum, bringing inflation to an end. One can see that, similar to

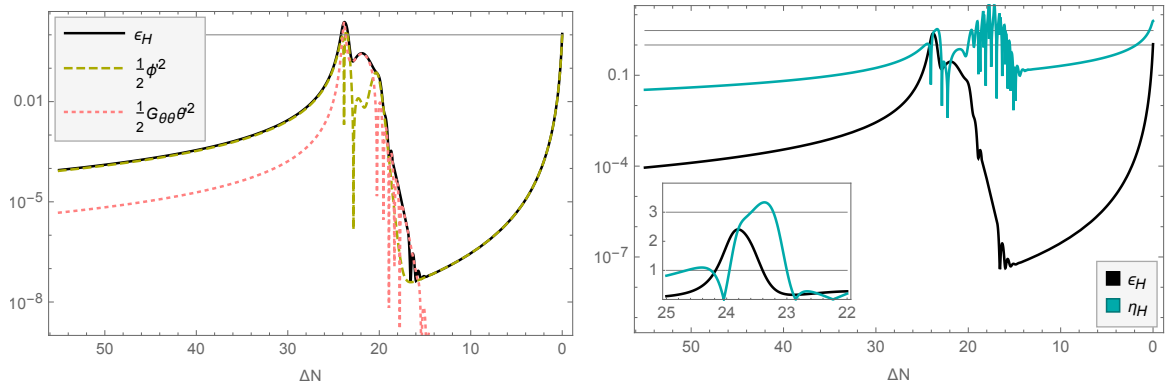

Figure 6.15: *Left panel:* slow-roll parameter ϵ_H (black line), decomposed into two parts coming from the kinetic energy of the radial (green-dashed line) and angular (pink-dotted line) fields. The horizontal grey line corresponds to 1. *Right panel:* ϵ_H (black line) and $|\eta_H|$ (blue line). The horizontal grey lines highlight the values 1 and 3 respectively. Both panels show the model $\{\alpha = 0.1, \phi_{\rm infl} = 0.542, \gamma = 10\}$ with $\theta_{\rm in} = 7\pi/10$.

the single-field case, inflation is made up of two slow-roll phases driven by ϕ, separated by an intermediate phase with rapidly decreasing ϵ_H. The transition between the two slow-roll solutions is an effect of the destabilisation induced in the background trajectory by the hyperbolic geometry of field space, see the discussion in section 2.4.

In the right panel of figure 6.15 the second slow-roll parameter, η_H defined in (2.16), is plotted against ΔN together with ϵ_H. The first and last phases of inflationary evolution are distinguished by slow roll where $\epsilon_H \ll |\eta_H|$, with an intermediate interval in which slow roll is violated, $|\eta_H| \gtrsim 1$. In particular, $|\eta_H| \simeq 3$, signals a very brief (less than 1 e-fold) ultra-slow-roll phase, as shown in the inset plot. In this example the first slow-roll parameter, ϵ_H, also briefly exceeds unity, signalling that inflation is interrupted (also for less than one e-fold) about this point, sometimes referred to as "punctuated" inflation [334, 335].

From the results above it is clear that the potential (6.58) can produce a rich background evolution whose properties depend on the initial condition $\theta_{\rm in}$. Although we selected $\theta_{\rm in} = 7\pi/10$ as an example, each case will be different, e.g., not all $\theta_{\rm in}$ would produce $|\eta_H| \gtrsim 3$.

As reviewed in section 2.4, a strong turn in field space ($\eta_\perp \gg 1$) and/or a highly curved field space ($\mathscr{R}_{\rm fs} \ll -1$) can lead to a situation in which enhanced isocurvature perturbations source the curvature fluctuation, with the coupling between them set by the bending parameter, $\eta_\perp$, see (2.137). In the top panel of figure 6.16 we represent the evolution of the absolute value of $\eta_\perp$ for the same model considered above, $\{\alpha = 0.1, \phi_{\rm infl} = 0.542, \gamma = 10, \theta_{\rm in} = 7\pi/10\}$, together with $\phi(N)$ and $\theta(N)$. In the first slow-roll phase, when

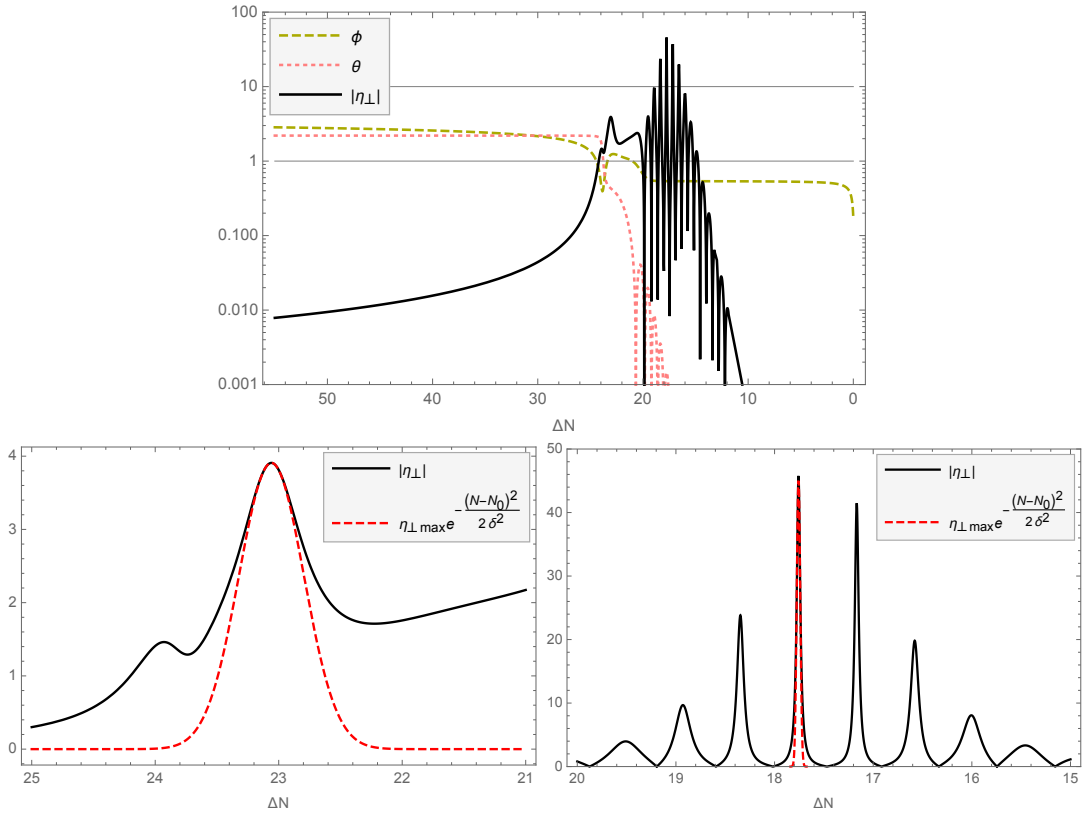

Figure 6.16: Evolution of the absolute value of the turn rate, $|\eta_\perp|$, with respect to ΔN (black line), shown together with the field values, ϕ (green-dashed line) and θ (pink-dotted line), for the model $\{\alpha = 0.1, \phi_{\rm infl} = 0.542, \gamma = 10\}$ and $\theta_{\rm in} = 7\pi/10$. The two thin horizontal lines highlight the values 1 and 10. The bottom panels show blow-ups of the behaviour of $|\eta_\perp|$ in restricted ranges of ΔN. The red-dashed lines show a Gaussian fit to the evolution about the maxima, see eq.(6.61).

θ is effectively frozen, $\eta_\perp \ll 1$. When θ is released and starts evolving, $\eta_\perp$ becomes $\mathcal{O}(1)$, signalling a turning trajectory. In order to compare with the results previously presented, e.g., in [117, 121], we fit the shape of $\eta_\perp$ around the peak with the Gaussian profile

$$\eta_\perp(N) = \eta_{\perp,\max}\, e^{-\frac{(N-N_0)^2}{2\delta^2}}\,, \tag{6.61}$$

where $\delta^2 \ll 1$ signals sharp turns in field space. In the bottom-left panel of figure 6.16 we zoom in on the first localised peak of $\eta_\perp$ and plot it together with the Gaussian profile in (6.61) described by $(\eta_{\perp,\max} = 3.9, N_0 = 23, \delta^2 = 0.07)$. The (sharp) bending is not as large as considered, e.g., in [117] for producing PBHs. During the subsequent field evolution, the oscillations that the field θ performs around its minimum are reflected in oscillations of $\eta_\perp$, signalling a series of turns. We zoom into $20 \leq \Delta N \leq 15$ in the bottom-right panel of figure 6.16, where we fit the peak with largest amplitude with the Gaussian profile

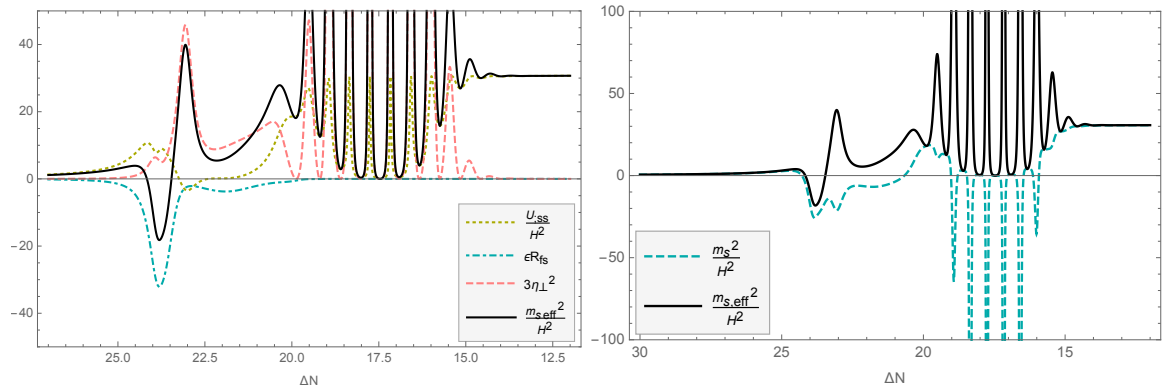

Figure 6.17: Evolution of the effective squared-mass of the isocuvature perturbation together with its contributions (left) and comparison with the squared-mass (right) for the model $\{\alpha = 0.1, \phi_{\rm infl} = 0.542, \gamma = 10\}$ and $\theta_{\rm in} = 7\pi/10$.

(6.61) and parameters ($\eta_{\perp,\rm max} = 45, N_0 = 17.7, \delta^2 = 0.0003$). Again, these turns in field space are strong and sharp.

The behaviour of the isocurvature perturbation is determined by its squared-mass (2.143) and its super-horizon effective squared-mass (2.146). We display ${m_{s,\rm eff}}^2/H^2$ in the left panel of figure 6.17. Around 24 e-folds before the end of inflation the super-horizon effective squared-mass turns negative, signalling a destabilisation of the background trajectory, and a transient instability of the isocurvature perturbation for the super-horizon modes. The plot displays several coloured lines accounting for the different components of ${m_{s,\rm eff}}^2/H^2$, see (2.146). In particular, it is the geometrical contribution $\epsilon_1 \mathscr{R}_{\rm fs}$ that causes the squared-mass to become negative, along the lines of what was investigated in [105, 112, 113] (see also [4]). In the right panel we plot ${m_s}^2/H^2$ and ${m_{s,\rm eff}}^2/H^2$ together. The difference between the squared-mass and the effective squared-mass is due to the contribution from the turn rate, which adds a negative contribution $(-\eta_\perp^2)$ to ${m_s}^2/H^2$, and a positive contribution $(+3\eta_\perp^2)$ to ${m_{s,\rm eff}}^2/H^2$ on super-horizon scales. The negative contributions from the geometry and the strong turn drive ${m_s}^2/H^2$ to negative values, signalling a tachyonic growth of the isocurvature perturbations.

We numerically evaluate the resulting scalar power spectrum, $P_\zeta(k)$, for this model using the *mTransport* Mathematica code provided in [336], with $\Delta N_{\rm CMB} = 55$. In figure 6.18 we represent the power spectrum, $P_\zeta(k)/P_0$, normalised at $k_{\rm CMB} = 0.05\,{\rm Mpc}^{-1}$ where $P_0 = 2.1 \times 10^{-9}$. As expected, on small scales the power spectrum grows due to the transient instability of the isocurvature perturbation, displaying a local peak around $10^{12}\,{\rm Mpc}^{-1}$. In this example the growth is very limited and it does not lead to an overall enhancement with respect to the power spectrum on CMB scales. In terms of the charac-

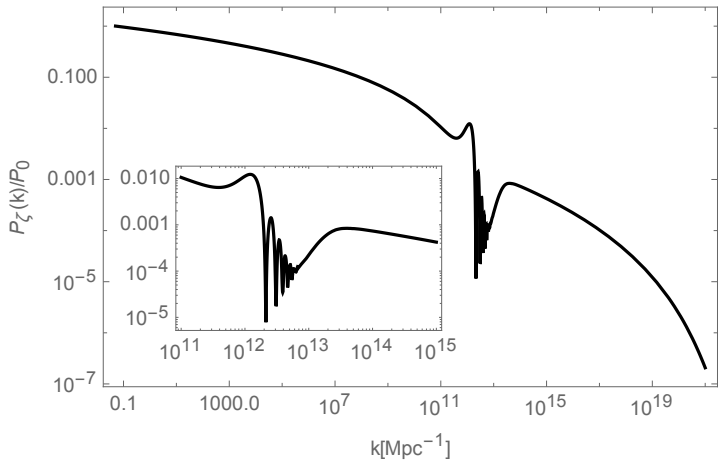

Figure 6.18: Normalised scalar power spectrum, $P(k)/P_0$, for the model described by $\{\alpha = 0.1, \phi_{\rm infl} = 0.542, \gamma = 10\}$ and initial condition $\theta_{\rm in} = 7\pi/10$. Here $P_0 = 2.1 \times 10^{-9}$.

teristics of the localised turn in field space, i.e., its maximum amplitude, $\eta_{\perp,\max}$, and its duration, δ, the overall amplification of $P_\zeta(k)/P_0$ following a strong turn is roughly given by the factor $e^{\eta_\perp \delta}$ [121]. In this case, for the first local peak of the bending parameter this factor is only ~ 2.8, which is consistent with the limited growth that we see.

The sharp turn in the field-space trajectory happening around $\Delta N = 23$ (see the bottom-left panel of figure 6.16) results in an oscillatory pattern in $P_\zeta(k)$ shown in figure 6.18, which is magnified in the inset plot. The decrease in $\epsilon_H(N)$ about the inflection point (see figure 6.15) explains the subsequent local maximum in $P_\zeta(k)$, around $k = 3 \times 10^{13}\,\mathrm{Mpc}^{-1}$. Although the subsequent evolution displays many sharp turns in field space (as shown in the bottom-right panel in figure 6.16) as θ oscillates about its minimum, the resulting features in the scalar power spectrum are suppressed relative to the first peak. Eventually the evolution returns to slow-roll, as seen on scales $k \gtrsim 10^{14}\,\mathrm{Mpc}^{-1}$, and the power spectrum gradually decreases as $\epsilon_H(N)$ grows.

In figure 6.19 we show $P_\zeta(k)/P_0$ resulting from the potential (6.58) with the same model parameters $\{\alpha = 0.1, \phi_{\rm infl} = 0.542, \gamma = 10\}$ but different choices of the initial condition $\theta_{\rm in}$. Each initial condition leads to a different outcome and with this choice of parameters the largest enhancement is produced with $\theta_{\rm in} = \pi/4$. Despite the rich and diverse behaviour, one can see that, for the model with $\alpha = 0.1$, none of the cases considered here can produce a significant amplification of the scalar power spectrum on small scales above the power on CMB scales.

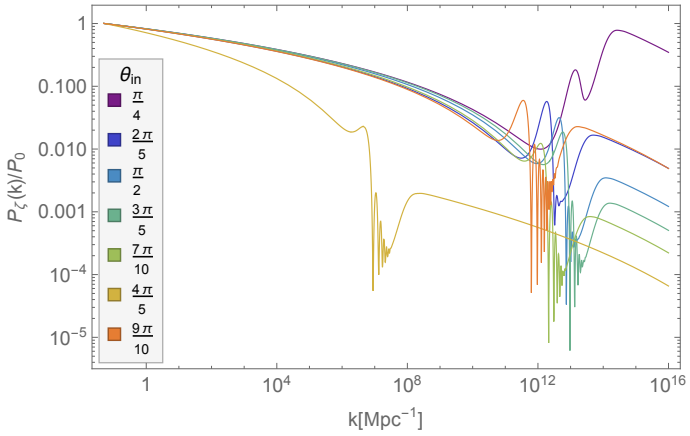

Figure 6.19: Normalised primordial scalar power spectrum for the potential (6.58) with $\{\alpha = 0.1, \phi_{\rm infl} = 0.542, \gamma = 10\}$ and different initial conditions $\theta_{\rm in}$. Here $P_0 = 2.1 \times 10^{-9}$.

6.4.3 Changing the hyperbolic field-space curvature

In the previous section we considered the dynamics for $\alpha = 0.1$. In order to investigate the role of the field-space curvature we consider now models with $\alpha = 0.01$ and $\alpha = 0.005$, which correspond to $\mathscr{R}_{\rm fs} \simeq -133.3$ and $\mathscr{R}_{\rm fs} \simeq -266.6$ respectively. We study a fixed initial angular direction, $\theta_{\rm in} = 7\pi/10$, and we also fix $\gamma = 10$ to facilitate the comparison. For each α, we select the value of $\phi_{\rm infl}$ in such a way that the power spectrum starts to grow roughly at the same comoving scale k. In particular, we study three different configurations of the potential (6.58), corresponding to

$$\begin{aligned}
&\text{model}_1 \rightarrow \{\alpha = 0.1, \phi_{\rm infl} = 0.5417\},\\
&\text{model}_2 \rightarrow \{\alpha = 0.01, \phi_{\rm infl} = 0.19\},\\
&\text{model}_3 \rightarrow \{\alpha = 0.005, \phi_{\rm infl} = 0.103\}\,.
\end{aligned}$$

In the following, we identify each model by the corresponding value of α.

We obtain the background trajectories by numerically solving eqs.(6.45)–(6.47) and represent them in the left panel of figure 6.20. We parametrise the trajectories in a slightly different fashion with respect to what was done previously, e.g. in figure 6.13, by plotting $\{\phi(N)\cos\theta(N), \phi(N)\sin\theta(N)\}$ in the last 55 e-folds of inflation, while in the right panel we display the evolution of ϵ_H against ΔN.

Cases with $\alpha = \{0.01, 0.005\}$ clearly differ with respect to the evolution for $\alpha = 0.1$. The two models with smaller α are characterised by a transient phase of angular inflation, which is defined as a regime in which the field's motion is mostly along the angular direction, with $\phi'(N)$ suppressed [305]. We show in figure 6.21 the terms contributing to

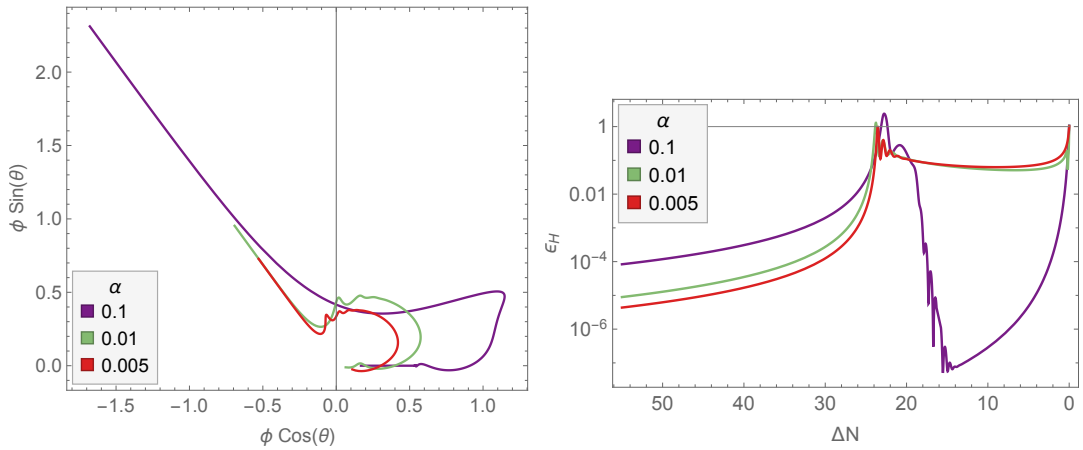

Figure 6.20: Numerical background evolution for three models with different values for the curvature of the hyperbolic field space, parameterised by α. *Left panel*: background trajectories $\{\phi(N)\cos\theta(N), \phi(N)\sin\theta(N)\}$. *Right panel:* evolution of ϵ_H with respect to ΔN.

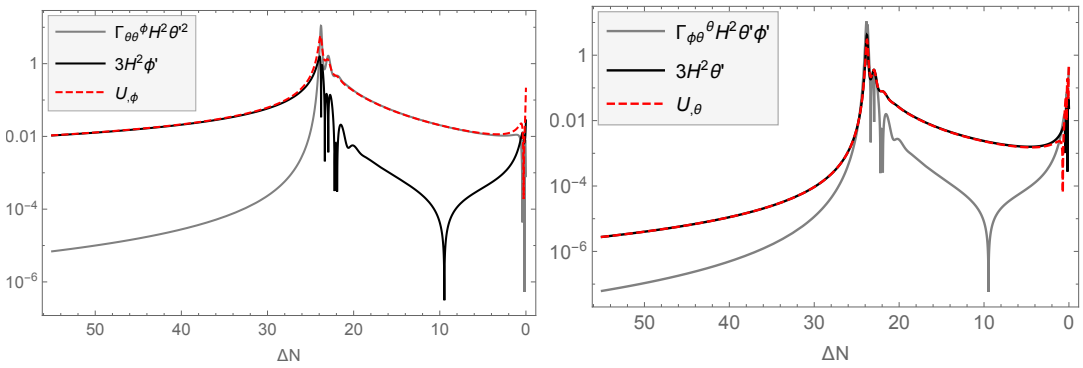

Figure 6.21: Terms contributing to the equations of motion (6.46) and (6.47) for the radial field, ϕ (left panel), and angular field, θ (right panel), obtained numerically for the model $\{\alpha = 0.01, \phi_{\rm infl} = 0.19, \gamma = 10\}$ and $\theta_{\rm in} = 7\pi/10$.

the equations of motion for ϕ and θ, eqs.(6.46) and (6.47), for the model with $\alpha = 0.01$. Only the models with $\alpha = \{0.01, 0.005\}$ lead to a phase of angular inflation as these values correspond to a large field-space curvature $\mathscr{R}_{\rm fs}$, which destabilises the background trajectory into the new attractor solution. During angular inflation, the geometry of the field space pushes the radial field towards the larger volume in field space at the boundary of the Poincaré disc [305]. The radial field remains approximately constant while the potential gradient is balanced against the geometrical effect, and the angular field slow rolls, see figure 6.21.

Another effect of having small α is that the dynamics at the inflection point is changed in the presence of a phase of angular inflation. We clarify this by plotting the

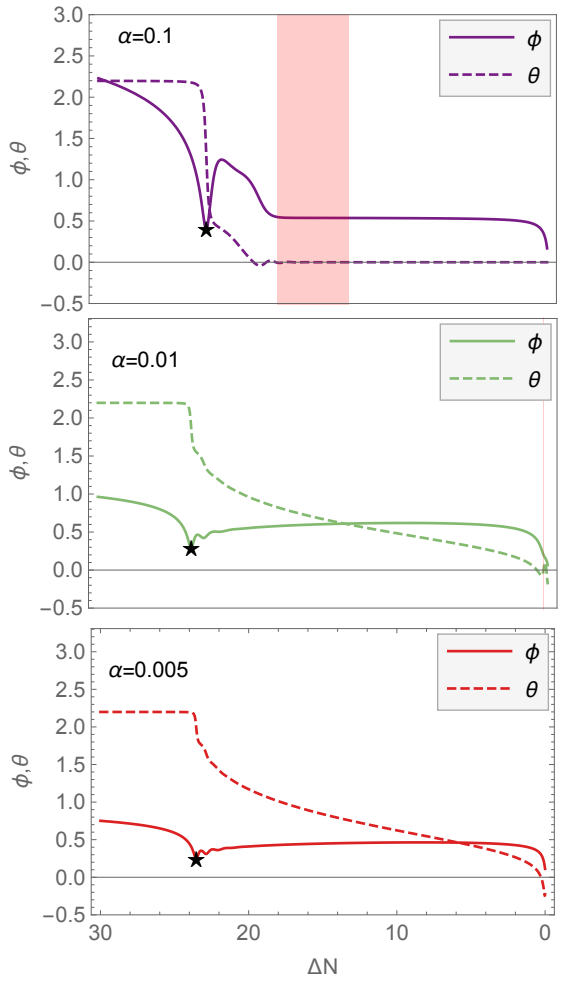

Figure 6.22: Evolution of the radial (continuous line) and angular (dashed line) fields against ΔN in the last 30 e-folds of inflation, with each panel corresponding to one of the models discussed, see the value of α in the top-left label. The black star signals the moment when the radial field is equal to the field-space curvature length, $\phi = \sqrt{3\alpha/2}$. The red area highlights when the radial field is within 1% of the inflection point, $\left|\left(\phi - \phi_{\rm infl}\right)\Big/\phi_{\rm infl}\right| \leq 0.01$. The persistence at the inflection point is quite extended for the model with $\alpha = 0.1$, rather short for $\alpha = 0.01$ (see the vertical, thin, red line in the central panel, close to the end of inflation), while inflation ends before ϕ reaches the inflection point in the model with $\alpha = 0.005$.

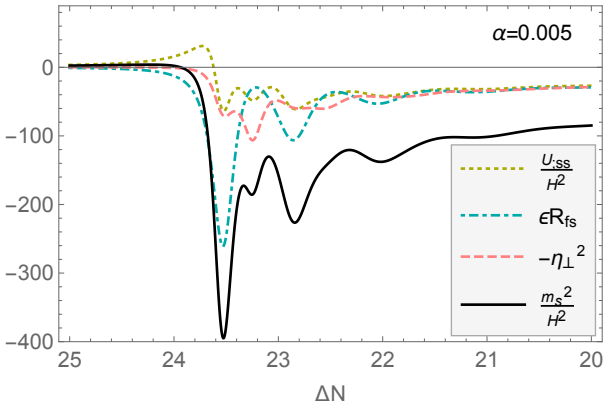

Figure 6.23: Evolution of the squared-mass of the isocurvature perturbation (black line) for the model with $\alpha = 0.005$, displayed together with its three components given in eq.(2.143).

fields evolution against ΔN in the last 30 e-folds of inflation in figure 6.22, where each panel corresponds to one of the models discussed. While for $\alpha = 0.1$ the radial field gets bounced back only transiently and then is able to settle around the inflection point (see the red area), when α is smaller the fields undergo a phase of angular inflation and ϕ is kept away from the inflection point. As displayed in the middle panel, for $\alpha = 0.01$ right before the end of inflation ϕ crosses the inflection point (see the vertical, thin, red line) and a consequent slight change in its velocity can be seen from the plot. Instead, for the smallest α considered, $\alpha = 0.005$, inflation ends before the radial field is able to cross the inflection point. In other words, the effect of the inflection point is washed out from the evolution of ϕ for small α. Nevertheless, given our parameterisation of the potential, the value of $\phi_{\rm infl}$ still has an effect on the large scales observables, as discussed in section 6.4.4, even in cases where inflation ends before the radial field is able to cross the inflection point. This is because $\phi_{\rm infl}$, together with the parameter γ, governs the mass of the angular field θ, as discussed in appendix F. Because of this $\phi_{\rm infl}$ determines the position of the transition between the first and second phases of inflationary evolution, which in turn affects the predictions for large-scales observables.

In figure 6.23 the squared-mass of the isocurvature perturbation is displayed for the model with $\alpha = 0.005$, together with its three component parts given in eq.(2.143). The figure shows how the first negative peak in ${m_s}^2/H^2$ is mainly driven by the geometrical component, $\epsilon_1 \mathscr{R}_{\rm fs}$.

In the top-left panel of figure 6.24 we show the evolution of the squared-mass of the isocurvature perturbation, eq.(2.143), for the three different values of α. As shown in figure 6.23, the first negative peak in each case is driven by the geometrical contribution

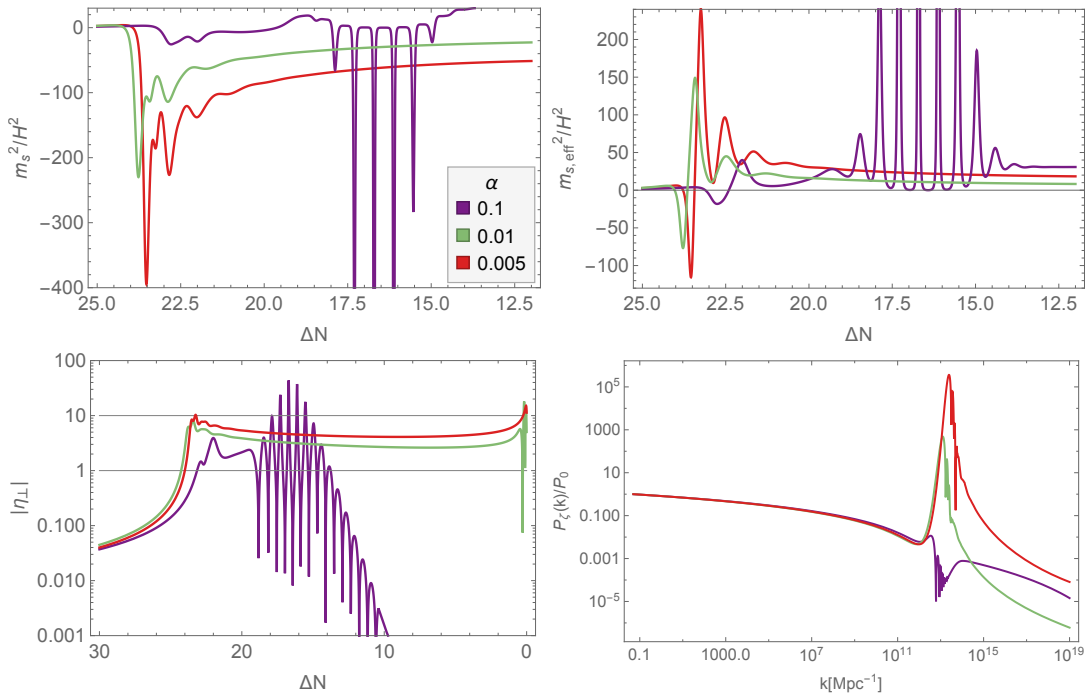

Figure 6.24: Evolution of the squared-mass (2.143) (top-left panel) and super-horizon squared-mass (2.146) (top-right panel) of the isocurvature perturbation, together with the magnitude of the bending parameter (2.137) (bottom-left panel) and numerical scalar power spectrum (bottom-right panel) obtained for the models with different α. In the bottom-right panel $P_0 = 2.1 \times 10^{-9}$. The legend is the same in each plot, see the top-left panel.

$\epsilon_1 \mathscr{R}_{\text{fs}}$, with $\mathscr{R}_{\text{fs}}$ inversely proportional to α. For smaller α the geometrical contribution to ${m_s}^2/H^2$ is boosted, which explains why ${m_s}^2/H^2$ shows a larger negative profile with decreasing α. This has a clear consequence for the curvature perturbations as well; we expect a larger enhancement for smaller α, as long as the background trajectory is turning, $\eta_\perp \neq 0$, which is the case for the models shown, see the bottom-left panel in the same figure. The top-right panel shows the evolution of the super-horizon effective squared-mass for the isocurvature modes, eq.(2.146), over the same range of ΔN as in the top-left panel. The bending parameter contributes positively in this case, explaining the difference between the squared-mass and the super-horizon effective squared-mass. Finally, in the bottom-right panel we show the normalised power spectra $P_\zeta(k)/P_0$ for the three cases, obtained numerically with a modified version of the *mTransport* code [336], where $\Delta N_{\text{CMB}} = 55$ and $P_0 = 2.1 \times 10^{-9}$. The numerical results confirm what was anticipated from the behaviour of ${m_s}^2/H^2$. The field space with the largest curvature considered, corresponding to $\alpha = 0.005$, leads to a five orders of magnitude enhancement

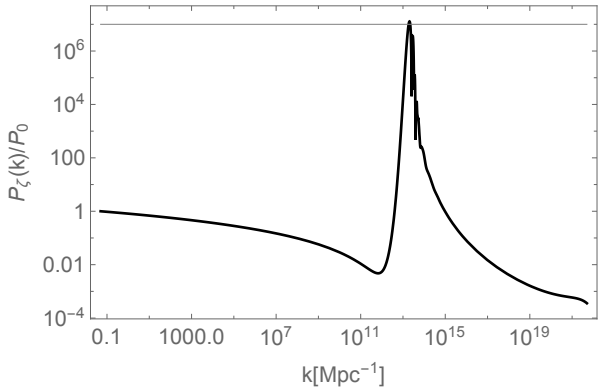

Figure 6.25: Normalised primordial scalar power spectrum for the potential (6.58) with $\{\alpha = 0.0035, \phi_{\rm infl} = 0.077, \gamma = 10, \theta_{\rm in} = 7\pi/10\}$. Here $P_0 = 2.1 \times 10^{-9}$.

in the power spectrum with respect to CMB scales. Further decreasing α could lead to even larger enhancements, even the seven orders of magnitude required to possibly produce PBHs. As an example, we display in figure 6.25 the normalised scalar power spectrum, $P_\zeta(k)/P_0$, obtained for the potential (6.58) with parameters $\{\alpha = 0.0035, \phi_{\rm infl} = 0.077, \gamma = 10, \theta_{\rm in} = 7\pi/10\}$.

6.4.4 Robustness of single-field predictions

We have explored multi-field effects in the presence of an inflection point in the context of α–attractor models of inflation[9] and seen that these models display a rich phenomenology. Depending on the initial condition, $\theta_{\rm in}$, and on the curvature of the hyperbolic field space, the power spectrum, $P_\zeta(k)$, can be significantly enhanced on small scales. We now assess what phenomenology is possible in models which are consistent with large-scale CMB observations, specifically of the spectral tilt, n_s, and the running of the spectral index, α_s.

The multi-field potential (6.58) is parametrised by $\{\alpha, \phi_{\rm infl}, \gamma\}$. We will fix $\alpha = 0.005$ and $\gamma = 10$, and study the effect of varying the position of the inflection point, $\phi_{\rm infl}$, which determines the scale at which the peak in the power spectrum is located and therefore also affects the CMB observables on large scales. We also fix the initial condition $\theta_{\rm in} = 7\pi/10$, which together with $\alpha = 0.005$, implies that the scalar power spectrum can be amplified on small scales by roughly five orders of magnitude, as discussed in section 6.4.3.

[9] See [337, 338] for a different multi-field set-up featuring a near-inflection point in the potential.

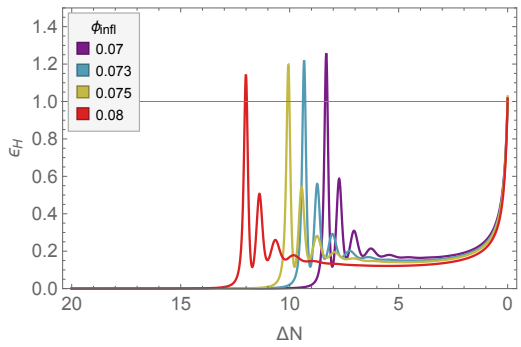

Figure 6.26: Evolution of $\epsilon_H(N)$ plotted against $\Delta N \equiv N_{\text{end}} - N$ in the last 20 e-folds of inflation. These results have been obtained numerically for multi-field models with $\{\alpha = 0.005, \gamma = 10\}$ and different positions for the inflection point, ϕ_{infl}.

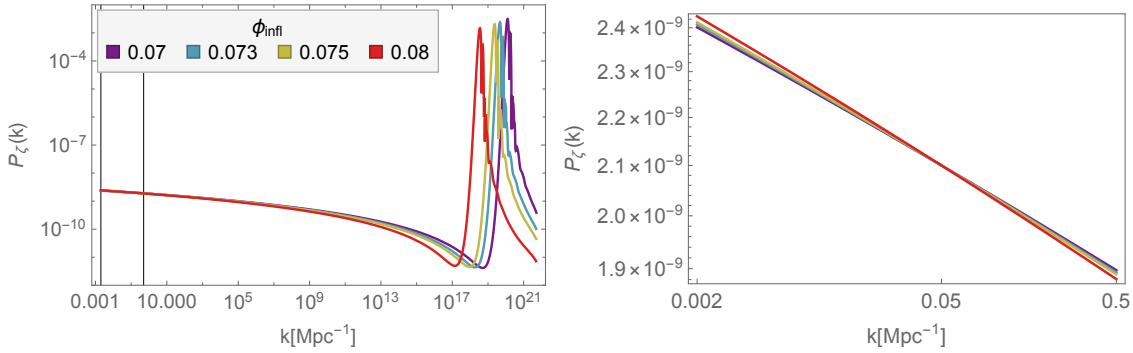

Figure 6.27: *Left panel:* numerically determined power spectrum, $P_\zeta(k)$, for multi-field models with $\{\alpha = 0.005, \gamma = 10\}$ and different ϕ_{infl}. The two vertical lines correspond to $k = \{0.002\,\text{Mpc}^{-1}, 0.5\,\text{Mpc}^{-1}\}$ and highlight the CMB scales. *Right panel:* zoomed-in plot of the power spectrum on CMB scales. The spectral tilt of $P_\zeta(k)$ is slightly different for each model.

We show in figure 6.26 the evolution of $\epsilon_H(N)$ against ΔN in the last 20 e-folds of inflationary evolution for $\phi_{\text{infl}} = \{0.07, 0.073, 0.075, 0.08\}$. Slow roll is violated close to the end of inflation in each model and this transition moves closer and closer to the end of inflation for smaller ϕ_{infl}. Also, after the angular field starts evolving and $\epsilon_H(N)$ peaks, each model displays a transient phase of angular inflation [305], as expected given the small value of α (large field-space curvature) in these cases.

We numerically evaluate $P_\zeta(k)$ with a modified version of *mTransport* [336] and represent the results in the left panel of figure 6.27. Equation (3.1)[10] allows us to estimate ΔN_{CMB}. On large scales the power spectrum is almost scale-invariant, while at higher frequencies it is enhanced due to multi-field effects and k_{peak} varies depending on the value of ϕ_{infl}, moving towards smaller scales with decreasing ϕ_{infl}. The amplitude of

[10]For simplicity we assume here instant reheating, $\rho_{\text{th}} = \rho_{\text{end}}$.

$\phi_{\rm infl}$	$\Delta N_{\rm CMB}$	$\Delta N_{\rm CMB} - \Delta N_{\rm peak}$	$k_{\rm peak}/{\rm Mpc}^{-1}$	n_s	$r_{0.002}$	α_s
0.07	55.1927	50.32	1.25×10^{20}	0.9569	2.6×10^{-5}	-0.00092
0.073	55.2318	49.28	4.6×10^{19}	0.9560	2.7×10^{-5}	-0.00096
0.075	55.2593	48.56	2.3×10^{19}	0.9554	2.8×10^{-5}	-0.00099
0.08	55.3201	46.59	3.4×10^{18}	0.9534	3×10^{-5}	-0.0011

Table 6.3: Details of multi-field models with $\{\alpha = 0.005, \gamma = 10\}$ and different $\phi_{\rm infl}$. For all models the fitted cubic and quartic coefficients are $\mathcal{O}(10^{-5})$ and $\mathcal{O}(10^{-6})$ respectively.

the peak is slightly different among the models, which can be explained in light of the fact that the first negative peak in the squared-mass of the iscocurvature perturbation is driven by the geometrical contribution $\epsilon_1 \mathcal{R}_{\rm fs}$, see eq.(2.143), as shown in figure 6.23 for a model with $\{\alpha = 0.005, \gamma = 10, \phi_{\rm infl} = 0.103, \theta_{\rm in} = 7\pi/10\}$. As seen in figure 6.26, ϵ_H peaks at higher values for decreasing $\phi_{\rm infl}$, which means in turn that the negative peak in ${m_s}^2/H^2$ is larger in magnitude for smaller $\phi_{\rm infl}$ (for fixed field-space curvature), explaining why the highest peak in P_ζ is reached for the smallest $\phi_{\rm infl}$.

In the right panel of figure 6.27, we zoom in on the large-scale behaviour of $P_\zeta(k)$, which shows how the presence of a peak on small scales affects the large-scale observables, in particular the tilt of the power spectrum. We list in table 6.3 key quantities obtained for each of the models considered. We show the predicted values for the spectral tilt, n_s, and running, α_s, obtained at $k_{\rm CMB} = 0.05\,{\rm Mpc}^{-1}$ by fitting the numerical results for $\ln\left(P_\zeta(k)\right)$ with a quartic function[11] of $\ln(k/k_{\rm CMB})$ on scales $0.002\,{\rm Mpc}^{-1} < k < 0.5\,{\rm Mpc}^{-1}$. The predicted values for the tensor-to-scalar ratio are calculated at $k = 0.002\,{\rm Mpc}^{-1}$ using the single-field slow-roll approximation on large scales, (2.87). For all models $r_{0.002}$ is well below the current upper bound (3.6).

In analogy with the analysis performed for the single-field inflection-point model, we can compare the CMB observables listed in table 6.3 with the modified universal predictions for n_s (6.18), $r_{\rm CMB}$ (6.19) and α_s versus n_s (6.25). In the left panel of figure 6.28 we plot eq.(6.18) together with coloured points representing numerical results $\left(\Delta N_{\rm CMB} - \Delta N_{\rm peak}, n_s\right)$ for each model considered. Similarly, the right panel shows eq.(6.19) with $\alpha = 0.005$ together with coloured points representing the numerical results $\left(\Delta N_{\rm CMB} - \Delta N_{\rm peak}, r_{\rm CMB}\right)$. We do not explicitly show the results for α_s versus $\Delta N_{\rm CMB} - \Delta N_{\rm peak}$ as the comparison between the universal prediction (6.24) and the numerical results is qualitatively the same as for the tilt n_s. Instead, we show α_s versus n_s in figure 6.29, alongside the α–attractors consistency relation (6.25).

As for the single-field case, the modified universal predictions describe well the

[11] We find that residual noise is minimised when we fit a polynomial that is quartic in $\ln(k/k_{\rm CMB})$.

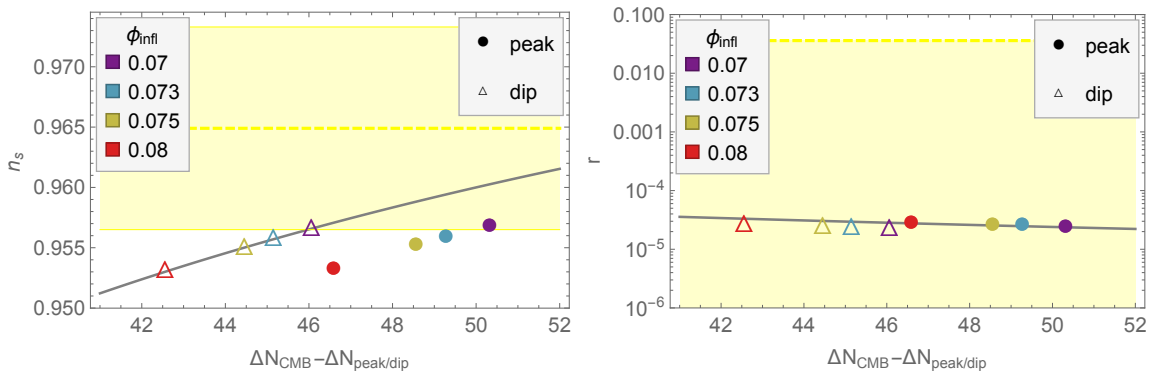

Figure 6.28: *Left panel:* the modified universal prediction for n_s (6.18) is plotted in grey together with numerical results obtained from multi-field models with $\{\alpha = 0.005, \gamma = 10\}$ and different $\phi_{\rm infl}$, as shown in the legend. In particular, coloured points represent numerical results for n_s against $\Delta N_{\rm CMB} - \Delta N_{\rm peak}$. The empty triangles represent instead the numerical tilt n_s against $\Delta N_{\rm CMB} - \Delta N_{\rm dip}$, i.e., the scale of the dip in $P_\zeta(k)$ is taken as a reference instead of $k_{\rm peak}$. The yellow-shaded area highlights the *Planck* 95 % C.L. region, see (3.5). *Right panel:* the approximation (6.19) with $\alpha = 0.005$ is plotted in grey together with the numerical results for the tensor-to-scalar ratio against $\Delta N_{\rm CMB} - \Delta N_{\rm peak}$ (coloured points) and $\Delta N_{\rm CMB} - \Delta N_{\rm dip}$ (empty triangles). Each colour is associated with a specific $\phi_{\rm infl}$, as detailed in the legend. The yellow-shaded area represents the 95 % C.L. region from the bound on $r_{\rm CMB}$ (3.6).

numerical results, with a small offset for the case of the tilt n_s and its running α_s. The match between the modified universal predictions and the numerical results can be further improved by substituting $\Delta N_{\rm CMB} - \Delta N_{\rm peak} \to \Delta N_{\rm CMB} - \Delta N_{\rm dip}$ or, in other words, by taking as a reference the scale associated with the local minimum in the power spectrum, $k_{\rm dip}$, instead of its local maximum, $k_{\rm peak}$. We demonstrate this in figure 6.28 by including the numerical results for n_s and $r_{\rm CMB}$ represented with empty triangles against $\Delta N_{\rm CMB} - \Delta N_{\rm dip}$. By comparing triangles and circles (of the same colour) with the grey lines, one can see that the CMB observables (especially n_s) can be described even better by the position of the dip in $P_\zeta(k)$. However, it is the peak in $P_\zeta(k)$ that could have potentially observable consequences, such as PBH production and second-order GW generation. Therefore we focus on the consequences of the modified universal predictions for $k_{\rm peak} > k_{\rm dip}$ when it comes to exploring the phenomenology. The numerical results for the tilt and its running are well described by the α–attractors consistency relation (6.25), as shown in figure 6.29. As for the single-field case, models which are compatible with the bound on the spectral index (3.3) predict α_s about one order of magnitude smaller than the current observational uncertainty in (3.4). We therefore compare the model predictions with the CMB constraints for the ΛCDM model, in particular with the lower

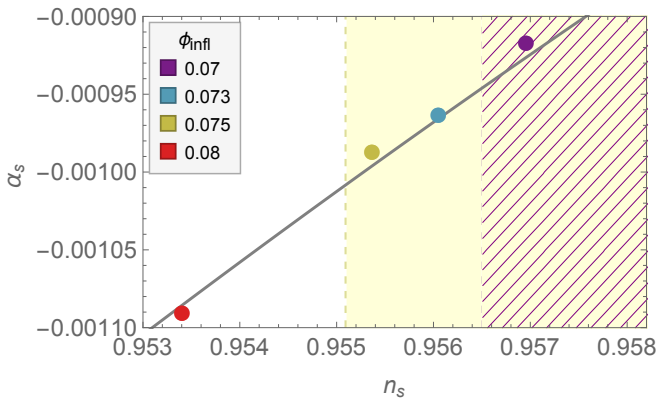

Figure 6.29: The α–attractors consistency relation (6.25) is plotted in grey together with the numerical results for the tilt and its running for multi-field models with $\{\alpha = 0.005, \gamma = 10\}$ and different position of the inflection point $\phi_{\rm infl}$, as detailed in the legend. The yellow region highlights part of the 95 % C.L. region when *Planck* data are compared with the ΛCDM + $r_{\rm CMB}$ + α_s model, (3.3), while the purple hatch-shaded area represents the lower 95 % C.L. region of n_s for the ΛCDM model instead. The range of α_s shown is within the observational bound (3.4).

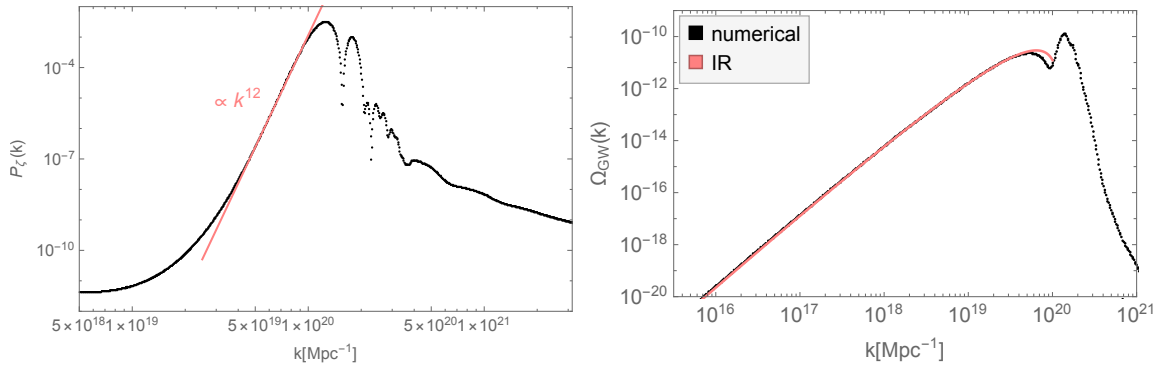

Figure 6.30: *Left panel:* numerical results of $P_\zeta(k)$ for the multi-field model with parameters $\{\alpha = 0.005, \gamma = 10, \phi_{\rm infl} = 0.07\}$ and initial condition $\theta_{\rm in} = 7\pi/10$. We display the results in the region of the peak, with the pink line representing the scaling of the infrared tail of it. *Right panel:* numerical results for the second-order GWs produced during radiation domination by the enhanced scalar perturbations whose power spectrum is displayed in the left panel. The pink line is obtained using eq.(5.16) of [214] with $n_{\rm IR} = 12$ and $n_{\rm UV} \to \infty$ and well approximates the spectral shape of the infrared tail of the numerical $\Omega_{\rm GW}(k)$.

bound on n_s given in eq.(6.16) in the absence of running. Given the numerical results for n_s this implies that only configurations with $\phi_{\rm infl} \lesssim 0.7$ are consistent with the CMB observations and the peak is located on scales $k_{\rm peak} \gtrsim 10^{20}\,{\rm Mpc}^{-1}$.

In the left panel of figure 6.30 we display the numerical results for the scalar power spectrum in the region around the peak, for a model which is compatible with large-scale

(CMB) measurements of n_s, $\phi_{\rm infl} = 0.07$. The pink line shows the scaling of the IR tail of the peak, $n_{\rm IR} \simeq 12$, which by far exceeds the limits on the growth of the power spectrum possible in single-field models [120, 339, 340]. In [117–119] it has been shown that multi-field models with strong turns in field space evade the single-field bound on the growth of P_ζ, and we demonstrate here that the same holds when the growth of the curvature perturbation is also due to the strong curvature of the hyperbolic field space.

The peak in the scalar power spectrum displays a series of peaks which is due to the strong and sharp turn in field space characterising the background evolution, see e.g., the bottom-left panel of figure 6.16 for a model with $\{\alpha = 0.1, \gamma = 10, \phi_{\rm infl} = 0.542\}$. In [121] it is shown that a strong and sharp turn can lead to an exponentially enhanced amplitude of P_ζ, with an oscillatory modulation. In particular, in [117, 121] the bending parameter $\eta_\perp$ is modelled with a Gaussian profile, see eq.(6.61), and the Hubble rate is assumed to be smooth and slowly-varying. The multi-field models discussed here are characterised by a more complicated background evolution, see e.g., $\epsilon_H(N)$ in figure 6.26, and a profile for the bending parameter which can only be partially described by a Gaussian function, see e.g., figure 6.16. It is therefore not surprising that the oscillations in P_ζ displayed in figure 6.30 cannot simply be identified as either sharp or resonant features [123, 341–343], but are instead more of a combination of the two, similar to models discussed e.g., in [119].

In the right panel of figure 6.30 we represent the numerical results for the second-order GWs produced by the enhanced scalar fluctuations after horizon re-entry during radiation domination. In particular, we display $\Omega_{\rm GW}(k)$ as numerically calculated using eq.(3.19) and the scalar power spectrum displayed in the left panel of the same figure. The sharpness of the peak of P_ζ (see the purple line in the left panel of figure 6.27) results in a two-peak structure for $\Omega_{\rm GW}(k)$, with a broader and smaller peak followed by a dip and a narrower principal peak located approximately at the scale $2/\sqrt{3}\, k_{\rm peak}$, see section 3.5.2. The oscillatory modulation of the scalar power spectrum due to the sharp turn in the background trajectory is imprinted in $\Omega_{\rm GW}(k)$ as an oscillatory pattern modulating the principal peak. The IR tail of the signal can be understood in terms of the IR and UV scaling of P_ζ around the first peak; substituting the values $n_{\rm IR} = 12$ and $n_{\rm UV} \to \infty$ into eq.(5.12) of [214], we get the pink line shown on top of the numerical results. The UV tail of $\Omega_{\rm GW}(k)$ (and P_ζ) displays a more complicated scaling, which cannot be understood in terms of such a simple approximation.

In figure 6.31 the numerical results for $\Omega_{\rm GW}(k)$ are plotted together with the sensitivity curves of upcoming space- and Earth-based GW observatories. The amplitude of

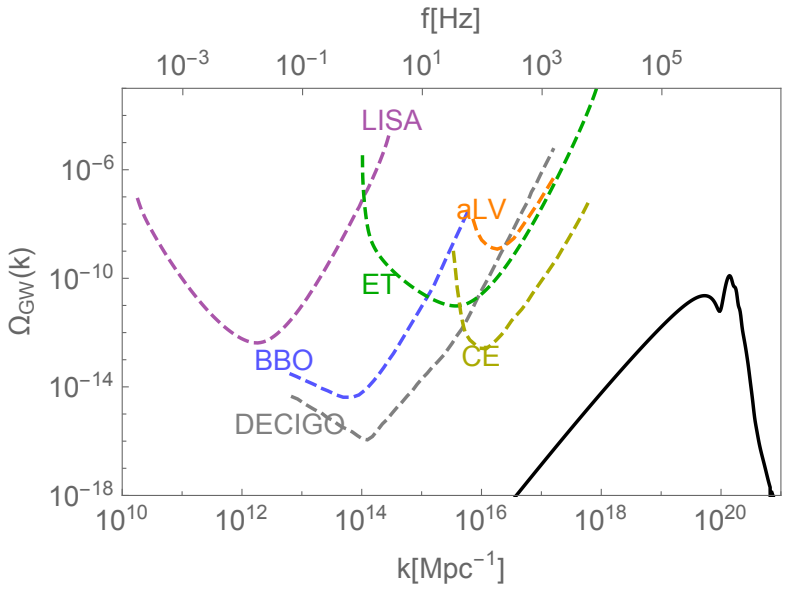

Figure 6.31: Numerical results for the second-order GWs produced within the multi-field model with parameters $\{\alpha = 0.005, \gamma = 10, \phi_{\rm infl} = 0.07\}$ and initial condition $\theta_{\rm in} = 7\pi/10$.

the GW signal is determined by the amplitude of the peak of the scalar power spectrum, which in turn mainly depends on the curvature of the hyperbolic field space, set by the parameter α, and the initial condition for the angular field, $\theta_{\rm in}$. In particular, after fixing all the other model parameters, reducing α enhances $P_\zeta(k_{\rm peak})$ and therefore the amplitude of the principal peak of $\Omega_{\rm GW}(k)$. Our numerical results show that the multi-field model described by $\{\alpha = 0.005, \gamma = 10, \phi_{\rm infl} = 0.07, \theta_{\rm in} = 7\pi/10\}$ produces $\Omega_{\rm GW} \simeq 10^{-10}$ at its peak.

The position of the principal peak in $\Omega_{\rm GW}(k)$ is set by the position of the largest peak in P_ζ, which is the first peak displayed in the left panel of figure 6.30. For models which are not[12] in tension with the large-scale measurements of n_s, the second-order GW principal peak is located at $f_{\rm peak} \gtrsim 50\,{\rm kHz}$, which is obtained by substituting the lower bound (6.23) in the position of the principal peak, $2/\sqrt{3}\,k_{\rm peak}$, and is consistent with our numerical results. Given that the modified universal predictions (in particular, the one for n_s (6.18)) hold also for the multi-field inflection-point potential, the considerations for PBH production discussed in section 6.3.2 for the single-field case apply also for the multi-field extension.

In summary, compatibility with the CMB observations of n_s place the peak of the

[12] As an example, for the principal peak of the second-order GWs to be located at LISA (LIGO) scales, the resulting large-scale spectral tilt is $n_s \simeq 0.9344$ ($n_s \simeq 0.9496$), well below the lower 95% measurement (6.16).

second-order GWs beyond the reach of current and upcoming GW observatories both for the single- and multi-field inflection-point potentials considered in this work, as well as bounding the mass of the PBHs that could possibly be produced to values $M_{\rm PBH} < 10^8\,{\rm g}$, which make the PBHs too light to constitute candidates for dark matter in the Universe today.

6.5 Discussion

In this work we explore the phenomenology of cosmological α–attractor models featuring an inflection point in the potential for scalar fields evolving in a hyperbolic field space. We consider both single-field examples and multi-field dynamics.

In all cases we show that the primordial perturbations generated on large (CMB) scales can be described by a simple modification of the universal predictions of α–attractors for the scalar spectral index, eq.(6.18), and the tensor-to-scalar ratio, eq.(6.19). A shift in the universal predictions was previously noted by [89] for the single-field inflection-point α–attractor potential, and also in a different context by [304]. This universal behaviour leads to a consistency condition relating the scalar spectral tilt and its running, eq.(6.25). A consequence of the tight bounds on the scalar spectral index from CMB observations is that the running of the spectral index must be small, and any deviations from the standard single-field α–attractor dynamics is constrained to lie close to the end of inflation. Hence any enhancement in the primordial power spectrum, P_ζ, is only allowed on small comoving scales, $k_{\rm peak} \gtrsim 5 \times 10^{18}\,{\rm Mpc}^{-1}$. By adopting the tight observational bounds on the spectral index obtained from CMB observations, in the absence of any running of the spectral index, eq.(6.16), which we emphasise is constrained by the consistency relation (6.25), we obtain a stronger constraints on the scale of the peak of P_ζ in comparison to the previous work of Dalianis *et al.* [89].

The lower bound on the comoving wavenumber, $k_{\rm peak}$, implies that any primordial black holes resulting from enhanced density perturbations on small scales can only be produced with masses $M_{\rm PBH} \lesssim 10^8\,{\rm g}$. These PBHs have long since evaporated by the present time so do not constitute a candidate for dark matter. Nonetheless they could yet leave interesting signatures if stable Planck mass relics are left behind [321–323], or resulting from an early black-hole-dominated era [313, 315–318].

Similarly the lower bound on $k_{\rm peak}$ also has implications for the induced gravitational waves produced at second order in perturbation theory after inflation, see eq.(3.19). The peak of the GW signal is constrained to be at very high frequencies, $f_{\rm peak} \gtrsim 50\,{\rm kHz}$, well

beyond the reach of current Earth-based or future space-based GW detectors. Rather they could provide a target for future ultra-high frequency detectors discussed in [344].

A key parameter for the inflationary dynamics is the curvature of the hyperbolic field space, $\mathscr{R}_{\rm fs} \equiv -4/(3\alpha)$. In single-field models the small-scale P_ζ is enhanced by the presence of the inflection point in the potential, leading to a phase of ultra-slow-roll dynamics. The effect of α is primarily to set the relative amplitude of the tensor modes with respect to scalar perturbations at CMB scales, see eq.(6.19). In multi-field embeddings a far richer dynamical behaviour is possible. We have seen that a large and negative curvature, $\alpha \ll 1$, can cause a geometrical instability in the inflationary trajectory, as previously studied in [105, 112]. A strongly-curved field space could also be accompanied by strongly non-geodesic motion and a tachyonic instability in the isocurvature perturbation, which gets transferred to the curvature fluctuation, potentially leading to a small-scale growth of the scalar power spectrum [4, 117, 173]. For these reasons we choose to focus on models characterised by $\alpha \ll 1$, see also [305]. The behaviour we see in this case differs from that seen in other multi-field α–attractor models studied, for example, in [303] where the authors consider a potential monotonic in the radial direction, with field-space curvature $\alpha = 1/3$. In that case the single-field predictions, eqs.(6.6) and (6.7), were found to be stable even in presence of a light angular direction. Here we introduce both a feature in the radial potential (the inflection point) and consider larger curvature ($\alpha \ll 1$), both of which amplify the geometrical destabilisation of the background trajectory, breaking the slow-roll and slow-turn approximations. While the radial field at early times follows the standard evolution close to the boundary of the Poincaré disc ($r \to 1$), the dynamics of the angular field then leads to a second distinct phase of inflation at late times. Nonetheless on large scales CMB observables can still be explained by means of a simple modification of the standard universal predictions of single-field α–attractors, see eqs.(6.18) and (6.19).

We find marked differences in the spectral shape of the scalar power spectrum found in the single- and multi-field cases. In the single-field case the peak in P_ζ is broad ($n_{\rm IR} \simeq 3.4, n_{\rm UV} \simeq -4$), while in the multi-field case it is narrower, with a much steeper infrared growth ($n_{\rm IR} \simeq 12$), and oscillations following the principal peak. Figure 6.32 shows a comparison of the scalar power spectra obtained in a single- and a multi-field inflection-point model. Multi-field effects can explain the oscillatory behaviour of the green line after the peak, caused by a sharp and strong turn in field space, providing an explicit realisation of the mechanism discussed in [121, 124] (see also [119]). The differences in the spectral shape seen in figure 6.32 can be traced back to the mechanisms

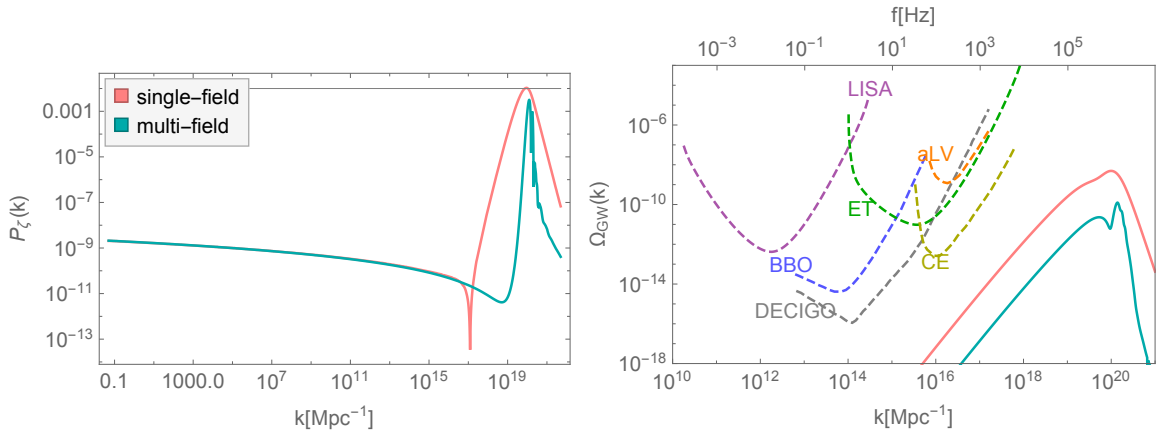

Figure 6.32: *Left panel:* numerical results of $P_\zeta(k)$ for a single-field inflection-point model, eq.(6.15), with parameters $\{\alpha = 0.1, \phi_{\rm infl} = 0.5, \xi = 0.0035108\}$ (pink line) and for a multi-field model, eq.(6.58), with parameters $\{\alpha = 0.005, \gamma = 10, \phi_{\rm infl} = 0.07\}$ and initial condition $\theta_{\rm in} = 7\pi/10$ (green line). These models predict $n_s = 0.9568$ and $n_s = 0.9569$ respectively and are both compatible with the CMB lower bound on n_s, (6.16). *Right panel:* numerical results for the second-order GWs produced during radiation domination by the enhanced scalar perturbations whose power spectra are displayed in the left panel, together with the sensitivity curves of current and upcoming GW observatories. The colour legend is the same as on the left.

that lead to the fluctuation enhancement in the two cases. More than being specific to the single- and multi-field potentials, they are linked to the η_H evolution across and after the ultra-slow roll phase in the single-field case and the geometric destabilisation at play in the multi-field setup.

The differences in the spectral shape of the peak in P_ζ are reflected in the power spectrum of the induced GWs, as shown in the right panel of figure 6.32. In particular, the narrower, oscillatory peak in the multi-field P_ζ leads to second-order GWs with a two-peak structure and an oscillatory modulation of the second (principal) peak, see the green line in the right panel of figure 6.32. In the single-field set-up, the two-peak structure is almost wiped out as a consequence of the broadness of the scalar power spectrum peak and the oscillations are absent, see the pink line in the right panel of figure 6.32.

CHAPTER 7

CONCLUSIONS

In this thesis we have studied models of inflation beyond single-field slow roll and explored ways of testing the extra particle content on small scales, especially considering their effects in the gravitational wave sector.

In chapter 4 we examined the case of light spin-2 fields non-minimally coupled with the inflaton. We described them within an effective field theory approach and found that, upon allowing time-dependent sound speed for the helicity-2 component, the spin-2 field can deliver blue-tilted GWs, growing towards interferometer scales. After ruling out a considerable region of the effective theory parameter space by using current bounds on the scalar and tensor sectors and by requiring that the dynamics does not run into a gradient instability, we have singled out the regions of parameter space which can be potentially constrained in the future by LISA.

As well as sourcing the tensor power spectrum, the helicity-2 component of the light spin-2 fields also mediates the tensor bispectrum. We studied the properties of this signal in chapter 5, and investigated its shape and amplitude in the squeezed and equilateral limit. We found that the mediated bispectrum interpolates between the local and equilateral configurations depending on the mass of the spin-2 particle. Since a direct detection of the tensor bispectrum on small scales is in general not expected, we explored ways of testing the ultra-squeezed limit of the bispectrum through the anisotropies induced by the long tensor mode on the short-scale GWs power spectrum. We provided two examples, exploring the ability of LISA and SKA to indirectly test ultra-squeezed non-Gaussianities from light spin-2 fields.

In chapter 6 we worked in the framework of cosmological α–attractors and considered the effect of an additional field in the scalar sector. These models include a radial and an angular field, living on a hyperbolic field space whose curvature is set by the parameter α. We focused on the case of strongly curved field spaces, $\alpha \ll 1$, and considered both single- and multi-field potentials endowed with an inflection point. We explored values of the model parameters leading to large scalar fluctuations on small scales. In the single-field set-up, ultra-slow-roll dynamics at the inflection point is responsible for the growth of the scalar perturbations, while in the multi-field case geometrical effects related to the field-space curvature are at play. We found that the predicted values of the large-scale observables are well described by modified versions of the universal predictions for α–attractors, both in the single- and multi-field cases. Enhanced scalar power spectra can lead to the formation of primordial black holes and generation of GWs at second-order in perturbation theory which are potentially detectable on small scales. We explored the small-scale phenomenology of these models and connected it with the modified universal predictions on large scales. We found that current measurements of the scalar spectral tilt constrain the masses of the PBHs produced to be very small, $M \lesssim 10^8\,\mathrm{g}$, and the peak of the second-order GWs to be at very high frequencies, $f \gtrsim 10\,\mathrm{kHz}$.

Our work shows how the future detection (and characterisation) of a cosmological background of GWs on small scales could shed light on the inflationary particle zoo.

As a consequence of the results described above, many future work directions are worth pursuing. In the following we discuss the most relevant ones.

The effective field theory formalism [98] we have employed in chapters 4 and 5 is the ideal framework to extend the analysis to different and additional particle content, including higher-spin fields. Also, while the effective field theory approach allows us to survey all the possible observational signatures associated with extra fields, it would be interesting to explore the parameter space of a full Lagrangian formulation, similarly to what was done, for example, in [245, 247].

While in chapter 6 we worked under the assumption of Gaussian scalar fluctuations when exploring the small-scale phenomenology of a class of α–attractors, a strong enhancement of the scalar perturbations is expected to be associated with significant non-Gaussianity. This can have an important impact on both the production of PBHs [90, 196, 345–356] and induced second-order GWs [214, 326, 335, 357–360]. It would be interesting to explore the scalar non-Gaussianities produced in these models, e.g. using the publicly available numerical codes [361–363], and understand their possible effects on the small-scale phenomenology.

The enhancement of the scalar power spectrum from multi-field effects discussed in chapter 6 does not rely on the presence of an inflection point. We have seen that in some cases where the enhancement is significant the fields do not meet the inflection point during their evolution. While the position of the inflection point, $\phi_{\rm infl}$, still has an effect on the large-scale predictions, this is due to the fact that $\phi_{\rm infl}$, together with the parameter γ in the multi-field potential (6.58), sets the mass of the angular field, as discussed in appendix F. This has very important consequences in widening the applicability of the results of chapter 6. We are currently exploring the wider parameter space of the multi-field α–attractor model of [303], in the limit of strongly-curved field spaces. We are studying potentials which include a term explicitly breaking the rotational symmetry, but are featureless in the radial direction. Our analysis is aimed at exploring the phenomenology ensuing from different areas of the parameter space, including the possibility of having large scalar perturbations on small scales.

While performing the numerical analysis of the single-field α–attractor models of chapter 6, we noticed that the number of e-folds elapsed between the horizon crossing of the CMB scale and the end of inflation, $\Delta N_{\rm CMB}$, calculated assuming instant reheating, depends (logarithmically) on the value of α, see e.g. table 6.2. This implies that not only the tensor-to-scalar ratio, but also the scalar spectral tilt predicted within these models is sensitive to the value of α, see e.g. the related work [364]. We are currently working to understand the full dependence of the observables on α, as well as quantifying constraints on the models parameter space from future CMB surveys [143, 147].

We believe that tests of cosmological inflation are one of the most promising ways for us to understand physics at high energies. We have made progress in illustrating the potential of small-scale GWs to test the inflationary field content beyond the simplest single-field models. The advent of a network of GWs detectors, which will be able to probe different frequency ranges, makes the future of early-universe physics very exciting.

APPENDIX A

RESULTS FOR THE $s_{EQ}(\nu)$ AND $s_{SQ}(\nu)$ COMPUTATIONS

While in section 5.2 our main focus was on the bispectrum mediated by spin-2 light fields with $\nu = 1.4$, we report here some of our findings for the numerical computation of $s_{eq}(\nu)$ and $s_{sq}(\nu)$ for the mass values $\nu = \{0.4, 0.8, 1.1, 1.48\}$. The

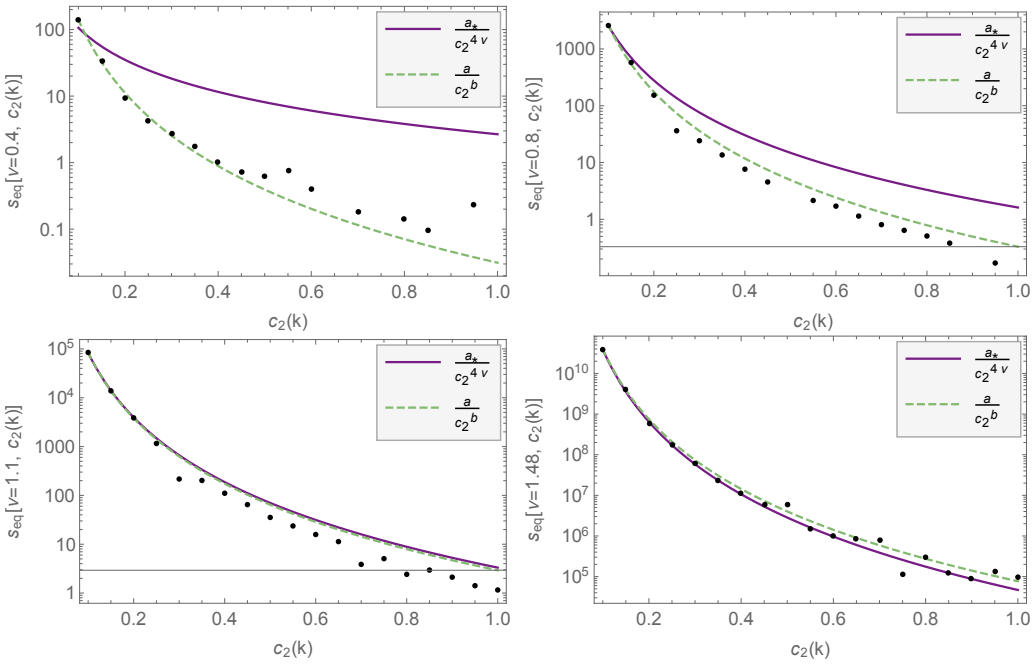

Figure A.1: Numerical results and fitting functions of $s_{eq}[\nu, c_2(k)]$ for $\nu = \{0.4, 0.8, 1.1, 1.48\}$. The plot corresponding to $\nu = 1.4$ can be found in the left panel of figure 5.3.

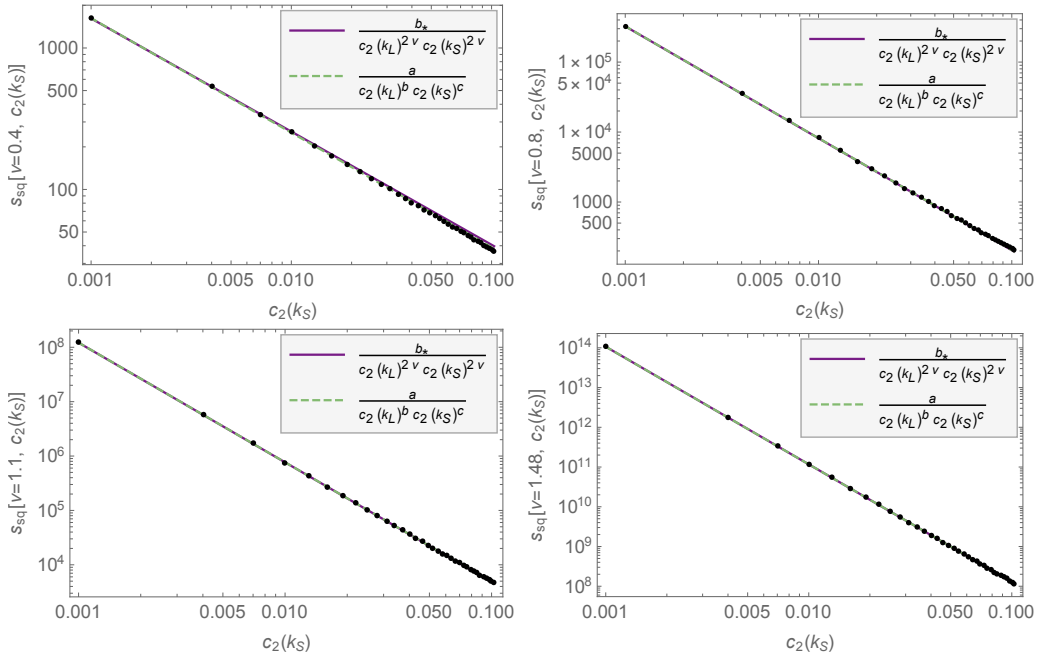

Figure A.2: Numerical results and fitting functions of $s_{\rm sq}[\nu, c_2(k_L), c_2(k_S)]$ for $\nu = \{0.4, 0.8, 1.1, 1.48\}$. In each plot, the sound speed on large scales has been fixed, $c_2(k_L) = 0.346$. The plot corresponding to $\nu = 1.4$ can be found in the left panel of figure 5.6.

results in the equilateral and squeezed configurations are displayed in figures A.1 and A.2 respectively. In particular, for each case analysed we fit the numerical values with the power law in eqs.(5.15) and (5.20) for the equilateral and squeezed configurations respectively. The fitting functions are plotted with a purple line, while the numerical results are represented with black dots. For completeness, we include also a fit with generic power laws, i.e. leaving the power of $c_2(k)$ free,

$$s_{\rm eq}[\nu, c_2(k)] = \frac{a}{c_2(k)^b}\,, \tag{A.1}$$

$$s_{\rm sq}[\nu, c_2(k_L), c_2(k_S)] = \frac{a}{c_2(k_L)^b c_2(k_S)^c}\,, \tag{A.2}$$

which are plotted in figures A.1 and A.2 with a green-dashed line.

The fitting functions with ν fixed, see eqs.(5.15) and (5.20), work better and better towards smaller values of the spin-2 mass ($\nu \to 3/2$). In the equilateral configuration, the overlap is slightly worse for heavier masses ($\nu \to 0$). This must be considered in light of the fact that numerical results for small ν should not be used for strict quantitative conclusions, as already pointed out in [286]. In table A.1, we list the fitted values of $a_\star$ and $b_\star$, defined in eqs.(5.15) and (5.20) respectively.

ν	m/H	$a_\star$	$b_\star$
0.4	1.44	2.7	2.8
0.8	1.27	1.6	0.9
1.1	1.02	3.3	2.9
1.4	0.54	324.4	482.8
1.48	0.24	46 876.3	19 545.5

Table A.1: Values of the fit parameters $a_\star$ and $b_\star$, see eqs.(5.15) and (5.20) respectively, obtained for different mass values, $\nu \equiv \sqrt{9/4 - (m/H)^2}$.

APPENDIX B

ADDITIONAL DETAILS ON THE SQUEEZED BISPECTRUM

We report here on the squeezed bispectrum computation, see chapter 5, showing how eq.(5.18) has been obtained, and why the leading contributions come from the A and B terms as spelled out in eqs.(5.10)-(5.11), whereas the other permutations and the C term (5.12) are subleading.

Let us start with the A term (5.10), and take the squeezed limit $k_3 \equiv k_L \ll k_1 \sim k_2 \equiv k_S$. For practical purposes, let us consider the large scale to be around the CMB scales, $k_L \sim 10^{-2}\,\mathrm{Mpc}^{-1}$, and the small scale to be located, for example, at LISA scales, $k_S \sim 10^{12}\,\mathrm{Mpc}^{-1}$. Upon the change of variable $y_4 \equiv (k_L/k_S)\,x_4$, eq.(5.10) can be rewritten as

(B.1)

$$\mathcal{M}_A(\nu, k_S, k_L) = \left(\frac{k_S}{k_L}\right)^{1/2} \int_{-\infty}^{0} dx_1 \int_{-\infty}^{x_1} dx_2 \int_{-\infty}^{x_2} dx_3 \int_{-\infty}^{k_L/k_S\, x_3} dy_4 \sqrt{\frac{x_2}{x_1 x_3 y_4}}\, \sin(-x_1)$$
$$\Im\left[H_\nu^{(1)}(-c_2(k_S)x_1)\, H_\nu^{(2)}(-c_2(k_S)x_2)\right]\, \Im\left[\mathrm{e}^{-iy_4} H_\nu^{(1)}(-c_2(k_L)y_4)\, H_\nu^{(2)}\left(-c_2(k_L)\frac{k_L}{k_S}x_2\right)\right]$$
$$\Im\left[\mathrm{e}^{ix_3} H_\nu^{(1)}(-c_2(k_S)x_2)\, H_\nu^{(2)}(-c_2(k_S)x_3)\right] .$$

The Hankel function in the last line, $H_\nu^{(2)}(-c_2(k_S)x_3)$, oscillates and, as a result, suppresses the integral for $c_2(k_S)|x_3| \gg 1$. On small scales the sound speed is of order 10^{-3}, see the left panel of figure 5.1, therefore only values $|x_3| \ll 10^3$ are relevant for the integral computation. As a consequence, the upper limit of the integral in y_4 is effectively zero for the reference scales considered.

Inspecting the Hankel function $H_\nu^{(1)}(-c_2(k_S)x_2)$, one can infer that only values $|x_2| \ll 10^3$ contribute to the integral. In addition, on large scales the sound speed is $c_2(k_L) \simeq 0.1$, see the right panel of figure 5.1, so the argument of the Hankel function $H_\nu^{(2)}(-c_2(k_L)k_L/k_S\, x_2)$ is very small, $\mathcal{O}(10^{-12})$. For this reason, we approximate the Hankel function in the small argument limit, $\lim_{x\to 0} H_\nu^{(2)}(x) = i\, 2^\nu \Gamma(\nu) x^{-\nu}/\pi$. As a result of these approximations, eq.(B.1) reduces to

$$\begin{aligned}\mathcal{M}_A(\nu, k_S, k_L) = {} & \frac{2^\nu \Gamma(\nu)}{\pi\, c_2(k_L)^\nu}\left(\frac{k_S}{k_L}\right)^{1/2+\nu} \int_{-\infty}^{0} dx_1 \int_{-\infty}^{x_1} dx_2 \int_{-\infty}^{x_2} dx_3 \\ & \times (-x_2)^{1/2-\nu}(-x_1)^{-1/2}(-x_3)^{-1/2}\, \sin(-x_1)\, \Im\left[H_\nu^{(1)}(-c_2(k_S)x_1) H_\nu^{(2)}(-c_2(k_S)x_2)\right] \\ & \times \Im\left[e^{ix_3} H_\nu^{(1)}(-c_2(k_S)x_2) H_\nu^{(2)}(-c_2(k_S)x_3)\right] \\ & \times \int_{-\infty}^{0} dy_4 (-y_4)^{-1/2}\, \Re\left[e^{-iy_4} H_\nu^{(1)}(-c_2(k_L)y_4)\right] ,\end{aligned} \tag{B.2}$$

where $\Im[x]$ and $\Re[x]$ are the imaginary and real part of x respectively.

A similar analysis can be performed for the B term in eq.(5.11), yielding

$$\begin{aligned}\mathcal{M}_B(\nu, k_S, k_L) = {} & \frac{2^\nu \Gamma(\nu)}{\pi\, c_2(k_L)^\nu}\left(\frac{k_S}{k_L}\right)^{1/2+\nu} \int_{-\infty}^{0} dx_1 \int_{-\infty}^{x_1} dx_2 \int_{-\infty}^{x_2} dx_3 \\ & \times (-x_3)^{1/2-\nu}(-x_1)^{-1/2}(-x_2)^{-1/2}\, \sin(-x_1)\sin(-x_2) \\ & \times \Im\left[H_\nu^{(1)}(-c_2(k_S)x_3) H_\nu^{(1)}(-c_2(k_S)x_3) H_\nu^{(2)}(-c_2(k_S)x_1) H_\nu^{(2)}(-c_2(k_S)x_2)\right] \\ & \times \int_{-\infty}^{0} dy_4 (-y_4)^{-1/2}\, \Re\left[e^{-iy_4} H_\nu^{(1)}(-c_2(k_L)\, y_4)\right] .\end{aligned} \tag{B.3}$$

The sum of these two contributions results in eq.(5.18), where the overall explicit[1] scaling behavior is

$$\frac{1}{k_L^{9/2-\nu} k_S^{3/2+\nu}} . \tag{B.4}$$

We proceed in a similar fashion to study the squeezed limit of the C term, eq.(5.12), and all the permutations in eq.(5.9) (here we refer to the permutations $k_3 \leftrightarrow k_2$ and $k_3 \leftrightarrow k_1$, while $k_1 \leftrightarrow k_2$ contributes with a factor 2). The resulting scalings are listed in table B.1. The contribution of each term relative to the those spelled out in eqs.(B.2)-(B.3) is classified by looking at the ratio of the scaling with respect to that in (B.4). For

[1]Note that in eq.(5.19), as well as for each term in eq.(5.9), there is also an additional hidden scaling due to the scale dependence of the sound speed $c_2(k)$, see section 5.2. For completeness, we have explicitly numerically evaluated all the contributions in eq.(5.9) for masses $\nu = \{0.4, 0.8, 1.1, 1.4, 1.48\}$ with $\{c_{2\mathrm{i}} = 1, k_L = 0.05\,\mathrm{Mpc}^{-1}, k_S = 10^{12}\,\mathrm{Mpc}^{-1}\}$ and confirmed the conclusions described in the main text: looking at the explicit scaling of each term is enough to establish whether it contributes or not.

Term	Permutation	Scaling
A	as spelled in eq.(B.2)	$k_S^{-9/2+\nu} k_L^{-3/2-\nu}$
	$k_3 \leftrightarrow k_1$	k_S^{-6}
	$k_3 \leftrightarrow k_2$	$k_S^{-5} k_L^{-1}$ and $k_S^{-6+2\nu} k_L^{-2\nu}$
B	as spelled in eq.(B.3)	$k_S^{-9/2+\nu} k_L^{-3/2-\nu}$
	$k_3 \leftrightarrow k_1$	$k_S^{-6+2\nu} k_L^{-2\nu}$
	$k_3 \leftrightarrow k_2$	$k_S^{-6+2\nu} k_L^{-2\nu}$
C	as spelled in eq.(5.12)	$k_S^{-6+2\nu} k_L^{-2\nu}$
	$k_3 \leftrightarrow k_1$	$k_S^{-6+2\nu} k_L^{-2\nu}$
	$k_3 \leftrightarrow k_2$	$k_S^{-6+2\nu} k_L^{-2\nu}$

Table B.1: Scaling behavior of the different contributions. For A ($k_3 \leftrightarrow k_2$) the scaling is different depending on the value of the mass: the first one is valid for $\nu < 1/2$ and the second for $1/2 < \nu < 3/2$.

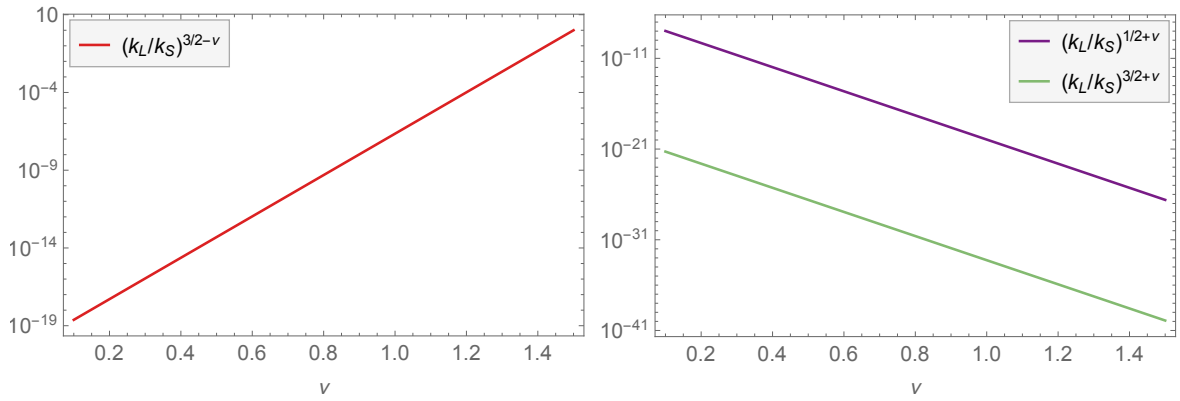

Figure B.1: Plots representing the functions in eqs.(B.5) (left) and (B.6)-(B.7) (right) with respect to the mass ν, with $k_S = 10^{12}\,\mathrm{Mpc}^{-1}$ and $k_L = 10^{-2}\,\mathrm{Mpc}^{-1}$.

$k_L = 0.05\,\mathrm{Mpc}^{-1}$ and $k_S = 10^{12}\,\mathrm{Mpc}^{-1}$, we plot on the left panel of figure B.1 the function

$$\frac{1}{k_S^{6-2\nu} k_L^{2\nu}} \Big/ \frac{1}{k_S^{9/2-\nu} k_L^{3/2+\nu}} = \left(\frac{k_L}{k_S}\right)^{3/2-\nu} \tag{B.5}$$

and on the right panel the functions

$$\frac{1}{k_S^{6}} \Big/ \frac{1}{k_S^{9/2-\nu} k_L^{3/2+\nu}} = \left(\frac{k_L}{k_S}\right)^{3/2+\nu} \tag{B.6}$$

$$\frac{1}{k_S^{5} k_L} \Big/ \frac{1}{k_S^{9/2-\nu} k_L^{3/2+\nu}} = \left(\frac{k_L}{k_S}\right)^{1/2+\nu} . \tag{B.7}$$

We conclude that the A term ($k_3 \leftrightarrow k_1$) is always subleading for all masses. For $\nu < 1/2$ also the $k_3 \leftrightarrow k_2$ permutation can be safely neglected. For $1/2 < \nu < 3/2$ the $k_3 \leftrightarrow k_2$ permutation of A can be safely neglected for most of the mass values, whereas must be considered for $\nu \to 3/2$ as the scaling is no more suppressed with respect to that in (B.4), see left panel figure B.1. The same consideration holds for $B(k_3 \leftrightarrow k_1)$, $B(k_3 \leftrightarrow k_2)$ and the C term.

APPENDIX C

UNIVERSALITY OF α–ATTRACTORS

Cosmological α–attractors correspond to a class of inflationary models which provide robust observational predictions despite having apparently different formulations (see [127] and references therein). In particular, the large-scale CMB spectral index and tensor-to-scalar ratio are given by eqs. (6.6) and (6.7) at leading order in the expansion in terms of $1/\Delta N_{\rm CMB}$. We review here how the α–attractor models form a universality class and derive the observables $(n_s,\, r_{\rm CMB},\, \alpha_s)$ for single-field α–attractor models given by a monomial potential in terms of the radial distance from the centre of the Poincaré disc (6.4)

$$V(\phi) = V_0 \tanh^p\left(\frac{\phi}{\sqrt{6\alpha}}\right). \tag{C.1}$$

In canonical single-field slow-roll inflation, $(n_s,\, r,\, \alpha_s)$ can be given in terms of potential slow-roll parameters as [365]

$$n_s = 1 - 6\epsilon_V + 2\eta_V\,,\quad r_{\rm CMB} = 16\epsilon_V\,,\quad \alpha_s = 16\epsilon_V\eta_V - 24{\epsilon_V}^2 - 2{\xi_V}^2\,, \tag{C.2}$$

where ϵ_V, η_V and ξ_V are expressed in terms of derivatives of the inflaton potential, see (2.15). Given the explicit form of the potential in eq. (C.1), it is possible to write these

potential slow-roll parameters in terms of ϕ,

$$\epsilon_V = \frac{p^2}{3\alpha}\operatorname{csch}^2\left(\frac{2\phi}{\sqrt{6\alpha}}\right), \tag{C.3}$$

$$\eta_V = \frac{2p}{3\alpha}\operatorname{csch}^2\left(\frac{2\phi}{\sqrt{6\alpha}}\right)\left(p - \cosh\left(\frac{2\phi}{\sqrt{6\alpha}}\right)\right), \tag{C.4}$$

$$\xi_V^2 = \frac{2p^2}{9\alpha^2}\operatorname{csch}^4\left(\frac{2\phi}{\sqrt{6\alpha}}\right)\left(3 + 2p^2 - 6p\operatorname{csch}\left(\frac{2\phi}{\sqrt{6\alpha}}\right) + \operatorname{csch}\left(\frac{4\phi}{\sqrt{6\alpha}}\right)\right). \tag{C.5}$$

Substituting the above into eq. (C.2) yields the large scales observables in terms of ϕ. They are evaluated when the CMB scales left the horizon, i.e., at $\phi = \phi_{\rm CMB}$. In order to do so, we use the inflaton equation of motion, eq. (2.14), which in the slow-roll approximation can be simplified to give

$$\frac{\mathrm{d}\phi}{\mathrm{d}N} \simeq -\frac{V_\phi}{V}\,. \tag{C.6}$$

Integrating the equation above yields the number of e-folds elapsed between the two field values $\phi_{\rm CMB}$ and $\phi_{\rm end}$,

$$\Delta N_{\rm CMB} \simeq \int_{\phi_{\rm end}}^{\phi_{\rm CMB}} \mathrm{d}\phi\, \frac{V}{V_\phi}\,. \tag{C.7}$$

Performing the integration above for the potential in eq. (C.1) yields

$$\Delta N_{\rm CMB} \simeq \frac{3\alpha}{2p}\left[\cosh\left(\frac{2\phi_{\rm CMB}}{\sqrt{6\alpha}}\right) - \cosh\left(\frac{2\phi_{\rm end}}{\sqrt{6\alpha}}\right)\right], \tag{C.8}$$

where the value of $\phi_{\rm end}$ is fixed by the condition $\epsilon(\phi_{\rm end}) = 1$, corresponding to

$$\sinh^2\left(\frac{2\phi_{\rm end}}{\sqrt{6\alpha}}\right) \simeq \frac{p^2}{3\alpha}\,. \tag{C.9}$$

Substituting eq. (C.9) into eq. (C.8) and expressing the equation in terms of $\phi_{\rm CMB}$ yields

$$\sinh^2\left(\frac{\phi_{\rm CMB}}{\sqrt{6\alpha}}\right) \simeq \frac{p\Delta N_{\rm CMB}}{3\alpha} + \frac{\sqrt{3\alpha + p^2}}{2\sqrt{3\alpha}} - \frac{1}{2}\,. \tag{C.10}$$

In this way the CMB observables in eq. (C.2) can be written as

(C.11)
$$n_s \simeq 1 - \frac{2\Delta N_{\rm CMB} + \sqrt{3\alpha(3\alpha+p^2)}\Big/ p + 3\alpha\Big/2}{\Delta N_{\rm CMB}^2 + \Delta N_{\rm CMB}\sqrt{3\alpha(3\alpha+p^2)}\Big/ p + 3\alpha\Big/4},$$

(C.12)
$$r_{\rm CMB} \simeq \frac{12\alpha}{\Delta N_{\rm CMB}^2 + \Delta N_{\rm CMB}\sqrt{3\alpha(3\alpha+p^2)}\Big/ p + 3\alpha\Big/4},$$

(C.13)
$$\alpha_s \simeq -8\frac{18\alpha^2 + p(3\alpha+4\Delta N_{\rm CMB})\sqrt{3\alpha(3\alpha+p^2)} + p^2\left[4\Delta N_{\rm CMB}^2 + 3\alpha(1+2\Delta N_{\rm CMB})\right]}{\left(3p\alpha + 4\Delta N_{\rm CMB}\sqrt{3\alpha(3\alpha+p^2)} + 4p\Delta N_{\rm CMB}^2\right)^2}.$$

In the large $\Delta N_{\rm CMB}$ expansion, these expressions reduce to eqs. (6.6) and (6.7) for the observables n_s and $r_{\rm CMB}$ respectively on large (CMB) scales, while we can relate the running of the spectral index to the spectral index itself

(C.14)
$$\alpha_s \approx -\frac{2}{\Delta N_{\rm CMB}^2} \approx -\frac{(n_s-1)^2}{2},$$

regardless of the parameters of V_0 and p appearing in the potential (C.1). The spectral index n_s and running α_s are dependent only on $\Delta N_{\rm CMB}$, while $r_{\rm CMB}$ depends only on $\Delta N_{\rm CMB}$ and α, such that

(C.15)
$$r_{\rm CMB} \approx 3\alpha(n_s-1)^2.$$

This is due to the potential (C.1) remaining finite at the boundary of the moduli space ($r \equiv \tanh\left(\phi/\sqrt{6\alpha}\right) \to 1$), which is a key feature of α–attractor models. The transformation to the canonical field ϕ (6.4), renders the potential a function of $\tanh\left(\phi/\sqrt{6\alpha}\right)$, which ensures the flatness of the potential for large field values ($\phi \to \infty$) and makes observational predictions on large scales approximately independent of the precise form of the function describing the potential dependence on $\tanh\left(\phi/\sqrt{6\alpha}\right)$.

APPENDIX D

NUMERICAL COMPUTATION OF THE SINGLE-FIELD SCALAR POWER SPECTRUM

In this appendix we present in detail how we compute the scalar power spectrum, $P_\zeta(k)$, for the single-field inflation models considered in section 6.2. Our procedure is closely related to similar strategies described in the literature, see for example [87, 91].

The inflaton potential in eq.(6.15) features an approximate stationary inflection point located at $\phi_{\rm infl}$ whose effect is to introduce a transient ultra-slow-roll phase. The slow-roll approximation breaks down and a full numerical analysis of the Mukhanov–Sasaki equation is needed. As an example, we refer to the power spectrum resulting from the specific model $\{\alpha = 0.1,\ \phi_{\rm infl} = 0.5,\ \xi = 0.0035108\}$, whose background evolution is displayed in figure 6.2. For illustrative purposes we consider here the case of instant reheating, which implies $\Delta N_{\rm CMB} \simeq 55$ (see table 6.1).

In the slow-roll approximation, valid on large scales, far from the inflection point, it is possible to estimate the scalar power spectrum using the expression for $P_\zeta(N)$ given in (2.69), by substituting in the background quantities $H(N)$ and $\epsilon_H(N)$. $P_\zeta(N)$ can be transformed into $P_\zeta(k)$ by means of eq.(6.21) for $k(N)$. We normalise the amplitude of the scalar power spectrum at $k_{\rm CMB} = 0.05\,{\rm Mpc}^{-1}$ by using the *Planck* 2018 measurement of $\mathscr{A}_s$ [67], see (3.2), which in turns identifies the amplitude of the potential as $V_0 = 7.7 \times 10^{-10}$. Eqs.(2.76), (2.77) and (2.87) predict for this configuration the large-scale

observables

$$n_s = 0.9569\,,\quad \alpha_s = -0.00092\,,\quad r_{0.002} = 4.956\times10^{-4}\,, \tag{D.1}$$

consistent with the latest *Planck* data release [67], see section 3.1, where the spectral tilt and its running are evaluated at $k_{\rm CMB}$.

While eq.(2.69) is reliable when the evolution is well described by slow roll, a full numerical analysis of the perturbations is necessary in order to compute the exact scalar power spectrum including non-slow-roll evolution, as occurs through the inflection point and approaching the end of inflation. The Mukhanov–Sasaki equation describes the evolution of the scalar curvature perturbation associated with the comoving wavenumber k, see eq.(2.52), which we rewrite here as [366]

$$v_k'' + (1-\epsilon_H)v_k' + \left[\frac{k^2}{a^2H^2} + (1+\epsilon_H-\eta_H)(\eta_H-2) - (\epsilon_H-\eta_H)'\right]v_k = 0\,, \tag{D.2}$$

where $' \equiv d/dN$ and the Hubble slow-roll parameters, ϵ_H and η_H, are defined in (2.18). We note that this equation does not assume slow roll.

We solve eq.(D.2) for modes ranging from $k_{\rm CMB} = 0.05\,{\rm Mpc}^{-1}$ to $k_{\rm end} = 2.6\times10^{22}\,{\rm Mpc}^{-1}$ and follow the evolution of v_k for each wavemode from the sub-horizon regime ($k \gg aH$, where canonical quantum commutation relations give the normalisation for the mode function, $|v_k^2| = 1/2k$, see eq.(2.64)) to super-horizon scales ($k \ll aH$). These solutions then enable us to calculate the scalar power spectrum on super-horizon scales, see eq.(2.69),

$$P_\zeta(k) = \frac{k^3}{2\pi^2}\left|\frac{v_k}{z}\right|^2, \tag{D.3}$$

where each mode is evaluated well after horizon crossing ($k \ll aH$), when $\zeta_k \equiv v_k/z$ approaches a constant value.

There are a few practical considerations regarding the strategy used to solve eq.(D.2):

- when numerically solving eq.(D.2), it is useful to express ϵ_H and η_H in terms of derivatives of the field $\phi(N)$, instead of using their definitions in terms of derivatives of $H(N)$. In particular, the relevant terms in eq.(D.2) reduce to [367]

$$1-\epsilon_H = 1-\frac{\phi'^2}{2}\,, \tag{D.4}$$

$$(1+\epsilon_H-\eta_H)(\eta_H-2) - (\epsilon_h-\eta_H)' = -2 - 3\frac{\phi''}{\phi'} - \frac{\phi'''}{\phi'} + \frac{\phi'^2}{2} + \frac{\phi'\phi''}{2}\,, \tag{D.5}$$

  see eqs.(2.20). Here the second and third derivatives of the field are given by the Klein–Gordon equation (2.14) for the field, re-written in terms of $\phi(N)$,

$$H^2\phi'' + HH'\phi' + 3H^2\phi' + V_\phi = 0\,, \tag{D.6}$$

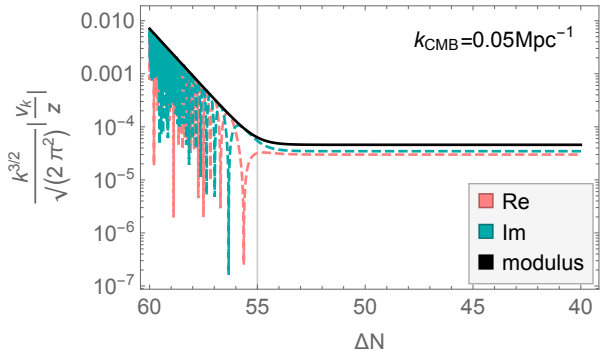

Figure D.1: Mode evolution, $v_k(N)/z$, for the CMB scale, $k_{\rm CMB}$. The real and imaginary parts, and modulus correspond to the pink- and green-dashed lines, and the black-solid line respectively. The vertical thin line signals the moment in which the CMB scale crosses the horizon $\Delta N_{\rm CMB} \sim 55$ e-folds before the end of inflation.

and its derivative;

- the factor k/aH can be normalised by noting that the scale $k_{\rm CMB} = 0.05\,{\rm Mpc}^{-1}$ crossed the horizon $\Delta N_{\rm CMB}$ e-folds before the end of inflation;

- in order to minimise numerical errors, one should evolve the background solution for a sufficiently long time before the relevant scales cross the horizon. This can be achieved by choosing a large enough initial value of ϕ;

- instead of solving directly for the complex perturbation, v_k, it is simpler to solve separately for its real and imaginary parts [368]. For each mode, the integration of eq.(D.2) is started 5 e-folds before horizon crossing, where Bunch–Davies initial conditions are applied, see eq.(2.64), and is integrated up until the end of inflation. In terms of the real and imaginary part of v_k, the initial conditions are

$$\text{(D.7)} \qquad {\rm Re}\{v_k\} = \frac{1}{\sqrt{2k}}\,,\ {\rm Re}\{v_k'\} = 0\,,\ {\rm Im}\{v_k\} = 0\,,\ {\rm Im}\{v_k'\} = -i\frac{\sqrt{k}}{\sqrt{2}\,k_{\rm in}}\,,$$

  where $k_{\rm in}$ is the mode that crossed the horizon when the integration is started;

- the correct normalisation on CMB scales for the power spectrum in eq.(D.3) at $k = k_{\rm CMB}$ is set by fixing V_0 and hence the Hubble scale when $k_{\rm CMB}$ leaves the horizon.

As an example, we solve eq.(D.2) for $k_{\rm CMB}$ and plot in figure D.1 the mode evolution, $v_k(N)/z$. The mode starts off in the Bunch–Davies vacuum, oscillates in the sub-horizon regime and freezes to a constant value after crossing the horizon.

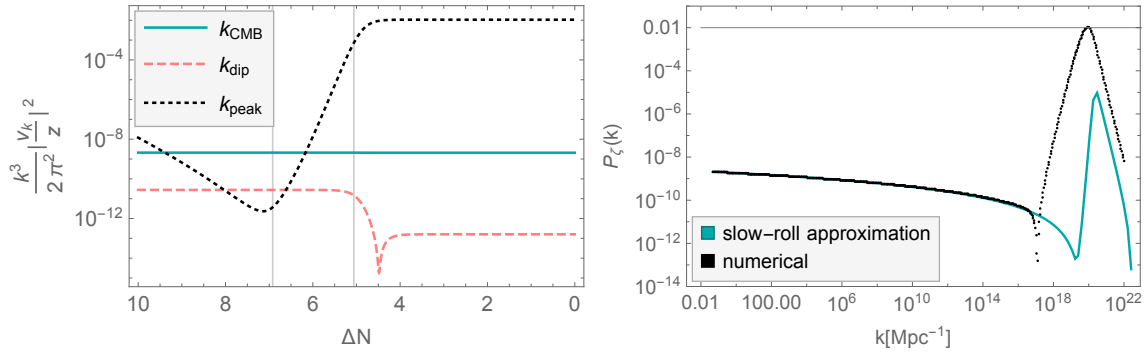

Figure D.2: *Left panel:* comparison between different modes' evolution in the last 10 e-folds of inflation. The region between the two thin vertical lines is characterised by $\eta_H > 3$. *Right panel:* numerical results for the scalar power spectrum, $P_\zeta(k)$, compared with the slow-roll approximation in eq.(2.69).

In the left panel of figure D.2, the evolution of three different modes is represented for comparison in the last 10 e-folds before the end of inflation. The continuous line is associated with the mode $k_{\rm CMB}$, which for the range of e-folds represented is well outside of the horizon and frozen at a constant value. The dashed line describes the scale $k_{\rm dip} = 10^{17}\,{\rm Mpc}^{-1}$, which corresponds to the dip in the scalar power spectrum. Finally, the mode corresponding to the peak in the scalar power spectrum, $k_{\rm peak} = 9\times 10^{19}\,{\rm Mpc}^{-1}$, is plotted with the dotted line. The mode associated to $k_{\rm peak}$ experiences the largest growth as it crosses the horizon close to the onset of the ultra-slow-roll phase. See [91] for a detailed discussion of the mechanism of growth (suppression) which shapes the modes' evolution and the scalar power spectrum.

In the right panel of figure D.2 we show a comparison of the numerical results for $P_\zeta(k)$ compared with the slow-roll approximation in eq.(2.69). On large scales the numerical results agree very well with the slow-roll approximation, showing that the slow-roll CMB predictions in (D.1) are reliable on these scales. On the other hand, on small scales the exact power spectrum differs substantially from the slow-roll approximation, both in terms of the position and the height of the peak. For the configuration under analysis, the power spectrum features a peak of $\mathcal{O}(0.01)$ at the comoving scale $k_{\rm peak}$.

APPENDIX E

LIMITING BEHAVIOUR OF THE SINGLE-FIELD POTENTIAL

In sections 6.2 and 6.3 we considered the phenomenology of the inflection-point potential in eq.(6.15) with the aim of realising an ultra-slow-roll phase and enhancing the scalar perturbations on small scales. For completeness we discuss here the limiting behaviour of the same potential when the inflection point is located at small or large ϕ values. For simplicity we restrict our discussion to the case $\xi = 0$ and choose $\alpha = 0.1$.

In the limit $\phi_{\rm infl} \to 0$, the dominant contribution to the potential in eq.(6.15) comes from the term proportional to $\tanh^3(\phi/\sqrt{6\alpha})$,

$$\lim_{\phi_{\rm infl}\to 0} V(\phi) \simeq V_0 \left[\frac{1}{3}\coth\left(\frac{\phi_{\rm infl}}{\sqrt{6\alpha}}\right)\right]^2 \tanh^6\left(\frac{\phi}{\sqrt{6\alpha}}\right). \tag{E.1}$$

It is therefore interesting to analyse the inflationary predictions of the inflection-point potential with $\phi_{\rm infl}$ small and compare them with those obtained from the α–attractor T-model potential [299]

$$U(\phi) = U_0 \tanh^6\left(\frac{\phi}{\sqrt{6\alpha}}\right). \tag{E.2}$$

On the other hand, when $\phi_{\rm infl}$ is large $\tanh(\phi_{\rm infl}/\sqrt{6\alpha}) \to 1$ and there is no simple limiting behaviour for the inflection-point potential, as illustrated in figure E.1. For large ϕ values ($\phi \gtrsim 2$ for the configuration plotted in figure E.1) the dominant contribution comes from the $\tanh^3(\phi/\sqrt{6\alpha})$ term (since $f_1 \approx -f_2$ in (6.14) and the $\tanh(\phi/\sqrt{6\alpha})$ and $\tanh^2(\phi/\sqrt{6\alpha})$ terms approximately cancel), but for smaller ϕ the potential receives contributions from all the terms.

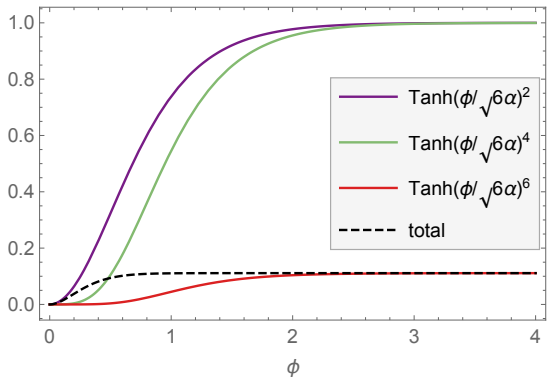

Figure E.1: Behaviour of the inflection-point potential in the large $\phi_{\rm infl}$ limit. The plot is produced with the parameters $\{\alpha = 0.1, \phi_{\rm infl} = 10, \xi = 0\}$. The potential $V(\phi)/V_0$ in eq.(6.15) (black-dashed line) is plotted together with the contributions coming from the single terms.

We consider two benchmark values, $\phi_{\rm infl} = \{0.1, 10\}$ in eq.(6.15), in order to study their background evolution and compare it with that obtained from the potential in eq.(E.2). The evolution of the Hubble slow-roll parameter, ϵ_H, and the inflaton field, ϕ, are plotted in the top row of figure E.2 against the number of e-folds to the end of inflation, $\Delta N \equiv N_{\rm end} - N$. As expected, the background evolution for the inflection-point potential with $\phi_{\rm infl} = 0.1$ is almost identical to that produced by the α–attractor T-model potential (E.2). The evolution corresponding to $\phi_{\rm infl} = 10$ is instead quite different and the reason why this is the case is clear from the bottom-left panel of figure E.2, where the potentials and the field values corresponding to scales observed in the CMB are shown. For the model with $\phi_{\rm infl} = 10$, the inflationary evolution observable in the CMB is located at $\phi < 2$ where the potential is not well-approximated by the function $\tanh^6(\phi/\sqrt{6\alpha})$, as discussed above and illustrated in figure E.1. The bottom-right panel in figure E.2 shows the CMB observables $(n_s, r_{\rm CMB})$ at the scale $0.002\,{\rm Mpc}^{-1}$ predicted by each potential. One sees that the predictions obtained with $\phi_{\rm infl} = 0.1$ are not distinguishable from those produced by the T-model for $\phi_{\rm infl} \leq 0.4$. The slightly lower value of n_s predicted by $\phi_{\rm infl} = 0.5$ could in future allow us to distinguish it form the α–attractor T-model. As expected, the predictions of the model with $\phi_{\rm infl} = 10$ differ from the T-model ones and the two could potentially be distinguished by the predicted value of $r_{0.002}$, lower for the inflection-point potential with $\phi_{\rm infl} = 10$.

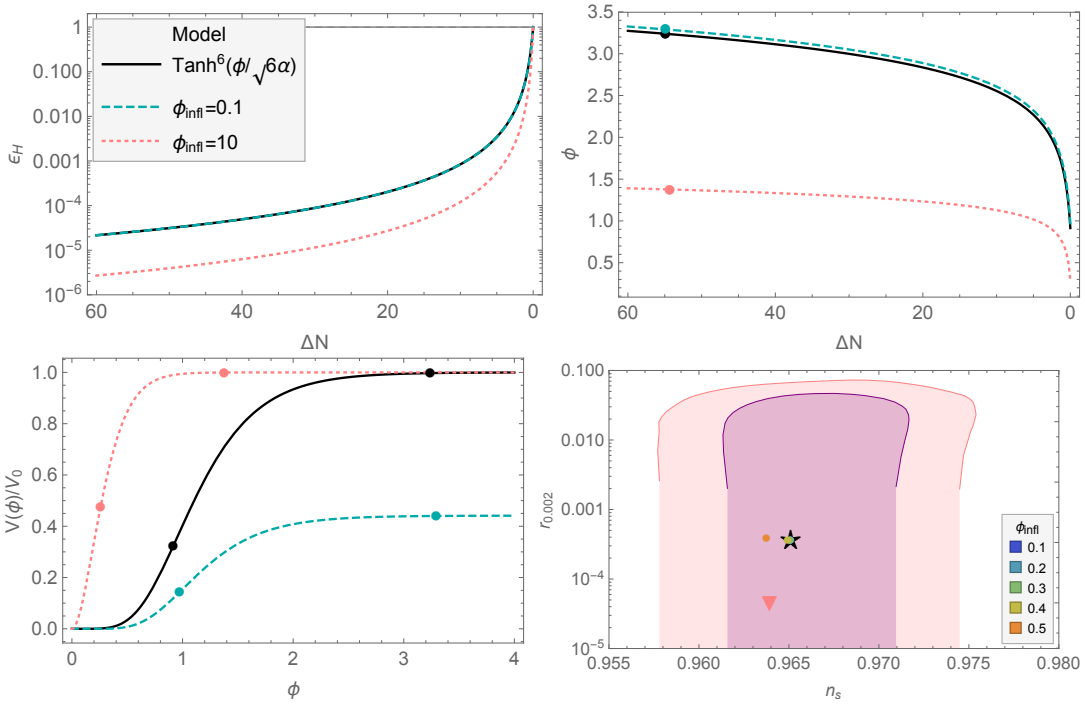

Figure E.2: *Top Row:* comparison between the background evolution of the inflection-point model with $\phi_{\rm infl} = \{0.1, 10\}$ and the α–attractor T-model in eq.(E.2). The bullet points in the right-hand plot indicate the field values when the CMB scale crossed the horizon. *Bottom Row:* in the left panel the potentials are plotted together with bullet points indicating the field values corresponding to the CMB scale (right bullet) and the end of inflation (left bullet). The legend identifying each line is the same as in the top-left panel. In the right panel the predictions of the CMB observables are represented together with the marginalised joint 68% and 95% C.L. regions in the (n_s, r) plane at $k = 0.002\,\mathrm{Mpc}^{-1}$ as obtained from *Planck*+BK15+BAO data assuming the ΛCDM+$r_{\rm CMB}$ cosmological model [67]. The black star corresponds to the α–attractor T-model potential (E.2), the pink triangle corresponds to the inflection-point potential with $\phi_{\rm infl} = 10$ and the remaining coloured circles correspond to different choices of small $\phi_{\rm infl}$ indicated in the legend.

APPENDIX F

PARAMETER STUDY OF THE MULTI-FIELD POTENTIAL

The multi-field potential (6.58) is parametrised by $\{\alpha, \phi_{\rm infl}, \gamma\}$. While in the main text we discuss the effect of varying α, we consider here the dependence on $\phi_{\rm infl}$ and γ, for trajectories with a fixed initial value $\theta_{\rm in} = 7\pi/10$. The models discussed in this appendix are not necessarily compatible with the CMB measurements on large scales, but instead they are selected because they demonstrate the impact of changing $\phi_{\rm infl}$ and γ.

First we numerically solve the background equations (6.45)–(6.47) for a model with $\{\alpha = 0.1, \gamma = 10\}$, testing $\phi_{\rm infl} = \{0.54, 0.542, 0.544\}$, and show the resulting $\epsilon_H(N)$ against

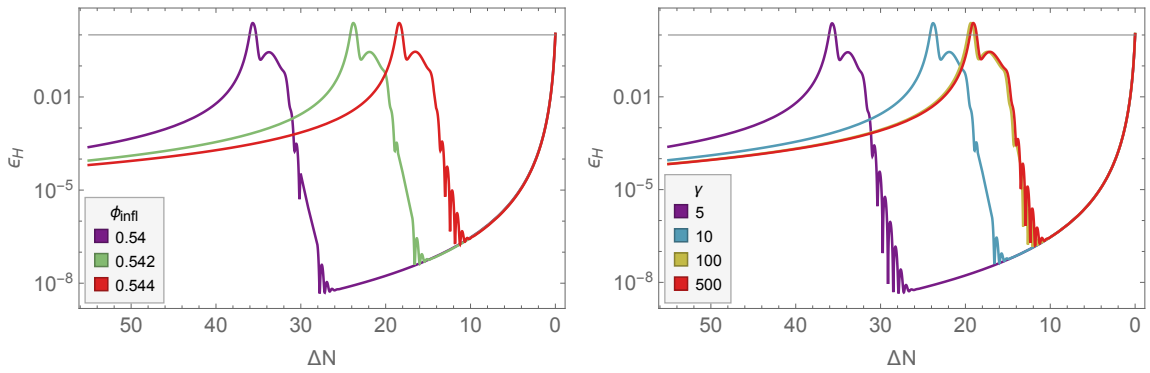

Figure F.1: *Left panel*: effect of varying the position of the inflection point in the multi-field potential (6.58) with parameters $\{\alpha = 0.1, \gamma = 10\}$ and initial conditions $\{\theta_{\rm in} = 7\pi/10, \theta'_{\rm in} = 0, \phi_{\rm in} = 3.1, \phi'_{\rm in} = 0\}$. *Right panel*: effect of changing the parameter γ in the potential (6.58) with parameters $\{\alpha = 0.1, \phi_{\rm infl} = 0.542\}$ and same initial conditions as in the left panel.

$\Delta N \equiv N_{\rm end} - N$ in the left panel of figure F.1. We see that the value of $\phi_{\rm infl}$ affects the time the fields spend around the inflection point and therefore the duration of the second slow-roll phase (which is itself an attractor solution regardless of the value $\phi_{\rm infl}$). In other words, $\phi_{\rm infl}$ determines the time at which the transition between the two inflationary phases happens.

Next, we test $\gamma = \{5, 10, 100, 500\}$ for the multi-field potential (6.58) with parameters $\{\alpha = 0.1, \phi_{\rm infl} = 0.542\}$. We consider $\gamma > 3$ so that the turn in field space happens within the last 60 e-folds of inflationary evolution, i.e. the second slow-roll phase lasts less than 60 e-folds. The resulting profile for $\epsilon_H(N)$ is displayed in the right panel of figure F.1 and demonstrates that the value of γ affects the duration of the second phase of inflation, similar to the effect of varying $\phi_{\rm infl}$. Also, increasing γ beyond $\gamma \sim 100$ does not significantly change the background evolution.

In order to understand the numerical results displayed in figure F.1 it is useful to calculate the effective squared-mass of the angular field, ${m_\theta}^2 \equiv \partial^2 U(r,\theta) \Big/ \partial\theta^2$. Using the multi-field potential (6.58), written in terms of the (non-canonical) radial field r, and assuming $H^2 \simeq U(r,\theta) \Big/ 3$, yields

$$\frac{{m_\theta}^2}{H^2} = 18\, r\, r_{\rm infl}\, \frac{\gamma}{1+\gamma}\, \frac{\left(r^2 + 3r_{\rm infl}^2 - \frac{3\, r\, r_{\rm infl}}{1+\gamma}\right)\cos\theta - \frac{3\gamma\, r\, r_{\rm infl}}{1+\gamma}\cos 2\theta}{\left(r^2 + 3r_{\rm infl}^2 - 3\, r\, r_{\rm infl}\, \frac{1+\gamma\cos\theta}{1+\gamma}\right)^2}\,, \tag{F.1}$$

where $r_{\rm infl} \equiv \tanh\left(\phi_{\rm infl}/\sqrt{6\alpha}\right)$. In the large γ limit, the mass (F.1) for a given r is independent of γ,

$$\lim_{\gamma\to\infty} \frac{{m_\theta}^2}{H^2} = 18\, r\, r_{\rm infl}\, \frac{\left(r^2 + 3r_{\rm infl}^2\right)\cos\theta - 3\, r\, r_{\rm infl}\cos 2\theta}{\left(r^2 + 3r_{\rm infl}^2 - 3\, r\, r_{\rm infl}\cos\theta\right)^2}\,, \tag{F.2}$$

which explains why the background evolution remains unchanged for sufficiently large values of γ, as observed in the right panel of figure F.1.

During the first phase of inflation the angular field is frozen, $\theta \simeq \theta_{\rm in}$, and the radial field satisfies $r \simeq 1$, see eq.(6.4), therefore the effective squared-mass of the angular field (F.1) is completely determined by γ and $\phi_{\rm infl}$. This explains why variations of the position of the inflection point or changes in γ have the same effect on the background evolution, i.e. both change the time at which the transition between the first and second phases of inflation happens. In this sense, the potential parameters $\phi_{\rm infl}$ and γ are degenerate and, for fixed α and $\theta_{\rm in}$, what really determines the duration of the second slow-roll phase overall is the effective mass of the angular field.

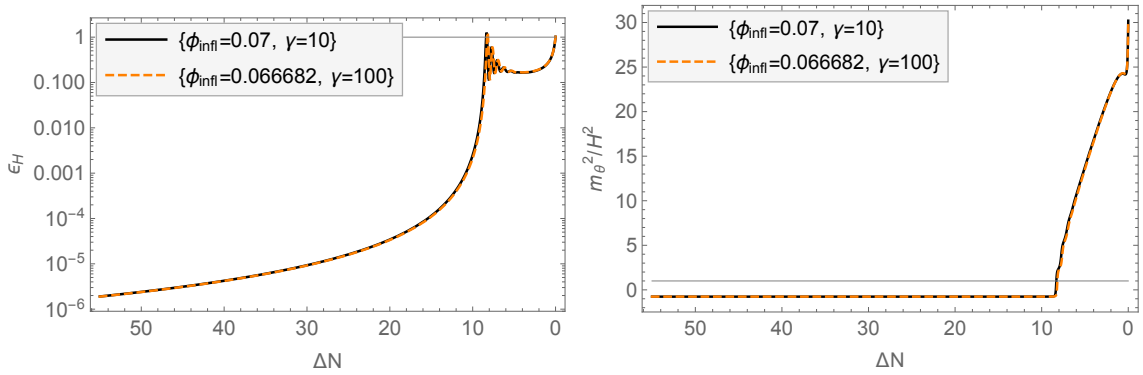

Figure F.2: Comparison between two models with same hyperbolic field-space curvature and the same initial value of the squared-mass of the angular field. The models parameters are listed in (F.3) and (F.4) and the same initial conditions $\{\theta_{\rm in} = 7/10\,\pi, \phi_{\rm in} = 1.05\}$ are considered in both cases. We show the numerical evolution of the slow-roll parameter on the left and the squared-mass (F.1) on the right. The two multi-field models display the same background evolution, which is due to selecting the values of γ and $\phi_{\rm infl}$ such that the angular mass is the same at the beginning of the evolution.

We demonstrate this by considering two different models formulated on the same hyperbolic field space, but whose potential parameters γ and $\phi_{\rm infl}$ are selected such that the initial mass of the angular field (F.1) is the same, $m_\theta{}^2/H^2 \simeq -0.762108$. The two models we consider are described by the parameters

$$\text{model}_1 \rightarrow \{\alpha = 0.005, \phi_{\rm infl} = 0.07, \gamma = 10\}, \tag{F.3}$$

$$\text{model}_2 \rightarrow \{\alpha = 0.005, \phi_{\rm infl} = 0.066682, \gamma = 100\}\,. \tag{F.4}$$

The slow-roll parameter $\epsilon_H(N)$ and the angular field mass $m_\theta{}^2/H^2$ are represented respectively in the left and right panels of figure F.2. The comparison between the lines shows that the background evolution stemming from the same initial angular mass is the same in the two models and that γ and $\phi_{\rm infl}$ are not independent parameters.

Given the degeneracy between γ and $\phi_{\rm infl}$, in section 6.4.4 we choose to fix γ and study the effect of changing the position of the inflection point and thus the initial mass of the angular field. The value of $\phi_{\rm infl}$ affects the position of the transition between the first and second phases of evolution, and therefore it affects the CMB predictions of the model, so needs to be adjusted in order to produce a model which is not in tension with the CMB measurements, as we study in section 6.4.4.

APPENDIX G

2D HYPERBOLIC FIELD SPACE: POLAR *vs* PLANAR COORDINATES

Different coordinate maps can be chosen to describe the (non-trivial) field space of multi-field models, where in this field space the coordinates are the fields themselves. The kinetic Lagrangian of α–attractor models displayed in eq.(6.5) employs polar coordinates on the hyperbolic field space, with radial and angular fields, (ϕ, θ), and the curvature of field space is $\mathscr{R}_{\rm fs} = -4/(3\alpha)$.

Other coordinate maps have been used in the literature to describe hyperbolic field spaces with constant, negative curvature, see e.g. [369–371] where planar coordinates have been selected. In this case, the kinetic Lagrangian reads

$$\mathscr{L}_{\rm planar} = -\frac{1}{2}(\partial u)^2 - \frac{1}{2}\mathrm{e}^{2bu}(\partial v)^2 \,, \tag{G.1}$$

where we label the set of planar coordinates as (u, v) and the curvature of field space is $\mathscr{R}_{\rm fs} = -2b^2$. Provided the curvature is the same, i.e. $b = \sqrt{2/(3\alpha)}$, the field-space geometry is the same as in eq.(6.5), while the coordinate map selected is different.

Planar coordinates were used in [4] to show how the hyperbolic geometry of field space could play a key role in enhancing the scalar power spectrum on small scales. In [4] the fields (u, v) have a separable potential

$$U(u, v) = U_0 \frac{u^2}{u_0^2 + u^2} + \frac{1}{2} m_v^2 v^2 \,, \tag{G.2}$$

where u has a plateau-type potential at large values of u, and the second field, v, has an apparently simple mass term. The authors of [4] demonstrate that the background

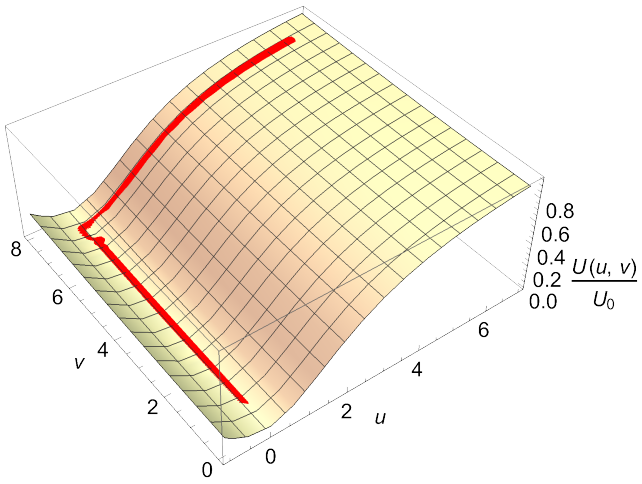

Figure G.1: Background evolution of the fields u and v represented on top of the potential profile, eq.(G.2). We are here reproducing the background evolution of a model originally discussed in [4]. The model parameters and initial conditions considered are $\{u_0 = \sqrt{6}, m_v^2 = U_0/500, b = 7.84, u_{\rm in} = 7, v_{\rm in} = 7.31\}$.

evolution and the geometry of field space following from (G.1) and (G.2) could result in a transient tachyonic instability of the isocurvature perturbation, $m_{s,\rm eff}{}^2/H^2 < 0$, which can lead to an enhancement of the scalar perturbation (see the discussion in section 2.4).

Among all the possible combinations of model parameters discussed in [4], we focus here on the inflationary potential described by $\{u_0 = \sqrt{6}, m_v^2 = U_0/500\}$, with $b = 7.84$ and initial conditions $\{u_{\rm in} = 7, v_{\rm in} = 7.31\}$, and refer the reader to the original work [4] for the equations describing the background evolution in planar coordinates. As demonstrated in [4], this set of parameters and initial conditions produces a peak in the scalar power spectrum $P_\zeta = \mathcal{O}(10^{-2})$ located at the scales where the Laser Interferometer Space Antenna (LISA) [222] operates. In this case the PBHs generated could potentially account for all of the dark matter in our Universe.

In figure G.1 the fields evolution is superimposed on top of the potential (G.2). The field u drives a first stage of inflation, while v is effectively frozen, with v' suppressed by the geometrical factor e^{-2bu} as long as $u \gg b^{-1}$, i.e. u takes values larger than the curvature length of the field space. When $u \sim b^{-1}$ the suppression is lifted and v starts evolving, driving a second stage of inflation as u settles into its effective minimum. At the transition between the two inflationary stages, slow roll is violated and the effective squared-mass of the isocurvature perturbation briefly becomes negative, see the top-right panel of figure 1 in [4].

We compare here the planar and polar coordinates description of an hyperbolic field

space. Although different coordinate choices in field space are physically equivalent, once the form of the kinetic Lagrangian of the model is fixed, a specific choice for the potential, such as the one in eq.(G.2), distinguishes between different physical models. Our aim is to place the inflationary model discussed in [4] (and therefore potentially other models formulated using planar coordinates, eq.(G.1)) in the context of multi-field α–attractors described using polar coordinates, and hence understand better the mechanism that allows for the enhancement of the curvature perturbation in that model.

In section G.1 we derive a coordinate transformation which allows us to transform from one coordinate map to the other. We re-analyse the model described in [4] employing polar coordinates in section G.2. We find that the potential is singular in polar coordinates, sharing the same singularity as the kinetic Lagrangian, and initial conditions close to the singularity are necessary in order to enhance the scalar perturbation. This explains why the second field v can lead to observable effects in this model, contrary to what was found in [303] for α–attractor models, i.e., for models with non-singular potentials.

G.1 Mapping between polar and planar coordinates

2D hyperbolic spaces with constant negative curvature (H_2) can be identified with spacelike hyperboloids embedded in a 3D Minkowski spacetime [372]. This embedding procedure provides an intermediate step to map between polar and planar coordinates in the field space. Using the 3D Minkowski spacetime line element

$$\mathrm{d}s^2 = -\mathrm{d}t^2 + \mathrm{d}x^2 + \mathrm{d}y^2 \,, \tag{G.3}$$

surfaces with a fixed timelike displacement from the origin, are given by

$$t^2 - x^2 - y^2 = R^2 \,. \tag{G.4}$$

These surfaces have hyperbolic (H_2) geometry, while hyperboloids with a fixed spacelike displacement from the origin have dS_2 geometry [372, 373].

Using polar coordinates, the line element of the hyperbolic field space is

$$\mathrm{d}s^2_{\text{polar}} = \mathrm{d}\phi^2 + R^2 \sinh^2(\phi/R)\mathrm{d}\theta^2 \quad (0 \leq \phi < +\infty, 0 \leq \theta < 2\pi) \,, \tag{G.5}$$

where the curvature length of field space is $R \equiv \sqrt{3\alpha/2}$. Choosing coordinates (ϕ, θ) on

the hyperboloid (G.4) such that

$$t = R\cosh(\phi/R)\,, \tag{G.6}$$

$$x = R\sinh(\phi/R)\cos\theta\,, \tag{G.7}$$

$$y = R\sinh(\phi/R)\sin\theta\,, \tag{G.8}$$

the line element (G.3) yields the H_2 line element in polar coordinates, eq.(G.5). The polar coordinates cover the whole upper ($t > 0$) hyperboloid for $0 \leq \phi < +\infty$.

The line element of the hyperbolic field space using planar coordinates is

$$\mathrm{d}s^2_{\text{planar}} = \mathrm{d}u^2 + e^{2bu}\mathrm{d}v^2 \quad (-\infty < u < +\infty,\, -\infty < v < +\infty)\,, \tag{G.9}$$

where the curvature length of field space is $R = b^{-1}$. It is useful to first rewrite the line element (G.9) in a conformally-flat form,

$$\mathrm{d}s^2_{\text{planar, conf}} = \Omega^2\left(\mathrm{d}w^2 + \mathrm{d}v^2\right)\,. \tag{G.10}$$

This is achieved by means of the transformation

$$w = -\frac{\mathrm{e}^{-bu}}{b}\,, \tag{G.11}$$

which leads to $\Omega^2 \equiv 1/(-bw)^2$. Note that we have chosen integration constants such that for $-\infty < u < \infty$ we have $-\infty < w < 0$. Choosing coordinates (w, v) on the hyperboloid (G.4) such that

$$t = -\frac{R^2}{2w}\left(1 + \frac{v^2}{R^2} + \frac{w^2}{R^2}\right)\,, \tag{G.12}$$

$$x = -\frac{R^2}{2w}\left(1 - \frac{v^2}{R^2} - \frac{w^2}{R^2}\right)\,, \tag{G.13}$$

$$y = -\frac{Rv}{w}\,, \tag{G.14}$$

the line element (G.3) yields the H_2 line element (G.10), with $R = b^{-1}$.

Using (G.12)–(G.14) to express the conformal planar coordinates (w, v) in terms of those in Minkowski spacetime gives

$$w = -\frac{R^2}{t + x}\,, \tag{G.15}$$

$$v = \frac{Ry}{t + x}\,. \tag{G.16}$$

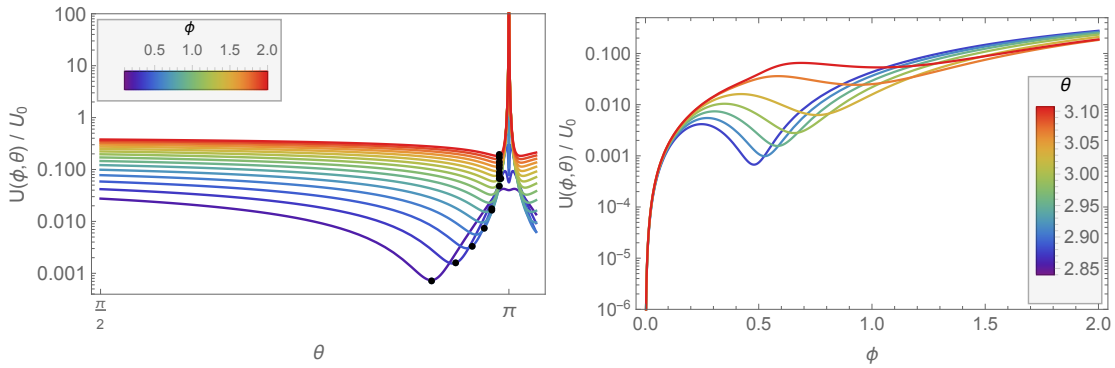

Figure G.2: *Left panel:* profile of the potential (G.19) as a function of the angular field θ for different fixed values of ϕ. The selected range of ϕ values shows the potential's divergence at $\theta = \pi$. Black dots show the background evolution of the fields superimposed on the potential. Earlier stages of inflation correspond to larger values of ϕ. *Right panel:* profile of the potential (G.19) for fixed values of θ as a function of the radial field ϕ. The range of θ corresponds to the values taken by the field during the background evolution displayed in figure G.3 and discussed in the main text.

Substituting (G.6)–(G.8) in the above expressions gives the conformal planar coordinates in terms of the polar coordinates. Finally expressing the conformal planar coordinates (w, v) in terms of the planar coordinates (u, v) yields

$$u = R \ln\left[\cosh(\phi/R) + \sinh(\phi/R)\cos\theta\right], \tag{G.17}$$

$$v = \frac{R\sinh(\phi/R)\sin\theta}{\cosh(\phi/R) + \sinh(\phi/R)\cos\theta}. \tag{G.18}$$

G.2 A hyperbolic model with a singular potential

In order to analyse the model of [4] using polar coordinates, we use the kinetic Lagrangian (6.5) and we express the potential (G.2) in terms of polar coordinates (ϕ, θ) by means of the coordinate map (G.17)–(G.18),

$$U(\phi,\theta) = U_0\left\{\frac{\left(R\ln\left[\cosh(\phi/R) + \sinh(\phi/R)\cos\theta\right]\right)^2}{6 + \left(R\ln\left[\cosh(\phi/R) + \sinh(\phi/R)\cos\theta\right]\right)^2} + \frac{1}{2\times 500}\left(\frac{R\sinh(\phi/R)\sin\theta}{\cosh(\phi/R) + \sinh(\phi/R)\cos\theta}\right)^2\right\}. \tag{G.19}$$

In equation (G.19), $R = \sqrt{3\alpha/2}$ and the model parameters have been substituted according to the parameters chosen in figure G.1. In particular, for the hyperbolic field space to be the same, $\mathscr{R}_{\text{fs, polar}} = \mathscr{R}_{\text{fs, planar}} \simeq -123$, we set $\alpha = 2/(3b^2) \simeq 0.01$.

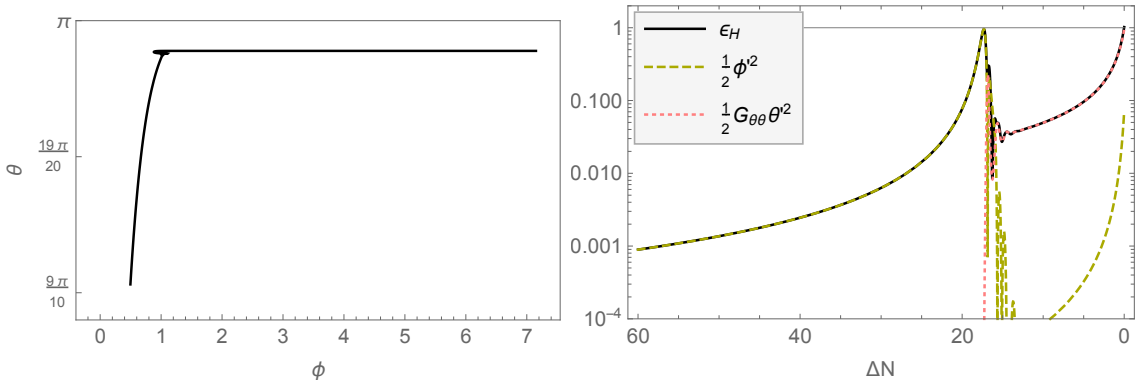

Figure G.3: *Left panel:* evolution of the background fields over the final 60 e-folds of inflation driven by the potential (G.19) in polar coordinates. *Right panel:* evolution of ϵ_H over the last 60 e-folds of inflation for the same potential. The black line shows ϵ_H, while the coloured lines show the contributions from the radial (green-dashed line) and angular (pink-dotted line) fields.

While being fairly simple in planar coordinates, the potential looks much more complicated when transformed to polar coordinates. The second term in eq.(G.19) corresponds to the mass term for v in the original potential (G.2) and is singular at $\theta \to \pi$ for large values of ϕ. We visualise the two-field potential as a function of ϕ and θ in figure G.2; from the left panel one can see that the potential diverges at $\theta = \pi$ for $\phi \gtrsim 1$.

We numerically solve eqs.(6.45)–(6.47) to obtain the background evolution for ϕ and θ. We select the initial conditions $\{\phi_{\rm in} = 7.1504, \theta_{\rm in} = 3.1067\}$ and slow-roll initial conditions for the velocities of the fields. We choose this set of initial conditions as they produce the same background evolution in terms of u and v shown in figure G.1. The corresponding evolution of the fields in polar coordinates, ϕ and θ, and the slow-roll parameter, ϵ_H, is shown in figure G.3. In particular, in the left panel we plot the trajectory in field space, showing how ϕ drives a first stage of inflation, after which there is a turn in field space and θ, previously frozen, starts evolving. In the right panel of the same figure, the evolution of the slow-roll parameter ϵ_H and its components are shown against the number of e-folds to the end of inflation, $\Delta N \equiv N_{\rm end} - N$. As expected, the major contribution to ϵ_H in the first phase of inflation comes from the kinetic energy of ϕ, while the evolution of θ dominates a second stage of inflation. Between the two phases, the slow-roll approximation is violated ($\epsilon_H \simeq 1$).

The numerical solutions obtained with the polar coordinates description with the potential (G.19) is identical to that employing planar coordinates with the potential (G.2), as expected given the one-to-one correspondence between the two models. To show this,

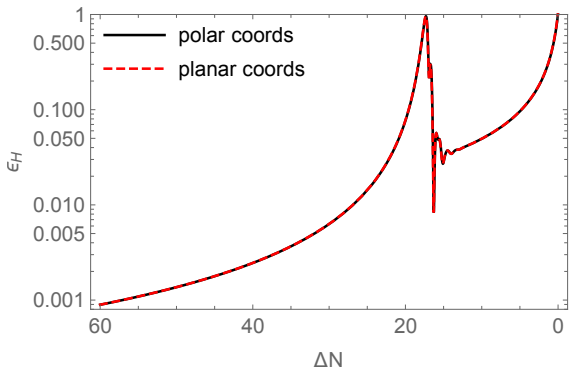

Figure G.4: Numerical solutions for the slow-roll parameter ϵ_H for the same model evolved using polar coordinates (black line) or planar coordinates (red-dashed line). The numerical solutions, using the corresponding potentials in polar (G.19) or planar (G.2) coordinates, are identical.

we compare the slow-roll parameter ϵ_H. Using polar coordinates, $\epsilon_H(N)$ is

$$\epsilon_H(N) = \frac{1}{2}\left(\phi'^2 + \frac{3\alpha}{2}\sinh^2\left(\sqrt{\frac{2}{3\alpha}}\phi\right)\theta'^2\right), \tag{G.20}$$

see eq.(6.45). When employing planar coordinates, we have instead

$$\epsilon_H(N) = \frac{1}{2}\left(u'^2 + \mathrm{e}^{2bu}v'^2\right). \tag{G.21}$$

Substituting in the corresponding numerical solutions for the fields, we show ϵ_H obtained from eq.(G.20) and (G.21) in figure G.4. As expected the two lines coincide exactly.

While we have been focusing on a configuration which was chosen in [4] to produce a peak in the scalar power spectrum (and consequently in the induced second-order GWs) at LISA scales, a range of different initial conditions in field space are discussed in [4] (see table 1 therein). In particular, varying the initial condition $v_{\rm in}$ allows them to move the peak in the scalar power spectrum to scales where other future GW detectors could operate, e.g., SKA, BBO and ET. Inverting (G.17) and (G.18) enables us to convert a set of initial conditions $(u_{\rm in}, v_{\rm in})$ into the corresponding set in polar coordinates $(\phi_{\rm in}, \theta_{\rm in})$. We have checked that the initial conditions listed in table 1 of [4] are all within 1.5% of $\theta_{\rm in} = \pi$. Thus we see that the configurations associated with enhanced scalar fluctuations on small scales stem from initial conditions very close to the singularity in the potential at $\theta = \pi$. As already pointed out in [105], when the potential and the kinetic Lagrangian share the same singularity, large-scale observables are sensitive to the specific shape of the potential and to the initial conditions.

It is straightforward to show that the kinetic Lagrangian (6.3) and the potential (G.19) share the same pole in the conformal polar coordinates (r,θ), where r is defined in (6.4). By following a similar procedure to what was done in deriving eqs.(G.17) and (G.18), we obtain the coordinate transformation

$$u = R\,\ln\left[\frac{1+r^2+2r\cos\theta}{1-r^2}\right], \tag{G.22}$$

$$v = \frac{2R\,r\,\sin\theta}{1+r^2+2r\cos\theta}\,. \tag{G.23}$$

In order to assess the behaviour of the fields close to $\theta=\pi$, we define $\delta\equiv\pi-\theta$ and expand eqs.(G.22) and (G.23) to obtain

$$\lim_{\delta\to 0} u = R\,\ln\left[\frac{1-r}{1+r}+\frac{r\delta^2}{1-r^2}\right], \tag{G.24}$$

$$\lim_{\delta\to 0} v = \frac{2R\,r\,\delta}{(1-r)^2+r\delta^2}\,. \tag{G.25}$$

From the expression above it is clear that as $\delta\to 0$ the term $m^2v^2/2$ in the potential (G.2) has a pole at $r=1$, as does the kinetic Lagrangian (6.3).

BIBLIOGRAPHY

[1] L. Iacconi, M. Fasiello, H. Assadullahi, E. Dimastrogiovanni, and D. Wands, "Interferometer Constraints on the Inflationary Field Content," *JCAP*, vol. 03, p. 031, 2020.

[2] L. Iacconi, M. Fasiello, H. Assadullahi, and D. Wands, "Small-scale Tests of Inflation," *JCAP*, vol. 12, p. 005, 2020.

[3] L. Iacconi, H. Assadullahi, M. Fasiello, and D. Wands, "Revisiting small-scale fluctuations in α-attractor models of inflation," *JCAP*, vol. 06, no. 06, p. 007, 2022.

[4] M. Braglia, D. K. Hazra, F. Finelli, G. F. Smoot, L. Sriramkumar, and A. A. Starobinsky, "Generating PBHs and small-scale GWs in two-field models of inflation," *JCAP*, vol. 08, p. 001, 2020.

[5] A. Einstein, "The Foundation of the General Theory of Relativity," *Annalen Phys.*, vol. 49, no. 7, pp. 769–822, 1916.

[6] F. W. Dyson, A. S. Eddington, and C. Davidson, "A Determination of the Deflection of Light by the Sun's Gravitational Field, from Observations Made at the Total Eclipse of May 29, 1919," *Phil. Trans. Roy. Soc. Lond. A*, vol. 220, pp. 291–333, 1920.

[7] B. P. Abbott *et al.*, "Observation of Gravitational Waves from a Binary Black Hole Merger," *Phys. Rev. Lett.*, vol. 116, no. 6, p. 061102, 2016.

[8] C. M. Will, "The Confrontation between General Relativity and Experiment," *Living Rev. Rel.*, vol. 17, p. 4, 2014.

[9] G. F. Smoot *et al.*, "Structure in the COBE differential microwave radiometer first year maps," *Astrophys. J. Lett.*, vol. 396, pp. L1–L5, 1992.

[10] M. Colless, "Cosmological results from the 2df galaxy redshift survey," in *Carnegie Observatories Centennial Symposium. 2. Measuring and Modeling the Universe*, pp. 196–206, 5 2003.

[11] S. W. Hawking and G. F. R. Ellis, *The Large Scale Structure of Space-Time*. Cambridge Monographs on Mathematical Physics, Cambridge University Press, February 2011.

[12] S. W. Hawking, "The beginning of time," 1996.

[13] V. Mukhanov, *Physical Foundations of Cosmology*. Oxford: Cambridge University Press, 2005.

[14] D. Baumann, "Inflation," in *Theoretical Advanced Study Institute in Elementary Particle Physics: Physics of the Large and the Small*, pp. 523–686, 2011.

[15] L. Kofman, A. Linde, and A. A. Starobinsky, "Towards the theory of reheating after inflation," *Phys. Rev. D*, vol. 56, pp. 3258–3295, Sep 1997.

[16] P. W. Higgs, "Broken symmetries and the masses of gauge bosons," *Phys. Rev. Lett.*, vol. 13, pp. 508–509, Oct 1964.

[17] T. W. B. Kibble, "Englert-Brout-Higgs-Guralnik-Hagen-Kibble mechanism (history)," *Scholarpedia*, vol. 4, no. 1, p. 8741, 2009. revision #137393.

[18] K. A. Olive, "The Thermodynamics of the Quark - Hadron Phase Transition in the Early Universe," *Nucl. Phys. B*, vol. 190, pp. 483–503, 1981.

[19] B. Follin, L. Knox, M. Millea, and Z. Pan, "First Detection of the Acoustic Oscillation Phase Shift Expected from the Cosmic Neutrino Background," *Phys. Rev. Lett.*, vol. 115, no. 9, p. 091301, 2015.

[20] L. Canetti, M. Drewes, and M. Shaposhnikov, "Matter and Antimatter in the Universe," *New J. Phys.*, vol. 14, p. 095012, 2012.

[21] A. D. Sakharov, "Violation ofCPin variance,casymmetry, and baryon asymmetry of the universe," *Soviet Physics Uspekhi*, vol. 34, pp. 392–393, may 1991.

[22] R. A. Alpher, H. Bethe, and G. Gamow, "The origin of chemical elements," *Phys. Rev.*, vol. 73, pp. 803–804, 1948.

[23] G. M. Fuller, G. J. Mathews, and C. R. Alcock, "The Quark - Hadron Phase Transition in the Early Universe: Isothermal Baryon Number Fluctuations and Primordial Nucleosynthesis," *Phys. Rev. D*, vol. 37, p. 1380, 1988.

[24] A. A. Penzias and R. W. Wilson, "A Measurement of excess antenna temperature at 4080-Mc/s," *Astrophys. J.*, vol. 142, pp. 419–421, 1965.

[25] H. I. Ewen and E. M. Purcell, "Observation of a Line in the Galactic Radio Spectrum: Radiation from Galactic Hydrogen at 1,420 Mc./sec.," *Nature*, vol. 168, p. 356, Sept. 1951.

[26] J. R. Pritchard and A. Loeb, "21-cm cosmology," *Rept. Prog. Phys.*, vol. 75, p. 086901, 2012.

[27] V. Bromm, N. Yoshida, L. Hernquist, and C. F. McKee, "The formation of the first stars and galaxies," *Nature*, vol. 459, pp. 49–54, 2009.

[28] R. H. Becker *et al.*, "Evidence for Reionization at Z ~ 6: Detection of a Gunn-Peterson trough in a Z = 6.28 Quasar," *Astron. J.*, vol. 122, p. 2850, 2001.

[29] N. Aghanim *et al.*, "Planck 2018 results. VI. Cosmological parameters," *Astron. Astrophys.*, vol. 641, p. A6, 2020.
[Erratum: Astron.Astrophys. 652, C4 (2021)].

[30] A. G. Riess *et al.*, "Observational evidence from supernovae for an accelerating universe and a cosmological constant," *Astron. J.*, vol. 116, pp. 1009–1038, 1998.

[31] S. Perlmutter *et al.*, "Measurements of ω and λ from 42 high-redshift supernovae," *The Astrophysical Journal*, vol. 517, pp. 565–586, jun 1999.

[32] D. N. Spergel *et al.*, "First year Wilkinson Microwave Anisotropy Probe (WMAP) observations: Determination of cosmological parameters," *Astrophys. J. Suppl.*, vol. 148, pp. 175–194, 2003.

[33] S. Weinberg, *Cosmology*.
Oxford: Oxford University Press, 2008.

[34] D. Baumann, "Cosmology." `http://cosmology.amsterdam/education/cosmology/`.

[35] D. Hilbert, "Die Grundlagen der Physik. 1.," *Gott. Nachr.*, vol. 27, pp. 395–407, 1915.

[36] S. M. Carroll, *Spacetime and Geometry*.
Cambridge University Press, July 2019.

[37] E. Hubble, "A relation between distance and radial velocity among extra-galactic nebulae," *Proceedings of the National Academy of Sciences*, vol. 15, no. 3, pp. 168–173, 1929.

[38] A. G. Riess *et al.*, "A Comprehensive Measurement of the Local Value of the Hubble Constant with 1 km/s/Mpc Uncertainty from the Hubble Space Telescope and the SH0ES Team," 12 2021.

[39] E. Di Valentino, O. Mena, S. Pan, L. Visinelli, W. Yang, A. Melchiorri, D. F. Mota, A. G. Riess, and J. Silk, "In the realm of the Hubble tension—a review of solutions," *Class. Quant. Grav.*, vol. 38, no. 15, p. 153001, 2021.

[40] T. Clifton, P. G. Ferreira, A. Padilla, and C. Skordis, "Modified Gravity and Cosmology," *Phys. Rept.*, vol. 513, pp. 1–189, 2012.

[41] L. Heisenberg, "A systematic approach to generalisations of General Relativity and their cosmological implications," *Phys. Rept.*, vol. 796, pp. 1–113, 2019.

[42] S. Weinberg, "The Cosmological Constant Problem," *Rev. Mod. Phys.*, vol. 61, pp. 1–23, 1989.

[43] S. Cole *et al.*, "The 2dF Galaxy Redshift Survey: Power-spectrum analysis of the final dataset and cosmological implications," *Mon. Not. Roy. Astron. Soc.*, vol. 362, pp. 505–534, 2005.

[44] J. S. Bullock and M. Boylan-Kolchin, "Small-Scale Challenges to the ΛCDM Paradigm," *Ann. Rev. Astron. Astrophys.*, vol. 55, pp. 343–387, 2017.

[45] V. Springel *et al.*, "First results from the IllustrisTNG simulations: matter and galaxy clustering," *Mon. Not. Roy. Astron. Soc.*, vol. 475, no. 1, pp. 676–698, 2018.

[46] K. Freese, "Status of Dark Matter in the Universe," *Int. J. Mod. Phys.*, vol. 1, no. 06, pp. 325–355, 2017.

[47] A. H. Guth, "The Inflationary Universe: A Possible Solution to the Horizon and Flatness Problems," *Phys. Rev. D*, vol. 23, pp. 347–356, 1981.

[48] Y. Akrami *et al.*, "Planck 2018 results. IV. Diffuse component separation," *Astron. Astrophys.*, vol. 641, p. A4, 2020.

[49] H. Georgi and S. L. Glashow, "Unity of All Elementary Particle Forces," *Phys. Rev. Lett.*, vol. 32, pp. 438–441, 1974.

[50] J. C. Pati and A. Salam, "Lepton Number as the Fourth Color," *Phys. Rev. D*, vol. 10, pp. 275–289, 1974.
[Erratum: Phys.Rev.D 11, 703–703 (1975)].

[51] G. 't Hooft, "Magnetic Monopoles in Unified Gauge Theories," *Nucl. Phys. B*, vol. 79, pp. 276–284, 1974.

[52] A. H. Guth and S. H. H. Tye, "Phase Transitions and Magnetic Monopole Production in the Very Early Universe," *Phys. Rev. Lett.*, vol. 44, p. 631, 1980.
[Erratum: Phys.Rev.Lett. 44, 963 (1980)].

[53] M. B. Einhorn, D. L. Stein, and D. Toussaint, "Are Grand Unified Theories Compatible with Standard Cosmology?," *Phys. Rev. D*, vol. 21, p. 3295, 1980.

[54] A. Rajantie, "Introduction to Magnetic Monopoles," *Contemp. Phys.*, vol. 53, pp. 195–211, 2012.

[55] A. D. Linde, "A New Inflationary Universe Scenario: A Possible Solution of the Horizon, Flatness, Homogeneity, Isotropy and Primordial Monopole Problems," *Phys. Lett. B*, vol. 108, pp. 389–393, 1982.

[56] A. A. Starobinsky, "A New Type of Isotropic Cosmological Models Without Singularity," *Phys. Lett. B*, vol. 91, pp. 99–102, 1980.

[57] A. Albrecht and P. J. Steinhardt, "Cosmology for Grand Unified Theories with Radiatively Induced Symmetry Breaking," *Phys. Rev. Lett.*, vol. 48, pp. 1220–1223, 1982.

[58] V. F. Mukhanov and G. V. Chibisov, "Quantum Fluctuations and a Nonsingular Universe," *JETP Lett.*, vol. 33, pp. 532–535, 1981.

[59] A. A. Starobinsky, "Dynamics of Phase Transition in the New Inflationary Universe Scenario and Generation of Perturbations," *Phys. Lett. B*, vol. 117, pp. 175–178, 1982.

[60] A. H. Guth and S. Y. Pi, "Fluctuations in the New Inflationary Universe," *Phys. Rev. Lett.*, vol. 49, pp. 1110–1113, 1982.

[61] S. W. Hawking, "The Development of Irregularities in a Single Bubble Inflationary Universe," *Phys. Lett. B*, vol. 115, p. 295, 1982.

[62] J. M. Bardeen, P. J. Steinhardt, and M. S. Turner, "Spontaneous Creation of Almost Scale - Free Density Perturbations in an Inflationary Universe," *Phys. Rev. D*, vol. 28, p. 679, 1983.

[63] D. S. Salopek and J. R. Bond, "Nonlinear evolution of long wavelength metric fluctuations in inflationary models," *Phys. Rev. D*, vol. 42, pp. 3936–3962, 1990.

[64] A. R. Liddle, P. Parsons, and J. D. Barrow, "Formalizing the slow roll approximation in inflation," *Phys. Rev. D*, vol. 50, pp. 7222–7232, 1994.

[65] J. Ellis, M. A. G. Garcia, D. V. Nanopoulos, and K. A. Olive, "Calculations of Inflaton Decays and Reheating: with Applications to No-Scale Inflation Models," *JCAP*, vol. 07, p. 050, 2015.

[66] D. Baumann, *Cosmology*.
Cambridge University Press, 7 2022.

[67] Y. Akrami *et al.*, "Planck 2018 results. X. Constraints on inflation," *Astron. Astrophys.*, vol. 641, p. A10, 2020.

[68] E. Lifshitz, "Republication of: On the gravitational stability of the expanding universe," *J. Phys. (USSR)*, vol. 10, no. 2, p. 116, 1946.

[69] M. Sasaki, "Large Scale Quantum Fluctuations in the Inflationary Universe," *Prog. Theor. Phys.*, vol. 76, p. 1036, 1986.

[70] V. F. Mukhanov, "Quantum Theory of Gauge Invariant Cosmological Perturbations," *Sov. Phys. JETP*, vol. 67, pp. 1297–1302, 1988.

[71] S. Weinberg, "Adiabatic modes in cosmology," *Phys. Rev. D*, vol. 67, p. 123504, 2003.

[72] D. H. Lyth and A. R. Liddle, *The primordial density perturbation: Cosmology, inflation and the origin of structure*.
2009.

[73] A. Ijjas, P. J. Steinhardt, and A. Loeb, "Inflationary paradigm in trouble after Planck2013," *Phys. Lett. B*, vol. 723, pp. 261–266, 2013.

[74] A. H. Guth, D. I. Kaiser, and Y. Nomura, "Inflationary paradigm after Planck 2013," *Phys. Lett. B*, vol. 733, pp. 112–119, 2014.

[75] A. Linde, "Inflationary Cosmology after Planck 2013," in *100e Ecole d'Ete de Physique: Post-Planck Cosmology*, pp. 231–316, 2015.

[76] R. Brandenberger, "Initial conditions for inflation — A short review," *Int. J. Mod. Phys. D*, vol. 26, no. 01, p. 1740002, 2016.

[77] K. Clough, E. A. Lim, B. S. DiNunno, W. Fischler, R. Flauger, and S. Paban, "Robustness of Inflation to Inhomogeneous Initial Conditions," *JCAP*, vol. 09, p. 025, 2017.

[78] R. H. Brandenberger and J. Martin, "The Robustness of inflation to changes in superPlanck scale physics," *Mod. Phys. Lett. A*, vol. 16, pp. 999–1006, 2001.

[79] J. Martin and R. H. Brandenberger, "The TransPlanckian problem of inflationary cosmology," *Phys. Rev. D*, vol. 63, p. 123501, 2001.

[80] R. H. Brandenberger and J. Martin, "Trans-Planckian Issues for Inflationary Cosmology," *Class. Quant. Grav.*, vol. 30, p. 113001, 2013.

[81] H. Motohashi and W. Hu, "Primordial Black Holes and Slow-Roll Violation," *Phys. Rev. D*, vol. 96, no. 6, p. 063503, 2017.

[82] W. H. Kinney, "Horizon crossing and inflation with large eta," *Phys. Rev. D*, vol. 72, p. 023515, 2005.

[83] K. Dimopoulos, "Ultra slow-roll inflation demystified," *Phys. Lett. B*, vol. 775, pp. 262–265, 2017.

[84] C. Pattison, V. Vennin, H. Assadullahi, and D. Wands, "The attractive behaviour of ultra-slow-roll inflation," *JCAP*, vol. 08, p. 048, 2018.

[85] J. Garcia-Bellido and E. Ruiz Morales, "Primordial black holes from single field models of inflation," *Phys. Dark Univ.*, vol. 18, pp. 47–54, 2017.

[86] C. Germani and T. Prokopec, "On primordial black holes from an inflection point," *Phys. Dark Univ.*, vol. 18, pp. 6–10, 2017.

[87] G. Ballesteros and M. Taoso, "Primordial black hole dark matter from single field inflation," *Phys. Rev. D*, vol. 97, no. 2, p. 023501, 2018.

[88] M. Cicoli, V. A. Diaz, and F. G. Pedro, "Primordial Black Holes from String Inflation," *JCAP*, vol. 06, p. 034, 2018.

[89] I. Dalianis, A. Kehagias, and G. Tringas, "Primordial black holes from α-attractors," *JCAP*, vol. 01, p. 037, 2019.

[90] S. Passaglia, W. Hu, and H. Motohashi, "Primordial black holes and local non-Gaussianity in canonical inflation," *Phys. Rev. D*, vol. 99, no. 4, p. 043536, 2019.

[91] G. Ballesteros, J. Rey, M. Taoso, and A. Urbano, "Primordial black holes as dark matter and gravitational waves from single-field polynomial inflation," *JCAP*, vol. 07, p. 025, 2020.

[92] S. Kuroyanagi, T. Takahashi, and S. Yokoyama, "Blue-tilted Tensor Spectrum and Thermal History of the Universe," *JCAP*, vol. 1502, p. 003, 2015.

[93] N. Bartolo *et al.*, "Science with the space-based interferometer LISA. IV: Probing inflation with gravitational waves," *JCAP*, vol. 1612, no. 12, p. 026, 2016.

[94] C. Caprini and D. G. Figueroa, "Cosmological Backgrounds of Gravitational Waves," *Class. Quant. Grav.*, vol. 35, no. 16, p. 163001, 2018.

[95] D. H. Lyth and D. Seery, "Classicality of the primordial perturbations," *Phys. Lett. B*, vol. 662, pp. 309–313, 2008.

[96] C. Cheung, P. Creminelli, A. L. Fitzpatrick, J. Kaplan, and L. Senatore, "The Effective Field Theory of Inflation," *JHEP*, vol. 03, p. 014, 2008.

[97] L. Senatore and M. Zaldarriaga, "The Effective Field Theory of Multifield Inflation," *JHEP*, vol. 04, p. 024, 2012.

[98] L. Bordin, P. Creminelli, A. Khmelnitsky, and L. Senatore, "Light Particles with Spin in Inflation," *JCAP*, vol. 1810, no. 10, p. 013, 2018.

[99] G. Gubitosi, F. Piazza, and F. Vernizzi, "The Effective Field Theory of Dark Energy," *JCAP*, vol. 02, p. 032, 2013.

[100] C. P. Burgess, "Introduction to Effective Field Theory," *Ann. Rev. Nucl. Part. Sci.*, vol. 57, pp. 329–362, 2007.

[101] C. P. Burgess, "Quantum gravity in everyday life: General relativity as an effective field theory," *Living Rev. Rel.*, vol. 7, pp. 5–56, 2004.

[102] E. C. G. Stueckelberg, "Theory of the radiation of photons of small arbitrary mass," *Helv. Phys. Acta*, vol. 30, pp. 209–215, 1957.

[103] D. Baumann and L. McAllister, *Inflation and String Theory*.
Cambridge Monographs on Mathematical Physics, Cambridge University Press, 2015.

[104] S. Renaux-Petel and K. Turzynski, "On reaching the adiabatic limit in multi-field inflation," *JCAP*, vol. 06, p. 010, 2015.

[105] S. Garcia-Saenz, S. Renaux-Petel, and J. Ronayne, "Primordial fluctuations and non-Gaussianities in sidetracked inflation," *JCAP*, vol. 1807, no. 07, p. 057, 2018.

[106] J.-O. Gong and T. Tanaka, "A covariant approach to general field space metric in multi-field inflation," *JCAP*, vol. 03, p. 015, 2011.
[Erratum: JCAP 02, E01 (2012)].

[107] M. Sasaki and E. D. Stewart, "A General analytic formula for the spectral index of the density perturbations produced during inflation," *Prog. Theor. Phys.*, vol. 95, pp. 71–78, 1996.

[108] S. Groot Nibbelink and B. J. W. van Tent, "Scalar perturbations during multiple field slow-roll inflation," *Class. Quant. Grav.*, vol. 19, pp. 613–640, 2002.

[109] D. Langlois and S. Renaux-Petel, "Perturbations in generalized multi-field inflation," *JCAP*, vol. 04, p. 017, 2008.

[110] J.-O. Gong, "Multi-field inflation and cosmological perturbations," *Int. J. Mod. Phys. D*, vol. 26, no. 01, p. 1740003, 2016.

[111] C. Gordon, D. Wands, B. A. Bassett, and R. Maartens, "Adiabatic and entropy perturbations from inflation," *Phys. Rev. D*, vol. 63, p. 023506, 2000.

[112] S. Renaux-Petel and K. Turzyński, "Geometrical Destabilization of Inflation," *Phys. Rev. Lett.*, vol. 117, no. 14, p. 141301, 2016.

[113] S. Renaux-Petel and K. Turzynski, "On reaching the adiabatic limit in multi-field inflation," *JCAP*, vol. 06, p. 010, 2015.

[114] S. Renaux-Petel, K. Turzyński, and V. Vennin, "Geometrical destabilization, premature end of inflation and Bayesian model selection," *JCAP*, vol. 11, p. 006, 2017.

[115] S. Garcia-Saenz and S. Renaux-Petel, "Flattened non-Gaussianities from the effective field theory of inflation with imaginary speed of sound," *JCAP*, vol. 1811, no. 11, p. 005, 2018.

[116] O. Grocholski, M. Kalinowski, M. Kolanowski, S. Renaux-Petel, K. Turzyński, and V. Vennin, "On backreaction effects in geometrical destabilisation of inflation," *JCAP*, vol. 05, p. 008, 2019.

[117] J. Fumagalli, S. Renaux-Petel, J. W. Ronayne, and L. T. Witkowski, "Turning in the landscape: a new mechanism for generating Primordial Black Holes," April 2020.

[118] G. A. Palma, S. Sypsas, and C. Zenteno, "Seeding primordial black holes in multifield inflation," *Phys. Rev. Lett.*, vol. 125, no. 12, p. 121301, 2020.

[119] M. Braglia, X. Chen, and D. K. Hazra, "Probing Primordial Features with the Stochastic Gravitational Wave Background," *JCAP*, vol. 03, p. 005, 2021.

[120] C. T. Byrnes, P. S. Cole, and S. P. Patil, "Steepest growth of the power spectrum and primordial black holes," *JCAP*, vol. 06, p. 028, 2019.

[121] J. Fumagalli, S. Renaux-Petel, and L. T. Witkowski, "Oscillations in the stochastic gravitational wave background from sharp features and particle production during inflation," *JCAP*, vol. 08, p. 030, 2021.

[122] A. Achucarro, J.-O. Gong, S. Hardeman, G. A. Palma, and S. P. Patil, "Features of heavy physics in the CMB power spectrum," *JCAP*, vol. 01, p. 030, 2011.

[123] X. Chen, "Primordial Non-Gaussianities from Inflation Models," *Adv. Astron.*, vol. 2010, p. 638979, 2010.

[124] J. Fumagalli, S. e. Renaux-Petel, and L. T. Witkowski, "Resonant features in the stochastic gravitational wave background," *JCAP*, vol. 08, p. 059, 2021.

[125] L. T. Witkowski, G. Domènech, J. Fumagalli, and S. Renaux-Petel, "Expansion history-dependent oscillations in the scalar-induced gravitational wave background," *JCAP*, vol. 05, no. 05, p. 028, 2022.

[126] J. Fumagalli, G. A. Palma, S. Renaux-Petel, S. Sypsas, L. T. Witkowski, and C. Zenteno, "Primordial gravitational waves from excited states," *JHEP*, vol. 03, p. 196, 2022.

[127] R. Kallosh and A. Linde, "Universality Class in Conformal Inflation," *JCAP*, vol. 07, p. 002, 2013.

[128] R. Kallosh and A. Linde, "Multi-field Conformal Cosmological Attractors," *JCAP*, vol. 12, p. 006, 2013.

[129] S. Ferrara, R. Kallosh, A. Linde, and M. Porrati, "Minimal Supergravity Models of Inflation," *Phys. Rev. D*, vol. 88, no. 8, p. 085038, 2013.

[130] R. Kallosh and A. Linde, "Superconformal generalization of the chaotic inflation model $\frac{\lambda}{4}\phi^4 - \frac{\xi}{2}\phi^2 R$," *JCAP*, vol. 06, p. 027, 2013.

[131] R. Kallosh and A. Linde, "Superconformal generalizations of the Starobinsky model," *JCAP*, vol. 06, p. 028, 2013.

[132] R. Kallosh and A. Linde, "Non-minimal Inflationary Attractors," *JCAP*, vol. 10, p. 033, 2013.

[133] R. Kallosh, A. Linde, and D. Roest, "Universal Attractor for Inflation at Strong Coupling," *Phys. Rev. Lett.*, vol. 112, no. 1, p. 011303, 2014.

[134] R. Kallosh, A. Linde, and D. Roest, "Superconformal Inflationary α-Attractors," *JHEP*, vol. 11, p. 198, 2013.

[135] D. Wands, K. A. Malik, D. H. Lyth, and A. R. Liddle, "A New approach to the evolution of cosmological perturbations on large scales," *Phys. Rev. D*, vol. 62, p. 043527, 2000.

[136] J. Martin, C. Ringeval, and V. Vennin, "Observing Inflationary Reheating," *Phys. Rev. Lett.*, vol. 114, no. 8, p. 081303, 2015.

[137] A. A. Starobinsky, "Spectrum of relict gravitational radiation and the early state of the universe," *JETP Lett.*, vol. 30, pp. 682–685, 1979.

[138] S. Dodelson, *Modern Cosmology*.
Amsterdam: Academic Press, 2003.

[139] J. Kovac, E. M. Leitch, C. Pryke, J. E. Carlstrom, N. W. Halverson, and W. L. Holzapfel, "Detection of polarization in the cosmic microwave background using DASI," *Nature*, vol. 420, pp. 772–787, 2002.

[140] D. Hanson *et al.*, "Detection of B-mode Polarization in the Cosmic Microwave Background with Data from the South Pole Telescope," *Phys. Rev. Lett.*, vol. 111, no. 14, p. 141301, 2013.

[141] L. A. Boyle, P. J. Steinhardt, and N. Turok, "The Cosmic gravitational wave background in a cyclic universe," *Phys. Rev. D*, vol. 69, p. 127302, 2004.

[142] P. A. R. Ade *et al.*, "Improved Constraints on Primordial Gravitational Waves using Planck, WMAP, and BICEP/Keck Observations through the 2018 Observing Season," *Phys. Rev. Lett.*, vol. 127, no. 15, p. 151301, 2021.

[143] K. N. Abazajian *et al.*, "CMB-S4 Science Book, First Edition," 10 2016.

[144] K. Abazajian *et al.*, "CMB-S4 Science Case, Reference Design, and Project Plan," July 2019.

[145] P. Ade *et al.*, "The Simons Observatory: Science goals and forecasts," *JCAP*, vol. 02, p. 056, 2019.

[146] M. Hazumi *et al.*, "LiteBIRD: A Satellite for the Studies of B-Mode Polarization and Inflation from Cosmic Background Radiation Detection," *J. Low. Temp. Phys.*, vol. 194, no. 5-6, pp. 443–452, 2019.

[147] S. Hanany *et al.*, "PICO: Probe of Inflation and Cosmic Origins," March 2019.

[148] T. L. Smith, M. Kamionkowski, and A. Cooray, "Direct detection of the inflationary gravitational wave background," *Phys. Rev. D*, vol. 73, p. 023504, 2006.

[149] K. Yagi and N. Seto, "Detector configuration of DECIGO/BBO and identification of cosmological neutron-star binaries," *Phys. Rev.*, vol. D83, p. 044011, 2011. [Erratum: Phys. Rev.D95,no.10,109901(2017)].

[150] H. V. Peiris *et al.*, "First year Wilkinson Microwave Anisotropy Probe (WMAP) observations: Implications for inflation," *Astrophys. J. Suppl.*, vol. 148, pp. 213–231, 2003.

[151] Y. Akrami *et al.*, "Planck 2018 results. IX. Constraints on primordial non-Gaussianity," *Astron. Astrophys.*, vol. 641, p. A9, 2020.

[152] P. A. R. Ade *et al.*, "Planck 2013 Results. XXIV. Constraints on primordial non-Gaussianity," *Astron. Astrophys.*, vol. 571, p. A24, 2014.

[153] J. M. Maldacena, "Non-Gaussian features of primordial fluctuations in single field inflationary models," *JHEP*, vol. 05, p. 013, 2003.

[154] E. Pajer, F. Schmidt, and M. Zaldarriaga, "The Observed Squeezed Limit of Cosmological Three-Point Functions," *Phys. Rev. D*, vol. 88, no. 8, p. 083502, 2013.

[155] G. Cabass, E. Pajer, and F. Schmidt, "How Gaussian can our Universe be?," *JCAP*, vol. 01, p. 003, 2017.

[156] S. Matarrese, L. Pilo, and R. Rollo, "Resilience of long modes in cosmological observables," *JCAP*, vol. 01, p. 062, 2021.

[157] D. Wands, "Local non-Gaussianity from inflation," *Class. Quant. Grav.*, vol. 27, p. 124002, 2010.

[158] L. Senatore, K. M. Smith, and M. Zaldarriaga, "Non-Gaussianities in Single Field Inflation and their Optimal Limits from the WMAP 5-year Data," *JCAP*, vol. 01, p. 028, 2010.

[159] N. Bartolo, M. Fasiello, S. Matarrese, and A. Riotto, "Large non-Gaussianities in the Effective Field Theory Approach to Single-Field Inflation: the Bispectrum," *JCAP*, vol. 08, p. 008, 2010.

[160] X. Chen, M.-x. Huang, S. Kachru, and G. Shiu, "Observational signatures and non-Gaussianities of general single field inflation," *JCAP*, vol. 01, p. 002, 2007.

[161] N. Arkani-Hamed, P. Creminelli, S. Mukohyama, and M. Zaldarriaga, "Ghost inflation," *JCAP*, vol. 04, p. 001, 2004.

[162] D. Wands, "Multiple field inflation," *Lect. Notes Phys.*, vol. 738, pp. 275–304, 2008.

[163] C. T. Byrnes and K.-Y. Choi, "Review of local non-Gaussianity from multi-field inflation," *Adv. Astron.*, vol. 2010, p. 724525, 2010.

[164] J. Fumagalli, S. Garcia-Saenz, L. Pinol, S. Renaux-Petel, and J. Ronayne, "Hyper-Non-Gaussianities in Inflation with Strongly Nongeodesic Motion," *Phys. Rev. Lett.*, vol. 123, no. 20, p. 201302, 2019.

[165] M. Shiraishi, "Tensor Non-Gaussianity Search: Current Status and Future Prospects," *Front. Astron. Space Sci.*, vol. 6, p. 49, 2019.

[166] E. Dimastrogiovanni, M. Fasiello, G. Tasinato, and D. Wands, "Tensor non-Gaussianities from Non-minimal Coupling to the Inflaton," *JCAP*, vol. 1902, p. 008, 2019.

[167] J. L. Cook and L. Sorbo, "Particle production during inflation and gravitational waves detectable by ground-based interferometers," *Phys. Rev. D*, vol. 85, p. 023534, 2012.
[Erratum: Phys.Rev.D 86, 069901 (2012)].

[168] J. L. Cook and L. Sorbo, "An inflationary model with small scalar and large tensor nongaussianities," *JCAP*, vol. 11, p. 047, 2013.

[169] E. Dimastrogiovanni, M. Fasiello, and T. Fujita, "Primordial Gravitational Waves from Axion-Gauge Fields Dynamics," *JCAP*, vol. 01, p. 019, 2017.

[170] R. Namba, M. Peloso, M. Shiraishi, L. Sorbo, and C. Unal, "Scale-dependent gravitational waves from a rolling axion," *JCAP*, vol. 01, p. 041, 2016.

[171] A. Agrawal, T. Fujita, and E. Komatsu, "Large tensor non-Gaussianity from axion-gauge field dynamics," *Phys. Rev. D*, vol. 97, no. 10, p. 103526, 2018.

[172] N. Bhaumik and R. K. Jain, "Primordial black holes dark matter from inflection point models of inflation and the effects of reheating," *JCAP*, vol. 01, p. 037, 2020.

[173] V. Aragam, R. Chiovoloni, S. Paban, R. Rosati, and I. Zavala, "Rapid-turn inflation in supergravity is rare and tachyonic," *JCAP*, vol. 03, no. 03, p. 002, 2022.

[174] B. J. Carr and S. W. Hawking, "Black Holes in the Early Universe," *Monthly Notices of the Royal Astronomical Society*, vol. 168, pp. 399–415, 08 1974.

[175] M. Sasaki, T. Suyama, T. Tanaka, and S. Yokoyama, "Primordial black holes—perspectives in gravitational wave astronomy," *Class. Quant. Grav.*, vol. 35, no. 6, p. 063001, 2018.

[176] S. Bird, I. Cholis, J. B. Muñoz, Y. Ali-Haïmoud, M. Kamionkowski, E. D. Kovetz, A. Raccanelli, and A. G. Riess, "Did LIGO detect dark matter?," *Phys. Rev. Lett.*, vol. 116, no. 20, p. 201301, 2016.

[177] G. Bertone and T. Tait, M. P., "A new era in the search for dark matter," *Nature*, vol. 562, no. 7725, pp. 51–56, 2018.

[178] N. Bartolo, V. De Luca, G. Franciolini, A. Lewis, M. Peloso, and A. Riotto, "Primordial Black Hole Dark Matter: LISA Serendipity," *Phys. Rev. Lett.*, vol. 122, no. 21, p. 211301, 2019.

[179] M. Sasaki, T. Suyama, T. Tanaka, and S. Yokoyama, "Primordial Black Hole Scenario for the Gravitational-Wave Event GW150914," *Phys. Rev. Lett.*, vol. 117, no. 6, p. 061101, 2016.
[Erratum: Phys.Rev.Lett. 121, 059901 (2018)].

[180] A. Hall, A. D. Gow, and C. T. Byrnes, "Bayesian analysis of LIGO-Virgo mergers: Primordial vs. astrophysical black hole populations," *Phys. Rev. D*, vol. 102, p. 123524, 2020.

[181] V. De Luca, G. Franciolini, P. Pani, and A. Riotto, "Primordial Black Holes Confront LIGO/Virgo data: Current situation," *JCAP*, vol. 06, p. 044, 2020.

[182] G. Franciolini, V. Baibhav, V. De Luca, K. K. Y. Ng, K. W. K. Wong, E. Berti, P. Pani, A. Riotto, and S. Vitale, "Searching for a subpopulation of primordial black holes in LIGO-Virgo gravitational-wave data," *Phys. Rev. D*, vol. 105, no. 8, p. 083526, 2022.

[183] B. Carr, K. Kohri, Y. Sendouda, and J. Yokoyama, "Constraints on primordial black holes," *Rept. Prog. Phys.*, vol. 84, no. 11, p. 116902, 2021.

[184] B. J. Carr, "The primordial black hole mass spectrum.," *ApJ*, vol. 201, pp. 1–19, Oct. 1975.

[185] J. C. Niemeyer and K. Jedamzik, "Near-critical gravitational collapse and the initial mass function of primordial black holes," *Phys. Rev. Lett.*, vol. 80, pp. 5481–5484, 1998.

[186] A. Kalaja, N. Bellomo, N. Bartolo, D. Bertacca, S. Matarrese, I. Musco, A. Raccanelli, and L. Verde, "From Primordial Black Holes Abundance to Primordial Curvature Power Spectrum (and back)," *JCAP*, vol. 1910, no. 10, p. 031, 2019.

[187] A. D. Gow, C. T. Byrnes, P. S. Cole, and S. Young, "The power spectrum on small scales: Robust constraints and comparing PBH methodologies," *JCAP*, vol. 02, p. 002, 2021.

[188] W. H. Press and P. Schechter, "Formation of Galaxies and Clusters of Galaxies by Self-Similar Gravitational Condensation," *ApJ*, vol. 187, pp. 425–438, Feb. 1974.

[189] J. M. Bardeen, J. R. Bond, N. Kaiser, and A. S. Szalay, "The Statistics of Peaks of Gaussian Random Fields," *ApJ*, vol. 304, p. 15, May 1986.

[190] S. Young, C. T. Byrnes, and M. Sasaki, "Calculating the mass fraction of primordial black holes," *JCAP*, vol. 07, p. 045, 2014.

[191] S. Young and M. Musso, "Application of peaks theory to the abundance of primordial black holes," *JCAP*, vol. 11, p. 022, 2020.

[192] M. Shibata and M. Sasaki, "Black hole formation in the Friedmann universe: Formulation and computation in numerical relativity," *Phys. Rev. D*, vol. 60, p. 084002, 1999.

[193] I. Musco, "Threshold for primordial black holes: Dependence on the shape of the cosmological perturbations," *Phys. Rev. D*, vol. 100, no. 12, p. 123524, 2019.

[194] I. Dalianis, "Constraints on the curvature power spectrum from primordial black hole evaporation," *JCAP*, vol. 08, p. 032, 2019.

[195] G. Sato-Polito, E. D. Kovetz, and M. Kamionkowski, "Constraints on the primordial curvature power spectrum from primordial black holes," *Phys. Rev. D*, vol. 100, no. 6, p. 063521, 2019.

[196] S. Young and C. T. Byrnes, "Primordial black holes in non-Gaussian regimes," *JCAP*, vol. 08, p. 052, 2013.

[197] C. Pattison, V. Vennin, H. Assadullahi, and D. Wands, "Quantum diffusion during inflation and primordial black holes," *JCAP*, vol. 10, p. 046, 2017.

[198] J. M. Ezquiaga, J. García-Bellido, and V. Vennin, "The exponential tail of inflationary fluctuations: consequences for primordial black holes," *JCAP*, vol. 03, p. 029, 2020.

[199] M. Biagetti, V. De Luca, G. Franciolini, A. Kehagias, and A. Riotto, "The formation probability of primordial black holes," *Phys. Lett. B*, vol. 820, p. 136602, 2021.

[200] N. Kitajima, Y. Tada, S. Yokoyama, and C.-M. Yoo, "Primordial black holes in peak theory with a non-Gaussian tail," *JCAP*, vol. 10, p. 053, 2021.

[201] S. W. Hawking, "Particle Creation by Black Holes," *Commun. Math. Phys.*, vol. 43, pp. 199–220, 1975.
[Erratum: Commun.Math.Phys. 46, 206 (1976)].

[202] B. J. Carr, K. Kohri, Y. Sendouda, and J. Yokoyama, "New cosmological constraints on primordial black holes," *Phys. Rev. D*, vol. 81, p. 104019, 2010.

[203] S. K. Acharya and R. Khatri, "CMB and BBN constraints on evaporating primordial black holes revisited," *JCAP*, vol. 06, p. 018, 2020.

[204] A. Barnacka, J. F. Glicenstein, and R. Moderski, "New constraints on primordial black holes abundance from femtolensing of gamma-ray bursts," *Phys. Rev. D*, vol. 86, p. 043001, 2012.

[205] K. Griest, A. M. Cieplak, and M. J. Lehner, "Experimental Limits on Primordial Black Hole Dark Matter from the First 2 yr of Kepler Data," *Astrophys. J.*, vol. 786, no. 2, p. 158, 2014.

[206] P. Tisserand *et al.*, "Limits on the Macho Content of the Galactic Halo from the EROS-2 Survey of the Magellanic Clouds," *Astron. Astrophys.*, vol. 469, pp. 387–404, 2007.

[207] H. Niikura *et al.*, "Microlensing constraints on primordial black holes with Subaru/HSC Andromeda observations," *Nature Astron.*, vol. 3, no. 6, pp. 524–534, 2019.

[208] K. Inomata, M. Kawasaki, K. Mukaida, Y. Tada, and T. T. Yanagida, "Inflationary Primordial Black Holes as All Dark Matter," *Phys. Rev. D*, vol. 96, no. 4, p. 043504, 2017.

[209] K. Tomita, "Non-Linear Theory of Gravitational Instability in the Expanding Universe," *Progress of Theoretical Physics*, vol. 37, pp. 831–846, 05 1967.

[210] S. Matarrese, S. Mollerach, and M. Bruni, "Second order perturbations of the Einstein-de Sitter universe," *Phys. Rev. D*, vol. 58, p. 043504, 1998.

[211] K. N. Ananda, C. Clarkson, and D. Wands, "The Cosmological gravitational wave background from primordial density perturbations," *Phys. Rev. D*, vol. 75, p. 123518, 2007.

[212] D. Baumann, P. J. Steinhardt, K. Takahashi, and K. Ichiki, "Gravitational Wave Spectrum Induced by Primordial Scalar Perturbations," *Phys. Rev. D*, vol. 76, p. 084019, 2007.

[213] H. Assadullahi and D. Wands, "Constraints on primordial density perturbations from induced gravitational waves," *Phys. Rev. D*, vol. 81, p. 023527, 2010.

[214] G. Domènech, "Scalar Induced Gravitational Waves Review," *Universe*, vol. 7, no. 11, p. 398, 2021.

[215] D. H. Lyth and A. Riotto, "Particle physics models of inflation and the cosmological density perturbation," *Phys. Rept.*, vol. 314, pp. 1–146, 1999.

[216] V. Acquaviva, N. Bartolo, S. Matarrese, and A. Riotto, "Second order cosmological perturbations from inflation," *Nucl. Phys. B*, vol. 667, pp. 119–148, 2003.

[217] J. R. Espinosa, D. Racco, and A. Riotto, "A Cosmological Signature of the SM Higgs Instability: Gravitational Waves," *JCAP*, vol. 09, p. 012, 2018.

[218] G. Domènech, "Induced gravitational waves in a general cosmological background," *Int. J. Mod. Phys. D*, vol. 29, no. 03, p. 2050028, 2020.

[219] G. Domènech, S. Pi, and M. Sasaki, "Induced gravitational waves as a probe of thermal history of the universe," *JCAP*, vol. 08, p. 017, 2020.

[220] S. Pi and M. Sasaki, "Gravitational Waves Induced by Scalar Perturbations with a Lognormal Peak," *JCAP*, vol. 09, p. 037, 2020.

[221] G. Janssen *et al.*, "Gravitational wave astronomy with the SKA," *PoS*, vol. AASKA14, p. 037, 2015.

[222] P. Amaro-Seoane *et al.*, "Laser Interferometer Space Antenna," 2017.

[223] M. Maggiore *et al.*, "Science Case for the Einstein Telescope," *JCAP*, vol. 03, p. 050, 2020.

[224] D. Reitze *et al.*, "Cosmic Explorer: The U.S. Contribution to Gravitational-Wave Astronomy beyond LIGO," *Bull. Am. Astron. Soc.*, vol. 51, no. 7, p. 035, 2019.

[225] B. P. Abbott *et al.*, "Upper Limits on the Stochastic Gravitational-Wave Background from Advanced LIGO's First Observing Run," *Phys. Rev. Lett.*, vol. 118, no. 12, p. 121101, 2017.
[Erratum: Phys.Rev.Lett. 119, 029901 (2017)].

[226] A. Achucarro, J.-O. Gong, S. Hardeman, G. A. Palma, and S. P. Patil, "Effective theories of single field inflation when heavy fields matter," *JHEP*, vol. 05, p. 066, 2012.

[227] C. P. Burgess, M. W. Horbatsch, and S. Patil, "Inflating in a Trough: Single-Field Effective Theory from Multiple-Field Curved Valleys," *JHEP*, vol. 01, p. 133, 2013.

[228] A. J. Tolley and M. Wyman, "The Gelaton Scenario: Equilateral non-Gaussianity from multi-field dynamics," *Phys. Rev.*, vol. D81, p. 043502, 2010.

[229] J.-O. Gong, S. Pi, and M. Sasaki, "Equilateral non-Gaussianity from heavy fields," *JCAP*, vol. 11, p. 043, 2013.

[230] E. Dimastrogiovanni, M. Fasiello, and A. J. Tolley, "Low-Energy Effective Field Theory for Chromo-Natural Inflation," *JCAP*, vol. 1302, p. 046, 2013.

[231] E. Silverstein, "The dangerous irrelevance of string theory," 2017.

[232] S. Garcia-Saenz, L. Pinol, and S. Renaux-Petel, "Revisiting non-Gaussianity in multifield inflation with curved field space," *JHEP*, vol. 01, p. 073, 2020.

[233] T. Noumi, M. Yamaguchi, and D. Yokoyama, "Effective field theory approach to quasi-single field inflation and effects of heavy fields," *JHEP*, vol. 06, p. 051, 2013.

[234] N. Arkani-Hamed and J. Maldacena, "Cosmological Collider Physics," 2015.

[235] D. Jeong and M. Kamionkowski, "Clustering Fossils from the Early Universe," *Phys. Rev. Lett.*, vol. 108, p. 251301, 2012.

[236] A. Higuchi, "Forbidden Mass Range for Spin-2 Field Theory in De Sitter Space-time," *Nucl. Phys.*, vol. B282, pp. 397–436, 1987.

[237] M. Fasiello and A. J. Tolley, "Cosmological Stability Bound in Massive Gravity and Bigravity," *JCAP*, vol. 1312, p. 002, 2013.

[238] L. H. Thomas, "On unitary representations of the group of de sitter space," *Annals of Mathematics*, vol. 42, no. 1, pp. 113–126, 1941.

[239] B. Himmetoglu, C. R. Contaldi, and M. Peloso, "Ghost instabilities of cosmological models with vector fields nonminimally coupled to the curvature," *Phys. Rev.*, vol. D80, p. 123530, 2009.

[240] D. Sorokin, "Introduction to the classical theory of higher spins," *AIP Conf. Proc.*, vol. 767, no. 1, pp. 172–202, 2005.

[241] N. Bouatta, G. Compere, and A. Sagnotti, "An Introduction to free higher-spin fields," in *Higher spin gauge theories: Proceedings, 1st Solvay Workshop: Brussels, Belgium, 12-14 May, 2004*, pp. 79–99, 2004.

[242] C. de Rham, G. Gabadadze, and A. J. Tolley, "Resummation of Massive Gravity," *Phys. Rev. Lett.*, vol. 106, p. 231101, 2011.

[243] S. F. Hassan and R. A. Rosen, "Bimetric Gravity from Ghost-free Massive Gravity," *JHEP*, vol. 02, p. 126, 2012.

[244] M. Biagetti, E. Dimastrogiovanni, and M. Fasiello, "Possible signatures of the inflationary particle content: spin-2 fields," *JCAP*, vol. 1710, no. 10, p. 038, 2017.

[245] E. Dimastrogiovanni, M. Fasiello, and G. Tasinato, "Probing the inflationary particle content: extra spin-2 field," *JCAP*, vol. 1808, no. 08, p. 016, 2018.

[246] G. Goon, K. Hinterbichler, A. Joyce, and M. Trodden, "Shapes of gravity: Tensor non-Gaussianity and massive spin-2 fields," *JHEP*, vol. 10, p. 182, 2019.

[247] E. Dimastrogiovanni, M. Fasiello, and A. E. Gümrükcüoglü, "Spinning guest fields during inflation: leftover signatures," *JCAP*, vol. 11, no. 11, p. 047, 2021.

[248] T. Fujita, S. Mizuno, and S. Mukohyama, "Primordial Tensor Non-Gaussianity from Massive Gravity," *JCAP*, vol. 01, p. 023, 2020.

[249] M. M. Anber and L. Sorbo, "Naturally inflating on steep potentials through electromagnetic dissipation," *Phys. Rev.*, vol. D81, p. 043534, 2010.

[250] N. Barnaby and M. Peloso, "Large Nongaussianity in Axion Inflation," *Phys. Rev. Lett.*, vol. 106, p. 181301, 2011.

[251] P. Adshead and M. Wyman, "Chromo-Natural Inflation: Natural inflation on a steep potential with classical non-Abelian gauge fields," *Phys. Rev. Lett.*, vol. 108, p. 261302, 2012.

[252] N. Barnaby, J. Moxon, R. Namba, M. Peloso, G. Shiu, and P. Zhou, "Gravity waves and non-Gaussian features from particle production in a sector gravitationally coupled to the inflaton," *Phys. Rev.*, vol. D86, p. 103508, 2012.

[253] A. Maleknejad, M. M. Sheikh-Jabbari, and J. Soda, "Gauge Fields and Inflation," *Phys. Rept.*, vol. 528, pp. 161–261, 2013.

[254] J. Garcia-Bellido, M. Peloso, and C. Unal, "Gravitational waves at interferometer scales and primordial black holes in axion inflation," *JCAP*, vol. 1612, no. 12, p. 031, 2016.

[255] B. Thorne, T. Fujita, M. Hazumi, N. Katayama, E. Komatsu, and M. Shiraishi, "Finding the chiral gravitational wave background of an axion-SU(2) inflationary model using CMB observations and laser interferometers," *Phys. Rev.*, vol. D97, no. 4, p. 043506, 2018.

[256] V. Domcke, B. Mares, F. Muia, and M. Pieroni, "Emerging chromo-natural inflation," *JCAP*, vol. 1904, p. 034, 2019.

[257] A. R. Liddle and S. M. Leach, "How long before the end of inflation were observable perturbations produced?," *Phys. Rev. D*, vol. 68, p. 103503, 2003.

[258] T. Fujita, J. Yokoyama, and S. Yokoyama, "Can a spectator scalar field enhance inflationary tensor mode?," *PTEP*, vol. 2015, p. 043E01, 2015.

[259] M. Biagetti, M. Fasiello, and A. Riotto, "Enhancing Inflationary Tensor Modes through Spectator Fields," *Phys. Rev.*, vol. D88, p. 103518, 2013.

[260] M. Biagetti, E. Dimastrogiovanni, M. Fasiello, and M. Peloso, "Gravitational Waves and Scalar Perturbations from Spectator Fields," *JCAP*, vol. 1504, p. 011, 2015.

[261] C. de Rham and A. J. Tolley, "Causality in curved spacetimes: The speed of light and gravity," *Phys. Rev. D*, vol. 102, no. 8, p. 084048, 2020.

[262] J. Chluba, R. Khatri, and R. A. Sunyaev, "CMB at 2x2 order: The dissipation of primordial acoustic waves and the observable part of the associated energy release," *Mon. Not. Roy. Astron. Soc.*, vol. 425, pp. 1129–1169, 2012.

[263] A. S. Josan, A. M. Green, and K. A. Malik, "Generalised constraints on the curvature perturbation from primordial black holes," *Phys. Rev.*, vol. D79, p. 103520, 2009.

[264] B. Carr, M. Raidal, T. Tenkanen, V. Vaskonen, and H. VeermÃ¤e, "Primordial black hole constraints for extended mass functions," *Phys. Rev.*, vol. D96, no. 2, p. 023514, 2017.

[265] R. Emami and G. Smoot, "Observational Constraints on the Primordial Curvature Power Spectrum," *JCAP*, vol. 1801, no. 01, p. 007, 2018.

[266] M. Ricotti and A. Gould, "A New Probe of Dark Matter and High-Energy Universe Using Microlensing," *Astrophys. J.*, vol. 707, pp. 979–987, 2009.

[267] B. P. Abbott *et al.*, "Search for the isotropic stochastic background using data from Advanced LIGOâs second observing run," *Phys. Rev.*, vol. D100, no. 6, p. 061101, 2019.

[268] L. Pagano, L. Salvati, and A. Melchiorri, "New constraints on primordial gravitational waves from Planck 2015," *Phys. Lett. B*, vol. 760, pp. 823–825, 2016.

[269] D. R. Lorimer, "Binary and Millisecond Pulsars," *Living Rev. Rel.*, vol. 11, p. 8, 2008.

[270] C. Caprini, D. G. Figueroa, R. Flauger, G. Nardini, M. Peloso, M. Pieroni, A. Ricciardone, and G. Tasinato, "Reconstructing the spectral shape of a stochastic gravitational wave background with LISA," *JCAP*, vol. 11, p. 017, 2019.

[271] P. Auclair *et al.*, "Cosmology with the Laser Interferometer Space Antenna," April 2022.

[272] E. Thrane and J. D. Romano, "Sensitivity curves for searches for gravitational-wave backgrounds," *Phys. Rev.*, vol. D88, no. 12, p. 124032, 2013.

[273] E. Pajer and M. Peloso, "A review of Axion Inflation in the era of Planck," *Class. Quant. Grav.*, vol. 30, p. 214002, 2013.

[274] K. Freese, J. A. Frieman, and A. V. Olinto, "Natural inflation with pseudo - Nambu-Goldstone bosons," *Phys. Rev. Lett.*, vol. 65, pp. 3233–3236, 1990.

[275] P. Adshead, E. Martinec, E. I. Sfakianakis, and M. Wyman, "Higgsed Chromo-Natural Inflation," *JHEP*, vol. 12, p. 137, 2016.

[276] Y. Watanabe and E. Komatsu, "Gravitational Wave from Axion-SU(2) Gauge Fields: Effective Field Theory for Kinetically Driven Inflation," 4 2020.

[277] T. Regimbau, "The astrophysical gravitational wave stochastic background," *Res. Astron. Astrophys.*, vol. 11, pp. 369–390, 2011.

[278] E. Dimastrogiovanni, M. Fasiello, and G. Tasinato, "Searching for Fossil Fields in the Gravity Sector," *Phys. Rev. Lett.*, vol. 124, no. 6, p. 061302, 2020.

[279] N. Bartolo, D. Bertacca, S. Matarrese, M. Peloso, A. Ricciardone, A. Riotto, and G. Tasinato, "Anisotropies and non-Gaussianity of the Cosmological Gravitational Wave Background," *Phys. Rev. D*, vol. 100, no. 12, p. 121501, 2019.

[280] N. Bartolo, V. De Luca, G. Franciolini, M. Peloso, D. Racco, and A. Riotto, "Testing primordial black holes as dark matter with LISA," *Phys. Rev. D*, vol. 99, no. 10, p. 103521, 2019.

[281] L. Dai, D. Jeong, and M. Kamionkowski, "Anisotropic imprint of long-wavelength tensor perturbations on cosmic structure," *Phys. Rev. D*, vol. 88, no. 4, p. 043507, 2013.

[282] S. Brahma, E. Nelson, and S. Shandera, "Fossilized Gravitational Wave Relic and Primordial Clocks," *Phys. Rev. D*, vol. 89, no. 2, p. 023507, 2014.

[283] E. Dimastrogiovanni, M. Fasiello, D. Jeong, and M. Kamionkowski, "Inflationary tensor fossils in large-scale structure," *JCAP*, vol. 12, p. 050, 2014.

[284] E. Dimastrogiovanni, M. Fasiello, and M. Kamionkowski, "Imprints of Massive Primordial Fields on Large-Scale Structure," *JCAP*, vol. 02, p. 017, 2016.

[285] X. Chen, M.-x. Huang, S. Kachru, and G. Shiu, "Observational signatures and non-gaussianities of general single-field inflation," *JCAP*, vol. 2007, Jan 2007.

[286] X. Chen and Y. Wang, "Quasi-Single Field Inflation and Non-Gaussianities," *JCAP*, vol. 04, p. 027, 2010.

[287] S. Weinberg, "Quantum contributions to cosmological correlations," *Phys. Rev. D*, vol. 72, p. 043514, 2005.

[288] P. Creminelli, G. D'Amico, M. Musso, J. Norena, and E. Trincherini, "Galilean symmetry in the effective theory of inflation: new shapes of non-Gaussianity," *JCAP*, vol. 1102, p. 006, 2011.

[289] K. Hinterbichler, L. Hui, and J. Khoury, "An Infinite Set of Ward Identities for Adiabatic Modes in Cosmology," *JCAP*, vol. 01, p. 039, 2014.

[290] A. Ricciardone and G. Tasinato, "Anisotropic tensor power spectrum at interferometer scales induced by tensor squeezed non-Gaussianity," *JCAP*, vol. 02, p. 011, 2018.

[291] C. R. Contaldi, "Anisotropies of Gravitational Wave Backgrounds: A Line Of Sight Approach," *Phys. Lett. B*, vol. 771, pp. 9–12, 2017.

[292] N. Bartolo, D. Bertacca, S. Matarrese, M. Peloso, A. Ricciardone, A. Riotto, and G. Tasinato, "Characterizing the cosmological gravitational wave background: Anisotropies and non-Gaussianity," *Phys. Rev. D*, vol. 102, no. 2, p. 023527, 2020.

[293] O. Ozsoy, M. Mylova, S. Parameswaran, C. Powell, G. Tasinato, and I. Zavala, "Squeezed tensor non-Gaussianity in non-attractor inflation," *JCAP*, vol. 09, p. 036, 2019.

[294] N. Bartolo *et al.*, "Probing Anisotropies of the Stochastic Gravitational Wave Background with LISA," 1 2022.

[295] M. Tsuneto, A. Ito, T. Noumi, and J. Soda, "Searching for bispectrum of stochastic gravitational waves with pulsar timing arrays," *JCAP*, vol. 2019, p. 032, Mar 2019.

[296] D. Alonso, C. R. Contaldi, G. Cusin, P. G. Ferreira, and A. I. Renzini, "Noise angular power spectrum of gravitational wave background experiments," *Phys. Rev. D*, vol. 101, no. 12, p. 124048, 2020.

[297] C. M. Mingarelli, T. Sidery, I. Mandel, and A. Vecchio, "Characterizing gravitational wave stochastic background anisotropy with pulsar timing arrays," *Phys. Rev. D*, vol. 88, no. 6, p. 062005, 2013.

[298] P. Adshead, N. Afshordi, E. Dimastrogiovanni, M. Fasiello, E. A. Lim, and G. Tasinato, "Multimessenger cosmology: Correlating cosmic microwave background and stochastic gravitational wave background measurements," *Phys. Rev. D*, vol. 103, no. 2, p. 023532, 2021.

[299] R. Kallosh and A. Linde, "Escher in the Sky," *Comptes Rendus Physique*, vol. 16, pp. 914–927, 2015.

[300] J. J. M. Carrasco, R. Kallosh, A. Linde, and D. Roest, "Hyperbolic geometry of cosmological attractors," *Phys. Rev. D*, vol. 92, no. 4, p. 041301, 2015.

[301] M. Galante, R. Kallosh, A. Linde, and D. Roest, "Unity of Cosmological Inflation Attractors," *Phys. Rev. Lett.*, vol. 114, no. 14, p. 141302, 2015.

[302] J. Fumagalli, "Renormalization Group independence of Cosmological Attractors," *Phys. Lett. B*, vol. 769, pp. 451–459, 2017.

[303] A. Achúcarro, R. Kallosh, A. Linde, D.-G. Wang, and Y. Welling, "Universality of multi-field α-attractors," *JCAP*, vol. 04, p. 028, 2018.

[304] A. Linde, D.-G. Wang, Y. Welling, Y. Yamada, and A. Achúcarro, "Hypernatural inflation," *JCAP*, vol. 07, p. 035, 2018.

[305] P. Christodoulidis, D. Roest, and E. I. Sfakianakis, "Angular inflation in multi-field α-attractors," *JCAP*, vol. 11, p. 002, 2019.

[306] T. Krajewski, K. Turzyński, and M. Wieczorek, "On preheating in α-attractor models of inflation," *Eur. Phys. J. C*, vol. 79, no. 8, p. 654, 2019.

[307] O. Iarygina, E. I. Sfakianakis, D.-G. Wang, and A. Achucarro, "Universality and scaling in multi-field α-attractor preheating," *JCAP*, vol. 06, p. 027, 2019.

[308] O. Iarygina, E. I. Sfakianakis, D.-G. Wang, and A. Achúcarro, "Multi-field inflation and preheating in asymmetric α-attractors," 5 2020.

[309] V. N. Senoguz and Q. Shafi, "Chaotic inflation, radiative corrections and precision cosmology," *Phys. Lett. B*, vol. 668, pp. 6–10, 2008.

[310] R. Kallosh and A. Linde, "BICEP/Keck and Cosmological Attractors," 10 2021.

[311] S. S. Mishra and V. Sahni, "Primordial Black Holes from a tiny bump/dip in the Inflaton potential," *JCAP*, vol. 04, p. 007, 2020.

[312] S. Wang, T. Terada, and K. Kohri, "Prospective constraints on the primordial black hole abundance from the stochastic gravitational-wave backgrounds produced by coalescing events and curvature perturbations," *Phys. Rev. D*, vol. 99, no. 10, p. 103531, 2019.
[Erratum: Phys.Rev.D 101, 069901 (2020)].

[313] D. Hooper, G. Krnjaic, and S. D. McDermott, "Dark Radiation and Superheavy Dark Matter from Black Hole Domination," *JHEP*, vol. 08, p. 001, 2019.

[314] J. Kozaczuk, T. Lin, and E. Villarama, "Signals of primordial black holes at gravitational wave interferometers," 8 2021.

[315] R. Anantua, R. Easther, and J. T. Giblin, "GUT-Scale Primordial Black Holes: Consequences and Constraints," *Phys. Rev. Lett.*, vol. 103, p. 111303, 2009.

[316] J. L. Zagorac, R. Easther, and N. Padmanabhan, "GUT-Scale Primordial Black Holes: Mergers and Gravitational Waves," *JCAP*, vol. 06, p. 052, 2019.

[317] J. Martin, T. Papanikolaou, and V. Vennin, "Primordial black holes from the preheating instability in single-field inflation," *JCAP*, vol. 01, p. 024, 2020.

[318] K. Inomata, M. Kawasaki, K. Mukaida, T. Terada, and T. T. Yanagida, "Gravitational Wave Production right after a Primordial Black Hole Evaporation," *Phys. Rev. D*, vol. 101, no. 12, p. 123533, 2020.

[319] T. Papanikolaou, V. Vennin, and D. Langlois, "Gravitational waves from a universe filled with primordial black holes," *JCAP*, vol. 03, p. 053, 2021.

[320] G. Domènech, C. Lin, and M. Sasaki, "Gravitational wave constraints on the primordial black hole dominated early universe," *JCAP*, vol. 04, p. 062, 2021.

[321] J. H. MacGibbon, "Can Planck-mass relics of evaporating black holes close the universe?," *Nature*, vol. 329, pp. 308–309, 1987.

[322] J. D. Barrow, E. J. Copeland, and A. R. Liddle, "The Cosmology of black hole relics," *Phys. Rev. D*, vol. 46, pp. 645–657, 1992.

[323] B. J. Carr, J. H. Gilbert, and J. E. Lidsey, "Black hole relics and inflation: Limits on blue perturbation spectra," *Phys. Rev. D*, vol. 50, pp. 4853–4867, 1994.

[324] I. Dalianis and G. Tringas, "Primordial black hole remnants as dark matter produced in thermal, matter, and runaway-quintessence postinflationary scenarios," *Phys. Rev. D*, vol. 100, no. 8, p. 083512, 2019.

[325] B. V. Lehmann, C. Johnson, S. Profumo, and T. Schwemberger, "Direct detection of primordial black hole relics as dark matter," *JCAP*, vol. 10, p. 046, 2019.

[326] V. Atal and G. Domènech, "Probing non-Gaussianities with the high frequency tail of induced gravitational waves," *JCAP*, vol. 06, p. 001, 2021.

[327] K. Inomata, K. Kohri, T. Nakama, and T. Terada, "Gravitational Waves Induced by Scalar Perturbations during a Gradual Transition from an Early Matter Era to the Radiation Era," *JCAP*, vol. 10, p. 071, 2019.

[328] H. Assadullahi and D. Wands, "Gravitational waves from an early matter era," *Phys. Rev. D*, vol. 79, p. 083511, 2009.

[329] K. Inomata and T. Terada, "Gauge Independence of Induced Gravitational Waves," *Phys. Rev. D*, vol. 101, no. 2, p. 023523, 2020.

[330] M. Magi and J. Yoo, "Second-order gauge-invariant formalism for the cosmological observables: complete verification of their gauge-invariance," *JCAP*, vol. 09, p. 071, 2022.

[331] J.-C. Hwang, D. Jeong, and H. Noh, "Gauge dependence of gravitational waves generated from scalar perturbations," *Astrophys. J.*, vol. 842, no. 1, p. 46, 2017.

[332] K. Tomikawa and T. Kobayashi, "Gauge dependence of gravitational waves generated at second order from scalar perturbations," *Phys. Rev. D*, vol. 101, no. 8, p. 083529, 2020.

[333] K. Inomata, K. Kohri, T. Nakama, and T. Terada, "Enhancement of Gravitational Waves Induced by Scalar Perturbations due to a Sudden Transition from an Early Matter Era to the Radiation Era," *Phys. Rev. D*, vol. 100, no. 4, p. 043532, 2019.

[334] R. K. Jain, P. Chingangbam, J.-O. Gong, L. Sriramkumar, and T. Souradeep, "Punctuated inflation and the low CMB multipoles," *JCAP*, vol. 01, p. 009, 2009.

[335] H. V. Ragavendra, P. Saha, L. Sriramkumar, and J. Silk, "Primordial black holes and secondary gravitational waves from ultraslow roll and punctuated inflation," *Phys. Rev. D*, vol. 103, no. 8, p. 083510, 2021.

[336] M. Dias, J. Frazer, and D. Seery, "Computing observables in curved multifield models of inflation—A guide (with code) to the transport method," *JCAP*, vol. 12, p. 030, 2015.

[337] Y. Aldabergenov, A. Addazi, and S. V. Ketov, "Primordial black holes from modified supergravity," *Eur. Phys. J. C*, vol. 80, no. 10, p. 917, 2020.

[338] R. Ishikawa and S. V. Ketov, "Exploring the parameter space of modified supergravity for double inflation and primordial black hole formation," 8 2021.

[339] P. Carrilho, K. A. Malik, and D. J. Mulryne, "Dissecting the growth of the power spectrum for primordial black holes," *Phys. Rev. D*, vol. 100, no. 10, p. 103529, 2019.

[340] O. Özsoy and G. Tasinato, "On the slope of the curvature power spectrum in non-attractor inflation," *JCAP*, vol. 04, p. 048, 2020.

[341] X. Chen, R. Easther, and E. A. Lim, "Generation and Characterization of Large Non-Gaussianities in Single Field Inflation," *JCAP*, vol. 04, p. 010, 2008.

[342] J. Chluba, J. Hamann, and S. P. Patil, "Features and New Physical Scales in Primordial Observables: Theory and Observation," *Int. J. Mod. Phys. D*, vol. 24, no. 10, p. 1530023, 2015.

[343] A. Slosar *et al.*, "Scratches from the Past: Inflationary Archaeology through Features in the Power Spectrum of Primordial Fluctuations," 3 2019.

[344] N. Aggarwal *et al.*, "Challenges and Opportunities of Gravitational Wave Searches at MHz to GHz Frequencies," 11 2020.

[345] J. S. Bullock and J. R. Primack, "NonGaussian fluctuations and primordial black holes from inflation," *Phys. Rev. D*, vol. 55, pp. 7423–7439, 1997.

[346] R. Saito, J. Yokoyama, and R. Nagata, "Single-field inflation, anomalous enhancement of superhorizon fluctuations, and non-Gaussianity in primordial black hole formation," *JCAP*, vol. 06, p. 024, 2008.

[347] C. T. Byrnes, E. J. Copeland, and A. M. Green, "Primordial black holes as a tool for constraining non-Gaussianity," *Phys. Rev. D*, vol. 86, p. 043512, 2012.

[348] E. V. Bugaev and P. A. Klimai, "Primordial black hole constraints for curvaton models with predicted large non-Gaussianity," *Int. J. Mod. Phys. D*, vol. 22, p. 1350034, 2013.

[349] S. Young and C. T. Byrnes, "Long-short wavelength mode coupling tightens primordial black hole constraints," *Phys. Rev. D*, vol. 91, no. 8, p. 083521, 2015.

[350] S. Young, D. Regan, and C. T. Byrnes, "Influence of large local and non-local bispectra on primordial black hole abundance," *JCAP*, vol. 02, p. 029, 2016.

[351] G. Franciolini, A. Kehagias, S. Matarrese, and A. Riotto, "Primordial Black Holes from Inflation and non-Gaussianity," *JCAP*, vol. 03, p. 016, 2018.

[352] V. Atal and C. Germani, "The role of non-gaussianities in Primordial Black Hole formation," *Phys. Dark Univ.*, vol. 24, p. 100275, 2019.

[353] V. De Luca, G. Franciolini, A. Kehagias, M. Peloso, A. Riotto, and C. Ünal, "The Ineludible non-Gaussianity of the Primordial Black Hole Abundance," *JCAP*, vol. 07, p. 048, 2019.

[354] O. Özsoy and G. Tasinato, "CMB μT cross correlations as a probe of primordial black hole scenarios," *Phys. Rev. D*, vol. 104, no. 4, p. 043526, 2021.

[355] M. Taoso and A. Urbano, "Non-gaussianities for primordial black hole formation," *JCAP*, vol. 08, p. 016, 2021.

[356] M. W. Davies, P. Carrilho, and D. J. Mulryne, "Non-Gaussianity in inflationary scenarios for primordial black holes," 10 2021.

[357] R.-g. Cai, S. Pi, and M. Sasaki, "Gravitational Waves Induced by non-Gaussian Scalar Perturbations," *Phys. Rev. Lett.*, vol. 122, no. 20, p. 201101, 2019.

[358] C. Unal, "Imprints of Primordial Non-Gaussianity on Gravitational Wave Spectrum," *Phys. Rev. D*, vol. 99, no. 4, p. 041301, 2019.

[359] C. Yuan and Q.-G. Huang, "Gravitational waves induced by the local-type non-Gaussian curvature perturbations," *Phys. Lett. B*, vol. 821, p. 136606, 2021.

[360] P. Adshead, K. D. Lozanov, and Z. J. Weiner, "Non-Gaussianity and the induced gravitational wave background," *JCAP*, vol. 10, p. 080, 2021.

[361] D. Seery, "CppTransport: a platform to automate calculation of inflationary correlation functions," 9 2016.

[362] D. J. Mulryne and J. W. Ronayne, "PyTransport: A Python package for the calculation of inflationary correlation functions," *J. Open Source Softw.*, vol. 3, no. 23, p. 494, 2018.

[363] J. W. Ronayne and D. J. Mulryne, "Numerically evaluating the bispectrum in curved field-space— with PyTransport 2.0," *JCAP*, vol. 01, p. 023, 2018.

[364] J. Ellis, M. A. G. Garcia, D. V. Nanopoulos, K. A. Olive, and S. Verner, "BICEP/Keck constraints on attractor models of inflation and reheating," *Phys. Rev. D*, vol. 105, no. 4, p. 043504, 2022.

[365] P. A. R. Ade *et al.*, "Planck 2013 results. XXII. Constraints on inflation," *Astron. Astrophys.*, vol. 571, p. A22, 2014.

[366] B. A. Bassett, S. Tsujikawa, and D. Wands, "Inflation dynamics and reheating," *Rev. Mod. Phys.*, vol. 78, pp. 537–589, 2006.

[367] K. Kefala, G. Kodaxis, I. Stamou, and N. Tetradis, "Features of the inflaton potential and the power spectrum of cosmological perturbations," 10 2020.

[368] J. A. Adams, B. Cresswell, and R. Easther, "Inflationary perturbations from a potential with a step," *Phys. Rev. D*, vol. 64, p. 123514, 2001.

[369] F. Di Marco, F. Finelli, and R. Brandenberger, "Adiabatic and isocurvature perturbations for multifield generalized Einstein models," *Phys. Rev. D*, vol. 67, p. 063512, 2003.

[370] F. Di Marco and F. Finelli, "Slow-roll inflation for generalized two-field Lagrangians," *Phys. Rev. D*, vol. 71, p. 123502, 2005.

[371] Z. Lalak, D. Langlois, S. Pokorski, and K. Turzynski, "Curvature and isocurvature perturbations in two-field inflation," *JCAP*, vol. 07, p. 014, 2007.

[372] A. Ball, E. Himwich, S. A. Narayanan, S. Pasterski, and A. Strominger, "Uplifting AdS_3/CFT_2 to flat space holography," *JHEP*, vol. 08, p. 168, 2019.

[373] M. Spradlin, A. Strominger, and A. Volovich, "Les Houches lectures on de Sitter space," in *Les Houches Summer School: Session 76: Euro Summer School on Unity of Fundamental Physics: Gravity, Gauge Theory and Strings*, 10 2001.

FORM UPR16

Research Ethics Review Checklist

Please include this completed form as an appendix to your thesis (see the Research Degrees Operational Handbook for more information

Postgraduate Research Student (PGRS) Information		**Student ID:**	912043
PGRS Name:	LAURA IACCONI		
Department:	ICG, DEPARTMENT OF TECHNOLOGY	**First Supervisor:**	DAVID WANDS
Start Date: (or progression date for Prof Doc students)	01/10/2018		

Study Mode and Route:	Part-time ☐	MPhil ☐	MD ☐
	Full-time ☒	PhD ☒	Professional Doctorate ☐

Title of Thesis:	TESTING THE FIELD CONTENT OF COSMIC INFLATION
Thesis Word Count: (excluding ancillary data)	45008

If you are unsure about any of the following, please contact the local representative on your Faculty Ethics Committee for advice. Please note that it is your responsibility to follow the University's Ethics Policy and any relevant University, academic or professional guidelines in the conduct of your study

Although the Ethics Committee may have given your study a favourable opinion, the final responsibility for the ethical conduct of this work lies with the researcher(s).

UKRIO Finished Research Checklist:
(If you would like to know more about the checklist, please see your Faculty or Departmental Ethics Committee rep or see the online version of the full checklist at: http://www.ukrio.org/what-we-do/code-of-practice-for-research/)

a) Have all of your research and findings been reported accurately, honestly and within a reasonable time frame?	YES ☒ NO ☐
b) Have all contributions to knowledge been acknowledged?	YES ☒ NO ☐
c) Have you complied with all agreements relating to intellectual property, publication and authorship?	YES ☒ NO ☐
d) Has your research data been retained in a secure and accessible form and will it remain so for the required duration?	YES ☒ NO ☐
e) Does your research comply with all legal, ethical, and contractual requirements?	YES ☒ NO ☐

Candidate Statement:

I have considered the ethical dimensions of the above named research project, and have successfully obtained the necessary ethical approval(s)

Ethical review number(s) from Faculty Ethics Committee (or from NRES/SCREC):	ETHIC-2019-780

If you have *not* submitted your work for ethical review, and/or you have answered 'No' to one or more of questions a) to e), please explain below why this is so:

Signed *(PGRS)*:	LAURA IACCONI	**Date:** 09/01/2023